

WARSAW UNIVERSITY OF TECHNOLOGY

FACULTY OF ELECTRONICS AND INFORMATION TECHNOLOGY

Ph.D. Thesis

Marcin Ziembicki, M.Sc.

Scintillating Fiber Detectors
for High Energy Physics Experiments

Supervisor
Janusz Marzec, Ph.D., D.Sc.

WARSAW, 2019

Abstract

Tracking detectors made of plastic scintillating fibers is a well-established technology in high energy physics experiments. They are continuously improved, and new applications are either developed or under consideration. The advantages which led to their widespread adoption in various experiments include excellent timing properties, decent spatial resolution, good radiation hardness, ability to withstand high hit rates, and finally, the possibility to manufacture almost any shape of the detector.

Building a detector is a complicated task requiring a thorough understanding of mechanisms of particle interactions, the scintillation process, detector optics, photosensors, readout electronics, and the methods used to extract time and position of the interactions. Moreover, it is an iterative process, with multiple interactions between physicists and engineering teams. A vital task of the engineering team, apart from assuring that the design meets physics requirements, is being able to predict the performance of the detector resulting from particular technology choices. Therefore, one usually develops accurate numerical models of the full detector and validates them with computer simulations and measurements. There are, however, situations when the project schedule takes precedence, limiting possibilities for R&D work due to tight timing constraints. This thesis is an example of such a case, in which unforeseen circumstances created a need for a new detector, that had to be designed and built in just over three months. Given the complexity of the construction process, those were very demanding conditions.

The described work covers the full design and manufacturing process of a scintillating fiber detector, followed by a review of its performance. The first part presents an in-depth study of the theory behind the operation of a scintillating fiber detector, as well as selected methods of analyzing data. The goal is to provide derivations of several engineering approximations that can be helpful in the design process. The next part puts theory into practice by formulating and validating the requirements of the detector. A vital element of this step is a rough estimation of its parameters, which does not need a dedicated numerical model. Afterward, a description of an actual construction process is presented, which ends in a working system. The final part presents an overview of the real performance of the detector, and compares it with the previous estimations, based on a study with an electron beam provided by the ELSA accelerator.

Even though the overall goal of this document is to be a one-stop reference for anyone involved in the construction or maintenance of scintillating fiber detectors,

several of the discussed topics are general and can be useful in other areas. In particular, a review of photosensors, readout systems, and signal processing algorithms may prove valuable.

Keywords: Scintillating fiber detector, Signal digitization, Front-end electronics, Photosensors, Time estimation from sampled waveform, Time resolution

Streszczenie

Jedną z powszechnie stosowanych i wciąż rozwijanych technik wykorzystywanych do śledzenia torów cząstek w eksperymentach fizyki wysokich energii są detektory śladowe wykonane z plastikowych światłowodów scyntylacyjnych. Swoją popularność zawdzięczają szeregowi zalet, spośród których najważniejsze obejmują: doskonałą rozdzielczość czasową, bardzo dobrą rozdzielczość przestrzenną, wysoką odporność na promieniowanie jonizujące, zdolność do pracy przy wysokich częstościach zliczeń oraz możliwość wyprodukowania niemal dowolnego kształtu detektora.

Proces konstrukcji detektora śladowego opartego o światłowody scyntylujące jest dość złożony i wymaga dogłębnej wiedzy na temat szeregu zagadnień, obejmujących m.in.: mechanizmy oddziaływania cząstek z materią, proces scyntylacji, optykę detektora, detekcję słabych impulsów świetlnych przy wykorzystaniu ultraczułych fotodetektorów, układy elektroniczne wykorzystywane do akwizycji sygnałów, a także metody przetwarzania sygnałów pozwalające na estymację czasu trafienia oraz położenia toru cząstki. Zazwyczaj budowa detektora jest związana z wielokrotnymi konsultacjami pomiędzy fizykami i inżynierami. W związku z tym, jednym z kluczowych aspektów tego procesu jest możliwość szybkiego przewidywania parametrów detektora na podstawie określonych decyzji konstrukcyjnych, umożliwiając tym samym ocenę, czy budowane urządzenie spełni wymogi stawiane przez konieczność pomiaru badanych procesów fizycznych. W związku z tym, zazwyczaj w pierwszej kolejności opracowywane są szczegółowe modele numeryczne projektowanego detektora, które są następnie weryfikowane przy użyciu symulacji Monte-Carlo oraz dedykowanych pomiarów. Wnioski płynące z tych działań są następnie uwzględniane w projekcie, często prowadząc do zmiany pierwotnych założeń konstrukcyjnych. Istnieją jednak sytuacje, w których ograniczenia czasowe związane z realizacją projektu uniemożliwiają tego typu prace badawczo-rozwojowe. Niniejsza rozprawa stanowi przykład takiego projektu, w którym w związku z zaistnieniem nieprzewidzianych okoliczności konieczne było zaprojektowanie i zbudowanie nowego detektora, w czasie krótszym niż cztery miesiące, co stanowiło to nie lada wyzwanie.

Prezentowane prace objęły pełny proces projektowania i konstrukcji światłowodowego detektora śladowego zbudowanego z plastikowych włókien scyntylacyjnych, a także analizę jego osiągnięć. W pierwszej kolejności dokonano analizy teorii leżącej u podstaw działania tego typu detektora, dzięki czemu możliwe było wyprowadzenie formuł pozwalających na zgrubną estymację parametrów detektora, które następnie zostały wykorzystane w procesie projektowania. Kolejna część pracy wprowadza teorię w życie, stosując ją do sformułowania wymagań i walidacji koncepcji detektora. W kolejnych rozdziałach przedstawiono opis procesu konstrukcyjnego zrealizowanego detektora, a także analizę jego rzeczywistych osiągnięć w odniesieniu do wcześniejszych szacunków. Uzyskano dobrą zbieżność osiągnięć detektora z estymatami

wynikającymi z teorii, co należy uznać za sukces, zważywszy na brak możliwości opracowania szczegółowego modelu numerycznego całego systemu. Badania zostały wykonane za pomocą wiązki elektronowej wyprodukowanej przez akcelerator ELSA.

Zamysłem autora niniejszej rozprawy było stworzenie dokumentu, który z jednej strony zaprezentuje metodę budowy poprawnie działającego światłowodowego detektora śladowego, bez konieczności czasochłonnego opracowania szczegółowych modeli numerycznych jego wszystkich elementów. Z drugiej strony, zgrupowanie większości aspektów związanych z funkcjonowaniem detektora powinno być użyteczne dla osób zaangażowanych w utrzymanie infrastruktury, gdyż może pomóc zidentyfikować przyczyny ewentualnych awarii bądź nieoptymalnych osiągnięć. Ponadto, pewne zagadnienia dyskutowane w pracy, związane z fotodetektorami, systemami odczytu oraz algorytmami przetwarzania sygnałów mogą być użyteczne także w innych obszarach techniki.

Słowa kluczowe: światłowodowy detektor śladowy, akwizycja sygnałów, elektronika front-end, detektory światła, estymacja czasu na podstawie zarejestrowanego przebiegu, rozdzielczość czasowa

Contents

Contents	7
1 Introduction	9
2 Theory	13
2.1 Principle of Operation	13
2.2 Interactions of Charged Particles with Matter	17
2.2.1 Electronic Losses	18
2.2.2 Radiative Losses	22
2.3 Scintillation and Light Collection	25
2.3.1 Scintillation Mechanism	25
2.3.2 Scintillator Light Yield	27
2.3.3 Collection and Transmission of Light	28
2.4 Fiber to Photosensor Coupling	36
2.5 Photosensors	40
2.5.1 Photomultipliers	44
2.5.2 Multi-Pixel Geiger-Mode Avalanche Photodiodes	57
2.6 Readout	65
2.6.1 Discriminator with a Time-to-Digital Converter	70
2.6.2 Sampling Systems	77
2.6.3 Time Estimation from Sampled Waveforms	84
3 Compact Scintillating Fiber Tracker for use in Test Beams	95
3.1 Motivation	95
3.2 Requirements and Concept	99
3.3 Concept Validation and Expected Performance	103
3.4 Planning and Schedule	115
3.5 Building the Detector	116
3.5.1 Preparation of Scintillating Fibers	116
3.5.2 Fiber Mats	120

3.5.3	Photomultiplier Housings	122
3.5.4	Electronics	127
3.5.5	Final Assembly	133
4	Performance Evaluation	136
4.1	Initial Commissioning	136
4.2	Beam Tests	143
4.2.1	Test Setup at the ELSA Accelerator in Bonn	143
4.2.2	Beam Profiles	143
4.2.3	Signal Level from Minimum Ionizing Particles	146
4.2.4	Timing Resolution	152
5	Summary	164
	Bibliography	166
	List of Acronyms	184

Chapter 1

Introduction

Tracking detectors made of plastic scintillating fibers is a well-established technology in the world of high energy physics experiments – in fact, they have already been in use back in the sixties of the past century [1]. Examples of more recent applications include: fiber hodoscopes used in the COMPASS experiment [2–5] at CERN, the central fiber tracker used in the DØ experiment [6], scintillating fiber detectors used in the Crystal Barrel experiment at ELSA [7–9], the fiber tracker in the CHORUS experiment [10, 11] at CERN or scintillating fiber detector used in the near detector of the K2K experiment [12, 13], to name just a few. Given the extreme versatility offered by this technology, there is a constant effort to improve it further, and new applications are either developed or under consideration. An example of an on-going effort could be the planned upgrade of the downstream tracking stations in the LHCb detector [14, 15], in which case currently installed equipment (straw-tubes and silicon micro-strip detectors) are to be replaced with new modules made from scintillating fibers.

There are several advantages of scintillating fiber detectors, which led to their widespread adoption in various experiments. The most prominent of them comprise:

- Excellent timing properties, which they owe to the fact that the fibers utilize organic scintillators, which have fast decay times. Therefore, they are usually the right candidate for inclusion into trigger systems.
- Excellent spatial resolution – depending on dimensions of used fibers and the number of tracking detectors, values as low as $50 \mu m$ are possible [16].
- Good radiation hardness and ability to withstand high hit rates.
- Possibility to manufacture almost any shape of the detector, for example, a helical hodoscope built for the EDDA experiment [17, 18]. Furthermore, the use of optical fibers allows the placement of photosensors and readout electronics far from areas exposed to the harsh radiation environment, thereby increasing the reliability of the

electronics thanks to reduced exposure. An additional advantage may result from fewer requirements related to shielding.

The last bullet is of particular interest – on the one hand, it allows for significant reduction of the production of unwanted secondary particles, which in turn is beneficial for subsequent data analysis, as there are less ‘unwanted’ events that need to be filtered out. The other, less obvious benefit reveals itself if one needs to have a detector with a large active area and a minimum amount of readout channels. One way to achieve this would be to combine multiple fibers into a single photosensor (or photosensor channel in case of multichannel sensors). However, such a solution may be troublesome. First, it may require a considerable number of fibers, possibly coupled to an optical concentrator (for example a Winston cone¹) – which is a potentially labor-intensive and costly solution and also causes an inevitable deterioration of light signal level. Furthermore, it creates a requirement for a photosensor with a sizeable photosensitive area, again increasing costs and dark rate. A more elegant approach is to use a solid block of a scintillator that covers the required area or volume, possibly with a reflector in order to maximize light yield, and a wavelength-shifting fiber² to extract the light signal out to the photodetector, which in this case must only match fiber diameter. This type of light collection system is widely used in the near detector station of the T2K experiment, for example, in the Side Muon Range Detector or the Fine-Grained Detector subsystems [19–21] . Another example is a new electromagnetic calorimeter ECAL0 that has been built for the COMPASS experiment. It uses Shashlik-type modules [22], where wavelength-shifting fibers are used to collect signals from rectangular scintillator tiles interlaced with lead tiles.

Given the specifics of high energy physics experiments, most of the detectors are built for the specific application. Quite often, a prototype is a final product, which is then used in the final solution – or at least it is assigned to a pool of spares. Since building a new detector is a considerable effort, which almost always requires significant involvement of resources and workforce, one wants to maximize chances that the first attempt is a successful one. Additionally, it is not so uncommon that strict timing constraints may arise concerning the completion of the project, as typically, it is a part of a larger system which must meet the beam schedule. Therefore, the decision-making process related to the construction of a new detector takes into account several factors, such as:

- Examination of the team’s experience gained in previous projects (provided that there were any), to avoid past mistakes.

¹Non-imaging light collector in the shape of an off-axis parabola of revolution with a reflective inner surface. *Source: Wikipedia, The Free Encyclopedia.*

²An optical fiber that absorbs light at one wavelength and re-emits it at another, longer wavelength. Some of the re-emitted light enters the transmissive mode and hence can be read out at the end of the fiber.

- A detailed study of physics requirements. One should note that the whole purpose of building the detector is to make predetermined physics measurements, which in turn require certain minimum performance levels from the equipment involved in the measurement. For example, assuring the required accuracy of particle tagging drives the need for timing precision.
- Research on how others approached the subject – which usually means extensive literature study and potentially face-to-face consultations with other people who built similar systems.
- Optimization of the detector design in order to meet all the physics-related requirements, while also assuring timely completion of the project and reasonable costs. Typically, this means that the system should be ‘good enough’ for a given application, with maybe a little performance margin. The proper way of implementing this would be that all the components of the detector exhibit similar performance levels – for example, there is no point in using super-fast electronics if neither photosensor nor scintillators provide comparable timing performance.
- Project schedule and its costs – those may not be very scientific factors, but ultimately they quite often determine whether the project receives a ‘go ahead’ from the funding agency.

Reaching the final specification and configuration of the detector is an iterative process, with multiple interactions between physicists and engineering teams. A vital task of the engineering team, apart from assuring that the design meets physics requirements, is being able to predict the performance of the detector resulting from particular technology choices. One way to accomplish this is to develop accurate numerical models and validate them with Monte-Carlo simulations and dedicated measurements. Since a complete model of the scintillating fiber detector is quite complicated – it includes particle interactions, detector optics, photosensors, readout electronics, and finally, the methods used to extract time and position of the interactions – the process of completing the full detector model is time and resource consuming. Nonetheless, this is the usual and the recommended way to go with the project. There are, however, situations when this type of approach is impossible due to an extremely short timescale, lack of human resources, and sometimes also insufficient funds. The work presented in this dissertation is an example of such a project.

The task assigned to the author’s team was to build a detector that could provide a position-sensitive trigger for beam tests of a subset of Shashlik modules comprising the ECAL0 calorimeter. The tests were performed using a low-intensity electron beam provided by the ELSA accelerator in Bonn, Germany. The challenge was that the need

for this detector came out very late during the preparation phase of the test, leaving just a little over three months to design and build the detector from scratch. Moreover, such a task was not foreseen in the team's budget related to the COMPASS experiment, so not only the timing requirements were strict, but there was also no money. One can, therefore, ask a question – how could it work out?

With such boundary conditions, there was no time even to attempt to develop a fully functional detector model. One needed to proceed with the design phase immediately, meaning that the only viable approach was the 'tried-and-true' one – so no testing, no new technologies, just solutions that were known to work. Moreover, since there was no money, it was necessary to maximize reuse of materials and tools from the previous projects. Most importantly, there was no room for mistakes – the design decisions had to be correct from the very beginning. That implied a thorough understanding of the theory behind the operation of the scintillating fiber detector – in particular, all the aspects mentioned earlier that are needed to develop a good model.

Fortunately, there already was extensive experience in simulating scintillating fibers [23] as well as the construction of actual detectors, the latter being a scintillating fiber tracker built for the COMPASS experiment and a scintillator and a wavelength shifter based muon system for the T2K experiment [24, 25]. Tools, materials and photosensors were also available, either as left-overs from the projects mentioned earlier or as spares from other detectors used in the COMPASS experiment. This aspect was crucial, as even if funds were available, it would not be possible to buy them due to manufacturer lead times.

All in all, the project was successful, and a compact scintillating fiber tracker was built [26] and installed in the experimental hall of the ELSA accelerator, allowing for the collection of valuable data. The next chapters will show the process which led to this achievement – analysis of the theory (chapter 2), construction of the detector (chapter 3), evaluation of its performance (chapter 4), and finally a short summary (chapter 5).

Chapter 2

Theory

2.1 Principle of Operation

The theory behind the operation of the scintillating fiber detector is relatively straightforward. However, before delving into details, it is worth to recall some basic concepts. The first of them is an optical fiber. In terms of our application, particularly interesting are plastic optical fibers, as, to the authors knowledge, they are in the most common use when it comes to detectors built for particle tracking. The technology of plastic optical fibers is well established in both science and industry, and has numerous applications. A good introduction to their technology can be found in [27]. In most of their applications, the diameter of the fiber is much larger than the wavelength of light. Therefore, they are considered as multi-mode fibers and, consequently, their operation can be adequately described using geometrical optics. The basic idea behind the fiber is simple – its central part (the core) is enclosed in a layer of material that has a lower index of refraction (the cladding) – i.e. $n_{cl} < n_{co}$, where n_{cl} and n_{co} are refractive indices of the cladding and the core, respectively (Fig. 2.1). This way, part of the light that hits the core-cladding

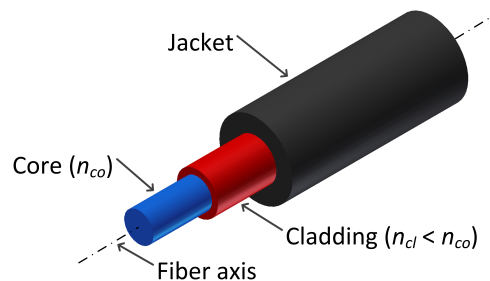


Figure 2.1: Example structure of a step-index plastic optical fiber (picture taken from [27], with minor modifications). The symbols n_{co} and n_{cl} are refractive indices of the core and the cladding, respectively.

boundary will meet the requirements for the total internal reflection. Consequently, light transmission becomes possible between both ends at a relatively little loss, subject to at-

attenuation of the materials comprising the fiber. The actual composition of the fiber varies depending on the application and it is not uncommon for a plastic fiber to have a graded or a multi-step index profile, which provides for lower intermodal dispersion. Control of refractive indices of particular fiber layers is achieved by fluorination of polymers [28–30]. Typical materials used for their production, in the context of applications in high energy physics, are summarized in table 2.1.

Material	Refractive index	Application	Attenuation (dB/km)
PS	1.592	core	55 (538 nm)
PMMA	1.493	core/cladding	330 (570 nm)
FP	1.301 to 1.500	core/cladding	various

Table 2.1: Common materials used for manufacturing optical fibers [27, 31] used in particle tracking detectors. PS – polystyrene, PMMA – poly(methyl methacrylate), FP – fluorinated polymer.

Turning an optical fiber into a radiation detector requires two things:

- The fiber needs to be ‘aware’ of radiation - i.e. it needs to generate light upon interaction with radiation, usually a charged particle. It also needs to be able to transport this light without significant self-absorption.
- Light signal that reaches the end of the fiber needs to be converted into an electrical form.

The former requirement is met by modifying fiber’s core so that it becomes a scintillator, usually by doping the base material (typically polystyrene) with various fluors, which ensure proper wavelength of generated light and also affect decay times. The latter is achieved with the use of photosensors, which must be capable of registering signals of the order of few to few hundreds of photons. Given the complexity of the involved processes, for the moment a ‘black box’ approach will be adopted – i.e. an assumption will be made that both, the scintillator and the photosensor, just do what they were designed for. The details concerning their inner working will be discussed in subsequent sections 2.2 through 2.5. With the above in mind, the principle of operation of the scintillating fiber detector could be described in the following way (Fig. 2.2):

1. When a high energy particle traverses a material, it produces ionization and leaves a trail of excited molecules.
2. The excited molecules return to their normal state. Some of them (approx. 3% [33]) will emit light in the process. The light will be emitted isotropically and a fraction of it will be transported towards ends of the fiber via the total internal reflection. The

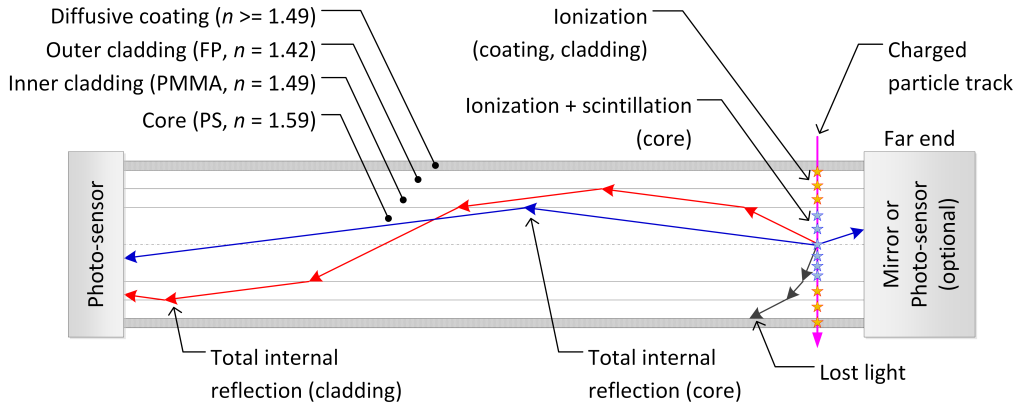


Figure 2.2: Principle of operation of a dual cladding scintillating fiber. Charged particle traverses fiber producing ionization. Part of the deposited energy is converted into light via the scintillation process. Fraction of this light is then transmitted via the total internal reflection and subsequently converted to an electrical signal by the photosensor(s). Fiber composition was taken from the datasheet of Kuraray SCSF-78MJ multi-cladding fibers [32]. Outer ‘diffusive coating’, used to suppress inter-channel cross-talk, is typically made of acrylic paint or epoxy glue, sometimes doped with titanium dioxide.

remaining light is suppressed by the outer diffusive coating, to prevent inter-channel cross-talk.

3. The light that exits the fiber will then be registered by the photo-sensor. Thus, an electrical signal will be produced, which is suitable for further processing.

Depending on the scenario, either one or two photo-sensors are used for registering light signals. In the latter case, it is possible to estimate position along the fiber axis, based on the difference between timing of the pulses from the sensors. However, the position resolution may be limited due to potentially low levels of light signal, which limit achievable timing accuracy. Speed of the photo-sensors and the electronics may also affect this limitation.

Single fiber detector is of little use when it comes to particle tracking. Much more common approach is to arrange fibers into mats and determine position of interaction based on channel number (Fig. 2.3). In this configuration, the spatial information is available in the direction transverse to the fiber axis, which is why usually two or more mats are used, with different orientations. The consequence of the fact that, most of the times, fibers are bonded into mats, is that the majority of commercially offered scintillating fibers are typically jacketless. The outermost layer is the outer cladding and it is in direct contact with the bonding agent, be it acrylic or epoxy resin. Since the index of refraction of the resins is similar or higher than that of the cladding [34–36], the total internal reflection does not occur. Most of the photons reaching the outer cladding exit into the resin and are attenuated by the coating. Nonetheless, some of them still get reflected, as Fresnel

equations predict a non-zero reflection for any media boundary. However, they would, would inevitably be lost at subsequent medium boundaries, so the probability that any of them would reach the fiber end is practically zero.

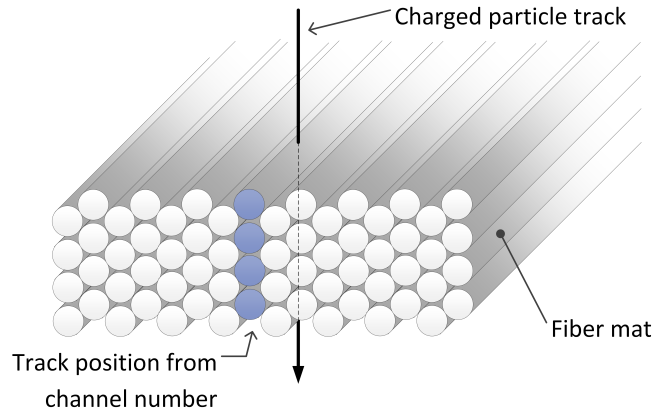


Figure 2.3: Typical configuration of the scintillating fiber detector. Fibers are arranged in a mat, potentially with several layers per each channel. Position in the direction transverse to the fiber axis is determined based on channel number.

One of the key parameters of any tracking detector is its position resolution. In case of a detector composed of scintillating fiber mats, it is determined by the fiber size, tolerance of its diameter, the precision of the manufacturing process of the mat and, finally, optical crosstalk between adjacent fibers. Optical inter-fiber crosstalk is typically suppressed by using a diffusive bonding agent, for example by mixing epoxy resin with titanium dioxide. In terms of fiber size, at first glance the best option seems to be to use fibers with the smallest diameter. However, organic scintillators that are used in the fibers are fast, which is why this type of detectors is well matched for time of flight or trigger applications. Hence, the second key parameter of the detector is its timing resolution. Now, the smaller the fiber, the shorter the distance that a particle traverses through the scintillator. Consequently, the level of light signal will also be diminished, which in turn deteriorates the timing response. To counteract this problem, one can use multiple fibers per channel, but that increases the risk of fiber misalignment, which may deteriorate position resolution. Also, handling small fibers is more difficult than those of larger diameters. All in all, a compromise needs to be made that suits particular application.

While generally the concept of the scintillating fiber is extremely useful, there is one aspect of detector's design that needs to be considered. Due to the fact that fiber is sensitive to radiation, it will react to particles that may be outside the area of interest. Most of these 'parasitic' hits can be detected and ignored by using a coincidence detector between the mats in different projections. Nevertheless, they will increase the load on the photo-sensor, especially in high-rate applications. Furthermore, because scintillating

fibers are doped with fluors, they usually exhibit bigger attenuation than similar fibers with an undoped core. Therefore, commonly used countermeasure is to use both – scintillating fibers for the ‘active area’ and clear fibers for guiding the light signals towards the photosensors (Fig. 2.4). Various techniques are used for joining the two fibers, for example custom connectors [37], gluing [3, 4, 24, 38] or heat splicing [2, 39]. The drawback of this approach is that the joint does introduce additional light loss, so once again one should weigh positives and negatives in the context of the desired application.

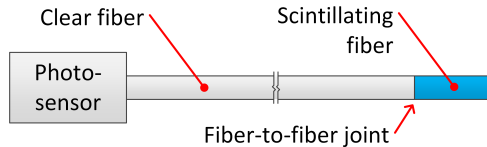


Figure 2.4: Limiting active area of the detector. Scintillating fiber is joined with a clear fiber, which does not generate light when irradiated. Usually it also exhibits smaller attenuation. Typically, clear fibers are much longer than the scintillating part.

2.2 Interactions of Charged Particles with Matter

A key parameter affecting performance of the scintillating fiber detector is the level of the light signal. Its estimation requires knowledge of mechanisms of the scintillation process as well as interactions of the incident particles with the material of the detector. The former issue is discussed in section 2.3. The latter one, which is briefly reviewed throughout the remainder of this section, is of crucial importance, as the amount of light produced due to scintillation is directly affected by the amount of energy deposited in the fibers.

Usually, beams used in accelerator-based experiments are formed from charged particles – protons, muons, pions, heavy ions or electrons, to name a few. Therefore, only interactions of fast charged particles are of interest in the context of this work. Fortunately, this topic has been studied over several decades and there are numerous resources available. An up-to-date summary of the subject can be found in the ‘Review of Particle Physics’ [33], which is published on a yearly basis by the Particle Data Group. Another good introduction can be found in an excellent textbook by Knoll [40].

The quantity that describes the energy loss of a charged particle traversing a given medium is called the ‘linear stopping power’:

$$S_{lin} = -\frac{dE}{dx} \quad \left(\frac{\text{MeV}}{\text{cm}}\right) \quad (2.1)$$

with E being the energy of the incident particle (in MeV) and x the traveled distance (in cm). In general, there are three contributions to the stopping power:

- Electronic losses – i.e. inelastic collisions between the particle and the bound electrons of the medium, which result in ionization and atomic or collective excitation. They are the most interesting from the point of view of this work, as they cause energy deposition in the fiber cores. Part of this energy is then radiated via the scintillation process.
- Nuclear stopping due to collisions between the particle and the target nuclei. Important for heavy charged particles at low energies. Does not apply to electrons and positrons.
- Radiative losses due to bremsstrahlung – applies mostly to electrons and positrons. At sufficiently high energies should also be considered for heavy charged particles.

Given specific aspects of this work, only electronics and radiative losses will be discussed, as the beams produced in accelerators are of rather high energies, so the nuclear stopping can be neglected. Furthermore, rather than using the ‘linear stopping power’, it is quite a common practice to divide it by the density of the material, denoted as ρ :

$$S = S_{lin}/\rho \quad \left(\frac{\text{MeV}\cdot\text{cm}^2}{\text{g}} \right) \quad (2.2)$$

This way, the stopping power is a function of the material only and is independent of the state of aggregation – i.e. for a given material it is the same for gases, liquids and solids.

2.2.1 Electronic Losses

The electronic mass stopping power for relativistic heavy charged particles is described by the well known Bethe formula [33]:

$$S_e = -\frac{1}{\rho} \frac{dE}{dx} = K z^2 \frac{Z}{A} \frac{1}{\beta^2} \left[\frac{1}{2} \ln \frac{2m_e c^2 \beta^2 \gamma^2 W_{\max}}{I^2} - \beta^2 - \frac{\delta}{2} \right] \quad \left(\frac{\text{MeV}\cdot\text{cm}^2}{\text{g}} \right) \quad (2.3)$$

Here, the W_{\max} is the maximum energy transfer in a single collision and is given by:

$$W_{\max} = \frac{2m_e c^2 \beta^2 \gamma^2}{1 + 2\gamma m_e/M + (m_e/M)^2} \quad (\text{MeV}) \quad (2.4)$$

In case of electrons and positrons, respectively, the formulas are [41]:

$$S_{e|e^-} = -\frac{1}{\rho} \frac{dE}{dx} = \frac{1}{2} K \frac{Z}{A} \frac{1}{\beta^2} \left[\ln \frac{m_e c^2 \beta^2 \gamma^2 \{m_e c^2 (\gamma - 1)/2\}}{I^2} + \right. \\ \left. + (1 - \beta^2) - \frac{2\gamma - 1}{\gamma^2} \ln 2 + \frac{1}{8} \left(\frac{\gamma - 1}{\gamma} \right)^2 - \delta \right] \quad \left(\frac{\text{MeV}\cdot\text{cm}^2}{\text{g}} \right) \quad (2.5)$$

$$S_{e|e^+} = -\frac{1}{\rho} \frac{dE}{dx} = \frac{1}{2} K \frac{Z}{A} \frac{1}{\beta^2} \left[\ln \frac{m_e c^2 \beta^2 \gamma^2 \{m_e c^2 (\gamma - 1)\}}{2I^2} + 2 \ln 2 + \right. \\ \left. - \frac{\beta^2}{12} \left(23 + \frac{14}{\gamma + 1} + \frac{10}{(\gamma + 1)^2} + \frac{4}{(\gamma + 1)^3} \right) - \delta \right] \quad \left(\frac{\text{MeV}\cdot\text{cm}^2}{\text{g}} \right) \quad (2.6)$$

The above formulas are valid for particles in the region of $0.1 \lesssim \beta\gamma \lesssim 1000$ and are accurate to within few percent for intermediate- Z materials [33]. Description of the symbols is presented in Table 2.2.

Symbol	Definition	Value and/or unit
c	speed of light in vacuum	2.99792458×10^8 m/s
m_e	electron rest mass	$0.510998928(11)$ MeV/ c^2
e	elementary charge	$1.60217662 \times 10^{-19}$ C
ϵ_0	vacuum permittivity	$8.8541878176 \times 10^{-12}$ F/m
r_e	classical electron radius: $e^2/(4\pi\epsilon_0 m_e c^2)$	$2.8179403267(27)$ fm
N_A	Avogadro's number	$6.02214129(27) \times 10^{23}$ mol $^{-1}$
K	$4\pi N_A r_e^2 m_e c^2$	0.307075 MeV \cdot cm 2 /mol
v	incident particle velocity	m/s
β	v/c	
γ	Lorentz factor: $1/\sqrt{1-\beta^2}$	
ρ	absorber density	g/cm 3
M	incident particle mass	MeV/ c^2
E	energy of incident particle: $\gamma M c^2$	MeV
T	kinetic energy of incident part.: $(\gamma - 1) M c^2$	MeV
x	distance traveled by incident particle	cm
z	charge number of incident particle	
Z	atomic number of absorber	
A	atomic mass of absorber	g/mol
I	mean excitation energy	eV
δ	density effect correction	

Table 2.2: Definitions of symbols used in equations 2.3 to 2.6. Table content adopted from [33], with amendments.

The density correction factor δ reflects the decrease of the stopping power that occurs due to polarization of the medium. It's parameterization is given by Sternheimer [42, 43]:

$$\delta = \begin{cases} 4.606 x - \bar{C} & \text{if } x \geq x_1; \\ 4.606 x - \bar{C} + a(x_1 - x)^m & \text{if } x_0 \leq x < x_1; \\ 0 & \text{if } x < x_0 \text{ (non-conductors);} \\ \delta_0 10^{2(x-x_0)} & \text{if } x < x_0 \text{ (conductors)} \end{cases} \quad (2.7)$$

Here, x is a kinematic variable defined as follows (note that **it is different** from the definition given in Table 2.2):

$$x = \log_{10} \left(\frac{p}{Mc} \right) = \log_{10} (\beta\gamma) \quad (2.8)$$

In the above definition p stands for the momentum of the incident particle, in MeV/ c , whereas β , γ , M , c have the meaning described previously in Table 2.2. The \bar{C} parameter is:

$$\bar{C} = -C = 2 \ln (I/\hbar\omega_p) + 1 \quad (2.9)$$

where I is the mean excitation energy of the material and $\hbar\omega_p$ is its corresponding plasma energy:

$$\hbar\omega_p = \sqrt{4\pi N_e r_e^3} \frac{m_e c^2}{\alpha} = 28.816 \sqrt{\rho Z/A} \quad (\text{eV}) \quad (2.10)$$

Symbols r_e , m_e , c , ρ , Z , A are defined as per table 2.2. The N_e is electron density (in units of fm^{-3}), \hbar is the Planck constant, equal to $4.135667662(25) \times 10^{15}$ eV·s, and α is the fine structure constant:

$$\alpha = e^2/(4\pi\epsilon_0\hbar c) = 1/137.035999074(44) \quad (2.11)$$

The x_a and a parameters are defined as follows:

$$\begin{aligned} x_a &= \bar{C}/4.606 \\ a &= 4.606 (x_a - x_0) / (x_1 - x_0)^m \end{aligned} \quad (2.12)$$

Finally, x_0 , x_1 , m and δ_0 are material dependant constants, determined by fitting the above parameterization to experimental data. Values of these parameters for various elements and compounds, as well as description of the fitting method, can be found in [44]. Alternatively, in case the pre-calculated values are not available, it is possible to make an approximation by assuming $\delta_0 = 0$ and the following defaults for x_0 , x_1 and m [43, 45]:

$$\begin{aligned} I < 100\text{eV} &= \begin{cases} x_0 = 0.2 & x_1 = 2.0 & m = 3.0 & \text{for } C < 3.681; \\ x_0 = 0.326\bar{C} - 1.0 & x_1 = 2.0 & m = 3.0 & \text{for } C \geq 3.681 \end{cases} \\ I \geq 100\text{eV} &= \begin{cases} x_0 = 0.2 & x_1 = 3.0 & m = 3.0 & \text{for } C < 5.215; \\ x_0 = 0.326\bar{C} - 1.5 & x_1 = 3.0 & m = 3.0 & \text{for } C \geq 5.215 \end{cases} \end{aligned} \quad (2.13)$$

The core of a plastic fiber is made from a polymer, such as for example polystyrene – $[(\text{C}_6\text{H}_5\text{CHCH}_2)_n]$. Since it is a compound material, one can use the principle of the Bragg additivity to get an approximation of the resulting mass stopping power [46], with corrections suggested in [47]. In principle, the I , δ and Z/A terms in equations 2.3, 2.5 or 2.6 should be substituted with \bar{I} , $\bar{\delta}$ and $\langle Z/A \rangle$, respectively, defined in the following way:

$$\ln \bar{I} = \sum_i f_i \ln I_i \quad (2.14)$$

$$\bar{\delta} = \sum_i f_i \delta_i \quad (2.15)$$

$$\left\langle \frac{Z}{A} \right\rangle = \frac{\sum_i n_i Z_i}{\sum_i n_i A_i} \quad (2.16)$$

with I_i representing the mean excitation energy of i -th component, δ_i the density correction factor for the i -th component, Z_i and A_i the atomic number and atomic mass of the

i -th component, n_i the number of atoms of the i -th component present in the compound material, and finally the f_i the oscillator strength of the atoms of the i -th constituent, defined as:

$$f_i = \frac{n_i Z_i}{\sum_i n_i Z_i} \quad (2.17)$$

A key element of all the stopping power formulas is the mean excitation energy. As indicated in [33], its determination is non-trivial and it is best to use values that were determined experimentally. Good reference is available in [48], which provides values of mean excitation energy both for selected chemical elements and compounds. The general recommendation for determining the stopping power is to use either on-line resources or pre-calculated tables. Estimates of dE/dx for electrons, protons and helium ions can be obtained using the ESTAR, PSTAR and ASTAR programs [49], respectively. Tabulated values for muons are available in tables provided by Groom et al. [50]. The estimates for positrons can be calculated using methodology presented by Pal et al. [51].

In case of scintillating fiber detectors, which fall into the category of ‘moderately thick detectors’, the most probable electronic energy loss of the traversing fast charged particle will in fact be smaller than the mean energy loss predicted by the dE/dx formulas. This is due to the fact that dE/dx calculations take into account the very rare collisions with large energy transfers, up to W_{\max} , whereas majority of the collisions occurring in a detector of moderate thickness is characterized by energy transfers smaller than the mean (see [33] for details, section 33.2). As such, rather than using the mean energy loss, one should use the ‘most probable energy loss’ for the purpose of estimation of the energy deposition within the fiber. The ‘most probable energy loss’ is described by the Landau function [52] or Landau-Vavilov function [53] (the former for electrons, the latter for heavy charged particles [54]), with subsequent corrections added by Bichsel [55] (valid for all particles).

The term ‘moderately thick detector’ means that the mean energy loss of the traversing particle is small compared to its initial energy E . More formally, if one defines the parameters ξ and κ as [53, 55]:

$$\xi = \frac{K Z}{2 A} z^2 (\rho x / \beta^2) \quad (\text{MeV}) \quad (2.18)$$

$$\kappa = \frac{\xi}{W_{\max}} \quad (2.19)$$

then the ‘moderately thick detector’ would mean that the parameter κ is restricted to range $\kappa \lesssim 0.1$ [33]. In such case, the most probable energy loss is given by the following formula (Landau-Vavilov-Bichsel) [55]:

$$\Delta p = \xi \left[\ln \frac{2m_e c^2 \beta^2 \gamma^2}{I} + \ln \frac{\xi}{I} + j - \beta^2 - \delta \right] \quad (\text{MeV}) \quad (2.20)$$

For high energy particles, the following approximation may be used [33]:

$$\Delta p_{\beta\gamma>100} \rightarrow \xi \left[\ln \frac{2m_e c^2 \xi}{(\hbar\omega_p)^2} + j \right] \quad (\text{MeV}) \quad (2.21)$$

The symbols used in equations 2.18 through 2.21, which were not explicitly defined, have the meaning described in table 2.2. The W_{\max} is defined in equation 2.4 and $j = 0.200$ [55].

Knowing all the above theory, it is now possible to estimate the mean and the most probable energy loss for particles traversing polystyrene layers having a thickness corresponding to the diameter of the typical commercially available scintillating fibers – for example 0.25 mm, 0.5 mm, 1 mm and 2 mm. Since, in the context of this work, only muons and electrons were of interest, the calculations were limited to these particles only. The results are shown in Fig. 2.5. The mean electronic energy loss was obtained using the Bethe dE/dx formula (equations 2.3 and 2.5). For comparison, the figure also shows dE/dx values for electrons, which were obtained using the ESTAR program, as well as dE/dx values for muons from relatively recent tables published by Groom. The most probable energy loss was calculated using the Landau-Vavilov-Bichsel formula (equation 2.20). Presented results are restricted to energies for which the assumption of moderate thickness of detector is valid – i.e. for $\kappa \lesssim 0.1$, with κ defined by equation 2.19. The values of κ with respect to thickness of polystyrene layer and particle energy are shown in Fig. 2.6. Material properties of polystyrene, which were used in the calculations, were adopted from [44, 50] and are provided in Table 2.3

Property	Value	Remarks
$\langle Z/A \rangle$	0.53768 mol/g	mean value for $[(C_6H_5CHCH_2)_n]$
ρ	1.060 g/cm ³	density
\bar{I}	68.7 eV	mean excitation energy
x_0	0.1647	density effect parameterization
x_1	2.5031	density effect parameterization
m	3.2224	density effect parameterization
δ_0	0	density effect parameterization

Table 2.3: Material properties of polystyrene [44, 50], used for calculations of Bethe dE/dx and Landau-Vavilov-Bichsel Δ_p .

2.2.2 Radiative Losses

For high energy charged particles, part of the energy loss comes from radiative processes related to Bremsstrahlung, pair production and/or photonuclear/electronuclear interactions¹ [33, 56, 57], in addition to the electronic losses. The higher the particle energy,

¹Detailed discussion of the mechanisms behind the radiative losses of charged particles is beyond the scope of this work – one should refer to multiple available textbooks and papers on this subject, for

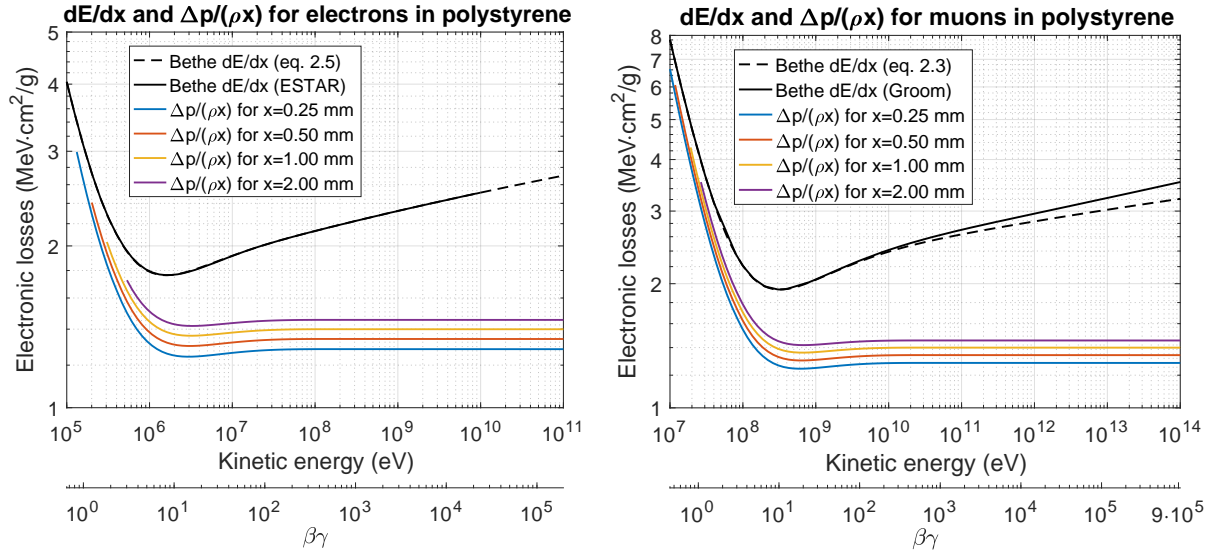


Figure 2.5: Electronic energy loss of electrons and muons in polystyrene. The dashed black lines represents mean energy loss (in $\text{MeV}\cdot\text{cm}^{-2}/\text{g}$) calculated using the Bethe dE/dx formula (equation 2.5 for electrons and 2.3 for muons). The solid black line represents data obtained using the ESTAR program [49] (electrons) or from relatively recent tables provided in [50] (muons). Coloured lines depict the most probable energy loss calculated using Eq. 2.20 for different thicknesses of polystyrene. Calculated Δp values were normalized to ρx , so that the unit is $\text{MeV}\cdot\text{cm}^{-2}/\text{g}$. Plot range was restricted to energies for which the assumption of moderate thickness of the material layer is valid (i.e. $\kappa \lesssim 0.1$ – see Eq. 2.19 for definition of κ).

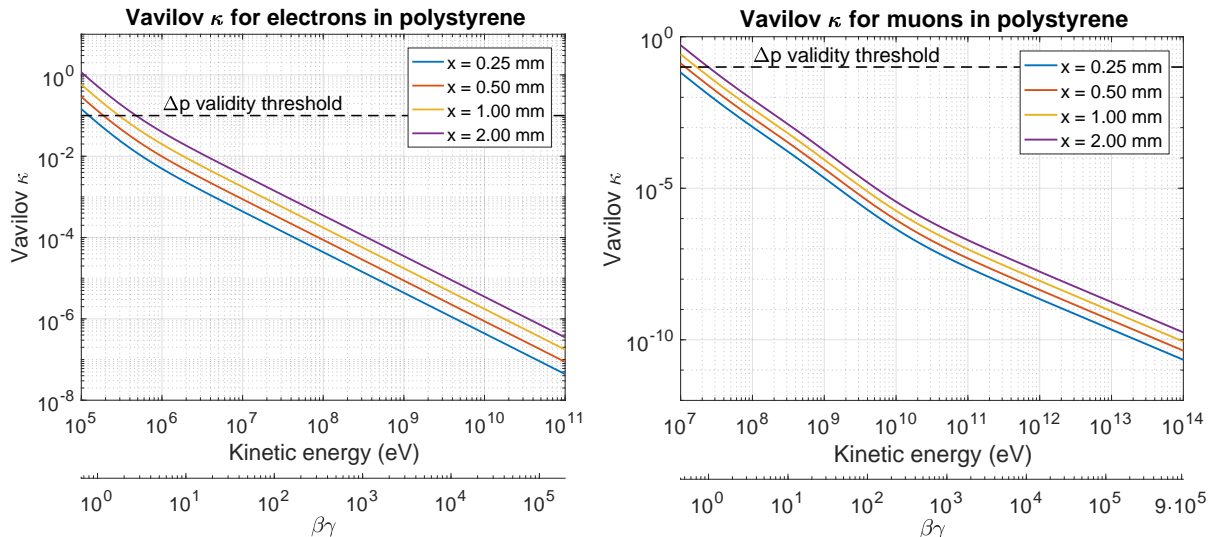


Figure 2.6: Vavilov κ (Eq. 2.19) for electrons and muons in polystyrene, as a function of energy. The values were calculated for polystyrene layers having thickness corresponding to the diameter of the typical commercially available scintillating fibers ($0.25 \text{ mm} \leq \varnothing \leq 2 \text{ mm}$).

the more prominent the radiative processes are. In fact, once certain energy threshold is crossed – called the ‘critical energy’² [58] – they become the major mechanism of energy loss. Figure 2.7 shows electronic and radiative energy losses for muons and electrons in polystyrene, which is common core material used in scintillating fibers. As can be seen, the critical kinetic energy for electrons is as low as $T_{c|e^-} \approx 107$ MeV, whereas for muons it is $T_{c|\mu^-} = 1189$ GeV. This means that for most cases where electron beams are planned, the radiative processes will dominate, given the fact that typical energies of electron beams used in high energy physics experiments are in the hundreds of MeV to multi-GeV range.

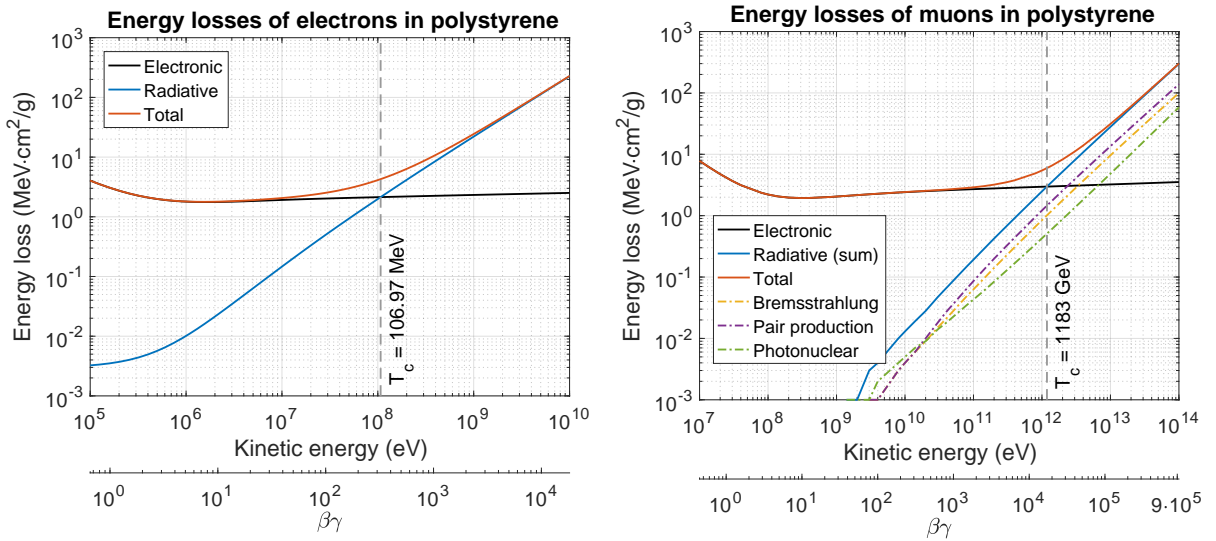


Figure 2.7: Total energy loss for electrons and muons in polystyrene. The data for electrons were obtained using the ESTAR program [49]. The data for muons come from tables published by Groom et al. [50]. Definition of ‘critical energy’ is the one used in [58] – i.e. the kinetic energy at which electronic and radiative losses are equal.

At this moment one might think in the following way. Scintillating fiber detectors are usually relatively thin. As an example, a detector consisting of two fiber mats with a structure shown in Fig. 2.3, each with four round 1 mm fibers per channel, would have an overall thickness equivalent to roughly one cm of polystyrene, taking into account the glue that would be needed to keep fibers in place. If such a detector is hit by a $T = 1$ GeV electron beam, then it can easily be seen from Fig. 2.7 that the expected radiative energy loss is little over 20 MeV - so approx. 2% of the initial electron energy. Furthermore, since detector thickness is known, the total change in electron energy can be taken into account when doing calibrations of the experiment – so the beam energy after the detector will

example already mentioned ‘Review of Particle Physics’ [33] or the introductory book by Knoll [40], as well as references therein.

²The other definition of the ‘critical energy’ (not used in this work) is the distance at which the ionization loss per radiation length is equal to the electron energy. See [33] for explanation of the difference between the two definitions.

still be known with relatively good precision. For muons with energies of the order of few hundred GeV, the problem seems not to exist. So, where is the catch?

Well, the actual problem is of completely different nature. In most cases, the scintillating fiber detector is part of a larger system that aims at measuring parameters of a specific physical phenomenon. This system is usually composed of multiple detectors of various nature – trackers, calorimeter, Cherenkov detectors, etc. The primary task of the scintillating fiber detector is to provide tracking and/or timing information. While it fulfills this task rather well, it also becomes a source of radiation (primarily photons), which then become unwanted background and need to be removed either at the experimental trigger level or in subsequent data analysis. In case of high rate experiments, which aim at measuring small cross-sections or rare events, this issue becomes especially troublesome, as the level of this background is significantly larger than that of the sought signal. This is why one usually adopts the so called ‘minimum mass in the beam’ principle. For a detector designer this means that the amount of fibers used for the construction of the detector should be minimized and the detector itself should only be ‘good enough’ to fulfill the provided specification. This specification is usually a result of careful Monte-Carlo studies of the whole experimental setup and is typically a compromise between the performance that can be achieved and the amount of parasitic radiation that can be tolerated.

2.3 Scintillation and Light Collection

2.3.1 Scintillation Mechanism

Scintillation is a process in which part of the energy deposited by a traversing high energy photon or particle is released as visible light. Organic materials which exhibit such properties are usually aromatic hydrocarbons [59]. Example materials are polyvinyltoluene (PVT) or polystyrene (PS), which are commonly used as the base material of plastic scintillators.

The actual generation of the light signal is a multi-step process [60]. The energy absorbed from ionizing radiation leads to excitation of the base material (>98% by weight), with approximately 4.8 eV needed to excite single molecule. However, the base itself is a poor scintillator – relaxation times are slow, the quantum efficiency is low (for polystyrene it is less than 3% [61]) and self absorption is high, as the emission and absorption spectrums have a significant overlap (Fig. 2.8). Therefore, the most common solution is to dope the base with a fluorescent dye at a high concentration (above 1% by weight). The desired properties of the dopant are the peak emission intensity at a wavelength for which the base is relatively transparent, high quantum efficiency (>95%) and significant Stokes’ shift (spectral difference between absorption and emission peaks – Fig. 2.9). The high

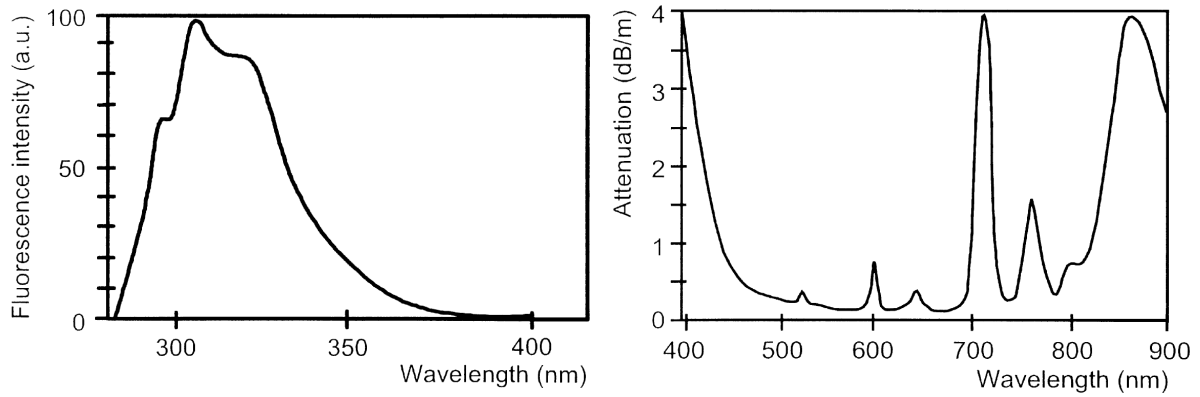


Figure 2.8: Emission (left) and absorption (right) of pure polystyrene; plots taken from [61].

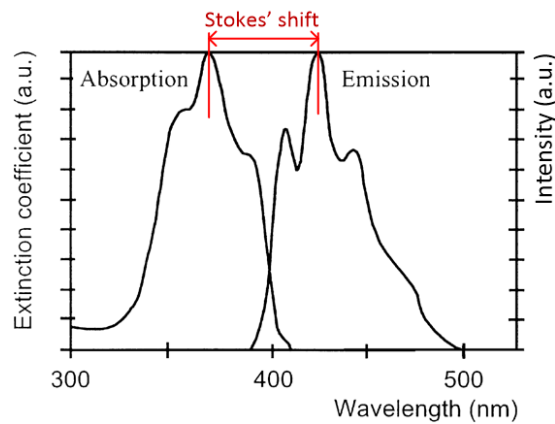


Figure 2.9: Illustration of Stokes' shift – emission and absorption spectrum of POPOP; plot taken from [61], with modifications.

concentration results in dye molecules located very close to excitation sites in the base polymer, so that the dominant energy transfer is a non-radiative, resonant dipole-dipole interactions known as Förster Transfer, which are very rapid ($\Delta T < 1\text{ns}$). Hence the decay time of the scintillator become that of the dye, which is usually much shorter than the one of the base, typically of the order of few ns. Such a scintillator is known as a binary composition, with the most typical dopants being PMP (1-phenyl-3-mesityl-2-pyrazoline), PTP (paraterphenyl), 3HF (3-hydroxyflavone), butyl-PBD (2-(4-biphenyl)-5-(4-tert-butylphenyl)-1,3,4-oxadiazole), PBBO (2-(4'-biphenyl)-6-phenylbenzoxazole), to name a few.

While large Stokes' shift is a desirable property of the primary dye, it has certain drawbacks. In case of dopants which emit light in the blue-green region, one should expect longer decay times [61]. Therefore, in case the primary dopant emits in the wavelength region highly attenuated by the base, a second dopant is used, in much smaller concentration, thus shifting the light towards longer wavelength, for which the base is more transparent. Hence, a ternary composition is formed, whose operation is illustrated in

Fig. 2.10. Example of such dye is 1,4-bis(5-phenyloxazol-2-yl) benzene, commonly known as POPOP.

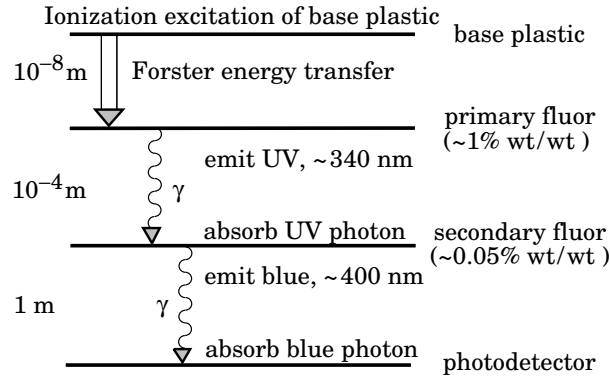


Figure 2.10: Scintillation ladder illustrating operation of a detector based on an organic scintillator, ternary composition [33].

2.3.2 Scintillator Light Yield

The most probable number of photons generated due to scintillation can be described by the following formula:

$$N_0 = \Delta p \frac{dn_\gamma}{dE} \quad (2.22)$$

with Δp being the Landau-Vavilov-Bichsel most probable energy loss (see section 2.2, Eq. 2.20) and dn_γ/dE the number of photons produced per unit of deposited energy³. While it is relatively easy to calculate Δp , estimation of dn_γ/dE is far more problematic. In principle, it is a function of quantum efficiency of a particular scintillator and as such will be different for each scintillator type. In case of polystyrene-based scintillator the reported values cover the range of 100 eV to 150 eV of deposited energy per emitted photon [33, 61], with values around 120 eV per photon reported for ternary-composition scintillators [60, 62].

As an example, it is useful to calculate a rough numerical estimate of the amount of photons generated within a round, $\varnothing = 1\text{ mm}$ multi-cladded scintillating fiber with a polystyrene core, uniformly illuminated by minimum ionizing particles. Assuming that each cladding layer is approximately $30\ \mu\text{m}$ thick, the diameter of the active fiber core is 0.88 mm. Then, the average most probable energy loss can be calculated using Eq. 2.20. Since Δp depends on the thickness of material traversed by the particle, which will vary depending on the distance of particle's track from the fiber's axis, it is most convenient

³Usually, one is interested in the expected location of the peak in the distribution of the number of photoelectrons per event. The amount of registered photoelectrons depends, among other things, on the amount of generated photons, which, in turn, depends on the amount of actually deposited energy. Hence, for thin detectors the location of the peak of the photoelectron distribution will depend on the most probable energy loss rather than on the mean energy loss.

to apply numerical techniques to do the calculation. For the given fiber configuration the resulting average most probable energy loss is ≈ 100 keV. Dividing that by the 120 eV needed to produce single optical photon gives roughly 880 photons.

A remark should be made in case the specific energy loss becomes high (mostly applies to low energy particles). Then, the light yield of the scintillator will be deteriorated due to recombination and quenching between the excited molecules. This effect is characterized by a widely accepted empirical formula that was provided by Birks [63]:

$$\frac{dN}{dx} = N_0 \frac{dE/dx}{1 + k_B dE/dx} \quad (2.23)$$

Here, dN/dx is the specific light yield, the N_0 stands for light yield under low specific ionization density, dE/dx is the mean specific energy loss provided by the Bethe formula (Eq. 2.3 to 2.6) and k_B is Birks constant, specific to each scintillator. For polystyrene it is 0.126 mm/MeV .

2.3.3 Collection and Transmission of Light

While the initial amount of photons may seem relatively large, only a fraction of them will reach the fiber end. When studying the light collection and transmission properties of the fiber, two quantities are of importance: the trapping efficiency and the attenuation of the fiber. The former affects the number of photons caught into the transmissive mode, while the latter describes their loss due to self-absorption of the fiber. Both were extensively studied over the years – a small glimpse at available experimental results can be found in [64–67], whereas example theoretical studies are presented in [61, 68, 69], as well as in author’s own study [23].

The quantity which is often provided for an optical fiber is its numerical aperture (NA). It is defined as:

$$NA = n_e \sin \theta_{max} = \sqrt{n_{co}^2 - n_{cl}^2} \quad (2.24)$$

with θ_{max} being the maximum angle of acceptance (i.e. the maximum half-angle of the cone of light that can enter the fiber), n_e being the ambient index of refraction and n_{co} , n_{cl} being the refractive indices of fiber’s core and outermost cladding, respectively (Fig. 2.11). One should note that the above definition assumes that the light source is coaxial with the fiber, i.e. all rays are considered meridional. The case of the scintillating fiber is different – since the light is generated within the fiber and the distance of particle tracks to the fiber axis is random, it is reasonable to assume that the light is generated uniformly within the cross-section of the fiber. Hence, most of the light sources will in fact be located off axis. Given the fact that the scintillation light is emitted isotropically, most of the light rays will not make an intercept with the fiber axis – they will be skewed rays with quasi-helical paths (Fig. 2.12).

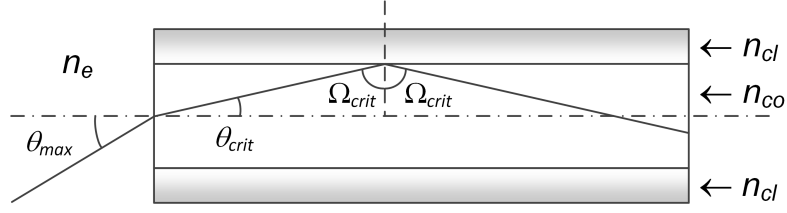


Figure 2.11: Explanation of the numerical aperture of the fiber (Eq. 2.24). The θ_{max} is the maximum acceptance angle, $\theta_{crit} = \pi/2 - \Omega_{crit} = \pi/2 - \arcsin(n_{cl}/n_{co})$ is the critical axial angle for the total internal reflection, n is the refractive index of the medium from which the ray is inbound, n_{co} , n_{cl} are the refractive indices of fiber's core and cladding, respectively. In case of multi-cladding fiber, n_{cl} refers to the outermost cladding layer.

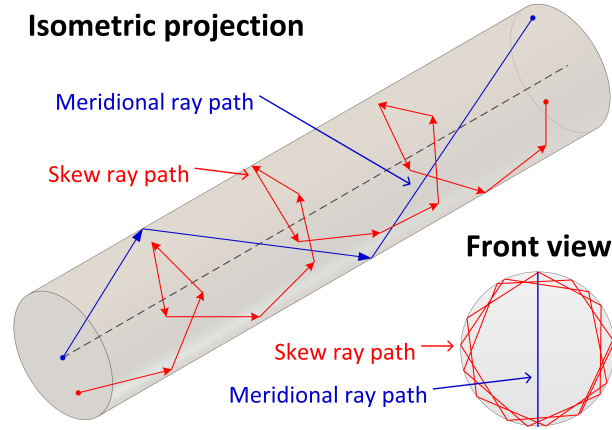


Figure 2.12: Possible ray paths within the fiber. Meridional rays are the fastest and least attenuated ones, while the skew rays have a quasi-helical path – longer and with more reflections, which is why they are subject to more attenuation. Most of the light collected by the fiber comes from rays with skewed paths.

The trapping efficiency of the fiber is the ratio of photons that entered the transmissive mode via the total internal reflection, in the direction towards the photosensor, to the total amount of photons emitted due to scintillation. The naive approach would be to take the ratio of the solid angle defined by the numerical aperture to the full 4π solid angle. However, if photon generation takes place close to the border of the fiber's core, it may be trapped into the transmissive mode even though the angle of its path to the fiber axis will be outside of the aperture of the fiber. It may happen because when the photon reaches the core-cladding interface, the angle of its path to the normal of the surface will still meet the requirements of the total internal reflection. An extreme example could be a photon emitted very close to the core-cladding interface, in a direction perpendicular to the fiber axis. The angle at which it will arrive at the border will be well above the critical angle, so it will end up making loops in a plane parallel to fiber cross-section until it gets attenuated. The above phenomenon has been verified by the author's own Monte-Carlo simulation of multi-cladding scintillating fiber [23] – see Figs. 2.13 and 2.15, where it is observable that the trapping efficiency increases as the particle track moves farther from

fiber's axis (Fig. 2.13).

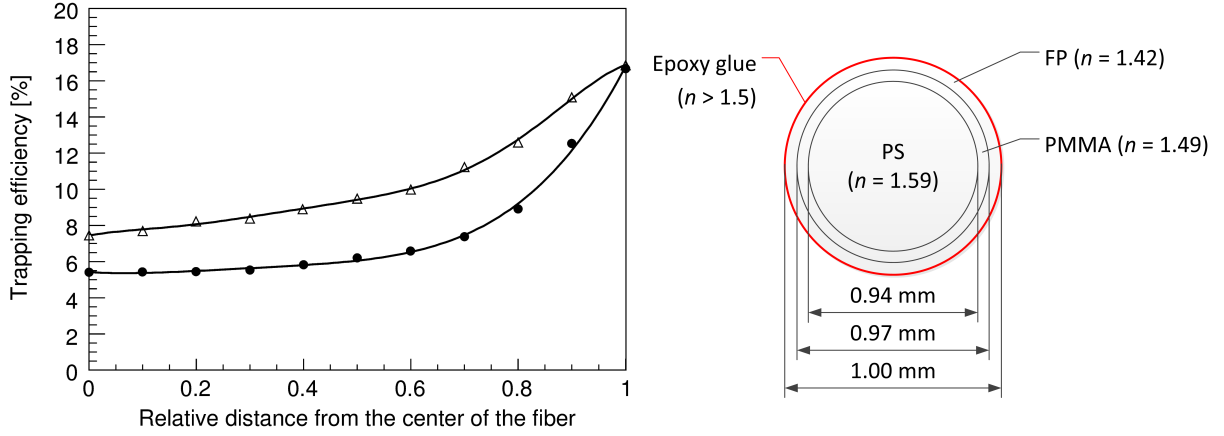


Figure 2.13: *Left:* Results of the author's Monte-Carlo simulations [23] of the trapping efficiency of a multi-cladding fiber as a function of the distance of the light generation point from the fiber axis (relative to the fiber radius). It was assumed that all photons that exit into the outer cladding are lost. Dots represent the results obtained for photons generated at a single point, whereas triangles show results for photons generated along a track. Fiber attenuation was explicitly set to zero. No wavelength-dependent effects were considered. *Right:* Cross-section of simulated fiber (PS – polystyrene; PMMA – acrylic glass; FP – fluoroacrylic). Note that the setup simulated in the paper used fiber diameter inconsistent with the datasheet of Kuraray multi-cladding fiber – with the cladding thickness of 30 μm the dimensions should be: $\varnothing_{\text{PS}}=0.88 \text{ mm}$ and $\varnothing_{\text{PMMA}}=0.94 \text{ mm}$.

Analytical derivation for a condition for trapping rays traveling at angles that are outside the numerical aperture of the fiber is as follows. The relation of the propagation angle to the axis of the fiber (θ) to the incident angle to the normal of the core-cladding interface (Ω) is [61]:

$$(\cos \theta)^2 + \left(\frac{r_{ic}}{r} \sin \theta\right)^2 = (\sin \Omega)^2 \quad (2.25)$$

where r is the radius of the core and r_{ic} is the closest approach of ray path to the axis of the fiber. Using Snell's law, one can calculate the critical angle for the total internal reflection and the corresponding critical angle of propagation:

$$\begin{aligned} \Omega_{crit} &= \arcsin(n_{cl}/n_{co}) \\ \theta_{crit} &= \arccos(n_{cl}/n_{co}) \end{aligned} \quad (2.26)$$

Now, requesting the $\Omega \geq \Omega_{crit}$ yields:

$$(\cos \theta)^2 + \left(\frac{r_{ic}}{r} \sin \theta\right)^2 \geq (\sin \Omega_{crit})^2 \quad (2.27)$$

After some calculations one arrives at the following condition for trapping skewed rays that are emitted outside the NA of the fiber:

$$(\sin \theta)^2 \leq \frac{(\sin \theta_{crit})^2}{1 - \left(\frac{r_{ic}}{r}\right)^2} \quad (2.28)$$

It is therefore easily observable that the further the distance of the emission point from the axis of the fiber, the higher the allowable θ that still fulfills the paradigm of the transmission via the total internal reflection. Accounting for the above, one can now define the trapping efficiencies for two distinct cases [61]. If the propagation angle is within the NA of the fiber, either for meridional or skewed rays, then we have so-called ‘bound rays’ and the trapping efficiency is:

$$\varepsilon_{br} = \frac{1}{2}(1 - \cos \theta_{crit}) = \frac{1}{2} \left(1 - \frac{n_{cl}}{n_{co}} \right) \quad (2.29)$$

If we now also include the skewed rays transmitted with $\theta > \theta_{crit}$ (so-called ‘tunneling rays’), then, assuming a perfect interface at the coupling (i.e., $n_e = n_{co}$) the trapping efficiency becomes:

$$\varepsilon_{trap} = \frac{1}{2} \left[1 - \left(\frac{n_{cl}}{n_{co}} \right)^2 \right] \quad (2.30)$$

A quick calculation for a case considered in Fig. 2.13 (PS/PMMA/FP) reveals that the numbers provided by Eq. 2.29 and Eq. 2.30 differ by a considerable amount – 5.4% vs. 10.1%, respectively. Unfortunately, in reality, it is the smaller of the two that is a better estimate. The reason for that will become clear after considering fiber’s attenuation and the behavior of rays at the coupling with the photosensor.

The two primary sources of the attenuation are the bulk absorption within the base material and reflection losses. Leading causes for the former one are Rayleigh scattering and self-absorption of scintillation light due to overlap between the emission and the absorption bands of the fluorescent dyes. The latter results from surface roughness or variation in the refractive indices. A simplified formula for the transmission function of a straight fiber can be written as [70]:

$$T(\theta) = T_d(\theta) = e^{-P(\theta)L_0/\Lambda_{bulk}} q^{m(\theta, r_{ic})L_0} \quad (2.31)$$

The L_0 stands for the axial distance from the emission point to the fiber end, θ is the angle between the photon path and the fiber axis, $P(\theta)$ denotes the total photon path length per unit axial fiber length for a photon traveling at angle θ to the axis of the fiber, Λ_{bulk} is the bulk attenuation length⁴, characterizing losses due to bulk absorption and scattering, $m(\theta, r_{ic})$ is the number of reflections per unit axial fiber length for a photon traveling at angle θ to the axis of the fiber whose path has closest approach r_{ic} to the fiber axis, and q represents the reflection coefficient for the total internal reflection. The first term describes losses due to bulk attenuation, the second accounts for the losses due to imperfect reflections. In case the open end of the fiber is equipped with a mirror, the

⁴Attenuation length is the distance at which the signal amplitude drops to 1/e of its original value.

above transmission function changes to:

$$T(\theta)|_{d+r} = T_d(\theta) + T_r(\theta) = e^{-P(\theta)L_0/\Lambda_{bulk}} q^{m(\theta,r_{ic})L_0} + R e^{-P(\theta)(2L_F-L_0)/\Lambda_{bulk}} q^{m(\theta,r_{ic})(2L_F-L_0)} \quad (2.32)$$

with L_F denoting the total fiber length and R being the reflectance of the mirror. The formulas for $P(\theta)$ and $m(\theta, r_{ic})$ are [61]:

$$P(\theta) = \frac{1}{\cos \theta} \quad (2.33)$$

$$m(\theta, r_{ic}) = \frac{\tan \theta}{2r} \sqrt{1 - \left(\frac{r_{ic}}{r}\right)^2} \quad (2.34)$$

Reasonable values of Λ_{bulk} are 3–5 m for the doped polystyrene and ≈ 8 m for the clear one [70]. The reported values of reflection coefficient q are in the range $5 \times 10^{-5} \leq 1 - q \leq 6.5 \times 10^{-5}$ [71]. Typical values of reflectance for the mirror vary from $\approx 70\%$ for various foils up to $\approx 90\%$ for layers of aluminum or silver deposited on polished surfaces.

Unfortunately, when it comes to actual estimation of the light yield of a particular fiber, defined as the number of photons that reach the fiber end at the photosensor side, the overall picture becomes fairly complicated. First, fluorescent dyes used in organic scintillators emit light at a range of wavelengths (for example, emission spectrum see Fig. 2.9). Given the attenuation properties of the fiber core (Fig. 2.8), suppression of shorter wavelengths is higher than the longer ones. The result is that the larger the distance from the emission point, the more the peak of the observed emission spectrum shifts towards the longer wavelengths. Hence, the attenuation of the fiber will decrease compared to the attenuation at the point of scintillation⁵. Consequently, the constant Λ_{bulk} in Eq. 2.31 should be replaced by a function that depends on the wavelength of light. Next, the index of refraction of the core and the cladding is also wavelength-dependent (Fig. 2.14). Since the ratio of the refractive indices defines the critical angle for the total internal reflection, the trapping efficiencies defined in Eq. 2.29 and Eq. 2.30 also depend on the wavelength of light.

Still next, an increased tail in the distribution of photon arrival times shown in the right plot of Fig. 2.15 indicates that that the farther the emission point from the fiber axis, the more skewed (and hence longer) the photon paths become, also leading to more reflections. Therefore, for this type of rays, it is reasonable to expect higher signal losses per axial fiber length than for the meridional counterpart, caused by increased bulk attenuation as well as reflection losses at the core-cladding boundary. Using formalism of Eq. 2.31, the above statement could be expressed as $P(\theta) \gg 1 \Rightarrow P(\theta)\Lambda_{bulk} \gg \Lambda_{bulk}$ and $q < 1 \Rightarrow q^{m(\theta)} \ll 1$.

⁵Please note that attenuation is defined as signal loss per unit length (for example dB/km), not per total fiber length. In other words, it is the specific signal loss of the fiber. With such a definition, the statement that attenuation is decreasing with increasing fiber length makes perfect sense, even though it may sound strange upon first impression.

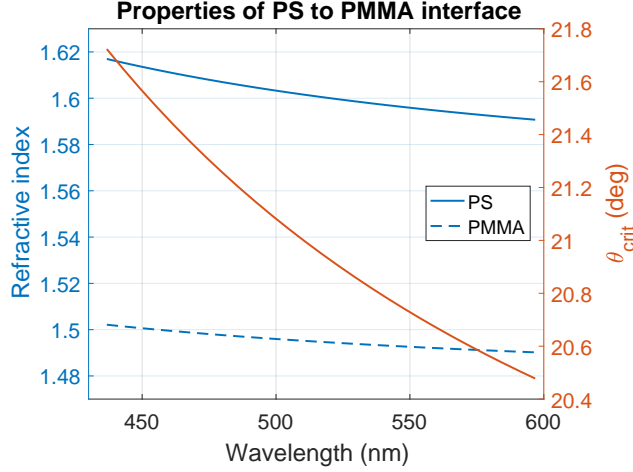


Figure 2.14: Refractive indices of polystyrene (PS) and acrylic glass (PMMA, also known as plexiglass) as a function of the wavelength of light. Critical axial angle θ_{crit} for transmission via the total internal reflection, for PS to PMMA boundary as a function of wavelength. Refractive index data were obtained from [72].

Recent measurements by Nieswand [73] seem to support this conclusion – Fig. 2.16 clearly shows that, even for a 25 cm fiber, the spatial intensity distribution of the light exiting a 1 mm fiber is already relatively uniform. The edge-to-center difference is on the order of roughly 10%, whereas based on trapping efficiency simulations (Fig. 2.13) a much higher number of rays would be expected close to the fiber edge. One explanation of these results could be that the rays close to the edge are the most skewed ones, so they are significantly attenuated. The other is that significantly skewed rays will undergo significant refraction at the core-coupling interface, meaning that their angle of incidence at the photodetector surface will be large. Since the photodetector efficiency usually drops at large angles of incidence, they may remain unregistered. Consequently, unless the fiber length is very short, the best bet is to neglect the contribution of the ‘tunneling rays’ and calculate the trapping efficiency using Eq. 2.29.

Finally, all the calculations become much more complex if one considers multi-cladding fibers. In principle, a transformation of Eq. 2.31 is necessary in order to account for the fact that a considerable fraction of photons will partially travel in the inner cladding, which will have different absorption characteristics from the core. Also, one should note that the photons that enter the inner cladding will undergo refraction, so the angle of their path to the fiber axis will change.

All in all, taking all the above factors into account, it is impractical to attempt to find analytical solution for the exact estimate of the light yield of the fiber. Given the CPU power that is currently available, as well as availability of the photon tracking code in most of the packages used for high energy physics simulation (for example GEANT4 [74–76]), the most convenient approach is to calculate this estimate using Monte-Carlo

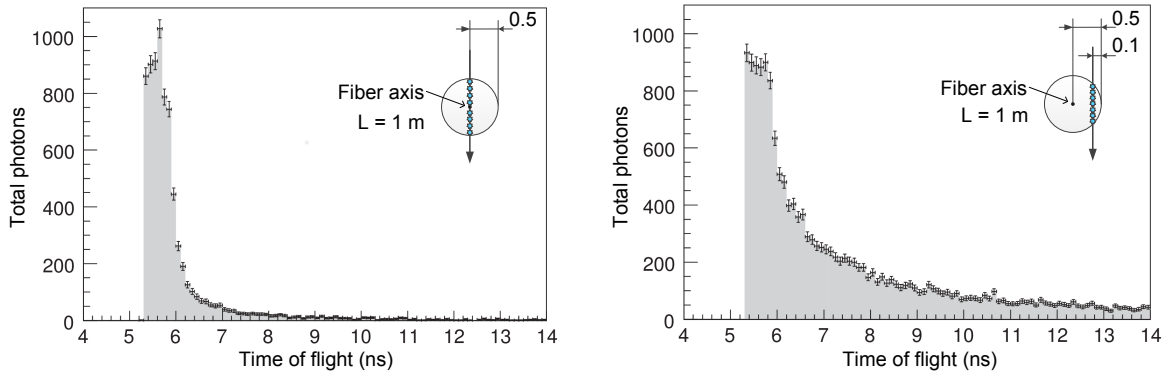


Figure 2.15: Results of the author’s Monte-Carlo simulations [23] of the time of flight of photons for a round $\varnothing = 1$ mm multi-cladding fiber of 1 m length. It was assumed that all photons that exit into the outer cladding are lost. (left) Time of flight for photons generated uniformly along a track traversing the center of the fiber. (right) Time of flight for photons generated uniformly along a track close to the border of the fiber. A long-tail towards longer times of flight indicates a significant contribution of skew rays with significantly longer paths, some of which would otherwise not enter the transmissive mode of the fiber. Fiber attenuation was explicitly set to zero. No wavelength-dependent effects were considered.

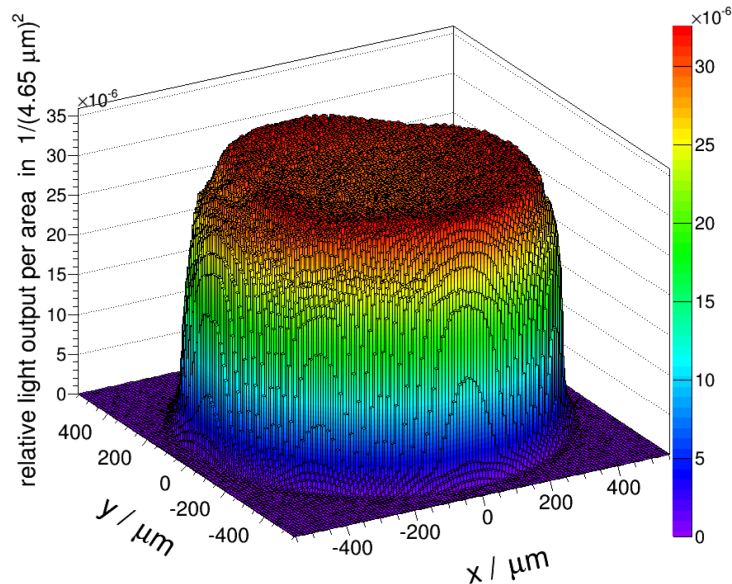


Figure 2.16: Example of measurements of the spatial distribution of the intensity of light exiting a 25 cm long, multi-cladding, wavelength-shifting fiber (Kuraray-Y11), obtained using a CCD camera. *Source: Redrawn from the thesis of Nieswand [73].*

techniques. If one nevertheless needs a quick, rough number, then:

- The trapping efficiency can be calculated using Eq. 2.29 (i.e., ‘bound rays’ only) and substituting n_{cl} and n_{co} with values of the refractive indices corresponding to the peak of the emission spectrum at the desired fiber length. This type of data can usually be obtained from manufacturer’s specifications.
- The attenuation of the fiber can be approximated using the effective attenuation length. The methodology is provided in [70], which suggest a value of $\Lambda_{eff} \approx 86\% \Lambda_{bulk}$. However, it is also stated that this approximation is valid only for fiber length above certain minimum length. If one defines the meridional approximation of fiber attenuation length as:

$$\Lambda_m = \frac{\cos \theta_{crit}}{1/\Lambda_{bulk} + (1 - q)(\sin \theta_{crit})/2r} \quad (2.35)$$

with Λ_{bulk} and q defined as in Eq. 2.31, r being the core radius and θ_{crit} the critical axial angle for the total internal reflection (Eq. 2.26), then the proposed approximation is valid if $L_F/\Lambda_m \geq 0.2$, with L_F being the fiber length. For smaller fiber lengths, the only solution is to find relevant measurement data or to make independent measurements. Example results for round $\varnothing = 0.5$ mm and $\varnothing = 1$ mm Kuraray fibers are reported in [65].

The final formula for the light output of the fiber is then:

$$N_{ph} = N_0 \varepsilon_{br} e^{-L_F/\Lambda_{eff}} = \frac{N_0}{2} (1 - \cos \theta_{crit}) e^{-L_F/\Lambda_{eff}} \quad (2.36)$$

To sum up, it is useful to consider a numerical example. In the previous subsection it was already calculated that a round $\varnothing = 1$ mm multi-clad fiber (from Kuraray [32]), uniformly illuminated by minimum ionizing particles, would on average generate approx. 880 photons. If the length of the fiber is 1 m and the expected peak emission wavelength is around 450 nm. The refractive index of the core (polystyrene) is then $n_{co} \approx 1.61$ and of the outer cladding (fluorinated polymer) it is $n_{cl} \approx 1.42$. Consequently, the critical axial angle for transmission of meridional rays via the total internal reflection is $\theta_{crit} \approx 28.1^\circ$ (Eq. 2.26) and the resulting average trapping efficiency for ‘bound rays’ is $\varepsilon_{br} \approx 5.4\%$ (Eq. 2.29). Using conservative estimates of the bulk absorption length of the core and the reflection coefficient, $\Lambda_{bulk} = 3$ m and $q = 0.9999$, and also neglecting transmission within the inner cladding, the meridional approximation of the attenuation length would be $\Lambda_m \approx 2.65$ m (Eq. 2.35). Since the fiber length is 1 m, the ratio $L_F/\Lambda_m \approx 0.38$, which is above the limiting value of 0.2. Hence, we can use the approximation of the effective attenuation length, which in this case will be $\Lambda_{eff} \approx 0.86 \Lambda_{bulk} = 2.58$ m. Knowing that, it is finally possible to estimate photon yield of the fiber:

$$N_{ph} = N_0 \varepsilon_{br} e^{-L_F/\Lambda_{eff}} = 880 \times 0.054 \times e^{-1/2.58} \approx 32 \quad (2.37)$$

2.4 Fiber to Photosensor Coupling

Since the level of the light signals available at the fiber end is rather small, it is of primary importance that the highest possible amount of photons arrive at the active area of the photosensor. An obvious requirement is that the geometry of the setup should ensure that almost all of the light exiting the fiber hits the photodetector. Another, equally important factor, is the type of substance used to couple the two – its most important properties are the attenuation and the refractive index. The requirements for the former one can usually be relaxed (i.e. it can be slightly opaque), as the coupling layer is typically relatively thin. The latter one deserves a deeper investigation, as the refractive index of the coupling gel can severely affect the amount of light that can exit the fiber.

According to Fresnel equations⁶, the reflectance at a boundary between two dielectrics is defined as follows:

$$R_s = \left| \frac{n_1 \cos \theta'_i - n_2 \cos \theta'_t}{n_1 \cos \theta'_i + n_2 \cos \theta'_t} \right|^2 \quad (2.38)$$

$$R_p = \left| \frac{n_1 \cos \theta'_t - n_2 \cos \theta'_i}{n_1 \cos \theta'_t + n_2 \cos \theta'_i} \right|^2 \quad (2.39)$$

In the above equations, R_s is the coefficient for light in which the electric field is perpendicular to the plane of incidence (s-polarized), R_p is the coefficient for light with the electric field parallel to the plane of incidence (p-polarized), n_1 and n_2 are indices of refraction of the two dielectrics and, finally, θ'_i and θ'_t are the angles between the normal of the interface and the incident and refracted (transmitted) rays, respectively.

The relationship between the angles of the incident and the refracted rays is given by the Snell's law:

$$n_1 \sin \theta'_i = n_2 \sin \theta'_t \quad (2.40)$$

Consequently, one can eliminate θ'_t from equations 2.38 and 2.39:

$$R_s = \left| \frac{n_1 \cos \theta'_i - n_2 \sqrt{1 - \left(\frac{n_1}{n_2} \sin \theta'_i\right)^2}}{n_1 \cos \theta'_i + n_2 \sqrt{1 - \left(\frac{n_1}{n_2} \sin \theta'_i\right)^2}} \right|^2 \quad (2.41)$$

$$R_p = \left| \frac{n_1 \sqrt{1 - \left(\frac{n_1}{n_2} \sin \theta'_i\right)^2} - n_2 \cos \theta'_i}{n_1 \sqrt{1 - \left(\frac{n_1}{n_2} \sin \theta'_i\right)^2} + n_2 \cos \theta'_i} \right|^2 \quad (2.42)$$

Corresponding transmittances can be calculated using the law of the conservation of energy:

$$T_s = 1 - R_s \quad (2.43)$$

⁶See https://en.wikipedia.org/wiki/Fresnel_equations

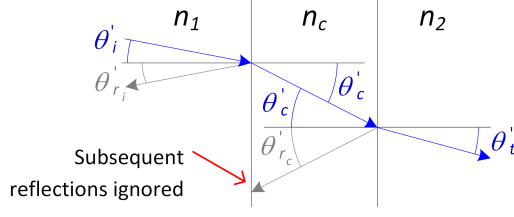


Figure 2.17: Analyzed case of transmission of light between two materials via a coupling grease. The refractive indices of both materials as well as the coupling grease are n_1 , n_2 , n_c , respectively. θ'_i is the angle between the incident ray and the normal to the plane of incidence, θ'_c is similar angle within the coupling grease (both refracted incident ray, depending on the boundary) and finally θ'_t is the angle of the ray transmitted to the second material. The law of reflection states that $\theta'_{r_i} = \theta'_i$ and $\theta'_{r_c} = \theta'_c$. Note that θ'_i in the figure is equivalent to the propagation angle through the fiber.

$$T_p = 1 - R_p \quad (2.44)$$

Now, let us consider a case when an additional material layer is introduced between materials 1 and 2, as shown in Fig. 2.17, and the refractive index of the new material is n_c . In such a scenario, if one neglects multiple reflections within the coupling layer, the transmittances for the s-polarized and the p-polarized light become:

$$T_{s_{1c}} = 1 - R_{s_{1c}} = 1 - \left| \frac{n_1 \cos \theta'_i - n_c \cos \theta'_c}{n_1 \cos \theta'_i + n_c \cos \theta'_c} \right|^2 \quad (2.45)$$

$$T_{s_{c2}} = 1 - R_{s_{c2}} = 1 - \left| \frac{n_c \cos \theta'_c - n_2 \cos \theta'_t}{n_c \cos \theta'_c + n_2 \cos \theta'_t} \right|^2 \quad (2.46)$$

$$T_{s_{12}} = T_{s_{1c}} T_{s_{c2}} \quad (2.47)$$

$$T_{p_{1c}} = 1 - R_{p_{1c}} = 1 - \left| \frac{n_1 \cos \theta'_c - n_c \cos \theta'_i}{n_1 \cos \theta'_c + n_c \cos \theta'_i} \right|^2 \quad (2.48)$$

$$T_{p_{c2}} = 1 - R_{p_{c2}} = 1 - \left| \frac{n_c \cos \theta'_t - n_2 \cos \theta'_c}{n_c \cos \theta'_t + n_2 \cos \theta'_c} \right|^2 \quad (2.49)$$

$$T_{p_{12}} = T_{p_{1c}} T_{p_{c2}} \quad (2.50)$$

The symbols are defined as follows: $T_{s_{1c}}$ is the transmittance of the s-polarized light from the first material to the coupling layer, $T_{s_{c2}}$ is the transmittance of the s-polarized light from coupling layer to the second material, $T_{p_{1c}}$ and $T_{p_{c2}}$ are corresponding transmittances for the p-polarized light. $T_{s_{12}}$ and $T_{p_{12}}$ are the resulting transmittances from the first to the second material via the coupling layer. Again, using Snell's law, it is possible to

express T_{s12} and T_{p12} as a function of the refractive indices of the three materials and the incidence angle only:

$$T_{s12} = \left(1 - \left| \frac{n_1 \cos \theta'_i - n_c \sqrt{1 - \left(\frac{n_1}{n_c} \sin \theta'_i\right)^2}}{n_1 \cos \theta'_i + n_c \sqrt{1 - \left(\frac{n_1}{n_c} \sin \theta'_i\right)^2}} \right|^2 \right) \left(1 - \left| \frac{n_c \sqrt{1 - \left(\frac{n_1}{n_c} \sin \theta'_i\right)^2} - n_2 \sqrt{1 - \left(\frac{n_1}{n_2} \sin \theta'_i\right)^2}}{n_c \sqrt{1 - \left(\frac{n_1}{n_c} \sin \theta'_i\right)^2} + n_2 \sqrt{1 - \left(\frac{n_1}{n_2} \sin \theta'_i\right)^2}} \right|^2 \right) \quad (2.51)$$

$$T_{p12} = \left(1 - \left| \frac{n_1 \sqrt{1 - \left(\frac{n_1}{n_c} \sin \theta'_i\right)^2} - n_c \cos \theta'_i}{n_1 \sqrt{1 - \left(\frac{n_1}{n_c} \sin \theta'_i\right)^2} + n_c \cos \theta'_i} \right|^2 \right) \left(1 - \left| \frac{n_c \sqrt{1 - \left(\frac{n_1}{n_2} \sin \theta'_i\right)^2} - n_2 \sqrt{1 - \left(\frac{n_1}{n_c} \sin \theta'_i\right)^2}}{n_c \sqrt{1 - \left(\frac{n_1}{n_2} \sin \theta'_i\right)^2} + n_2 \sqrt{1 - \left(\frac{n_1}{n_c} \sin \theta'_i\right)^2}} \right|^2 \right) \quad (2.52)$$

Given the fact that the light produced within the scintillator is unpolarized, the ratio of the s-polarized to the p-polarized light is exactly $1/2$. Therefore, the resulting transmittance between the materials is:

$$T_{12} = \frac{1}{2} (T_{s12} + T_{p12}) \quad (2.53)$$

Let us now consider a simplified case, when the light is incoming at an angle normal to the plane of incidence (i.e. $\theta'_i = 0$). Then, the expression for transmittance simplifies to:

$$\begin{aligned} T_{12} &= \frac{1}{2} \left[\left(1 - \left| \frac{n_1 - n_c}{n_1 + n_c} \right|^2 \right) \left(1 - \left| \frac{n_c - n_2}{n_c + n_2} \right|^2 \right) + \left(1 - \left| \frac{n_1 - n_c}{n_1 + n_c} \right|^2 \right) \left(1 - \left| \frac{n_c - n_2}{n_c + n_2} \right|^2 \right) \right] = \\ &= \frac{4n_1 n_c}{(n_1 + n_c)^2} \cdot \frac{4n_c n_2}{(n_c + n_2)^2} = \frac{16n_1 n_2 n_c^2}{(n_1 + n_c)^2 \cdot (n_2 + n_c)^2} \quad (2.54) \end{aligned}$$

Determining optimal value of n_c , which would maximize the transmission, requires finding the maxima of the Eq. 2.54 – that is differentiating it with respect to n_c and determining zeros of the derivative:

$$\frac{\partial T_{12}}{\partial n_c} = \frac{32n_1 n_2 n_c}{(n_1 + n_c)^2 \cdot (n_2 + n_c)^2} \cdot \left(1 - \frac{n_c}{n_1 + n_c} - \frac{n_c}{n_2 + n_c} \right) \quad (2.55)$$

$$\frac{\partial T_{12}}{\partial n_c} = 0 \quad (2.56)$$

Solving Eq. 2.56 yields following results:

$$\begin{aligned} n_{c_1} &= 0 \\ n_{c_2} &= \sqrt{n_1 n_2} \\ n_{c_3} &= -\sqrt{n_1 n_2} \end{aligned} \quad (2.57)$$

Quick examination of the solutions reveals that only the second one is viable (i.e. n_{c_2}), as negative refractive indices as well as those equal to zero are invalid for typical dielectrics. The result means that it is best to maintain the same ratio of refractive indices at each dielectric boundary, in which case Eq. 2.54 simplifies to:

$$T_{12} = \frac{16n_1 n_2}{(\sqrt{n_1} + \sqrt{n_2})^4} \quad (2.58)$$

In practice, the exact value of the refractive index of the coupling gel is not that important. Plots showing the transmittance as a function of the angle of incidence and parameterized by refractive indices of the coupling layer, for an example coupling between a multi-cladding fiber and a photomultiplier tube (polystyrene or PMMA to borosilicate glass – $n_{PS} = 1.59$, $n_{PMMA} = 1.49$, $n_{glass} = 1.517$), are shown in Fig. 2.18.

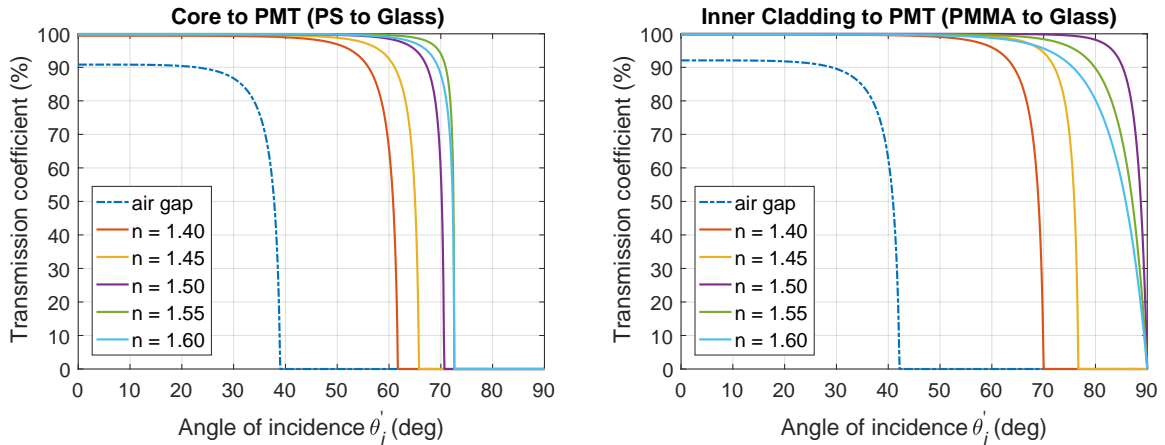


Figure 2.18: Transmission coefficient from the fiber to the photomultiplier via a gel, as a function of the incidence angle of the light beam from within the fiber. The plots are parameterized by various refractive indices of optical coupling gels used to mate the fiber to the photomultiplier window (borosilicate glass). The parameters used for the simulation were: $n_{PS} = 1.59$, $n_{PMMA} = 1.49$, $n_{glass} = 1.517$. For comparison, the dash-dot line shown transmission curve in case no gel is used (i.e. there is an air gap, $n = 1.0$).

As can be seen, as long as the refractive index is within the range of 1.4–1.6, the effect on light transmission is negligible. One could argue that, with proper choice of the index of refraction of the coupling gel, a clear improvement of the transmission coefficient can be observed at incidence angles above approximately 60° . However, for a light beam to have such large incidence angle, it would have to travel along a helical path within the

fiber – i.e. a significant fraction of skew rays would have to be present. It was already discussed in section 2.3 that the skew rays are attenuated rapidly, so any benefits of perfectly matched gel would be noticeable only in case of very short fibers.

2.5 Photosensors

Photosensors are among the most crucial elements of every scintillation detector. Their sole purpose is to convert an incoming light signal into a corresponding electrical pulse that is suitable for subsequent processing. Ideally, one would like this conversion to be made in a way that does not deteriorate detector performance – i.e. errors introduced by the photosensor should be small compared to the limitations imposed by radiation interactions, scintillation process and detector optics. Therefore, when selecting the photosensor for a given detector, one should pay attention to several key parameters, briefly summarized below.

- **Mechanics.** Not much to comment here – the sensor must match fiber(s) size while providing best possible geometry for light collection. It also must fit within the structure of the detector.
- **Mode of operation.** The sensor can be operated in one of the two modes: pulse counting mode or continuous mode. In pulse counting mode each individual pulse is registered. This the most common mode of operation of most detectors based on scintillating fibers, as it provides precise timing and, if needed, also amplitude of the pulses. This information can be used to provide trigger for the whole experiment. However, sometimes the timing information is irrelevant. In this case, a more convenient way may be to just measure the current generated by the photosensor coupled to a specific detector channel. The benefit is that for this mode of operation one can use much slower photosensors and electronics, which can provide significant cost savings.
- **Quantum efficiency**, which describes probability of converting an incident photon into a corresponding charge carrier⁷:

$$\eta(\lambda) = \frac{\text{number of generated primary charge carriers}}{\text{number of incident photons}} \quad (2.59)$$

with λ being the wavelength of the incident light. One should pick sensors that have maximum quantum efficiency at a wavelength that matches the peak in the emission

⁷The exact definition of the term ‘charge carrier’ varies according to the sensor type, which is why a general term was used in the definition of the quantum efficiency.

spectrum of the fiber (note that it changes with fiber length because fiber attenuation is also wavelength-dependent), while also taking into account transmission characteristics of the fiber-to-sensor coupling and the window of the photosensor. Usually, it is the combination of all the above factors, integrated over the range of wavelengths that are of interest, that should be maximized. Somehow more systematic approach to matching the photosensor to the scintillator can be derived from the methodology presented in [77], where so called ‘matching factors’ were defined. In case of the scintillating fiber detector, if the limiting wavelengths are denoted as λ_{min} , λ_{max} and the normalized quantum efficiency of the photosensor as $\eta_{norm}(\lambda) = 1/\max(\eta(\lambda))$, then the matching factor can be expressed as:

$$a = \frac{\int_{\lambda_{min}}^{\lambda_{max}} s(\lambda, L_F) t_{coupling}(\lambda) t_{window}(\lambda) \eta_{norm}(\lambda) d\lambda}{\int_{\lambda_{min}}^{\lambda_{max}} s(\lambda, L_F) d\lambda} \Bigg|_{L_F=const} \quad (2.60)$$

Here, s denotes normalized emission spectrum of the fiber with length L_F (note that the emission spectrum of the fiber changes with its length due to unequal attenuation of various wavelength), $t_{coupling}$ is transmission of the fiber-to-sensor coupling, t_{window} transmission of the photosensor window and η_{norm} is normalized quantum efficiency of the photosensor.

- **Gain and charge resolution.** Due to weak level of light signal (few to several hundred photons), the initial charge generated from the converted light is very low. Therefore, it requires significant amplification, so that the output pulse of the sensor can be seamlessly processed by the accompanying electronics. The amplification process is subject to statistical fluctuations, so variation of the response charge and amplitude are to be expected. In case of tracking detectors this is less of an issue, as one usually just wants to detect whether a fiber was hit and then to estimate the timing of this hit. However, depending on adopted pulse processing techniques, some additional timing jitter may be introduced due to the so-called ‘amplitude walk’ effect (Fig. 2.19 – see t_1 vs. t_2).
- **Collection efficiency (CE)** or, in other words, probability that already generated primary charge carrier will reach the part of the photosensor that is responsible for charge amplification:

$$CE = \frac{\text{number of primary charge carries that got amplified}}{\text{number of generated primary charge carriers}} \quad (2.61)$$

One would like this parameter to be nearly 100%, as the overall efficiency of the sensor always includes a combination of the collection and quantum efficiencies. It

is also worth mentioning that this parameter may vary with the location of the light interaction point on the photosensitive area of the sensor.

- **Time resolution and pulse shape stability.** Each primary charge carrier needs to travel inside the detector in order to gain sufficient energy to produce secondary carriers upon collision with elements (or atoms/molecules) of the structure comprising the photosensor. Moreover, most of sensors usable with scintillating fibers employ some kind of avalanche process to achieve required charge gain, in which secondary carriers are accelerated again to produce tertiary charges and so on. One source of randomness is the variability of charge carrier paths. The other could come from the fact that the electric field that accelerates them is non-uniform within the volume of the sensor – it can even depend on the actual charge of particular response due to space-charge effects, where avalanche charge may create electric field that counteracts the accelerating field. The consequence is that each output pulse arrives at slightly different time and may be with slightly different shape, thus introducing additional time jitter (Fig. 2.19 – see t_1 vs. t_3 & t_4). Again, the magnitude of the jitter will depend on the applied pulse processing method. It will also vary inversely with the square root of the number of the primary charge carriers, which follows the Poisson distribution (i.e., $\sigma \sim 1/\sqrt{N_{PE}}$, with N_{PE} being the number of the primary carriers). Given the fact that scintillating fiber detectors are fast and are frequently used in trigger systems and/or for time-of-flight applications, this parameter is of crucial importance.

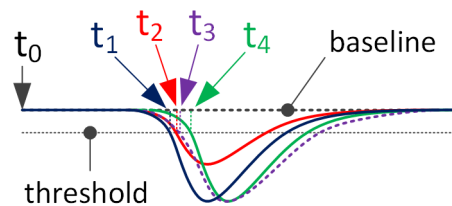


Figure 2.19: Fluctuation of the photosensor response to a single photon signal and their consequences for the timing accuracy. The t_0 is the time that photon hits the photocathode. Pulse timing is obtained from detecting threshold crossing. If the ‘reference’ response is chosen arbitrarily – say blue curve with time t_1 , then timing of subsequent responses may differ due to: gain fluctuation (red, t_2 - the ‘amplitude walk’ effect), pulse shape instability (dotted purple, t_3) or fluctuation of charge transit time (green, t_4).

- **Dark count rate**, sometimes called ‘dark noise’, is the rate at which pulses are generated without incident photons. It is usually related to thermionic generation of carriers, hence an exponential relationship to temperature is to be expected. It will also highly depends on type of particular sensor (may even vary between

sensors of the same type). Fortunately, this parameter is not very critical in case of scintillating fiber detectors, as typical detector consists of several fiber planes with different orientations. Since photons generated by a passing particle will be correlated in time, so will be the pulses produced by the photosensors. On the other hand, pulses from thermal generation will not be correlated, so spontaneous counts can be effectively suppressed by a coincidence unit. Furthermore, typical scintillation event produces several photons, so one can also discriminate events based on pulse amplitude.

- **Afterpulsing**, also known by the name ‘correlated noise’, is the process of producing spurious pulses triggered by the charge multiplication process associated with the preceding pulse. Typically, it is caused by trapping one (or more) charge carriers in some metastable states and then releasing it at a later time. The exact relaxation times vary depending on the material type and are usually in the range of hundreds of ns to μ s. The amplitude of the ‘afterpulse’ will usually be lower than that of the original pulse. This type of noise is far more difficult to suppress, as it is correlated in time with the actual pulse from the particle. Therefore, one should generally avoid sensors with large afterpulsing. If this is not an option, then possible workarounds include using a coincidence unit with sufficiently narrow time window (as there will be statistical fluctuations between timing of afterpulses from two different sensors), coupled with some form of amplitude discrimination.
- **Susceptibility to magnetic fields**. Given abundance of strong magnets in high energy physics experiments, this property may become quite important. It may severely affect detector design in case magnetic shielding is necessary (as it tends to be of rather heavy weight, thus impacting structure design).
- **Susceptibility to temperature**. It was already mentioned that dark rate count is a function of temperature. However, several other parameters may also be affected, for example charge gain (especially in semiconductor sensors) or afterpulsing probability. If effects of operating temperature are significant, then it may be necessary to employ some form of active temperature stabilization or apply proper calibrations. In any case, this factor should be considered carefully when selecting sensor for the detector.
- **Radiation hardness**. Severity of this parameter depends on actual usage scenario. It is a well known fact that ionizing radiation does cause damage to various materials and will affect lifetime of photosensors. The most common way in which this damage manifests itself is, among other things, increased dark rate, decreased gain and loss of detection efficiency [78–80]. One should also notice that it is possible to recover

some performance of the sensors by annealing [81]. In any case, if the detector is to work in high-radiation environment, then careful studies are necessary in order to ensure adequate performance within the desired operation period.

Currently, two types of the photosensors stand out in applications in scintillating fiber tracking detectors used in high energy physics experiments: photomultiplier tubes, which are in use for several decades, and relatively new Geiger-mode multi-pixel avalanche photodiodes, also known by the name of Multi-Pixel Photon Counters (MPPCs) or Silicon Photomultipliers (SiPMs). Both will be briefly described in the following subsections. More in-depth coverage of the subject can be found in textbooks [40, 82] or various materials provided by the manufacturers [83–86].

2.5.1 Photomultipliers

The principle of photomultiplier tube (PMT) operation is presented in Fig. 2.20. The three main components of the PMT are: an evacuated glass tube, the photocathode – a thin photo-sensitive semiconductor layer, placed on the inner side of the entrance window, and the electron multiplier structure – several electrodes which are responsible for electron collection and multiplication. By convention, these electrodes are called the dynodes. The photocathode is biased at the lowest (i.e. the most-negative) potential, which is then increased with each consecutive dynode, thus producing electric field inside the tube. When an incident photon passes through the entrance window and interacts with the photocathode, it excites an electron from the valence band to the conduction band. The electron then drifts towards the surface of the photocathode facing the vacuum. If it does not recombine on the way and still has enough energy to overcome the surface potential barrier, it escapes and accelerates towards the first dynode (since it originated from the photocathode, it is commonly named ‘a photoelectron’, abbreviated PE or p.e.). Once it reaches the first dynode, it has gained sufficient energy that, on impact, it excites several other electrons, some of which again escape into the vacuum and accelerate towards the second dynode. Then, upon reaching the second dynode, these electrons again liberate even more electrons, which accelerate towards the next dynode, and so on – until the charge is collected at the anode. Typical electron gains are on the order of 10^5 to 10^7 .

From the usability point of view, one should be aware of few issues when using PMTs. First of them is a direct consequence of the principle of operation presented above. As already mentioned, the photoelectron that is liberated from the photocathode needs to travel some distance before it hits the first dynode. The speed at which it moves depends on the strength of the electric field between the photocathode and the first dynode. Being a charged particle, the electron is sensitive not only to electric fields, but also to

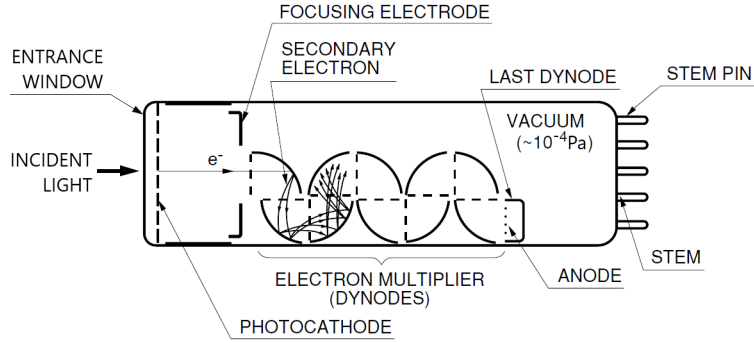


Figure 2.20: Principle of the operation of the photomultiplier tube. Picture taken from [83] (with modifications).

magnetic fields. As such, if the external magnetic field is sufficiently strong compared to the electric field inside the tube, it will affect electron trajectory and may result in deteriorated collection efficiency – i.e. the photoelectrons will either miss the first dynode or hit it at a sub-optimal position, in which case not all secondaries will hit the next dynode (same applies to subsequent dynodes in the multiplier chain). In case of large PMTs even Earth’s magnetic field may affect their operation – though this is not the case of scintillating fiber trackers, as usually small PMTs are used to collect signals from the fibers. Nevertheless, one should note that typical high energy physics experiments utilize strong magnets in order to properly identify particle types, so even the fringe field from the magnets can be non-negligible. Bottom line is that one should carefully examine conditions at which the photomultiplier will operate and evaluate the need of magnetic shielding. Example measurements of a small multi-channel PMT (Hamamatsu Photonics H6568, effective photocathode area of 18.1 mm × 18.1 mm) that were used in scintillating fiber trackers built for the COMPASS experiment [87] are shown in Fig. 2.21. As can be seen, depending on orientation of the PMT axis with respect to the magnetic field, one can observe significant drop in gain at field strength of approx. 20 mT.

Second factor which should be carefully considered when considering PMTs for particular application is the proper choice of the type of photocathode and the type of glass for the entrance window. Combination of both should provide the highest possible photoelectron yield for the given fiber. Since the majority of plastic scintillating fibers have emission peak in either violet-to-blue (430 nm to 450 nm) or green (490 nm to 530 nm) wavelength range, one can use PMTs with standard borosilicate glass, as the transmission in the UV range is not needed. When it comes to photocathode selection, the key player is its quantum efficiency, which is defined as [83, 88]:

$$\eta(h\nu) = (1 - R(h\nu)) \frac{\alpha_{PE}(h\nu)}{\alpha_T(h\nu)} \left(\frac{1}{1 + 1/[\alpha_T(h\nu) L]} \right) P_S \quad (2.62)$$

with R being the reflection coefficient, α_{PE} the absorption coefficient for events which

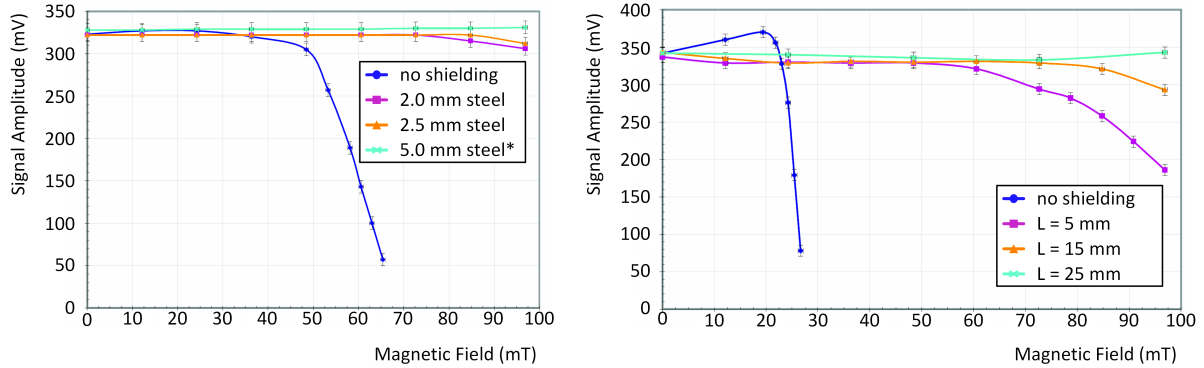


Figure 2.21: Example of effects of magnetic field on performance of the photomultiplier tube (PMT). Measurement results for Hamamatsu Photonics H6568 PMT, which was used for construction of scintillating fiber tracking detectors for the COMPASS experiment. Left: Signal amplitude with field orthogonal to the PMT axis. Various colors show effects of shielding with different thickness of steel walls (asterix denotes a 5 mm total wall thickness composes of 2 mm and 3 mm layers of steel). Right: Signal amplitude with field parallel to PMT axis. Coloured lines show the effects of the distance (L) between the PMT window and the edge of a 5 mm thick steel shield (i.e. by how much the shield sticks out above the PMT window). Results and plots from PhD thesis of Andreas Teufel [87].

excite electrons above the vacuum level, α_T the total absorption coefficient, L the mean escape depth and P_S the probability that electrons that reached photocathode surface will escape into the vacuum. Reflection coefficient R as well as two absorption coefficients (α_{PE} , α_T) depend on the energy of the photon (end hence wavelength), while L and P_S are greatly affected by the crystal quality and electron affinity, respectively [83]. A well known work by Spicer and Bell [89] showed that reducing electron affinity can yield an order of magnitude improvement in quantum efficiency. There may be, however, potential drawbacks related to elevated rate of dark counts.

In typical engineering practice it is quite common approach to either rely on manufacturer's data or to make own measurements, without delving into photocathode theory. Afterwards, the type is selected that best matches the needs of particular application. Taking as an example recent quantum efficiency data provided by the Hamamatsu Photonics company (Fig. 2.22) one can reach conclusions that in case of registering light signals from plastic scintillating fibers, the best candidates are bialkali (K-Cs-Sb – potassium, cesium, antimony) or GaAsP photocathodes. While the GaAsP photocathodes offer better quantum efficiency than the bialkali photocathodes in the wavelength range of interest (peak efficiency of 50% for GaAsP vs. 26% for bialkali), they are also significantly more expensive. A good alternative may be provided by improved variants of bialkali photocathodes – a super-bialkali (SBA) or an ultra-bialkali (UBA) type [90], recently introduced by the Hamamatsu Photonics company. An SBA photocathode can

reach quantum efficiencies as high as approx. 35%, whereas for an UBA one it can go as high as $\approx 42\%$, well over roughly 26% offered by the bialkali type.

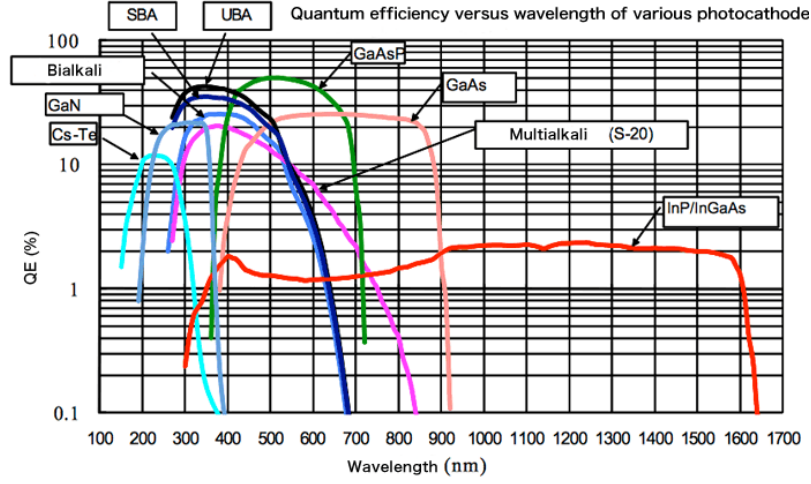


Figure 2.22: Quantum efficiency of various photocathodes as a function of wavelength of incident light. Picture taken from information provided by Hamamatsu Photonics [91].

The third issue to pay attention to is the power supply scheme of the PMT. This becomes apparent once part of the theory related to the operation of the PMT is revisited in more detail. The gain of the PMT is a function of the secondary emission ratio of the dynodes. For a single dynode, it is defined as:

$$\delta = a \cdot E^k \quad (2.63)$$

with δ being the emission ratio, a and k being material constants, typically in the range of 0.7 to 0.8 [83], and E being the interstage voltage between the dynodes (or the voltage between the photocathode and the first dynode). The overall expression for the photo-multiplier gain is then:

$$\mu = \alpha \cdot \delta_1 \cdot \delta_2 \cdot \dots \cdot \delta_n \quad (2.64)$$

where n denotes the number of dynodes and α the collection efficiency - i.e. the probability that the photoelectron emitted from the photocathode will hit the first dynode. If one assumes that all the dynodes are the same and the supply voltage is uniformly distributed across all the stages (i.e. $E = \text{const}$), then substituting Eq. 2.63 into Eq. 2.64 yields:

$$\mu = \alpha \cdot \delta^n = \alpha \cdot (aE^k)^n = \alpha \cdot a^n \left(\frac{V}{n+1} \right)^{kn} = \alpha \cdot \frac{a^n}{(n+1)^{kn}} \cdot V^{kn} = A \cdot V^{kn} \quad (2.65)$$

with V being the supply voltage and A being some constant characteristic for the particular PMT. From here one can clearly see that there is a strong, exponential dependence of the PMT gain on the supply voltage. Hence, it is worth to take a closer look at the PMT power supply schemes.

The most commonly used circuit is a passive bleeder (Fig. 2.23). Its main building block is a resistor divider, which provides gradually increasing voltages in the direction towards the anode. One can use either positive or negative supply voltage. The former option has an advantage of reduced dark rate, thanks to absence of the electric field within the glass of the entrance window of the PMT (the photocathode is at ground potential) and the fact that the dynodes are at a higher potential than the glass envelope, so any electron that misses the consecutive dynode is not attracted to the walls of the PMT. The disadvantage is that it is necessary to use a coupling capacitor to separate the anode from the readout circuit, which results in baseline shifts that depend on pulse amplitudes and their rate (the net current through the capacitor is zero). The latter option, with the photocathode at the negative potential, has a benefit of allowing DC-coupling – thus no baseline shifts occur, which is a huge advantage in high-rate applications. The disadvantage is higher dark rate, especially if the mechanical structure that holds the PMT in place is at ground level. In this case there exists electric field that attracts electrons to the walls. Furthermore, sparking can occur between the glass and the holder. However, this negative effect can be greatly reduced by application of so-called HA coating – i.e. by wrapping the PMT with a metallic foil that is put at the photocathode potential⁸. Therefore, the negative high voltage supply is usually the preferred option – especially considering that with rates on the order of 10^5 or 10^6 hits per second – which is not uncommon with fiber trackers – increasing dark rate from few hundred to even few thousand hits per second is hardly meaningful.

While being very simple and reliable, the passive bleeder circuit has its deficiencies, especially faced with an application that requires high pulse rate or high linearity while maintaining wide dynamic range. To fully understand it one needs to revisit Fig. 2.23. From there it is easy to notice that photocathode and each of the dynodes act as current sources, which correspond to net charge change resulting from photoemission and subsequent electron multiplication. For the photocathode and the first few dynodes this current is negligible. However, for the latter dynodes this may no longer be the case. For very large pulses or very high rate of pulses these currents can become comparable with the quiescent current of the divider. The consequences will manifest themselves as amplitude-dependent or rate-dependent gain fluctuations. This, in turn, can deteriorate timing performance of the whole detector. One of the reasons for this deterioration stems from change in transit time of the electrons flowing through the tube, which is caused by unstable electric fields between the dynodes. The other potential deterioration can be caused by the previously described ‘amplitude walk’ effect – especially if fixed threshold discriminators are used in the readout chain.

⁸Detailed explanation of the idea of HA-coating is provided in [83]

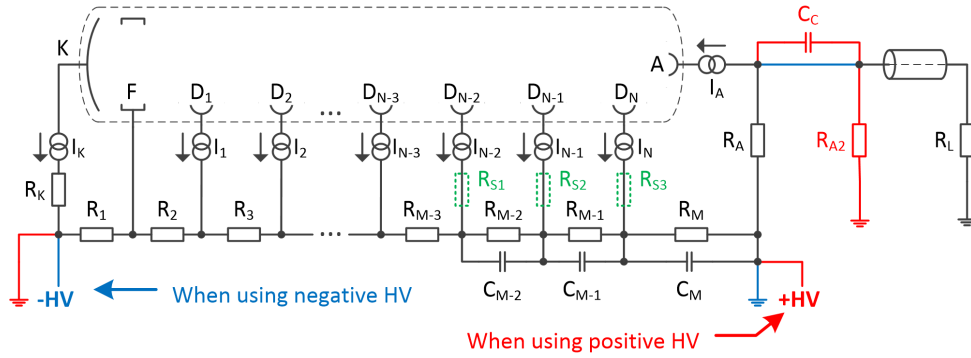


Figure 2.23: Passive bleeder circuit. Blue and red colorer lines mark parts of the schematic valid for negative or positive supply voltage, respectively. K – photocathode; F – focusing electrode; $D_1 \dots D_N$ – dynodes; A – anode; I_K – photocathode current; $I_1 \dots I_N$ – current sources representing net charge change at particular dynodes; I_A – anode current (output signal); R_K – resistor that protects photocathode from excessive current; $R_1 \dots R_M$ – resistors comprising the voltage divider used to polarize the dynodes; R_A – resistor polarizing the anode; C_C – coupling capacitor to separate high potential at the anode from the readout circuits; R_{A2} – resistor that prevents high potential at the output in case load is disconnected; $C_{M-2} \dots C_M$ – buffer capacitors; $R_{S1} \dots R_{S3}$ – optional damping resistors; R_L – load resistance.

To counteract these effects, the buffer capacitors are used, which act as charge reservoirs and minimize inter-dynode voltage changes in case of large pulses. Another way to look at their function is to notice that they provide a low-impedance path to ground for fast AC signals to ground. One should note that in small signal analysis the power supply is replaced by ground, so the above statement is valid for both positive and negative high voltage polarity. Another commonly used trick is to use the so-called ‘tapered divider’, where the latter stages of the multiplier are provided with higher dynode-to-dynode voltages, so that an accidental change of voltage resulting from a large pulse is negligible compared to the nominal voltage. An additional benefit of this solution is the reduction of space-charge⁹ effects within the PMT. When it comes to high pulse rates, one should note that each individual pulse will change the charge accumulated in the buffer capacitors, so they will need time to recharge. The time constants are defined by the capacitances and resistances and are huge compared to the pulse duration – typically used values are in hundreds of nF and hundreds of k Ω to M Ω range, respectively. As such, a period with high rate of pulses with significant amplitude will lead to non-negligible change in supply voltages resulting in gain fluctuation. Moreover, this fluctuation will also have systematic

⁹Electrons that exit a dynode have different kinetic energies. Therefore, some spread in space is expected, which will result in their arriving at the next dynode at different times. Given the fact that they are charged particles, they create an electric field that opposes to the electric field between the two neighboring dynodes. In sufficiently large numbers, the ‘early’ electrons can create strong enough field to significantly affect the energies that will be achieved by ‘late’ electrons (hence the name ‘space charge’). In extreme cases the field can be strong enough to inhibit their arrival at subsequent dynode. The net result is that the PMT gain will decrease with increasing pulse amplitude.

dependency on the time during which the PMT is subjected to high-rate condition. The longer the period, the bigger the gain change will be. Convenient figure of merit here is the average current at the last dynode, which is similar to average anode current (but opposite sign). General rule of thumb is that ensuring quiescent current of the resistor divider that is at least ten times larger than the expected maximum average anode current during the high-rate period should allow to circumvent most of major problems. That, however, comes at a price – increasing quiescent current increases power consumption of the divider, so a more powerful power supply is needed (which usually is more expensive). The other factor that should be considered is the heat that would be generated by the divider – it needs to ‘go somewhere’, which may be troublesome if the electronics is placed in confined spaces. One of simple and effective solutions to this problem is to use a bleeder circuit with a ‘booster’ (Fig. 2.24). The idea is simple – since a large dynode

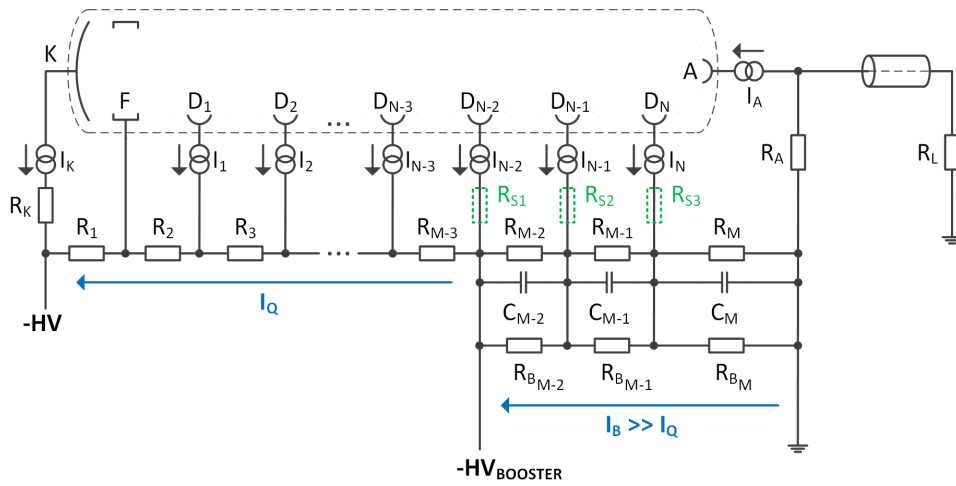


Figure 2.24: Bleeder circuit with a booster. Additional power supply is used to provide second voltage for the latter dynodes. $R_{B_{M-2}} \dots R_{B_M}$ – booster resistors, $R_{B_i} \ll R_i$; I_Q – nominal quiescent current of the divider; I_B – quiescent current in booster part. Remaining labels are the same as for the passive bleeder circuit.

current is only present in last few dynodes, then the large quiescent current of the divider is required only there. As such, small-valued, high power rating resistors are applied only for the latter stages and a second power supply is used to enforce voltage between the parts of the divider with high and low resistances. The disadvantage is the cost of this extra power supply and necessity of additional cabling.

More elegant solution is to use an active voltage divider, where each dynode is supplied via a transistor (Fig. 2.25). This way a low-impedance path is provided for recharging buffer capacitors, with the overall impedance that depends on the resistance of the channels of P-MOS transistors. Assuming resistance of a fully open transistor channel of few tens of Ohms¹⁰, the overall impedance of a fully opened transistor chain would reach only

¹⁰Datasheet value of the resistance of fully open channel of an example high-voltage P-MOS transistor

few hundreds of Ohms – far less than in the case of the standard bleeder or even the booster bleeder circuits. Resulting time constants related with recharging the capacitors would therefore be on the order of hundreds of ns to few μs . To understand how the circuit works it is best to consider a moment when the supply voltage ramps up from zero voltage. Initially, all the transistors are off. With increasing supply voltage the gate voltages will also increase and will be distributed according to the resistive divider composed of $R_1 \dots R_D$, subject to some delay related to charging the capacitors $C_1 \dots C_D$. If one assumes that the starting condition was with all the nodes of the circuit at ground potential, then each transistor starts to become active once its gate-source voltage reaches the threshold voltage, thus lowering resistance of their channels. However, should the resistance the channel of a particular transistor become too low, its source voltage would also decrease (i.e. become more negative), resulting in decreased gate-source voltage and, consequently, increase in channel resistance. This is a mechanism of a negative feedback that ensures that, in idle state, the voltages at the nodes connecting the sources and drains of consecutive transistors closely resemble the voltage distribution at the gates, subject to the difference caused by the threshold voltage. This, in turns means that the voltage at the source of the last transistor in the chain (Q_N) is well defined by the voltage at its gate and hence the quiescent current of the whole circuit is defined by the resistor R_Q . The resistances of the channels of all the transistors would setup itself such that they are compatible with R_Q , thus forming a second resistive divider that is parallel to the one connected to the gates. The diodes shown at the schematic serve only a protective role that prevents exceeding maximum gate-source and source-drain voltages and are not active during normal circuit operation.

Generation of an output signal by the PMT causes some charge to be injected into the buffer capacitors at each node (current sources $I_1 \dots I_N$) – with the most noticeable one at the last stage of the divider. This, in turn, increases the source voltage, also increasing the gate-source voltage and consequently causes wider opening of the transistor channel. Then, the increased voltage is propagated to the subsequent transistor thanks to lowered channel resistance of the preceding transistor. This process goes on down to the first transistor that is directly connected to the filtered supply voltage. Hence, the more current that is injected by the PMT, the lower the resistance of the channels and the faster recharging of the buffer capacitors. This mode of operation is extremely beneficial, as the R_Q can be chosen relatively high, so that the quiescent current of the divider can be on the order of tens of μA , much lower than in case of a standard, purely resistive divider. Thus, savings can be made in terms of power consumption.

While the active divider solution seems to have only advantages, the are nevertheless

type TP2540 from Supertex equals 25Ω .

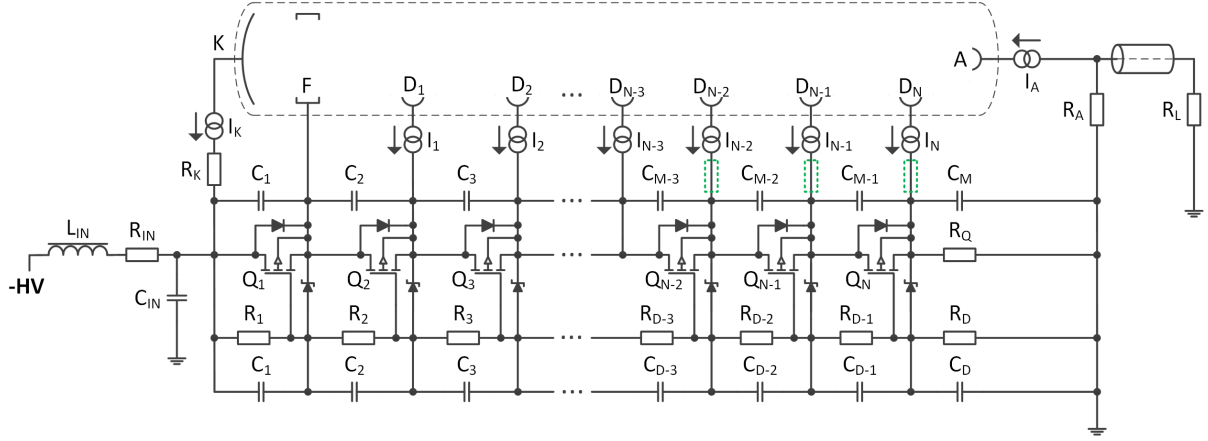


Figure 2.25: Active bleeder circuit. $Q_1 \dots Q_N$ – P-MOS high-voltage transistors; $C_1 \dots C_M$ – buffer capacitors; $R_1 \dots R_D$ – divider that sets gate voltages; $C_1 \dots C_D$ – filtering capacitors for the resistive divider; R_Q – resistor to define quiescent current; R_{IN} , L_{IN} , C_{IN} – elements of the filter for the power supply line. Remaining labels are the same as for the passive bleeder circuit.

some drawbacks involved. One can be the cost – though this is still relatively cheap circuit. The other is related with reliability, as it uses active elements that work with high voltages. That can become an issue if the circuit is to work in high radiation environment, as malfunction of even a single transistor due to radiation damage will result in lack of accelerating voltage between two consecutive dynodes, thus rendering the PMT inoperative.

Yet another option related to providing power to the PMTs involves Cockcroft-Walton voltage multipliers, for example [92, 93]. The nice property of this approach is that the high voltage is generated directly at the base of the PMT, with its pins connected to the taps of the voltage multiplier. However, given the fact that a generator is placed very close to the signal source (PMT), there may be problems related to electromagnetic interference – especially if ability to detect even single photo-electron pulses is required.

The thing to note is that even if the voltage at each of the dynodes is perfectly stable, there will still be fluctuations of the output signal – they are intrinsic features of the photoemission and charge multiplication processes. A convenient way of expressing these fluctuations is the signal to noise ratio - i.e., the ratio of the average charge of the anode pulse to the magnitude of its fluctuation. Assuming that the amplitude of input pulses is a random process with an average number of photons \bar{N}_{ph} and variance of σ_{ph}^2 , the formula expressing the signal-to-noise ratio (SNR) of the anode pulse is [84]

$$SNR_{anode} = \sqrt{\frac{\eta \alpha \bar{N}_{ph}}{1 - \eta \alpha + \frac{\eta \alpha \sigma_{ph}^2}{\bar{N}_{ph}} + \frac{1}{\delta - 1}}} \quad (2.66)$$

where η is the average quantum efficiency, α the collection efficiency, and δ the secondary

emission coefficient¹¹. If the light emission adheres to Poisson statistics (i.e., $\sigma_{ph}^2 = \bar{N}_{ph}$), then Eq. 2.66 simplifies to:

$$SNR_{anode} = \sqrt{\frac{\eta \alpha \bar{N}_{ph}}{\delta - 1}} \quad (2.67)$$

From the above, it is evident that maximizing the number of photoelectrons is of paramount importance - meaning one should aim at the largest possible number of photons and high quantum and collection efficiencies.

Yet another, not so obvious source of gain instability in PMTs may be related to thermal effects or hysteresis effect which is caused by charge buildup at the dynodes [94–98]. Time constants of these effects are on the order of seconds to minutes. The hysteresis effect may become an issue in case of fixed target experiments, where a high intensity beam is delivered in few seconds spills, followed by few seconds of break. An example could be an acquisition system with a fixed threshold discriminator and a time-to-digital converter – due to the ‘amplitude walk’ effect there may be a systematic shift in measured time of PMT pulses that is correlated with the time of the beginning of the spill. According to PMT manufacturer’s claims, this effect has been greatly reduced in modern PMTs by coating the dielectric support of the dynodes with weakly conductive layers. Nevertheless, author’s own measurements [99] indicate that in certain conditions this effect should still be taken into consideration.

Having analyzed issues related to PMT power supply schemes as well as those arising from intrinsic gain fluctuations, the next factor to consider when selecting sensor for given application is its timing performance. In this case, the crucial parameter is the transit time spread (TTS) – in other words minute differences in the the time that the electrons need to travel through the structure of the PMT (i.e. the transit time). The mechanism by which these times are different is simple – looking back at Fig. 2.20 it is easy to notice that the electron paths vary from event to event. It is of paramount importance in case of the travel of primary photoelectrons from the photocathode to the first dynode, which happens due to unequal distance between the two, variations of the electric field or is an effect of disturbance caused by external magnetic field. The net result is that each consecutive anode pulse will be randomly shifted in time with respect to the preceding one (Fig. 2.26). The TTS is the measure of this spread, usually expressed as FWHM (full width at half maximum) of the histogram of transit times for single photoelectron pulses. Typical values of TTS of PMTs used in fiber trackers used for timing applications are below 400 ps (FWHM). Given the averaging effect, the timing accuracy of the PMT will improve with the number of primary photoelectrons (provided they arrive at very short times with respect to the TTS) – a general rule of thumb is that to obtain the timing

¹¹According to the PMT Handbook by Hamamatsu Photonics [83], typical values of average secondary emission ratio are $\delta \approx 6$

accuracy at given photoelectron level one should divide the TTS by the square root of the number of initial photoelectrons.

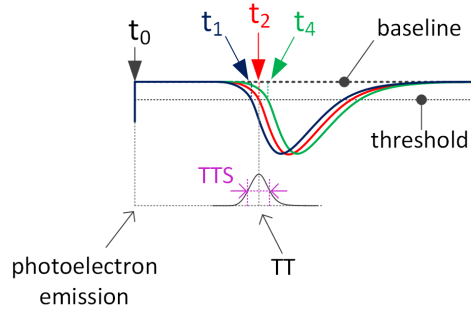


Figure 2.26: The mean transit time (TT) and the transit time spread (TTS) of the photomultiplier tube. Here the TTS is defined at the FWHM of the histogram of the transit times.

Still another topic that deserves some attention is the dark rate. In PMTs its main causes are: thermionic emission from the photocathode, scintillation from the glass envelope or electrode supports, field emission, events from cosmic rays and radiation from radioisotopes contained in the glass or originating from the environment. In normal operating conditions the dominant component comes from the thermionic emission from the photocathode and, to a lesser extent, from radioisotopes contained in the glass envelope. The simplified equation describing the magnitude of the thermionic emission (per unit area) is given by the Richardson equation in the form [100]:

$$N = A(1 - r) T^2 \exp(-\phi/kT) \quad (2.68)$$

where r is a mean reflection coefficient for electrons of thermal energies approaching the emitting surface from either direction, T is absolute temperature (in Kelvin), k is the Boltzmann constant, A is a constant determined by the band structure of the emitters and finally ϕ stands for the work function. The latter can be further divided into temperature-independent component (so called Richardson work-function, denoted below as ϕ_R) and a component that linearly depends on temperature (denoted as bT):

$$\phi = \phi_R + bT \quad (2.69)$$

Typical applications of scintillating fiber trackers involve medium to high pulse rates, usually orders of magnitude higher than the dark rate of the PMTs (well below 100 counts per second at below 0.25 photoelectron level [101]). Therefore, though it should not be completely neglected, this is usually not a decisive factor when selecting the PMT. In rare cases when it is indeed necessary to minimize input from the dark rate counts introduced by the PMT (i.e. for low background applications), then from Eq. 2.68 it is evident that

one way to proceed it is to cool the PMT. One should be aware, though, that this will result in an increase of the resistance of the photocathode. Another effective solution is to minimize photocathode area per detector channel – it should allow for nearly perfect light collection from the fibers, but nothing more than that. Still another method of reducing random counts from PMTs comes from the fact that typical scintillating fiber detector will have more than one detection plane. Thus, requiring a coincidence between all the planes will nearly eliminate the dark counts, as they are uncorrelated – provided that the planes do not share the PMTs.

Far more troublesome issue is related to afterpulsing, as it is correlated with the actual PMT signal. In PMTs it is mainly caused by ion feedback – i.e. residual gases that got ionized by collisions with electrons. Some of these ions hit the photocathode or first dynodes, thus producing relatively large pulse that is slightly delayed with respect to the original pulse. Under high rate condition this may cause accidental coincidences with subsequent pulses from actual scintillation light. Sudden or gradual increase of afterpulsing in a given PMT may suggest problems with the vacuum inside the glass envelope.

Another not entirely obvious problem may be related to placement of the PMTs with respect to the particle beam. Sometimes it is beneficial to place the PMTs close to the beam, as this minimizes length of the fibers, which in turn reduces their attenuation. While tempting, this may turn to be a rather bad decision. There is a non-negligible risk that fraction of the beam hits some obstacle upstream of the detector, which produces showers of secondary particles. These stray particles can then travel through the glass of the PMTs, emitting Cherenkov light. Since particles in a particular shower result from an interaction of a single particle, the Cherenkov light will be coincident among all the PMTs that are on the path of the shower. The intensity of the light will be severe (typically much higher than the scintillation light), resulting in significant load of the PMTs, which may limit their lifetime. An example of such a scenario that was experienced by the author during a project related to one of the detectors at the M2 beamline in CERN is presented in Fig. 2.27

Last but not least issue that is worth mentioning when selecting the PMT is related to space constraints. Since scintillating fiber tracker by definition have multiple channels, the best option is to use compact multi-channel PMTs – for example ones with the metal channel dynode structure (Fig. 2.28), which are available with up to 64 channels per single PMT. This type of dynode structure allows for spatial separation of electron avalanches, which are then collected by separate anodes, in close relationship to the place at the photocathode at which the light was initially registered. Thanks to their small size they also have excellent timing properties, with the TTS not exceeding 400 ps (FWHM). One

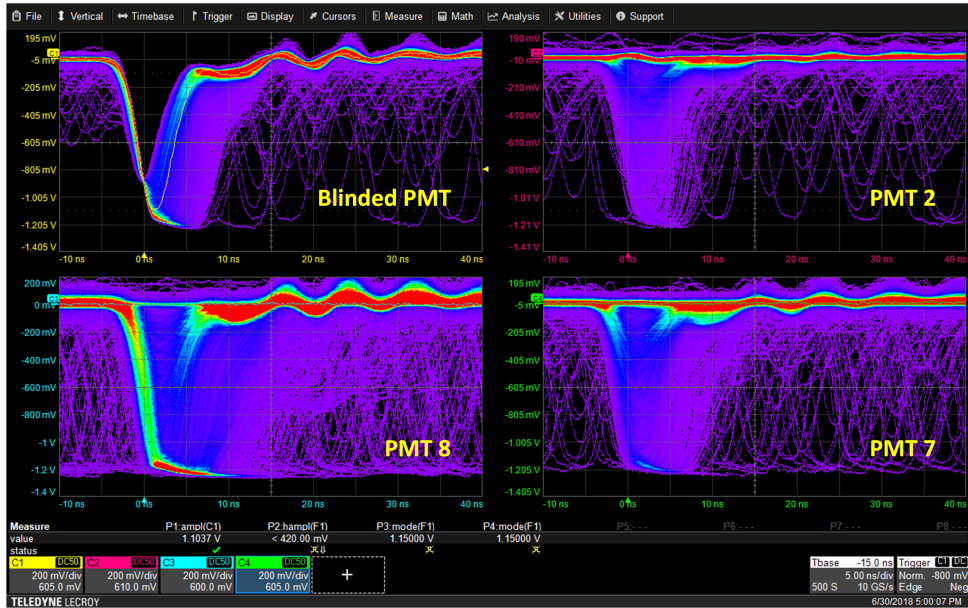


Figure 2.27: Example of coincident signals from particle showers, which originated in a beamline, upstream of a detector (own measurements, M2 beamline at CERN, pion beam). Amplitude of pulses was well above the signal level expected for nominal detector operation and signal was present even in a blinded PMT. The acquisition was triggered on the blinded PMT.

disadvantage may be related to non-negligible variations in the collection efficiency, which will lead to fluctuations in pulse amplitudes. However, with a sufficiently strong signal from the fibers (at least ten photoelectrons) this is a relatively little price to pay compared to the benefits gained thanks to the excellent timing properties and space savings that can be achieved. The other problem connected with multi-channel PMTs may arise from channel-to-channel crosstalk due to light leakage at the optical coupling. As such, care should be taken that sufficient separation is maintained among the fibers belonging to different channels and that they are in firm contact with the glass of the entrance window of the PMT.

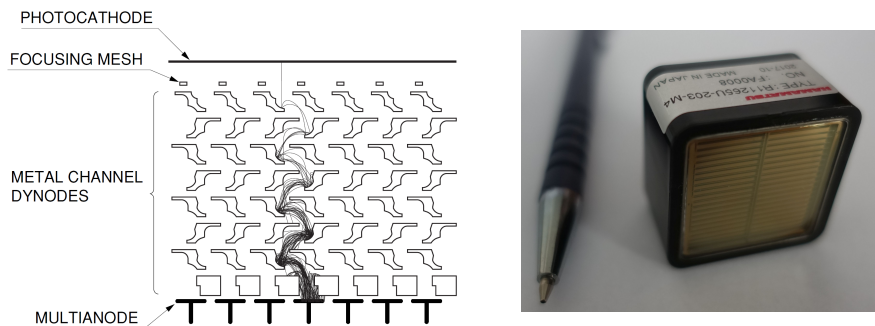


Figure 2.28: (left) Principle of operation of a multi-channel PMT with the metal channel dynode structure [83]. Each electron avalanche is spatially isolated and collected at dedicated anodes. (right) Photograph of an example multi-channel PMT with metal channel dynodes. (type: Hamamatsu R11265U-203-M4).

2.5.2 Multi-Pixel Geiger-Mode Avalanche Photodiodes

Multi-Pixel Geiger-mode Avalanche Photodiodes (Fig. 2.29), also known as ‘silicon photomultipliers’ (SiPMs) or ‘multi-pixel photon counters’ (MPPC), are relatively novel photosensors that consist of an array of avalanche photodiodes (APD) operating in Geiger mode. Compared to traditional photomultiplier tubes, they have several advantages, among which the most prominent ones include: comparable electron gain, excellent timing resolution, high detection efficiency, small size, ruggedness, insensitivity to external magnetic fields, low operating voltage and finally smaller cost. Detailed description of these type of photosensors is beyond the scope of this thesis – an excellent introduction to their technology and applications in physics experiments can be found in [102–104] and references therein. Nevertheless, a short summary will be presented, as their use in scintillating fiber detectors is becoming the mainstream, yet there are few caveats that one should be aware of when planning for a potential application.

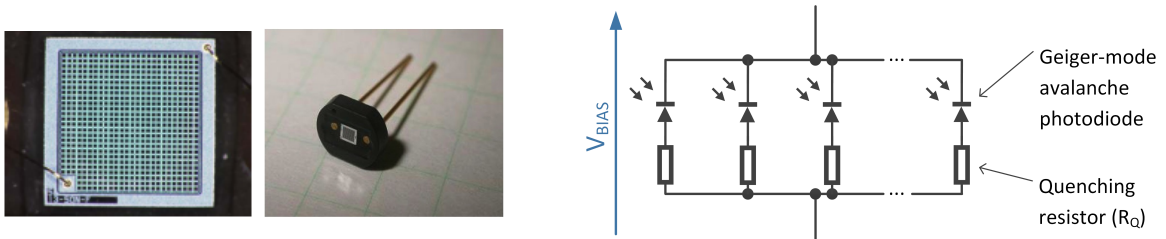


Figure 2.29: (left) Picture of an MPPC sensor used by the near detector (ND280) of the T2K experiment [105]. (right) Conceptual drawing of a multi-pixel Geiger-mode avalanche photodiode sensor.

The principle of the SiPM/MPPC operation is relatively simple and can be easily summarized by referring to an electrical model of a single pixel (Fig. 2.30) [106]. In a

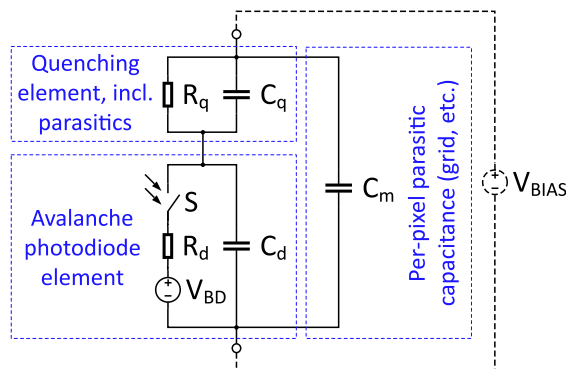


Figure 2.30: Electrical model of a single SiPM/MPPC pixel with passive quenching [106].

steady state, every pixel of the detector is a photodiode that is reverse-biased (V_{BIAS}) above the electrical breakdown voltage (V_{BD}). Therefore, the p-n junction comprising the photodiode is fully depleted and can be modeled by a capacitance (C_d), which is

proportional to the thickness and the area of the junction. The silicon structure is doped in a way that creates two regions:

- a high field region, with electric field strong enough to accelerate carries to energies sufficient to produce additional charge carriers by impact ionization;
- a low field region (also called the ‘drift region’), where charge carriers drift towards either the high field region or the substrate (depending on whether it is an electron or a hole).

Once a charge carrier is generated inside the depleted region and reaches the high field region, it triggers an avalanche. Since the bias voltage is above the breakdown voltage, the electric field in the high field region is high enough so that this process is divergent – i.e. secondary carries gain enough energy to produce more carriers, which again generate more carriers and so on (Geiger-mode operation). The result of this excess number of carriers is an abrupt decrease of junction resistance, resulting in a low-impedance path (R_d) through which the junction capacitance (C_d) gets discharged. The time at which the avalanche builds up is very fast, so its occurrence can be modeled by a switch (S). The avalanche process goes on as long as the voltage across the junction is above the breakdown voltage V_{BD} .

If left unrestricted, the low impedance resulting from the Geiger process would lead to excessive current, effectively destroying the device. To prevent that, a quenching resistor (R_Q) is put in series with the photodiode. Its role is to limit the current from the power supply to below the latching current (approx. $100 \mu\text{A}$, from hereon denoted as I_{TH}). At such low currents, when the voltage across the diode approaches the breakdown voltage V_{BD} , it may happen that, due to the statistical nature of the avalanche process, the number of carriers becomes so low that none of them gains enough energy to cause impact ionization [107]. Once this condition occurs, the avalanche is stopped. Model-wise this is equivalent to opening the switch S , at which point the voltage at the photodiode starts to recover back to the bias voltage (V_{BIAS}). It is therefore straightforward to deduce that the overall voltage drop at the capacitance C_d resulting from the Geiger-mode discharge roughly equals to:

$$\Delta V = V_{BIAS} - V_{BD} \quad (2.70)$$

The model also includes stray capacitance C_q associated with the quenching resistor¹² and parasitic capacitance C_m , representing the per-pixel fraction of the capacitance related to the terminals of the package and the metallic grid at the surface of the sensor. The full model of the sensor can be built by simply replicating the single pixel model, taking into

¹²The description presented here only mentions a passive quenching mechanism. However, other quenching methods are also possible – for details see [107].

account that only a fraction of the pixels will be triggered. Then, the equivalent elements for the triggered pixels, the passive pixels and the parasitics can be calculated according to Eq. 2.71.

$$\begin{aligned}
 R_{d,N_f} &= \frac{R_d}{N_f}, & R_{d,N_p} &= \frac{R_d}{N_p}, & C_{d,N_f} &= N_f C_d, & C_{d,N_p} &= N_p C_d \\
 R_{q,N_f} &= \frac{R_q}{N_f}, & R_{q,N_p} &= \frac{R_q}{N_p}, & C_{q,N_f} &= N_f C_q, & C_{q,N_p} &= N_p C_q \\
 C_{m,N} &= N C_m
 \end{aligned} \tag{2.71}$$

with N_f , N_p denoting number of triggered and passive pixels, respectively and $N = N_f + N_p$ being the total number of pixels within the device. Finally, after accounting for the load resistance (R_L), one gets the electrical model shown in Fig. 2.31 [106]. Methods of measurement-based determination of the values of the parameters of the model are described in [108, 109].

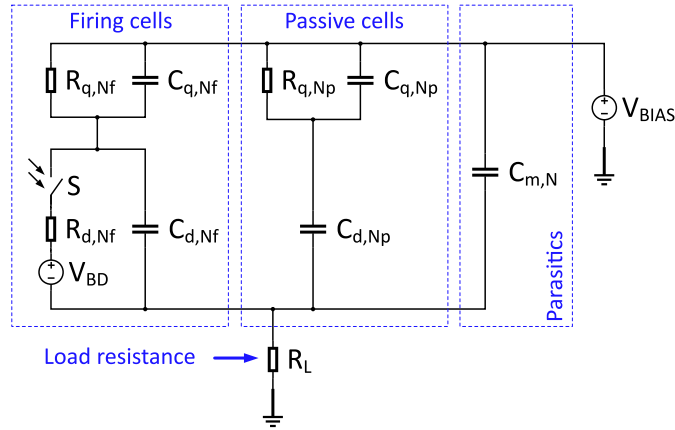


Figure 2.31: Electrical model of the whole SiPM/MPPC, including the resistance of the readout circuit [106].

Since an individual photodiode works in the Geiger-mode, then once fired it will produce the same signal irrespective of the number of the incident photons. While this mode of operation does not allow measuring the intensity of incoming light using a single diode, it does provide a high output charge for events triggered by even a single photoelectron. The electron gains achievable in currently available sensors can easily exceed the level of 10^6 . The proportionality of the response is achieved by segmentation of the photosensitive area, under the assumption that the incoming photons will be distributed among different pixels. Hence, a good approximation of the total charge produced by the whole sensor can be expressed as:

$$Q_{\text{OUT}} \cong N_f C_d \Delta V \tag{2.72}$$

Given good uniformity of the pixels achievable thanks to the advancements in the semiconductor manufacturing technology, the junction capacitance (C_d) is very well defined

and repeatable. As a result, these devices offer excellent charge resolution (Fig. 2.32) – far superior to that of photomultiplier tubes. Nevertheless, one should note that if the amount of photons in the incoming signal becomes too high with respect to the number of pixels comprising the device, then saturation effects are to be expected. If amplitude

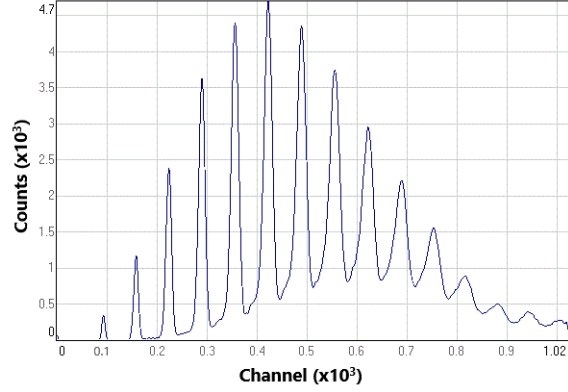


Figure 2.32: Example charge histogram from an MPPC illuminated with a multi-photon pulse (own measurements). Left-most peak corresponds to the pedestal, other peaks correspond to events triggered by one (2nd peak) or more photoelectrons.

or charge information is needed and the signals have a high dynamic range, then it will be necessary to pick the sensor with high pixel density – usually resulting in small pixel size and small associated junction capacitance. Consequently, the gain will also be lower, which will deteriorate signal to noise ratio, limiting the ability to set thresholds below a single photoelectron level. Fortunately, in most of the cases involving fiber trackers, only the timing information is needed and linearity of the response is not a crucial requirement. As such, it would seem that a safe bet would be to pick a sensor with large pixels (i.e. largest possible junction capacitance C_d), working at the highest possible overvoltage ΔV . This way the electron gain would be maximized, thus improving the signal to noise ratio. While generally true, the picture is slightly more complex.

Similarly to PMTs, one of the most important aspects which should be considered at the very beginning of the selection of the sensor is its photon detection efficiency (PDE). Not surprisingly, it should be maximized for the emission spectrum of the particular fiber. For multi-pixel Geiger-mode APDs, the PDE is defined as [103]:

$$PDE(\Delta V; \lambda) = \eta(\lambda) P_T(\Delta V, \lambda) FF \quad (2.73)$$

where $\eta(\lambda)$ is the quantum efficiency, $P_T(\Delta V, \lambda)$ is the Geiger discharge probability and FF denotes the fill factor. The quantum efficiency depends on two factors: the probability that the photon will pass through the transparent coating of the silicon structure and that it will produce a charge carrier that will reach the high field region. Maximizing the transmission through the coating requires proper choice of the material (in terms of

transparency and the refractive index – see section 2.4). Probability of producing a charge carrier depends on absorption depth of photons¹³, collection efficiency of the generated charge carriers and carrier lifetime. Since most common scintillating fibers have a peak in the emission spectrum between 400 nm and 500 nm, one should pick sensors optimized for the blue light – i.e. with the junction depth of a few microns, so that nearly all photons are absorbed. Furthermore, since under these conditions a significant fraction of carriers will be generated in the drift region, sensors made of high quality silicon should be used (i.e. least possible amount of metal impurities, lattice defects and sometimes lithography defects [103]). Fulfilling the above guidelines minimizes amount of traps with energy levels near the middle of the bandgap, thus decreasing the recombination rate in the drift region¹⁴ and thereby maximizing the chance that the photo-generated carriers reach the high-field region, where they can trigger an avalanche.

The probability of triggering the Geiger discharge (P_T) is related to the ionization rate of electrons and holes, the former being about twice as high as the latter. Both increase with the electric field, so it is favourable to use sensors working with higher overvoltage (ΔV). Furthermore, one should note that the triggering probability depends on the location of carrier generation along the junction, as the carrier needs to reach the high field region. Therefore, for certain applications some consideration is recommended whether to use sensors involving structure with a buried n+/p junction or a shallow p+/n junction. Fortunately, for blue light both structures are more or less equivalent [103].

The fill factor (FF) is linked to presence of inactive regions at the detector surface. The role of these structures is to quickly decrease electric field at the borders of individual pixel and to provide electrical and optical isolation of the pixels. Some additional decrease of the active area can come from metallic grid at the surface of the detector (though it usually overlap isolation structure) and a polysilicon resistor used for quenching the avalanche. Typically, the higher the pixel density of the device, the smaller the fill factor – so, for typical applications in scintillating fibers the preferred sensors would be those having larger pixels.

Another factor that needs attention when it comes to the choice of SiPM for a particular application is related to the recovery time - i.e. how fast individual pixels return to the nominal overvoltage ΔV . This is especially important for high rate applications, as it is this parameter that determines the maximum pulse rate at which the sensor can operate. To explore the topic in more detail, it is worth to take another look at the SiPM model [106]. Examining the plots shown in Fig. 2.33 reveals that the output waveform, corresponding to the current flowing through the load resistance R_L , has three distinct phases:

¹³Optical properties of silicon, including absorption coefficients can be found in [110].

¹⁴Fulfilling these guidelines will also result in reduction of the dark rate.

- the rise phase, which is connected to the time needed by the avalanche within the particular diode to be transferred to the load resistance;
- the quenching phase, occurring between the peak diode current (flowing through the R_d) and the moment at which the diode current drops to zero;
- the recharging phase, when equivalent diode capacitances (C_d) are recharged via the quenching resistor (R_q).

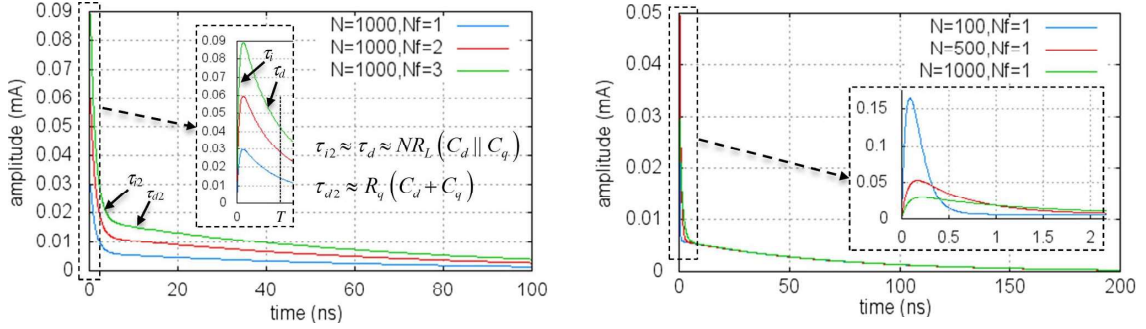


Figure 2.33: Analytical waveforms of SiPM output current, calculated under the following assumptions: $R_L = 50 \Omega$, $\Delta V = 2 \text{ V}$, $I_{TH} = 100 \mu\text{A}$, $R_d = 300 \Omega$, $R_q = 300 \text{ k}\Omega$, $C_d = 200 \text{ fF}$, $C_q = 20 \text{ fF}$, $C_m = 5 \text{ fF}$. *Left:* Plots for a 1000-pixel device with increasing number of fired pixels ($N = 1000$, $N_f \in [1, 2, 3]$). *Right:* plots of a single photoelectron waveforms for devices with varying number of pixels ($N \in [100, 500, 1000]$, $N_f = 1$). *Source:* Redrawn from [106].

Sections of the presented waveforms are characterized by four time constants: τ_i and τ_d , respectively account for the rising and quenching of the avalanche, while τ_{i2} and τ_{d2} are related to the recovery process. Assuming that the avalanche buildup is much faster than the quenching, the quenching resistance significantly larger than both the load resistance and the photodiode resistance ($R_q \gg N_f R_L$, $R_q \gg R_d$), relatively small number of fired pixel ($N \gg N_f$) and finally neglecting the parasitic capacitance C_m , these time constants are defined as follows [106]:

$$\tau_i \approx \frac{NR_d R_L C_d C_q}{R_d(C_d + C_q) + NR_L(C_d \parallel C_q)} \quad (2.74)$$

$$\tau_d \approx R_d(C_d + C_q) + NR_L(C_d \parallel C_q) \quad (2.75)$$

$$\tau_{i2} \approx \frac{NR_q R_L C_d C_q}{R_q(C_d + C_q) + NR_L(C_d \parallel C_q)} \quad (2.76)$$

$$\tau_{d2} \approx R_q(C_d + C_q) + NR_L(C_d \parallel C_q) \quad (2.77)$$

The sought recovery time is very well approximated by τ_{d2} , which is the largest of the time constants and in fact dominates the overall duration of the response.

Still another very useful figures of merit are connected to estimation of pulse bandwidth and the overall SNR. The bandwidth of the signal is determined by the leading edge of the response and can easily be calculated using its peaking time (T_{peak}). Later on, in case one prefers to preserve shape of the SiPM signal, the same bandwidth should be used in estimating the amount of noise inherent to the front-end circuit. The overall SNR can then be obtained by comparing the noise level to the peak value of the output current. Using similar assumptions as was the case of equations 2.74 through 2.77 (i.e. $R_q \gg N_f R_L$, $R_q \gg R_d$, $N \gg N_f$, negligible C_m), the formulas for the peaking time and the peak current are given below [106]:

$$I_{peak} \approx \frac{N_f \Delta V C_q}{R_d(C_d + C_q) + N R_L(C_d \parallel C_q)} \quad (2.78)$$

$$T_{peak} \approx \frac{N R_d R_L C_d C_q}{R_d(C_d + C_q) + N R_L(C_d \parallel C_q)} \log \left(\frac{1}{N R_d R_L C_d C_q} \right) \quad (2.79)$$

One of the great advantages of SiPMs is excellent timing resolution, superior to that offered by the photomultiplier tubes. For these devices it is usually expressed as the Single Photon Timing Resolution (SPTR). In modern devices, the distribution of the pulse arrival times typically resembles a Gaussian with an exponential tail, with FWHM somewhere in the range of 20 ps to 40 ps for a single pixel and below 200 ps for the whole device ($3 \times 3 \text{ mm}^2$ device) [111], with the latter mainly affected by the output capacitance of the sensor and noise contributions from the front-end electronics. The main components affecting the SPTR are [103]:

- timing jitter of the avalanche buildup process;
- non-uniformity of the electric field either within a single photodiode or among the photodiodes comprising the device;
- time spread in the collection time of the photo-generated charge carriers from the absorption point to the high-field region;
- different signal shapes and signal arrival times depending on pixel location within the device;
- noise introduced from the front-end electronics.

In fact, it is the last of the above components that has the most profound effect, once the output capacitance of the sensor is taken into account. On one hand, big capacitance increases noise gain of the front-end amplifier, on the other it also degrades the leading

edge of the signal. Taking the above into account, an approximate analytical expression for the expected SPTR in case of using a leading-edge discriminator is: [103]:

$$\sigma_{time} \cong \frac{\sigma_{base}}{\left. \frac{dx}{dt} \right|_{thr}} \quad (\text{s}) \quad (2.80)$$

with σ_{time} being the standard deviation of the timing jitter, σ_{base} the standard deviation of the baseline noise and $\left. dx/dt \right|_{thr}$ the slope of the leading edge at the threshold crossing level.

One of the few areas where the SiPMs are inferior compared to the photomultiplier tubes is related to the dark rate – though, as indicated at the beginning of this section, this is not a crucial parameter due to requirement of a coincidence among multiple fiber channels. In SiPMs, it is quite common to experience rates at the level of up to tens of kcps/mm²(thousands of counts per second per mm²) – far more than below hundreds of cps for the whole multichannel PMT. The origin of the dark rate has two primary categories: the ‘primary noise’ and the ‘correlated noise’. The former is caused by the generation of carriers in the silicon, either by thermionic emission or tunneling. The latter is related to a previous avalanche that happened within the device. One way is by emitting a photon from the avalanche, which is then absorbed in a nearby pixel and triggers additional discharge (cross-talk). Another possibility involves charge trapping of some of the carriers created during the avalanche and then releasing them at a later time (afterpulsing). In both cases, the carrier must reach the high field region and trigger an avalanche.

Consequently, apart from depending on temperature, the overall dark noise is correlated with the applied overvoltage (ΔV), as it directly affects the probability of triggering the Geiger discharge. Furthermore, as indicated in [103], the thermionic generation in the drift region is well described by the Shockley-Read-Hall model. However, in the high field region, there is an increase of tunneling of electrons, caused by the high electric field. In fact, at room temperature, it is this effect that is the dominant contributor.

Reduction of the cross-talk and the afterpulsing has been one of the ‘hot topics’ of the research related to improving the SiPM. The recent generation of devices features significantly reduced afterpulsing and cross-talk rates, thanks to improvements in the manufacturing technologies and introduction of trenches that provide optical isolation of the pixels [102].

Final remarks that are of importance for a scintillating fiber (SciFi) detector concern radiation hardness. Given mainstream use of these type of sensor for various applications, this topic has been studied in great detail [79, 80]. The main issues observed as an effect of irradiation, even with relatively low fluences of $\Phi_{eq} \approx 10^{10} \text{ cm}^{-2}$ manifest themselves as increased dark count rate and loss of single photoelectron resolution. Furthermore, the increased dark count rate may increase pixel occupancy, causing some of them to be

unable to recover, leading to decreased photon detection efficiency of the whole device. Another mechanism that may be involved is related to local heating of particular pixels, leading to local increases of the breakdown voltage (V_{BD}) and hence lower gain. As indicated in [112], single photoelectron performance can be recovered after annealing at room temperature for devices irradiated up to approx. $\Phi_{eq} \approx 10^{10} \text{ cm}^{-2}$. Alternatively, higher temperature annealing can also be applied, in which cases single photoelectron resolution can be recovered for devices irradiated with fluences up to $\Phi_{eq} \approx 10^{12} \text{ cm}^{-2}$ [113]. However, the general remark is that SiPMs are not as rad-hard as PMTs. Nevertheless, their small size is beneficial – for example, they are not sensitive to large unwanted pulses coming from particles passing through the glass of the PMT bulb (see Fig. 2.27).

2.6 Readout

The readout system is yet another essential part of the scintillating fiber detector that should be selected with utmost care. Its primary role is to acquire signals from the detector and record them in a persistent form, suitable for analysis. Nowadays, this means storing the information in digital form, which implies the use of a digitizer. Since typical applications of this type of detectors involve particle tracking, one is mostly interested in precise estimation of the position and the timing of the hit, though some applications may also prefer to save pulse amplitudes or even full waveforms corresponding to the hits. In this context, the hit is a particle interaction with the fiber, which produces a signal that is detected by the photosensor, which in turn outputs an electrical pulse of adequate amplitude. Furthermore, given the excellent timing properties of the scintillating fibers and the photosensors (either PMTs or SiPMs), these detectors are commonly used as part of a trigger system, in addition to tracking applications.

In terms of actual implementations of the readout systems, one can think of two main categories, each having their pros and cons:

- A system comprising a discriminator followed by a time-to-digital converter (TDC), which provides only timing information.
- A sampling system that digitizes the full waveform from the photosensor and uses digital signal processing to extract timing and (if needed) amplitude information.

In both of the above systems the hit position can be determined in two ways: from the channel number or, in case of double-sided fiber readout, also from the difference of pulse arrival times between the two fibers ends.

Before delving into a detailed discussion of the properties of the readout options as mentioned above, it is worth to summarize a few aspects that are worth considering when

choosing a system for a particular application. The actual implementation will always be a trade-off among them, the most prominent of which include:

- **Compatibility with the photosensor.** The properties of input circuitry should reflect the output capabilities of the used photosensor, allowing reliable signal reception. In other words, the system should ensure a sufficient signal-to-noise ratio (SNR), appropriate dynamic range, protection against excessive voltage and finally proper impedance matching in case the photosensors or front-end and the readout system are far away, connected by a transmission line. In practice, if the PMTs are used as photosensors, then the signal is large enough and does not require any additional amplification. It is therefore sufficient to couple them directly to the transmission line and use a simple resistive termination at the receiving end. Sometimes, if there is a non-negligible risk of excessive voltage spikes, then it may be advisable to use additional protection circuitry to improve overall reliability. In the case of using SiPMs, a proper front-end circuit may be necessary close to the sensor to ensure decent SNR and adequate line driving capability. A good overview of available SiPM front-ends is available in [114].
- **Timing resolution.** This is one of the most vital parameters of the readout system, especially if one considers timing-critical applications for which the SciFi detectors are well suited, such as trigger systems or time-of-flight measurements. Typically, it is desirable to maintain the performance of the detector driven by the limitations originating from the scintillator or the photosensor. Consequently, the timing resolution of the readout should not exceed a couple of percent of that of the upstream elements, so that the overall error contributions from the electronics are negligible. The two main factors affecting the timing resolution are the amount of noise and the slope of the leading edge of the input signal (Eq. 2.80). A complementary formula, which takes into account improvements possible due to various signal processing methods, can be expressed as:

$$\sigma_{time} \approx f \left(\frac{t_{rise}}{SNR} \right) \quad (\text{s}) \quad (2.81)$$

where t_{rise} is the 10%-90% rise time of the input pulse, SNR is signal-to-noise ratio, and f is some function. Hence, achieving the best possible timing resolution requires low noise (maximizes SNR) and high bandwidth system (preserves sharp edges), which are conflicting requirements. Of the two, it is the preservation of the edges of the signal that should be prioritized. When choosing bandwidth of the system, it is a good idea to match that of the output signal of the photosensor. Furthermore, one should always pick a solution that fits the application. So, sometimes

it may be beneficial to deliberately decrease the bandwidth of the system, which will provide savings in power consumption and cost at the expense of deteriorated timing resolution.

- **Hit rate capability.** The ultimate limit of the maximum rate of incoming particles comes from the shape of the analog signal. The shape of the signal is affected by the scintillator decay time and the response of the photosensors. The latter is especially valid for a detector using SiPMs, as their recovery time may be the dominant factor. The bottom line is that pile-up occurs once two consecutive pulses are too short apart. In the case of a discriminator-based system, this means that a rough approximation of the upper bound of acceptable average count rate will be the reciprocal of the time over the threshold, though dead time losses are inevitable given the statistical fluctuation of the pulse rate. For the sampling system, it will be approximately the reciprocal of pulse FWHM. Therefore, for the same analog input, the sampling system is more capable – provided that additional signal processing is applied to disentangle pile-up.
- **Signal shaping.** The need for signal shaping depends on the application. In sampling systems, especially those operating at frequencies that cannot accommodate the full bandwidth of the signal from the photosensors, it will occur in the anti-aliasing low-pass filter. When using SiPMs, shaping may provide a way to cut the tail of the signals resulting from the recovery time, via the pole-zero cancellation technique. In the case of using the PMTs with an adequately fast readout system, it is preferred to avoid using shapers - the time of the PMT response is short and, as already mentioned, it is preferred to preserve the slope of the leading edge. Nonetheless, if one decides to use a shaper, then it is worth consulting [115, 116] in order to choose an optimum one. One thing to note is that it is the ratio of pulse rise time to SNR that should be optimized, rather than just the SNR.
- **Input coupling.** The choice of DC vs. AC coupling (i.e., direct vs. capacitive or inductive coupling) is yet another factor deserving quite some thought. The advantage of AC coupling is that it is an easy solution to deal with offsets introduced by preceding stages of the signal chain (for example amplifiers) - either constant or slowly drifting. This way, the design is simplified, especially if connecting multiple amplifiers in series. However, the AC coupling also introduces rate-dependent baseline fluctuation, since it blocks the DC component, thus requiring the average to be zero. While one can use baseline restorers or bipolar shaping to solve this problem, in a typical SciFi detector case, it is easier to use a DC-coupled system. The signals

from the photosensors are usually large enough that little amplification is needed, and having a stable baseline is a considerable benefit.

- **Output data rate.** In a discriminator-based system, the expected data rate is a relatively straightforward estimation – it is the width of the TDC codeword multiplied by the average hit rate. For a sampling system, one can distinguish the ‘raw rate’ driven by speed and resolution of the analog-to-digital converter (ADC) – which tends to be on the high side – and the ‘processed rate’, after feature extraction (i.e., estimation of time of pulse arrival and optionally its amplitude). The actual rate can be a combination of the two, in case of recording segments of waveforms containing the signal. From the design point of view, one should ensure sufficient capacity of the downstream data acquisition system (DAQ) as well as adequate throughput of the link connecting it with the digitizer.
- **ASICs vs commercial components.** A much-debated question without an easy answer, as each approach has advantages and disadvantages. Using commercial components is beneficial from the maintenance point of view, as even if a particular part is phased-out, there will usually be a pin-to-pin compatible replacement. Furthermore, it is easier to make a custom-based solution for a particular application, as one controls almost all aspects of the design. On the other hand, ASICs (application-specific integrated circuits) have a benefit of significantly larger integration scale, as they contain multiple channels, each implementing several stages of the acquisition chain. Hence, they allow smaller circuits and are the preferred option for applications where space is limited. The ASIC-approach will also offer a lower overall power consumption, simplifying the cooling systems. An example of designs made using commercial components can be found in [117–119] as well as this thesis, while [120–125] describe few of the plethora of available integrated circuits dedicated to photosensor readout.
- **Power consumption.** The general conclusion is that this factor should be considered in the design, as it has the potential of a non-negligible effect on the costs. A higher power system will require a more capable and more expensive cooling system, which may pose a challenge in large-scale applications where space is at a premium. It will also require stronger power supplies.
- **Immunity to electromagnetic interference (EMI).** This is an aspect that should be considered early in the design. Among other things, it involves the proper design of the grounding and the shielding. An excellent introduction to the topic is presented in [126]. Typically, one wants floating power supplies and the signal ground of the detector connected via a low-impedance path to the ground of the

acquisition system. Furthermore, it is essential to avoid ground loops, which is a non-trivial task given the fact that structural elements of the detector must also be grounded to the ‘dirty’ safety ground, which may capacitively couple to the ‘clean’ signal ground. Therefore, it is a good idea to eliminate the ground from the signal path, which is why it is recommended to use differential transmission and also properly shield sensitive parts of the circuit and, where necessary, the cables. However, there is one caveat. If the asymmetric-to-differential transformation is done using symmetrizing transformers, then the coupling becomes AC, so one should employ proper techniques to deal with rate-dependent baseline fluctuations.

- **Radiation hardness.** Another application-specific issue that deserves consideration if there is a risk of non-negligible radiation exposure. The exact description of mechanisms of radiation damage to electronics circuits is beyond the scope of this thesis, but a good overview of the subject can be found in [127]. One way of reducing the risk of a malfunction or a glitch, especially in the case of digital electronics, is to move it further away from the radiation source (for example, beam or experimental target). Another option is to provide extra shielding. Still another is to use rad-hard technologies – usually implying that one should try to avoid CMOS-based technologies for analog circuitry and employ various redundant and self-correcting solutions in case of digital electronics.
- **Reliability and serviceability.** Though it does not affect the performance of the detector in terms of data quality, it can make life miserable and ruin overall efficiency by making the system inoperable. The thing to note is the acceptable failure rate within the expected lifetime of the experiment. Typically, high energy physics experiments run for several years and use systems with a magnitude of channels. As such, the question is not whether a failure will occur but rather when will it happen and what action should be taken to correct it. The answer depends on several factors. It is anyhow a good idea to improve reliability early in the circuit design stage, for example by employing FMECA/FMEDA methodologies¹⁵ – especially for mission-critical systems or for implementations with severely limited access. An example of the latter could be a high-luminosity collider experiment with densely packed detectors, requiring cooldown time to enter the hall and dismounting of multiple systems in order to access electronics. The usual way of dealing with

¹⁵FMECA and FMEDA are extensions of FEMA (Failure Mode and Effects Analysis) – a bottom-up, inductive analytical method which may be performed at either the functional or piece-part level, aiming at reviewing as many components, assemblies, and subsystems as possible to identify failures, and their causes and effects. FMECA extends FMEA by including a ‘criticality analysis’, which is used to chart the probability of failure modes against the severity of their consequences. FMEDA extends FEMA with calculation of failure rates. *Source: Wikipedia (links: FEMA, FMECA, FMEDA)*

these types of problems involves making the whole experimental setup redundant so that loss of a segment of a single detector does not affect physics data quality. Nonetheless, one should make a modular system, ensure an adequate supply of spare parts, think about the possibility of replenishing the pool of spares with a time horizon of several years ahead and also try to make a design that facilitates the replacement of broken modules (if possible).

- **Cost.** Not much to comment here – the chosen solution should fit within the budget. As simple as that.

2.6.1 Discriminator with a Time-to-Digital Converter

A system comprising of a discriminator followed by a time-to-digital converter (Fig. 2.34) is one of the simplest methods of digitizing information from a scintillating fiber tracker. As already mentioned, it provides only the position and timing of the hit, while ignoring the amplitude – however, in the majority of applications, such an approach is sufficient. The principle of operation is relatively straightforward. First, the discriminators compare the photosensor (or front-end) signal with a pre-determined threshold, thereby separating useful signals from noise. If the signal in a particular channel is above the threshold, then they produce a digital pulse, which is then fed into a time-to-digital converter (TDC). The TDC is a high-speed counter with separate ‘start’ and ‘stop’ inputs, optimized for accurate time measurements – i.e., small (picosecond range) and highly uniform steps. Most of the time, the TDCs start counting after receiving a global trigger and stop after receiving a signal from discriminators or due to a global reset. The data is saved only in case there was a discriminator signal.

Moreover, given the excellent timing properties of both the scintillating fibers and the photosensors, it is a common practice to use these detectors as part of a trigger for other systems or even the whole experiment. Therefore, the readout system may also incorporate a coincidence unit made using fast logic elements. Its task is to detect coincidence among the detector planes and output a signal only in case all of them register at least a single hit within a pre-defined time window. In some solutions, this coincidence unit can also allow the selection of particular channels, thus effectively masking parts of the detector from the trigger.

The most straightforward application of this type of system utilizes a fixed threshold discriminator. Hence it is advisable to take a more in-depth look at factors affecting its timing performance. The left plot in Fig. 2.35 illustrates the mechanism of timing jitter originating from noise (i.e., baseline fluctuations) superimposed on an input signal, causing pre-mature or delayed threshold crossings. Any fluctuation in the threshold level will have similar consequences so that one can account for them in the overall level of

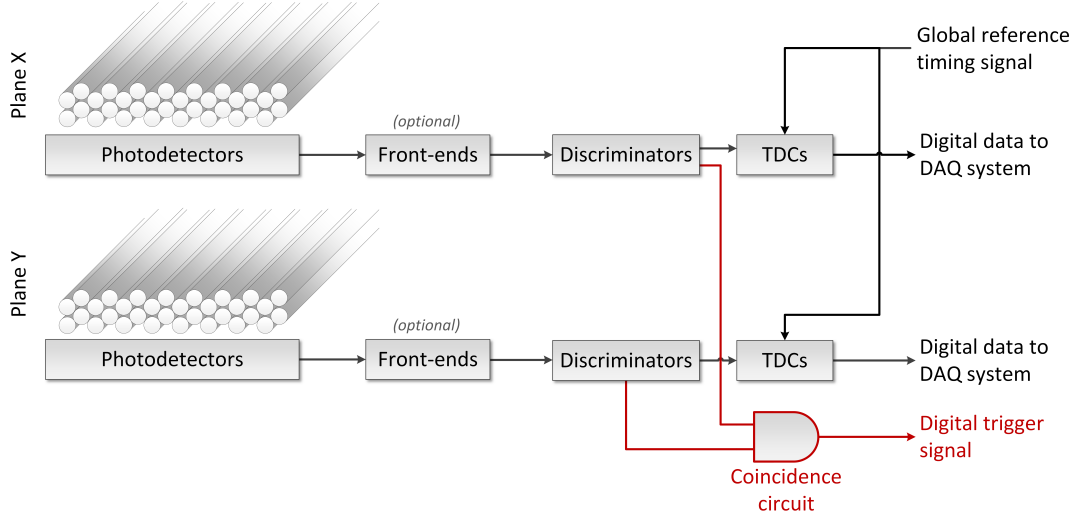


Figure 2.34: Schematic drawing of an example discriminator-based readout system of a two-plane detector, with a coincidence output. The ‘TDC’ (Time-to-Digital Converter) measures time offset between the global reference timing signal and the discriminator output. Front-end circuits are sometimes used to ensure sufficient signal-to-noise ratio at the input of the discriminator, or to provide impedance matching to the transmission line as well as adequate line driving capability.

the signal noise. Even though Eq. 2.80 already provided an analytical expression for this type of error, let us redefine it for the sake of clarity, slightly changing notation:

$$\sigma_{thr} = \frac{\sigma_{noise}}{\left. \frac{dx}{dt} \right|_{thr}} \quad (s) \quad (2.82)$$

A direct conclusion from the above equation is that if the range of pulse amplitudes is relatively narrow, then it is possible to optimize the threshold setting to improve overall timing accuracy. Various analyses of typical pulses show that an optimum lies somewhere in the region of the maximum slope of the leading edge. For typically observed pulses shapes this is somewhere between 10% to 40% of the average pulse amplitude [128] (Fig. 2.36).

An additional source of timing inaccuracies comes from unequal time-steps of the TDC – in other words from its differential and integral nonlinearities. From hereon, let us denote the magnitude of these errors as σ_{TDC} . If the TDC time step is small compared to the time of the rise time of the pulse, then for typical scenarios with moderate SNR the errors resulting from differential nonlinearity of the TDC will be small compared to errors originating from the noise present in the signal. Unfortunately, the integral nonlinearity of the TDCs, especially in the FPGA-based solutions¹⁶, is more significant and cannot be neglected. Therefore, various methods are used to overcome this limitation by smart

¹⁶FPGA stands for a Field-Programmable Gate Array. Given recent advances in programmable circuits technologies, FPGA-based TDC implementation are becoming very common. For an example, see [129].

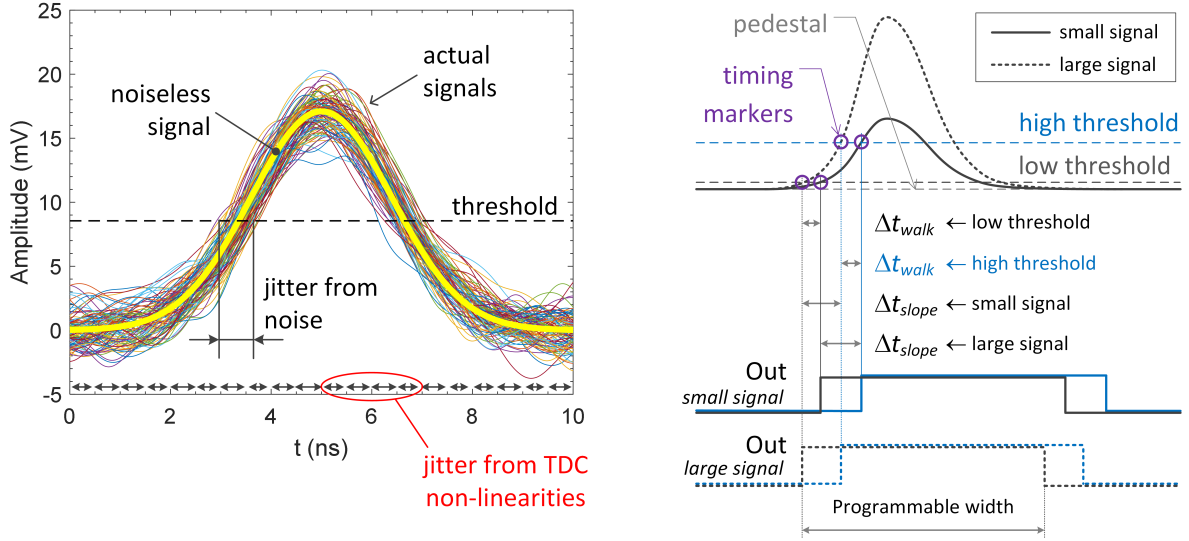


Figure 2.35: Principle of operation of a fixed threshold discriminator. *Left*: Sources of timing errors from noise and non-linearities of the TDC (unequal bin sizes). *Right*: Error contributions from variations of amplitude signals. Solid and dashed lines, respectively, denote waveforms corresponding to a signal with small and large amplitude. Purple circles mark timing markers (i.e., points at which the discriminator fires and where the timing is measured). Δt_{walk} denotes timing jitter resulting from the fixed threshold and varying pulse amplitudes (so-called amplitude walk). Blue color marks lines and text related to an optional second discriminator with a higher threshold, which allows the possibility of correcting the amplitude walk based on slope measurements (Δt_{slope}).

calibration and use of look-up tables, for example, the one used the Wave Union TDC [129].

Another factor contributing to substantial timing errors comes from the so-called ‘amplitude walk’ effect, denoted as Δt_{walk} in the right plot of Fig. 2.35. If there is a significant variation in pulse amplitudes, then, by definition, it will lead to differences in threshold crossing times – in fact, it can even be the dominant source of timing errors. Note that there will always be some uncertainty in pulse amplitudes, as it is inherent to the physics related to the operation of the detector. One source, mainly relevant for single photoelectron level pulses, is related to fluctuations of photosensor gain (more in case of PMTs, less in case of SiPMs). However, the primary one is a result of fluctuations in the number of photons produced in the scintillation process.

In order to qualitatively estimate how big the walk-related error is, one can apply the following reasoning. For the moment let us assume that the shape of the analog pulse can be modeled by the Gaussian function. The analytical formula of the signal is then

$$x(t) = A e^{-\frac{(t-b)^2}{2\sigma^2}} \quad (\text{V}) \quad (2.83)$$

where A stands for amplitude (random variable, in Volts), b stands for the time of arrival

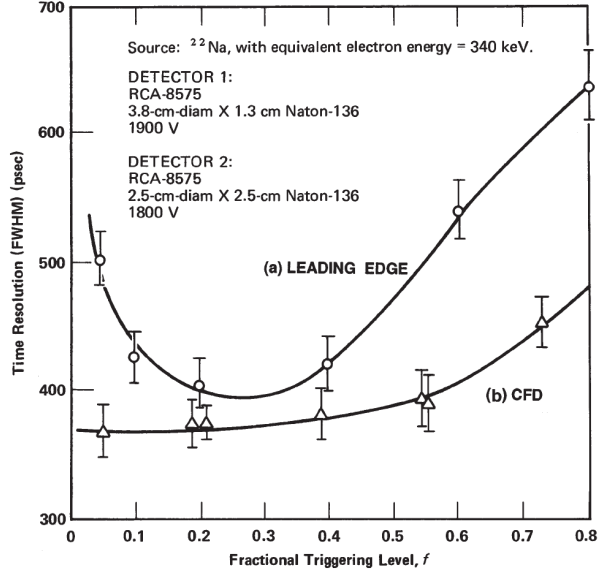


Figure 2.36: Timing resolution of a fixed-threshold leading-edge discriminator and a constant fraction discriminator as a function of fractional triggering level, for a case with a narrow range of pulse amplitudes. *Source: Redrawn from [128].*

and c is related to the width of the pulse (both constant, in seconds)¹⁷. Now, denoting threshold level as v_{thr} , the threshold crossing time is expressed as:

$$T_{thr} = b - c \sqrt{2 \ln \frac{A}{v_{thr}}} \quad (\text{s}) \quad (2.84)$$

with T_{thr} also being a random variable. Now, using \bar{A} and σ_A to denote the average pulse amplitude and the magnitude of its fluctuation, respectively, the walk-related error contribution is:

$$\sigma_{walk} = \left| \frac{dT_{thr}}{dA} \right|_{\bar{A}} \times \sigma_A = \frac{c}{\bar{A} \sqrt{2 \ln \left(\frac{\bar{A}}{v_{thr}} \right)}} \sigma_A \quad (\text{s}) \quad (2.85)$$

For the sake of usability, it is also worth to express Eq. 2.85 in terms of charge fluctuations. Knowing that the integral of a Gaussian is:

$$\int_{-\infty}^{\infty} \bar{A} e^{-(x-b)^2/2c^2} dx = \bar{A} \sqrt{2\pi c^2} \quad (\text{Vs}) \quad (2.86)$$

the formula for the average amplitude as a function of average pulse charge \bar{q} is:

$$\bar{A} = \frac{R_L \bar{q}}{\sqrt{2\pi c^2}} \quad (\text{V}) \quad (2.87)$$

with R_L denoting load resistance. Then, the variance of the amplitude becomes:

$$\sigma_A^2 = \frac{R_L^2}{2\pi c^2} \sigma_q^2 \quad (\text{V}) \quad (2.88)$$

¹⁷The b and c are constants since, for the moment, only walk error due to amplitude fluctuation is of interest.

Substituting Eq. 2.87 and Eq. 2.88 into Eq. 2.85 converts it to:

$$\sigma_{walk} = \frac{c}{\bar{q} \sqrt{2 \ln \left(\frac{R_L \bar{q}}{v_{thr} \sqrt{2\pi c^2}} \right)}} \sigma_q \quad (\text{s}) \quad (2.89)$$

The formulas defined above are valid only in case the amplitude fluctuation is small enough so that it is justified to use the derivative to approximate the slope of the function defined in Eq. 2.85 and Eq. 2.89 over the range of interest. If this is not the case, then Monte-Carlo techniques should be used.

Fairly often the Gaussian does not resemble the actual analog signal, but a combination of a Gaussian and an exponential does. This type of function is called the exponentially modified Gaussian distribution and is given by¹⁸:

$$x_1(t) = C e^{\frac{\lambda}{2}(2\mu + \lambda\sigma^2 - 2t)} \operatorname{erfc} \left(\frac{\mu + \lambda\sigma^2 - t}{\sqrt{2}\sigma} \right) \quad (\text{V}) \quad (2.90)$$

with μ denoting the mean of the Gaussian component, σ^2 its variance, λ the rate of exponential component, and C a constant proportional to the amplitude of the signal (note that it may happen that $\max[x_1(t)] \neq 1$ for $C = 1$). Similarly to the previously described derivations, μ , σ , and λ are constants, whereas C is a random variable. The formula is rather complex, but a simple trick can be used to simplify it to the Gaussian case described above. Given the use of a fixed-threshold discriminator, only the leading edge of the signal is meaningful for the estimation of the walk-related jitter. Therefore, after establishing the parameters of Eq. 2.90 to closely resemble the actual signal, one can try to find a Gaussian $x(t)$ (Eq. 2.83) with the same rise time and amplitude as the signal given by Eq. 2.90. The amplitude of the Gaussian will equal the amplitude of $x_1(t)$. One other thing that is needed is the ratio of the integrals of the scaled Gaussian to the exponentially modified Gaussian. Let us denote them as:

$$A_1 = \max[x_1(t)] \quad (\text{V}) \quad (2.91)$$

$$\alpha_q = \frac{\int_{-\infty}^{\infty} x(t) dt}{\int_{-\infty}^{\infty} x_1(t) dt} \quad (2.92)$$

Then the expression for the walk error based on amplitude fluctuation is a straightforward substitution to Eq. 2.85, yielding:

$$\sigma_{walk} = \frac{c}{\bar{A}_1 \sqrt{2 \ln \left(\frac{\bar{A}_1}{v_{thr}} \right)}} \sigma_{A_1} \quad (\text{s}) \quad (2.93)$$

with $\sigma_{A_1}^2$ being the variance of the amplitude of $x_1(t)$. Corresponding expression for the walk error based on charge fluctuations (i.e., uncertainty of the integral of $x_1(t)$) can be

¹⁸Source: https://en.wikipedia.org/wiki/Exponentially_modified_Gaussian_distribution

derived from Eq. 2.89, after substituting $\bar{q} = \alpha_q \bar{q}_1$:

$$\sigma_{walk} = \frac{c}{\bar{q}_1 \sqrt{2 \ln \left(\frac{R_L \alpha_q \bar{q}_1}{v_{thr} \sqrt{2\pi c^2}} \right)}} \sigma_q \quad (s) \quad (2.94)$$

The most straightforward technique to find A_1 , α_q and to match the rise times of the Gaussian and the exponentially modified Gaussian function is to use numerical calculation. Fig. 2.37 shows examples of matching both functions for various ratios of rise time to fall time.

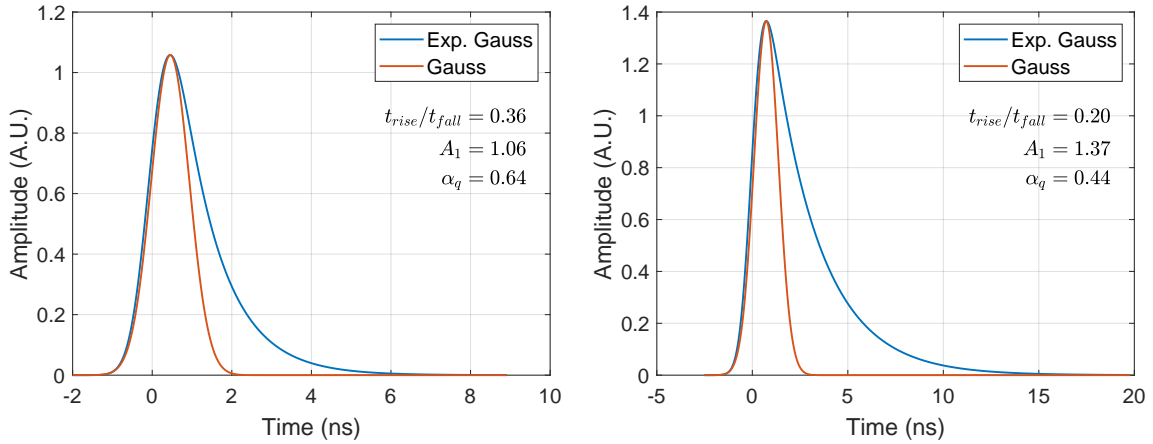


Figure 2.37: Examples of matching rise times of a Gaussian to the exponentially modified Gaussian distribution for different ratios of rise time to fall time.

Because of severely detrimental effects that the ‘amplitude-walk’ effect can have on the timing resolution, various methods can be used to correct it. One involves using a track-and-hold circuit in parallel with the discriminator and subsequently using an ADC to digitize the amplitude. Other involves measuring the time-over-threshold and using this information to estimate the amplitude. Afterward, the digitized time is corrected based on the recorded amplitude information. Another potential solution is to use two discriminators with different thresholds to measure the slope of the pulse and perform correction based on that. Such a solution is currently used in fiber trackers in the COMPASS experiment in CERN [87]. However, a far more elegant solution is to use a constant fraction discriminator and trigger at the desired fraction of the pulse rather than at a fixed level.

The idea behind the operation of the digital constant fraction discriminator is the following (Fig. 2.38). The input signal is split into two paths – an attenuated one and a delayed one. The delay is achieved either by using actual delay lines (a viable option for discrete circuits, since delays are nanosecond level) or by using, among other possibilities, a distributed RC delay line [130] or Padé approximants [131]. Then, there are two possible implementations. One inverts the delayed signal and form a bipolar signal and detects

the zero-crossing point (Fig. 2.38, left). Usually, this involves using an additional arming circuit to detect a moment when the binary signal exceeds a pre-defined threshold before the zero-crossing point so that one does not trigger because of the noise [128]. Another implementation (Fig. 2.38, right) uses the attenuated signal to drive the threshold of a discriminator that examines the delayed signal [118].

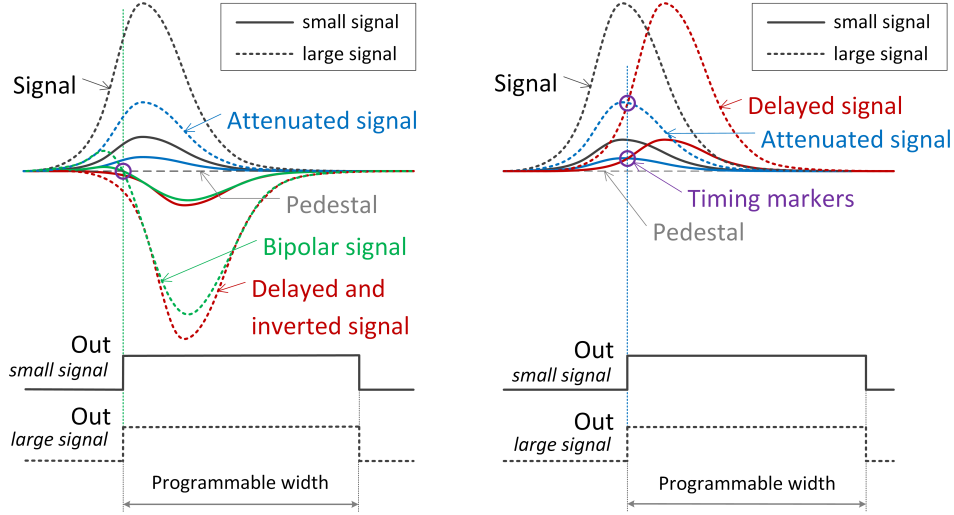


Figure 2.38: Principle of operation of a constant fraction discriminator. *Left:* Implementation based on the zero-crossing principle. A bipolar signal (green) is formed by adding an attenuated (blue) and a delayed and inverted (red) copies of the original signal (black). Discriminator detects the zero-crossing point (purple circle) of the bipolar signal. *Right:* Implementation that uses an attenuated (blue) copy of the original signal (black) to set the threshold for the delayed signal (red). Timing markers are marked by purple circles.

Taking all the above discussion into account, a rough estimate of the overall timing accuracy is then:

$$\sigma_{time} = \sqrt{\sigma_{thr}^2 + \sigma_{TDC}^2 + \sigma_{walk}^2} \quad (s) \quad (2.95)$$

with $\sigma_{walk} = 0$ for the constant fraction discriminator. For a more in-depth discussion of the accuracy of discriminator-based timing measurements, taking into account the effects of both uncorrelated and correlated noise, please refer to [132].

One of the critical issues in any system that uses a discriminator is preventing multiple triggers due to noise. Therefore nearly any system allows setting a minimum width of the digital output pulse, thereby masking any triggers that could appear after the first detection of crossing the noise threshold. Since any new pulse arriving when the output of the discriminator is active will not cause output change, this is equivalent to introducing dead time to the system. The actual width of the output pulse depends then on both the time-over-threshold (the extending dead time) and an additional delay once the signal drops back below the threshold (the non-extending dead time). If one denotes them as T_e and T_{ne} , then, assuming constant rate during over the time of observation, the expected

loss of counts (i.e., inefficiency) due to rate can be estimated according to [128]:

$$r = \frac{R}{e^{RT_e} + U(T_{ne} - T_e) R(T_{ne} - T_e)} \quad (2.96)$$

with r being the rate registered by the system, R the actual rate at the input and $U(T_{ne} - T_e)$ a unit step function defined as:

$$U(T_{ne} - T_e) = \begin{cases} 0 & \text{for } T_{ne} \leq T_e; \\ 1 & \text{for } T_{ne} > T_e \end{cases} \quad (2.97)$$

The dead time of the discriminator should be set in a way that there is nearly no effect on the detector efficiency at the expected rate of incoming particles.

2.6.2 Sampling Systems

Waveform sampling presents an entirely different approach to signal digitization. Contrary to techniques using a combination of discriminators and TDCs, here the whole signal is converted to a digital form, using a high-speed analog-to-digital converter. Then, signal processing methods are used to estimate its features (either online or offline), namely the time of arrival and sometimes also the amplitude or the charge. Having access to the full waveform has several benefits, among them:

- Ability to disentangle pile-up at the analog signal level (at least to some extent). In this aspect, the sampling method is superior to the discriminator-based one, as it does not introduce additional dead time to the system. The latter approach, by definition, counts piled-up events as one.
- It allows the application of digital filters to the raw data stream exiting the ADC, which can be helpful in case there is a pickup of stationary electromagnetic interference. Note that interference problems are quite common, given dimensions of typical high energy experiments, as well as a multitude of various types of equipment (for example high voltage supplies, chillers, air conditioning units, etc.).
- It provides amplitude information, though in the case of scintillating fiber detectors this is of minor importance.

There is, however, a price to pay – and this is higher power usage, higher cost, and significantly higher data rate than would be the case of a discriminator-based system.

Fig. 2.39 presents a schematic of an example sampling system. It consists of several distinct elements – an anti-aliasing filter, an analog-to-digital converter and a processing stage that allows feature extraction. Depending on the implementation, the latter can be either online or offline. Similarly to the discriminator-based systems, it may be necessary

to utilize additional front-end circuits, if ensuring decent signal quality requires them. If the detector is also used to trigger other systems, then, given low-latency requirements, a parallel signal chain will typically be used, comprising discriminators and fast logic circuitry.

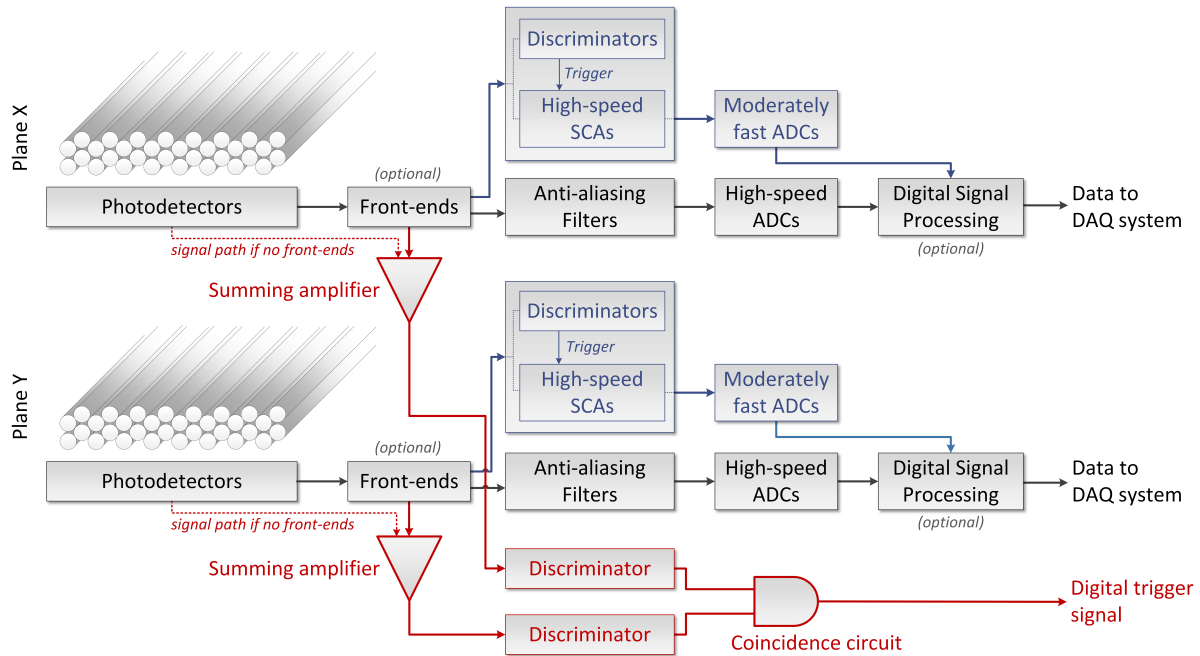


Figure 2.39: Schematic drawing of an example sampling readout system of a two-plane detector, with a coincidence output. Front-end circuits are sometimes used to ensure sufficient signal-to-noise ratio at the input of the discriminator, or to provide impedance matching to the transmission line as well as adequate line driving capability.

An interesting variant of the waveform sampling system involves the utilization of switched capacitor arrays (SCAs – Fig. 2.40). Here, one takes note that only parts of the waveforms are of interest – and those are segments containing signals from the photosensors. Hence, it is possible to digitize only those parts and disregard the remaining segments. Moreover, since the system operates in pulse mode, usually there is plenty of time between the ‘interesting’ segments – so one can sample fast and then digitize slow. The SCA is a chip that allows precisely that – it is a fast analog memory arranged in the form of a circular buffer, which typically operates at sampling frequencies of several GHz. It samples the input signal but does not quantize nor digitize it, so an additional circuit is necessary to detect the presence of the signal. Usually, it is achieved with a discriminator connected in parallel with the analog memory, with proper buffering of the input. Once it detects the signal above the threshold, the control logic latches the analog memory. There is no longer a need to use high-speed ADC – the memory can keep the signal for a reasonably long time without a deterioration in quality. So, a time-stretching effect is achieved, which is hugely advantageous – it allows for a significant reduction of power consumption and overall cost of the system while maintaining a high sampling frequency. For signals

typically produced by the photosensors used in fiber trackers, this allows the elimination of the anti-aliasing filter from the signal chain. The negative side of this solution is an introduction of dead time – as long as the analog memory is latched, the SCA is insensitive to any new signals, which, depending on the rate of incoming pulses, may or may not be a problem. One way of alleviating the dead time problem is to use multiple analog memories to sample the same signal – when one array is frozen, the other is still alive and ready to record new signals. Another method involves using SCA with segmented analog memories. All in all, given a multitude of available ASICs [133–136], this approach continues to gain in popularity, as the benefits seem to outweigh the disadvantages.

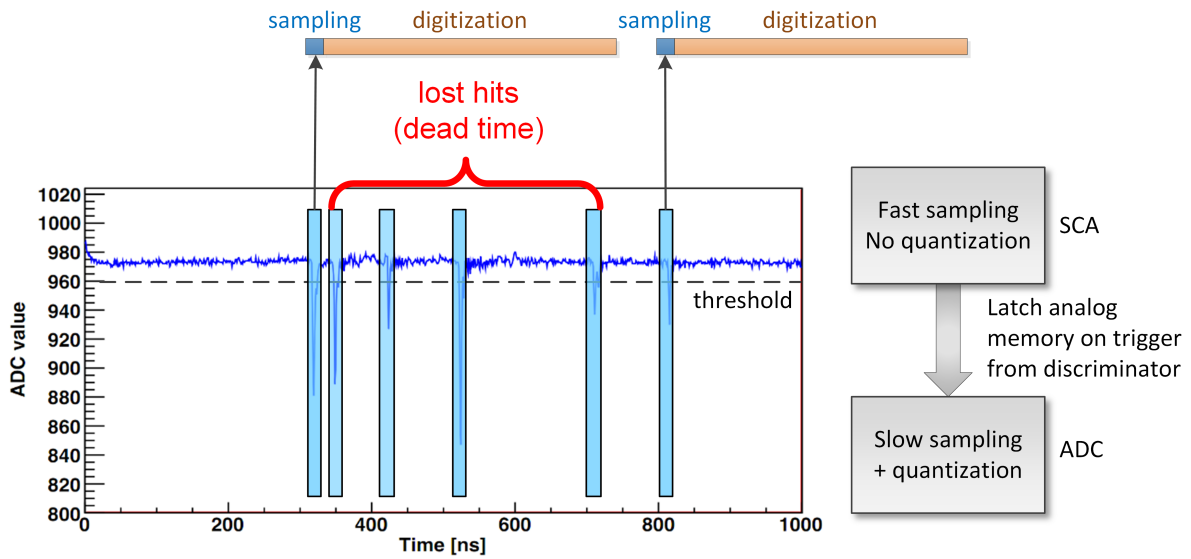


Figure 2.40: Principle of operation of a system using a switched capacitor array (SCA). The SCA provides for high-speed sampling (typically GHz-range) but stores waveform in analog memory (capacitors). The SCA is latched upon a signal from a discriminator, connected in parallel to the SCA. Then, the segment of a waveform is digitized using a moderately-fast ADC. During digitization, the SCA is insensitive to changes in the input signal (dead time). *Source: Redrawn from [137], with modifications.*

Usually, it is not the actual waveform that is of interest, but rather certain features that are useful for physics analyses (such as, for example, time of arrival). Nonetheless, a prerequisite to their estimation is an accurate digital representation of the analog waveform. With that in mind, the issue which is of absolutely paramount importance is the proper choice of the sampling frequency (F_S), which must satisfy the Nyquist sampling criterion. In other words, the sampling frequency should be at least twice the maximum frequency component of the signal (F_{MAX}). It is a well-known fact that the sampling process leads to duplication of signal spectra, with each multiple of F_S receiving its copy of left-for-right flipped spectra (Fig. 2.41). If the sampling frequency is too small, these copies overlap, thus changing the spectrum of the signal, leading to irreversible distortions. One way to prevent that is to use very high F_S , thus ensuring that nearly no

frequency component is over $F_S/2$ (the SCA approach). The other option is to use an anti-aliasing low-pass filter in front of the ADC, guaranteeing sufficient attenuation of frequency components above $F_S/2$ (lower left plot in Fig. 2.41). It will distort the signal, but at least do so in a known and deterministic way so the subsequent signal processing can account for that.

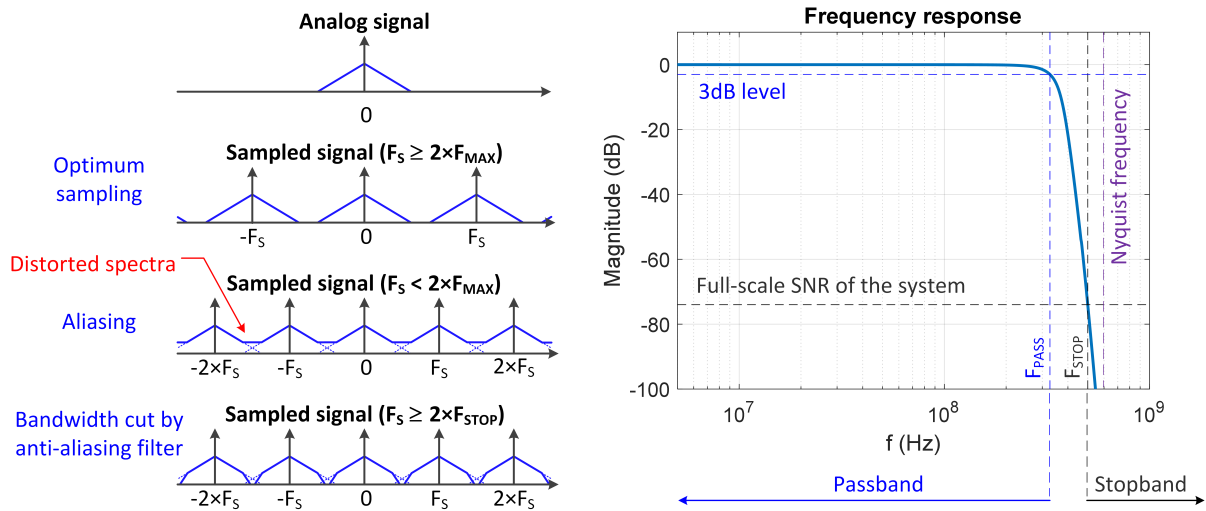


Figure 2.41: The phenomenon of aliasing. *Left*: Sampling causes duplication of spectrum around each multiple of sampling frequency F_S . If F_S is too low compared to the maximum frequency present in the signal F_{MAX} , then distortion due to overlapping of duplicated signal spectra. An anti-aliasing filter is used to prevent that – it limits analog bandwidth in order to ensure fulfilling the Nyquist criteria ($F_{STOP} \leq F_S/2$, resulting in $F_{MAX} \leq F_S/2$). *Right*: Example frequency response of an anti-aliasing filter. Attenuation at $F_S/2$ should ensure suppressing high-frequency components of a full-scale signal down to the noise level of the system. For shape-sensitive applications, it is preferred to use linear-phase filters.

When it comes to the choice of the anti-aliasing filter, there are two crucial requirements:

- a) The stopband frequency (F_{STOP} in Fig. 2.41) should be at most half the sampling frequency, preferably slightly less.
- b) The stopband attenuation should ensure that even if a full-scale signal is present at the input, the filter will suppress the frequency components that exceed F_{STOP} down to the noise level of the system.

One way of fulfilling the latter requirement is to design a filter with stopband attenuation equal to full-scale SNR of the system, as is presented in the right plot in Fig. 2.41. However, if the input signal is of Gaussian-shape, then its Fourier transform will also be a Gaussian, meaning that even for the full-scale signal the frequency components on the high-side of the spectrum will not be at maximum levels. Consequently, it is possible

to decrease the stopband attenuation of the filter, as long as the full-scale signal at its output does not have any frequency components above the F_{STOP} that exceed the noise levels.

Another aspect that deserves some attention is the choice of the filter type. Since waveform shape is crucial for accurate estimation of timing, a natural choice is a filter with a linear phase – such as a multi-stage RC filter or Bessel/linear-phase with equiripple error filters built using biquads. The huge benefit of these types of filters is that they have a smooth impulse response, meaning that they do not introduce oscillations to their output signals. The downside is slow roll-off, meaning that the transition band between the passband and the stopband is relatively wide. The consequence is that for a given stopband frequency, the passband frequency is rather low. Hence, if the sampling frequency is small compared to the bandwidth of the analog signal, then a significant fraction of useful information is removed from the signal. Shape-wise it results in smearing edges of the pulse, which will have detrimental effects on the timing accuracy – it relies both on signal-to-noise ratio and the slope of the leading edge. Therefore, sometimes it is worth considering using filters with a sharper roll-off, which will allow for broader passband (i.e., sharper edges) while still having sufficient stopband attenuation – for example, Butterworth, Chebyshev or elliptic filters. One should be aware, though, that sharp roll-off results in an oscillatory response. However, if additional oscillations do not pose a problem for time estimation, then the timing accuracy may be improved thanks to sharper edges.

Apart from aliasing, other factors contributing to non-negligible degradation of the accuracy of signal representation come from (Fig. 2.42):

- Noise introduced by circuit stages preceding the ADC, combined with thermal, flicker and shot noise of the ADC itself.
- Quantization noise, resulting from the fact that the ADC will assign the same code-word to a range of voltages corresponding to a single bit.
- Sampling clock jitter and ADC aperture jitter, causing fluctuations due to shifts of sampling time.
- ADC non-linearity.

A convenient measure of the effects of these errors is the SNR of the system. In the best-case scenario, one would measure the noise floor of the system and thus know the real value of the SNR. If this is not possible, for example, because the system is not yet available, then relatively good estimation can be obtained using a few simple steps.

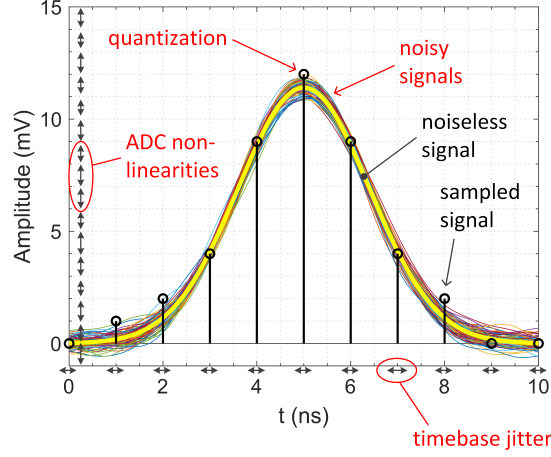


Figure 2.42: Basic sources of errors in waveform representation: noise from input circuits, quantization (inaccuracy in representation due to a finite step size – 1 mV on the drawing), non-linearities of the ADC (unequal voltage steps) and timing jitter from the instability of the timebase.

First, it is necessary to calculate the noise level originating in the circuits preceding the ADC. This metric, from hereon denoted as σ_{input} , must be calculated by standard circuit analysis techniques and values of input-referred voltage and current noise densities obtained from amplifier datasheets.

In terms of the ADC itself, Kester et al. [138] provide the following formula:

$$SNR_{ADC} = -20 \log_{10} \left[\sqrt{(2\pi f_a \sigma_{tjitt})^2 + \frac{2}{3} \left(\frac{1 + \varepsilon}{2^N} \right)^2 + \left(\frac{2\sqrt{2} \sigma_{eff}}{2^N} \right)^2} \right] \quad (\text{dBFS}) \quad (2.98)$$

where f_a stands for the frequency of analog input full-scale sine wave (in Hz), σ_{tjitt} is RMS value of the combined ADC aperture jitter and the jitter of the external clock (in seconds), ε is the average differential non-linearity (DNL), N denotes the number of bits, and finally σ_{eff} represents the effective input noise of the ADC chip. Calculating the equivalent RMS voltage of the ADC-borne noise is then straightforward:

$$\sigma_{ADC} = \frac{V_{PP}}{2\sqrt{2} \times 10^{\frac{SNR_{ADC}}{20}}} \quad (\text{V}) \quad (2.99)$$

with V_{PP} being the maximum peak-to-peak voltage accepted by the ADC. While providing nearly an instant estimate of the performance of the ADC, there are two problems with the usability of Eq. 2.98 during the design process of the readout system for a scintillating fiber detector. First of them is related to the value of σ_{eff} , as many datasheets do not provide it. Second concerns the formula for the contribution from the combined sampling clock and aperture jitters – it is defined for a sine signal (note the presence of the term f_a), so a single frequency. The signals coming out of photosensors are of pulse nature – i.e., they are wideband, which means that Eq. 2.98 cannot be applied directly.

Fortunately, almost all datasheets nowadays provide a value called ‘the effective number of bits’ (ENOB). It is a synthetic benchmark of ADC performance that takes into account all internal sources of errors, including quantization, electronic noise, aperture jitter. Using ENOB, one can easily calculate the value called SINAD – the ratio of Signal-to-Noise-and-Distortion:

$$SINAD = 6.02 \times ENOB + 1.76 \quad (\text{dBFS}) \quad (2.100)$$

The SINAD is defined as the ratio of the RMS value of the full-scale sine signal applied to the input of the ADC to the mean of root-sum-square (RSS) of all the other spectral components, excluding the DC [138]. Hence, an approximation of the noise level inherent to the ADC is a simple modification of Eq. 2.99, substituting SNR_{ADC} with $SINAD$:

$$\sigma_{ADC} = \frac{V_{PP}}{2\sqrt{2} \times 10^{\frac{SINAD}{20}}} \quad (\text{V}) \quad (2.101)$$

Usually, the above estimate is sufficient to achieve a reasonably accurate estimate on ADC noise, but accounting for the effects of sampling clock jitter deserves a bit more attention. The two quantities that are of interest are:

- The RMS value of the clock jitter (σ_{tjitt}), which can be derived from measurements of the phase noise of the clock signal [138].
- The slope of the signal during sampling ($\left. \frac{dx}{dt} \right|_{t_{sample}}$).

The relationship between the two is:

$$\sigma_{njitt} = \sigma_{tjitt} \times \left. \frac{dx}{dt} \right|_{t_{sample}} \quad (\text{V}) \quad (2.102)$$

Now, it is crucial to examine the datasheet of the ADC and find measurement conditions which were used to provide either $SINAD$ or $ENOB$, in order to decide whether one needs to account for additional jitter-related errors. The σ_{njitt} contribution is non-negligible if any of the below conditions is true:

- The jitter of the sampling clock used in the readout system is larger than the one quoted in the datasheet under the description of test conditions.
- The slope of the signal can exceed the one inherent to the full-scale sine wave at the test frequency quoted in the datasheet. The slope is easy to estimate the average slope using the 10%-90% rise or fall time, whichever is shorter, and the expected average amplitude of photosensor signals.

Otherwise, it is reasonably safe to neglect σ_{njitt} , as σ_{ADC} already accounts for the clock jitter errors.

With all the above in mind, the final formula for the amount of noise introduced by the readout system based on full waveform sampling is:

$$\sigma_{noise} = \sqrt{\sigma_{input}^2 + \sigma_{ADC}^2 + \sigma_{njitt}^2} \quad (V) \quad (2.103)$$

The above equation assumes that the overall noise dominates over the pickup of electromagnetic interference.

2.6.3 Time Estimation from Sampled Waveforms

Digital Constant Fraction Algorithm

One of the simplest and least resource hungry methods of estimating the time of pulse arrival based on a sampled waveform is the digital constant fraction discriminator (Fig. 2.43). Its operation is similar to the zero-crossing variant of the analog counterpart, with one difference when it comes to the creation of the bi-polar waveform. Rather than attenuating the original signal, the inverted waveform is multiplied, which prevents precision loss in subsequent calculations. The step-by-step operation is as follows:

1. Dump all data until the signal crosses a pre-defined threshold.
2. Latch a segment containing the full waveform with the whole pulse. Leave a few samples before and after the pulse.
3. Calculate and subtract a pedestal estimate. If needed, use FFT (fast Fourier transform) interpolation to increase sample density.
4. Create an additional signal delaying the signal obtained in step 3 by a certain amount of samples, inverting it and, depending on implementation, multiply by a constant factor. If FFT interpolation was used in step 3, then sub-sample delays are possible.
5. Create a bipolar signal by adding signals obtained in steps 3 and 4.
6. Calculate the sample number corresponding to the intersection point of the bipolar signal from step 5 with the zero-level. Use linear interpolation to get sub-sample precision.

Two crucial parameters of the digital constant fraction algorithm are the delay of the inverted waveform and its multiplication coefficient. Depending on their setting, it is possible to operate using either leading edge only or both edges. The former variant is the choice in when the trailing edge is too unpredictable – which is the case for most

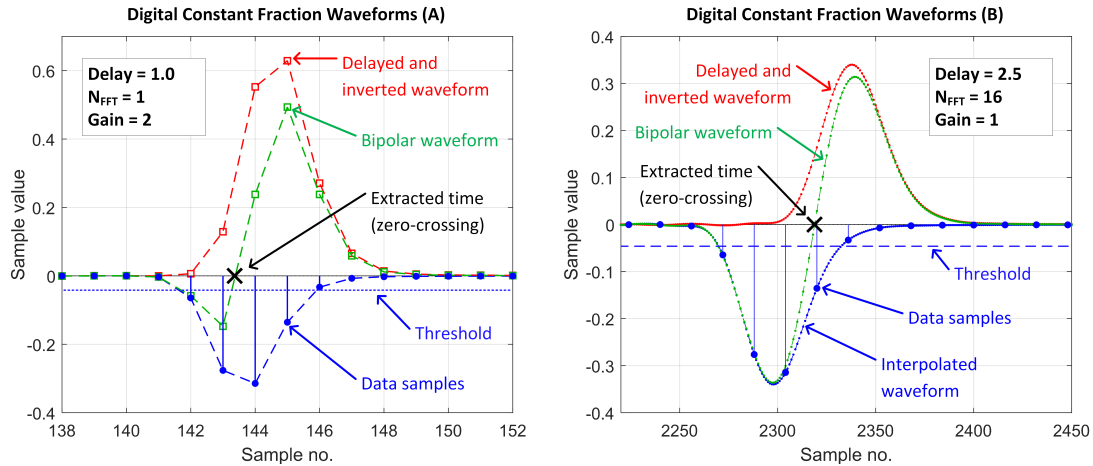


Figure 2.43: Principle of the digital constant fraction discriminator algorithm. *Left*: A variant using the leading edge only, with a fixed sample delay of two and the inverted waveform gain of two, without any interpolation of mid-sample values. *Right*: A variant that uses both leading and trailing edges for construction of bi-polar waveform. The FFT interpolation factor was $\times 16$, the delay was 2.5 sample and the inverted waveform gain was 1.

scintillation detectors, due to decay time as well as fluctuations of the photosensor response. The latter option may provide better performance if the sampling frequency does not allow maintaining the full bandwidth of the photosensor pulse and the decay time of the scintillator is short. In such a case the cut-off frequency of the anti-aliasing is low compared to the bandwidth of the original signal, meaning that the photosensor pulse is almost a delta input for the anti-aliasing filter. Consequently, each output will have nearly the same shape, resembling the impulse response of the filter. Therefore, both leading and trailing edges will be well defined, and using both of them has several advantages.

Similarly to the analog case, the timing accuracy is proportional to the ratio of noise to the slope of the signal. So, using both leading and trailing edge maximizes the slope. Furthermore, one can apply the inverted waveform gain of one, leading to a decrease in the noise. Each sample of the bipolar waveform uses two different samples of the original signal. A gain of one means that noise in the bipolar waveform is averaged, leading to an improvement of the SNR compared to a variant with amplified inverted waveform. Finally, a longer delay means less noise correlation between the samples, leading to more substantial SNR gain from averaging.

In order to provide an analytical expression for the timing resolution provided by the digital constant fraction discriminator algorithm, one can perform a derivation similar to that presented in [139], with modifications accounting for the implementation based on timing the zero-crossing point of the bipolar waveform¹⁹.

¹⁹Rather than using the zero-crossing approach, the implementation in [139] assumes using some algorithm to estimate the amplitude of the pulse and then calculates the time at which the waveform

First, let us define the samples used for estimation of the zero-crossing point as:

$$\begin{aligned} y_p &= y_{n+d} - a y_n \\ y_q &= y_{n+d+1} - a y_{n+1} \end{aligned} \quad (2.104)$$

with n being an arbitrary sample index, d the delay of the discriminator and a the gain of the inverted waveform. Since every sample is associated with a voltage fluctuation, let us define the corresponding random variables, denoting the error of the n -th sample as ∂y_n . Thus, Eq. 2.104 becomes:

$$\begin{aligned} Y_p &= y_p + \partial y_p = (y_{n+d} + \partial y_{n+d}) - a (y_n + \partial y_n) = Y_{n+d} - a Y_n \\ Y_q &= y_q + \partial y_q = (y_{n+d+1} + \partial y_{n+d+1}) - a (y_{n+1} + \partial y_{n+1}) = Y_{n+d+1} - a Y_{n+1} \end{aligned} \quad (2.105)$$

The variance of Y_p and Y_q is then:

$$\begin{aligned} \text{Var}(Y_p) &= \text{Var}(Y_{n+d}) + a^2 \text{Var}(Y_n) - 2a \text{cov}(Y_{n+d}, Y_n) \\ \text{Var}(Y_q) &= \text{Var}(Y_{n+d+1}) + a^2 \text{Var}(Y_{n+1}) - 2a \text{cov}(Y_{n+d+1}, Y_{n+1}) \end{aligned} \quad (2.106)$$

Now, assuming noise ergodicity, we get:

$$\begin{aligned} \text{Var}(Y_n) &= \text{Var}(Y_{n+1}) = \text{Var}(Y_{n+d}) = \text{Var}(Y_{n+d+1}) = \sigma_n^2 \\ \text{cov}(Y_{n+d}, Y_n) &= \text{cov}(Y_{n+d+1}, Y_{n+1}) \end{aligned} \quad (2.107)$$

Therefore, Eq. 2.106 becomes:

$$\text{Var}(Y_p) = \text{Var}(Y_q) = (1 + a^2)\sigma_n^2 - 2a \text{cov}(Y_{n+d}, Y_n) \quad (2.108)$$

Let us now assume that the ideal, noiseless bipolar signal crosses the zero-level at time t . Using samples Y_p and Y_q to calculate the voltage at time t using linear interpolation will result in the following error:

$$\Delta Y = \partial y_q \frac{t}{T_S} + \partial y_p \frac{T_S - t}{T_S} \quad (2.109)$$

where T_S is the sampling period. As per [139], the average variance of this error is:

$$\overline{\text{Var}(\Delta Y)} = \frac{1}{3} \text{Var}(Y_p) + \frac{1}{3} \text{Var}(Y_q) + \frac{1}{3} \text{cov}(Y_p, Y_q) \quad (2.110)$$

crosses the threshold, defined as the fraction F of the estimated amplitude. In such a case, the formula for the timing accuracy is:

$$\overline{\sigma_{time}} = \sqrt{\frac{\frac{2}{3}(1 + F^2\alpha^2)\sigma_n^2 + \frac{1}{3}\text{cov}(\partial y_n, \partial y_{n+1})}{(dy/dt)^2} + \frac{2}{3}\sigma_{jitter}^2 + \frac{1}{3}\text{cov}(\partial t_n, \partial t_{n+1})} \quad (s)$$

The meaning of other symbols is: σ_n is voltage noise present at the input of the ADC, ∂y_n , ∂y_{n+1} and ∂t_n , ∂t_{n+1} respectively denote random voltage and timing errors of two consecutive samples at the opposite sides of the threshold crossing point, dy/dt is the slope of the analog signal and σ_{jitter} is the combined fluctuation of the sampling clock and ADC aperture jitter. Since the estimate of the amplitude will typically use several samples, its fluctuation will be a fraction α of that of a single sample, with $\alpha \leq 1$

Substituting Eq. 2.108 and taking into account ergodicity of the noise yields:

$$\overline{\text{Var}(\Delta Y)} = \frac{2}{3} [(1 + a^2)\sigma_n^2 - 2a \text{cov}(Y_{n+d}, Y_n)] + \frac{1}{3} \text{cov}(Y_p, Y_q) \quad (2.111)$$

Further on, substituting Eq. 2.105 into the term $\text{cov}(Y_p, Y_q)$ results in:

$$\begin{aligned} \text{cov}(Y_p, Y_q) &= \text{cov}(Y_{n+d} - aY_n, Y_{n+d+1} - aY_{n+1}) = \\ &= \text{cov}(Y_{n+d}, Y_{n+d+1}) - a \text{cov}(Y_{n+d}, Y_{n+1}) - a \text{cov}(Y_n, Y_{n+d+1}) + a^2 \text{cov}(Y_n, Y_{n+1}) \end{aligned} \quad (2.112)$$

Again, assuming ergodicity and knowing that $\text{cov}(Y_n, Y_{n+1}) = \text{cov}(Y_{n+1}, Y_n)$ gives:

$$\text{cov}(Y_p, Y_q) = (1 + a^2) \text{cov}(Y_{n+1}, Y_n) - a \text{cov}(Y_{n+d}, Y_{n+1}) - a \text{cov}(Y_{n+d+1}, Y_n) \quad (2.113)$$

Now, substituting Eq. 2.113 into Eq. 2.111 provides for the final expression for $\overline{\text{Var}(\Delta Y)}$:

$$\begin{aligned} \overline{\text{Var}(\Delta Y)} &= \frac{2(1 + a^2)}{3} \sigma_n^2 - \frac{4a}{3} \text{cov}(Y_{n+d}, Y_n) + \\ &+ \frac{1 + a^2}{3} \text{cov}(Y_{n+1}, Y_n) - \frac{a}{3} \text{cov}(Y_{n+d}, Y_{n+1}) - \frac{a}{3} \text{cov}(Y_{n+d+1}, Y_n) \end{aligned} \quad (2.114)$$

The timing jitter corresponding to $\overline{\text{Var}(\Delta Y)}$ can then be easily calculated using the relationship for the leading edge discriminator (Eq. 2.82):

$$\overline{\sigma_{time,n}^2} = \frac{\overline{\text{Var}(\Delta Y)}}{(dx/dt|_{t_{zero}})^2} \quad (2.115)$$

The second factor that affects the resolution of the digital constant fraction algorithm originates from the jitter of the sampling clock. Its estimation is straightforward [139] – one needs to translate the timebase jitter (σ_t) into the voltage noise using Eq. 2.82, then use Eq. 2.114 to estimate its variance and finally once again translate the result into the time domain again using Eq. 2.82. The resulting formula is:

$$\begin{aligned} \overline{\sigma_{time,jitt}} &= \frac{2(1 + a^2)}{3} \sigma_t^2 - \frac{4a}{3} \text{cov}(T_{n+d}, T_n) + \\ &+ \frac{1 + a^2}{3} \text{cov}(T_{n+1}, T_n) - \frac{a}{3} \text{cov}(T_{n+d}, T_{n+1}) - \frac{a}{3} \text{cov}(T_{n+d+1}, T_n) \end{aligned} \quad (2.116)$$

with T_i denoting the random variable corresponding to the sampling time of the i -th sample.

The final formula for the timing accuracy of the algorithm is:

$$\overline{\sigma_{time}} = \sqrt{\overline{\sigma_{time,n}^2} + \overline{\sigma_{time,jitt}^2}} \quad (2.117)$$

In order to get rough estimates of actual resolutions, the very first approximation could be to use σ_{ADC} and σ_{input} from Eq. 2.103 to calculate σ_n in Eq.2.114 and then the specification of the oscillator to get σ_t in Eq. 2.116. Further simplification may result from an

assumption of either uncorrelated or correlated noise. In the former case, Eq. 2.114 and Eq. 2.116 reduce to:

$$\overline{\sigma_{time,n}^2} = \frac{2(1+a^2)}{3} \sigma_n^2 \left/ \frac{dx}{dt} \right|_{t_{zero}} \quad (2.118)$$

$$\overline{\sigma_{time,jitt}^2} = \frac{2(1+a^2)}{3} \sigma_t^2 \quad (2.119)$$

From the above, the benefit of using a variant that utilizes both edges is clear – large delays decrease correlation, and the inverted waveform gain of one decreases the $(1+a^2)$ term in both expressions. So, as long as the trailing edge is well defined, it is recommended to use it.

An additional improvement in timing accuracy is possible by applying a correction of the fact that the real signal between the samples neighboring the zero-crossing point is not a straight line (Fig. 2.44, left). This effect causes a systematic error, which depends on the value of the calculated sub-sample delay of the zero-crossing point and hence can be easily corrected – provided that the pulse shape is relatively constant. All that is needed is a simple simulation that maps the ratio of:

$$CR = \frac{P}{P+Q} \quad (2.120)$$

to the real sub-sample shifts of the template. The result is the so-called $CR-\theta$ curve (Fig. 2.44, right), which is then used to cancel this error [140].

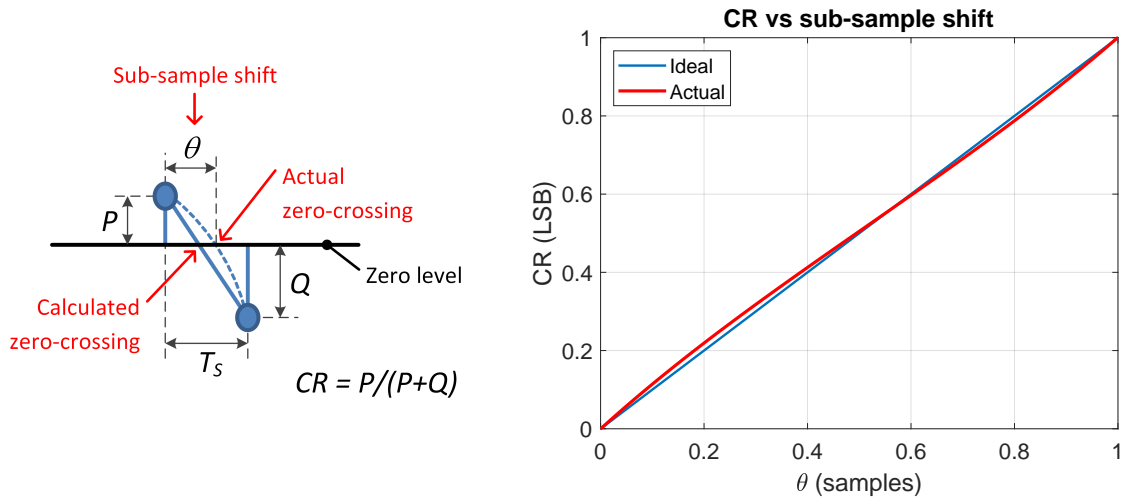


Figure 2.44: The principle of so-called $CR-\theta$ correction. *Left:* A deterministic timing error is introduced by linear interpolation because the real signal is not a straight line between points P and Q . *Right:* A mapping of the ratio of $CR = P/(P+Q)$ vs. the actual sub-sample shift θ of the pulse template can be used to cancel this error. The plot presents a curve for the digital discriminator constant fraction algorithms with a delay of three, inverted waveform gain of two and the leading edge time of the template equal to $2.06 T_S$.

Cross-correlation and Sinc Interpolation

Another method of timing the arriving input pulse utilizes cross-correlation of the sampled input pulse $x[n]$ with a known signal template $s[n]$. Since the sampling clock of the ADC is uncorrelated with the arrival time of the analog input pulse, then even if the analog versions of the signal $x(t)$ and the template $s(t)$ are the same, their sampled versions $x[n]$ and $s[n]$ will differ. The reason is a random sub-sample offset Δt between the sampling times of both signals (Fig. 2.45, left). The goal of the algorithm is to find the value of Δt , with the following steps:

1. Select the initial size of the sub-sample step. Set the estimate of the sub-sample shift θ to zero.
2. Calculate the cross-correlation function between $x[n]$ and $s[n]$:

$$(x \star s)[n] = \sum_{m=-\infty}^{\infty} x[m-n] s[m] \quad (2.121)$$

3. Use interpolation to simulate sampling the template $s(t)$ at different time instants $n(T_S + \theta)$ and $n(T_S - \theta)$. The new values are calculated using the Whittaker-Shannon interpolation formula (sinc interpolation):

$$x(t) = \sum_{n=-\infty}^{\infty} x[n] \operatorname{sinc} \left(\frac{t - nT_S}{T_S} \right) \quad (2.122)$$

4. Re-compute cross-correlation of $x[n]$ with the shifted version of $s[n]$ and compare the maximums with the maximum of the original cross-correlation function.
5. Select either positive or negative increment of the sub-sample shift θ , depending on which one resulted in a higher maximum of the cross-correlation function and add the current step to the estimate of the sub-sample shift θ .
6. Finish if the minimum step is at the desired limit of sub-sample accuracy. Otherwise, apply the bi-section method – i.e., decrease the sub-sample step by half and proceed to step 5.

Once finished, the template should be resampled at the same time instants as the signal, leading to maximized cross-correlation function (Fig. 2.45, right). The final value of the sub-sample shift θ is the sought sub-sample timing of the arriving analog pulse.

As far as practical applications of this method are concerned, one thing to note is that usually is it beneficial to subtract the pedestal estimate before calculation of the cross-correlation function. The other is that, given the finite length of the buffers encompassing the pulses, it may be advisable to apply a windowed version of the sinc function to minimize artifacts from clipping it at the boundaries with non-zero values.

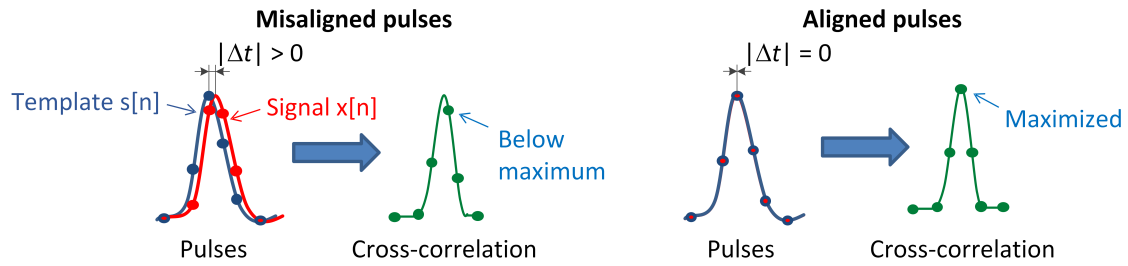


Figure 2.45: Principle of pulse timing using cross-correlation of the arriving signal $x[n]$ with its template $s[n]$. The template is resampled using the sinc interpolation to maximize the peak value of the discrete cross-correlation function.

Finite Impulse Response Filters

The idea of pulse processing using finite impulse response filters (FIRs) relies on transforming an input signal to some other signal that is more optimal for a given task (Fig. 2.46). For a scintillating detector, one can distinguish three of these tasks: detection, timing, and amplitude/charge estimation. In the case of detection, the most important criterion is to minimize or even avoid missing a pulse (false negative) or mistakenly identifying the pulse (false positive). Fulfilling it requires the best possible signal to noise ratio at the detection time. If accurate timing is the priority, then not only signal to noise ratio is important, but also the slope of the signal. If the time of arrival is extracted using the zero-crossing point of a bipolar waveform, then an additional important factor affecting the accuracy will be the ability to reject the pedestal. For amplitude/charge estimation, the optimal filter will be a one with a flat-top section, so that one avoids errors due to sampling the peak of the filter output at varying times. Furthermore, if this flat section is few samples long, then additional gain can be achieved thanks to averaging.

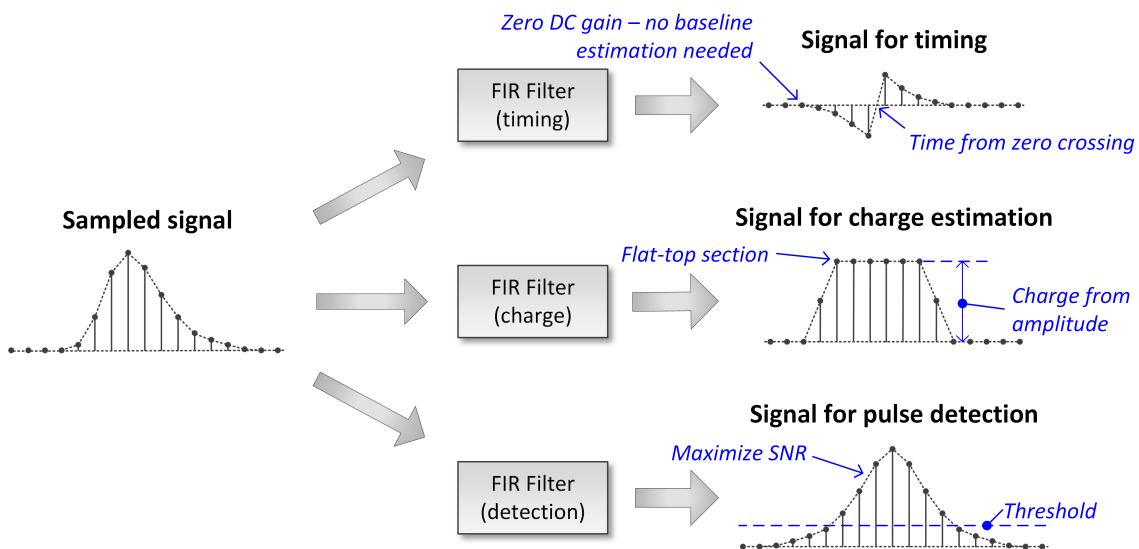


Figure 2.46: Principle of signal processing using optimum finite impulse response (FIR) filters.

The FIR filters have several nice features. They are, by definition, linear and always stable. Furthermore, they allow for arbitrary characteristics. All the above means that one can use optimization techniques to synthesize the filter (i.e., to calculate its impulse response). So, rather than using an analytical method, one defines the cost function that accounts for the parameters specific to a particular problem and then lets the optimization algorithm do its magic. A familiar name often used for such methodology is the ‘black box’ approach – one knows the input, gets the desired output but does not care how.

The methods of synthesizing optimal filters (i.e., finding the ‘black box’ content) have been studied over several decades [141–149]. The current trend is biased towards using fully automatic synthesis via constrained optimization. Of interest here are both the actual calculation of the filter’s impulse response as well as the choice of the constraints used during this calculation and, among them, the optimal shape of the filter’s response to the input signal.

Of the many available methods of synthesizing an FIR filter, it is worth to mention the Digital Penalized Least Means Square (DPLMS) method developed by Riboldi et al. and Gatti et al. [145, 146], which can be summarized as follows. First, let us express the input signal $x[n]$ as a combination of a noiseless signal $s[n]$ and additive stationary noise $v[n]$ that is uncorrelated to $s[n]$:

$$x[n] = s[n] + v[n] \quad (2.123)$$

Next, knowing that the filter is linear, its response to the input signal is given by the convolution theorem:

$$y[n] = \sum_{m=0}^{N-1} x[m]h[n-m] = \sum_{m=0}^{N-1} s[m]h[n-m] + \sum_{m=0}^{N-1} v[m]h[n-m] \quad (2.124)$$

where $h[n]$ denotes the impulse response of an N -tap FIR filter. Therefore, it is possible to divide the optimization into two separate problems. One is to minimize the variance of the filter output – for a stationary noise it is independent of the sample index:

$$\varepsilon_{var}^2 = \text{Var}(\mathbf{y}) = \mathbf{h}^H \mathbf{R}_v \mathbf{h} \quad (2.125)$$

with $\mathbf{h} \equiv h[n]$ being a column vector representing the impulse response, \mathbf{h}^H its conjugate transpose, $\mathbf{y} \equiv y[n]$ the signal at the output of the filter and \mathbf{R}_v the noise covariance matrix, defined as:

$$\mathbf{R}_v = \text{E} \{ \mathbf{v} \mathbf{v}^H \} \quad (2.126)$$

where $\mathbf{v} \equiv v[n]$ is the column vector with representing noise and \mathbf{v}^H is its conjugate transpose.

The other optimization task refers to minimizing the error between the actual and the desired response of the filter to the template. For a k -th sample, it is:

$$\varepsilon_{shape}^2(k) = \{ \text{E}(y_k) - u_k \}^2 = \{ \mathbf{h} [\mathbf{s}(k)]^T - u_k \}^2 \quad (2.127)$$

where y_k and u_k are k -th samples of the actual and the desired response, respectively, and $\mathbf{s}(k)$ denotes an N -element column vector containing a segment of the template ending on sample k .

In addition to the two constraints introduced above, the DPLMS method also allows for imposing specific requirements on the frequency response of the filter – namely its real and imaginary parts. The corresponding error term is then:

$$\begin{aligned}\varepsilon_{freq}^2(f_0) &= [\text{Re}(H(f_0)) - \text{Re}(H_0)]^2 + [\text{Im}(H(f_0)) - \text{Im}(H_0)]^2 = \\ &= \left[\sum_{l=0}^{N-1} h_l \cos(2\pi f_0 T_S l) - \text{Re}(H_0) \right]^2 + \left[\sum_{l=0}^{N-1} h_l \sin(2\pi f_0 T_S l) - \text{Im}(H_0) \right]^2\end{aligned}\quad (2.128)$$

with $H(f_0)$ and H_0 denoting actual and desired frequency response at the frequency f_0 and T_S the sampling period. A special case of Eq. 2.128 occurs for the DC gain of the filter – i.e., for $f_0 = 0$. In such a case, it simplifies to a constraint comparing the integral of the impulse response and the ratio of integrals of the output and the template:

$$\varepsilon_{area}^2 = \left(\sum_{l=0}^{N-1} h[l] - \frac{\sum_{l=0}^{N-1} y[l]}{\sum_{l=0}^{N-1} s[l]} \right)^2 \quad (2.129)$$

A particular case of Eq. 2.129 is related to the pedestal rejection constraint, in which case it simplifies to:

$$\varepsilon_{pedestal}^2 = \left(\sum_{l=0}^{N-1} h[l] \right)^2 \quad (2.130)$$

Finally, the last constraint can be related to the ability of the filter to reject quantization noise – so-called ‘bit gain’ of the filter. The number of bits that is recovered or lost due to application of the FIR filter to the signal is [146]:

$$\text{Bit Gain} = -\log_2 \left(\sum_{l=0}^{N-1} (h[l])^2 \right) \quad (2.131)$$

Consequently, the corresponding error term is:

$$\varepsilon_{bitgain}^2 = \sum_{l=0}^{N-1} (h[l])^2 \quad (2.132)$$

With all the error terms defined, the final cost function supplied to the optimizer is:

$$\varepsilon^2 = \alpha_{var} \varepsilon_{var}^2 + \sum_{k=0}^{N-1} \alpha_{shape}[k] \varepsilon_{shape}^2(k) + \sum_{i=1}^M \alpha_{freq}[i] \varepsilon_{freq}^2(f_i) + \alpha_{area} \varepsilon_{area}^2 + \alpha_{bitgain} \varepsilon_{bitgain}^2 \quad (2.133)$$

Individual error terms were already defined in Eq. 2.125 to Eq. 2.132. The α terms correspond to weights associated with each error term, with α_{shape} being an N -element vector allowing prioritization of selected samples of the desired filter response to the template and α_{freq} an M -element vector that assigns weights to particular frequency constraints.

Example applications using filters synthesized by the DPLMS method, as well as a comparison of their performance against FIR filter calculated by other means, can be found in [140, 148, 150]. When it comes to the selection of parameters of the DPLMS method in terms of optimal weights for the cost function and the filter's response, the author's own experience suggests the following approach:

- A bipolar, zero-average response of the filter to the input signal, with the slope comparable to the fastest slope in the original signal.
- Highest priority to pedestal rejection, then similar priorities to noise minimization and output shape.

One exception to the entirely 'black box' method is the matched filter, which is the filter of choice for the 'detection' problem – i.e., maximization of SNR at the detection time. Since SNR is the only priority, there is an analytical solution to the optimization problem. The well-known formula providing the impulse response of the matched filter is²⁰:

$$\mathbf{h} = \alpha \mathbf{R}_v^{-1} \mathbf{s} \quad (2.134)$$

where α is a real normalization constant. The meaning of \mathbf{h} , \mathbf{s} and \mathbf{R}_v is the same as in the description of the DPLMS method – i.e., impulse response, signal template, and noise covariance matrix, respectively. In order to get a normalized filter response, the value of α should be:

$$\alpha = 1/\sqrt{\mathbf{s}^H \mathbf{R}_v^{-1} \mathbf{s}} \quad (2.135)$$

Apart from pulse detection, it is also possible to use the matched filter for estimating the time of arrival of the pulses, using a method similar to cross-correlation and sinc interpolation. The only difference would be that, rather than calculating the cross-correlation, one evaluates the maximum of convolution of various sub-sample shifts of the impulse with the signal. The advantage of using the filter-based method is that the matched filter maximizes the SNR taking into account the noise properties of the system, whereas the cross-correlation method assumes that the noise is white. Consequently, if the noise is not white – which usually is the case – the SNR of the cross-correlation signal will be inferior to that of the output of the matched filter. Since the timing accuracy depends

²⁰Numerous sources present the derivation of the matched filter in the presence of additive colored noise – for example, see [149] or Wikipedia (https://en.wikipedia.org/wiki/Matched_filter).

on the quality of estimation of the maximum value of either the cross-correlation signal or the filter response, better SNR provided by the filter-based method directly translates into better timing accuracy.

Chapter 3

Compact Scintillating Fiber Tracker for use in Test Beams

3.1 Motivation

The need for building a new small scintillating fiber tracker resulted from one of the projects comprising the planned upgrades related to the second phase of the COMPASS experiment (COMPASS II [151]). COMPASS is a fixed-target experiment situated at the high-intensity M2 beamline of the CERN SPS accelerator. One of the goals of COMPASS II was a measurement of Generalized Parton Distributions (GPD) [152]. In order to achieve it, significant modifications of the experimental apparatus were necessary. One of the most prominent ones involved providing a new 2.5 m long liquid hydrogen target along with associated detectors required to extend the acceptance of the spectrometer¹. One of these was a new 4 m long recoil proton detector (CAMERA), which surrounded the target. Another was a new electromagnetic calorimeter (ECAL0), located right after the CAMERA. Fig. 3.1 shows pictures of the new detectors after installation in the experimental hall.

The ECAL0 is a sampling-type electromagnetic calorimeter that covers particle angles from 5 to 30 degrees and energy range from 0.2 up to 30 GeV. It is composed of Shashlyk-type modules [22, 153]. The module (Fig. 3.2) consists of nine independent channels with a cross-section of 3×3 cm, each made of 109 alternating layers of 0.8 mm lead and 1.5 mm polystyrene scintillator tiles, giving total module thickness of 25.2 cm. Light signal from scintillator tiles is extracted using 16 Bicron BCF91AMC wavelength-shifting fibers ($\varnothing=1.2$ mm), grouped into bundles (each approx. 6.5 mm in diameter) and coupled to Hamamatsu S12572-010 MPPC-type photo-sensors (Multi-Pixel Photon Counters). These are 3×3 mm² devices with pixel density up to 10,000/mm². Since

¹The name COMPASS stands for ‘COmmon Muon Proton Apparatus for Structure and Spectroscopy’. Hence, sometimes the experiment is also called ‘the spectrometer’.



Figure 3.1: New detectors related to the second phase of the COMPASS experiment. *Left:* ECAL0 calorimeter during installation in the hall of the COMPASS experiment (March 2016). *Right:* A four-meter long recoil proton detector (CAMERA) and ECAL0 in final position (still unconnected to acquisition).

the fiber-bundle size is larger than the photosensor size, Winston-cones are used to maximize light collection efficiency. The photosensors are mounted on a copper block equipped with a Peltier-device so that their operating temperature is kept constant at 16°C to 18°C . Thus, the dark rate of MPPCs stays at an acceptable level. The remaining parts of the readout, grouped into the so-called ‘registration unit’, are: a 9-channel front-end amplifier card, a power-supply/slow-control card and a motherboard that connects everything.

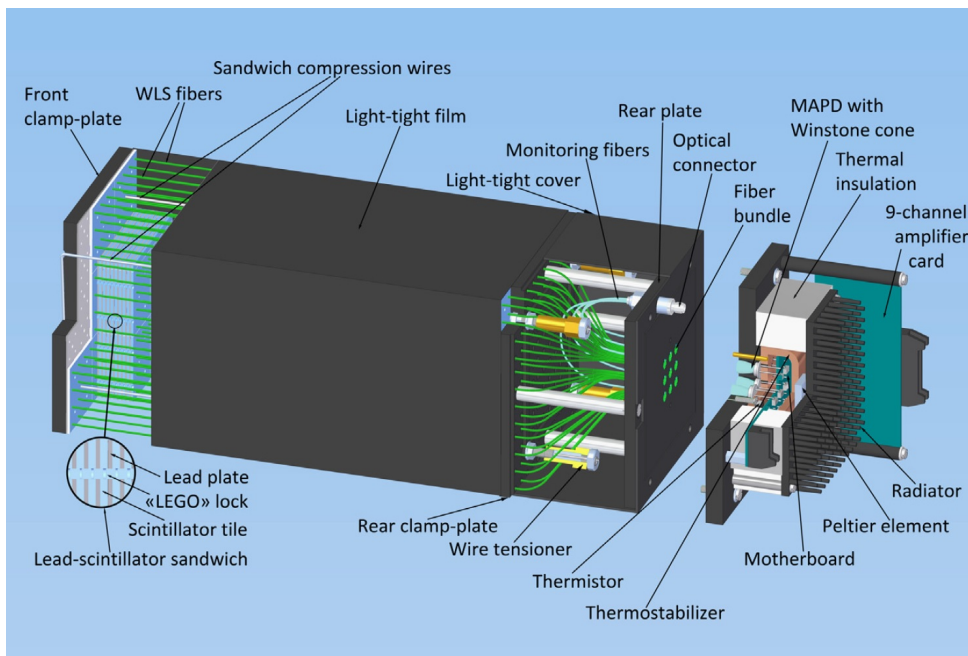


Figure 3.2: Schematic drawing of the Shashlyk-type module of the ECAL0 calorimeter [153].

Since the design of the module was relatively new, especially in terms of photosensors, a series of tests was planned using electron beams with known energies, hitting the

calorimeter at various angles to the axis of the Shashlik module. The goal was to verify linearity, energy resolution, and the ability to reconstruct electromagnetic showers. One of these tests involved placing a 3×3 matrix of Shashlik modules on a remote-controlled 3-axis movable table (Fig. 3.3). The possible movement directions were: horizontal, vertical, and rotation, allowing for precise control of the beam interaction point and orientation of the matrix to the beam axis. These tests were carried out using an electron beam provided by the ELSA accelerator in Bonn [154], with electron energies of 0.8 GeV, 1.6 GeV, and 3.2 GeV.

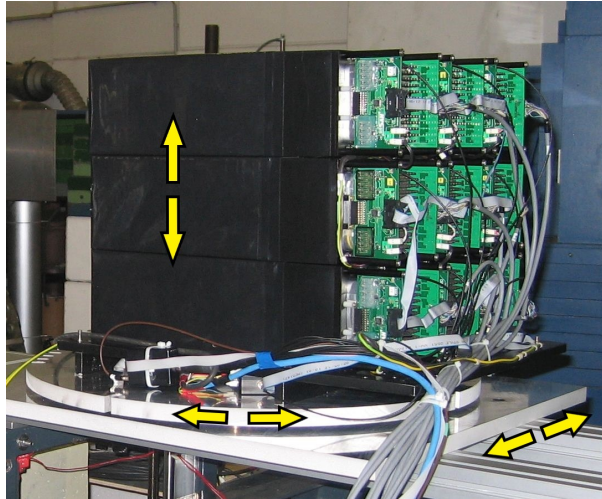


Figure 3.3: A 3×3 matrix of Shashlik modules, placed on a movable 3-axis stand. Yellow arrows mark possible movement directions (horizontal, vertical, rotation).

The ELSA accelerator (ELeCtron Stretcher Accelerator) is a facility located in Bonn, Germany, and operated by the University of Bonn in Nordrhein-Westfalen. It consists of three stages: injector LINACs, a booster synchrotron, and a stretcher ring (Fig. 3.4). It currently houses two running experiments – an upgraded version of the Crystal Barrel [156] and the BGO-OD [157]. Modules of the ECAL0 were tested in the experimental area of the Crystal Barrel experiment. The nominal beam for the Crystal Barrel is a high-intensity photon beam, yet ECAL0 tests required a low-intensity electron beam, $\approx 2 \cdot 10^3$ particles per second. As such, several modifications were required both to the Crystal Barrel detector and to the beamline (Fig. 3.5):

- Crystal Barrel modifications: removal of TAPS, gas Cherenkov detector, and the polarized target system. The latter was necessary to provide an electron beam, as the Crystal Barrel experiment works with a photon beam.
- Beamline modifications: removal of cleaning magnet and collimator system.
- Addition of an evacuated beam pipe through all the remaining parts of the Crystal Barrel, up to the ECAL0 test area, to minimize the number of interactions between

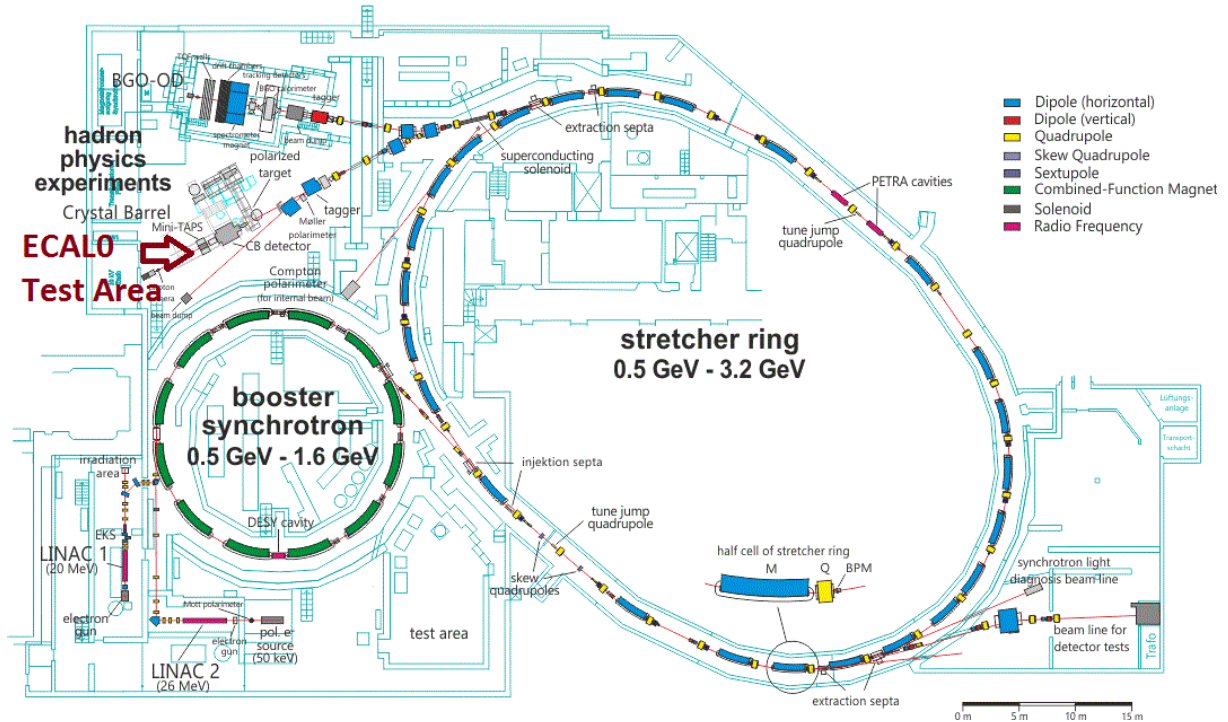


Figure 3.4: Layout of the ELSA in Bonn [155]. Tests of ECAL0 were conducted in the hall of the Crystal Barrel experiment.

electrons and air.

Such modifications, together with the low-intensity of the beam, created a particular challenge related to beam monitoring. Under nominal operating conditions, the final beam tuning is done with a high-intensity photon beam, using monitoring equipment located at the end of the hall (Gamma Intensity Monitor). Once a switch to a low-intensity electron beam would be made, with the calorimeter modules put in the beam, it would no longer be possible to monitor the beam. Since the sole principle of the calorimeter is to measure the energy of interacting particles, it absorbs them – i.e., it ‘eats the beam’. As such, no information would be available neither about the position nor the shape of the beam – one would have to trust the original accelerator tuning done at high intensity. For measurement relying on accurate positioning of the beam interaction point, this would be a risky assumption.

Moreover, removal of selected elements of the Crystal Barrel equipment, necessary to install the evacuated beam pipe, also removed fast scintillation detectors that could otherwise provide a trigger signal. While it would be possible to trigger acquisition using the sum output of the calorimeter modules, the position information would still be lost. Therefore, it was decided to build a new position-sensitive trigger hodoscope, to be put right in front of the ECAL0 modules.

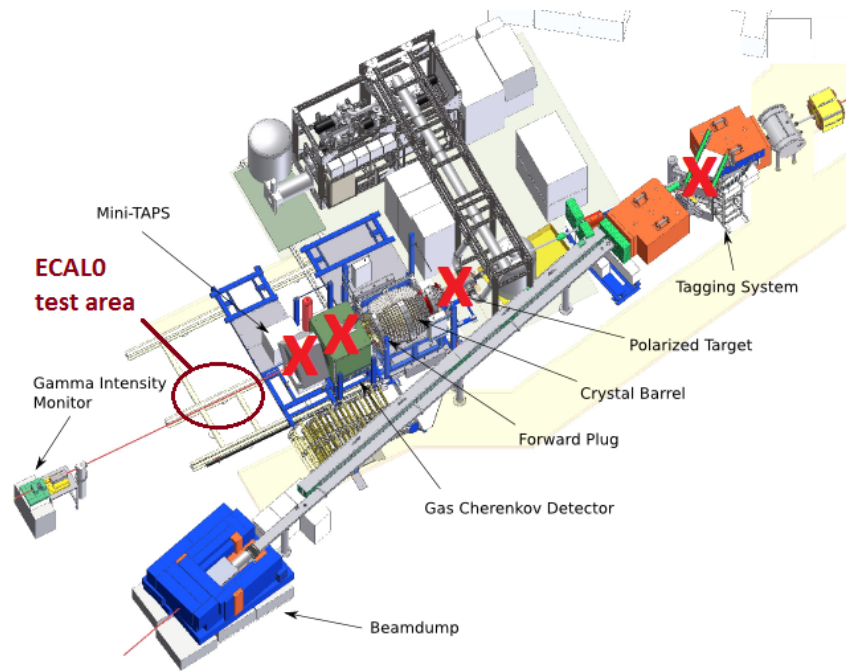


Figure 3.5: Modifications of the Crystal Barrel experimental setup [158] necessary for the ECAL0 tests. Red ‘X’ denotes equipment that was to be removed specifically for the tests.

3.2 Requirements and Concept

Specifics of the planned test setup at ELSA resulted in the following initial set of requirements:

- Two detector planes (X and Y), minimum $1.5 \times 1.5 \text{ cm}^2$ of active area, position resolution of $\approx 0.5 \text{ mm}$ or better.
- Coincidence output of X and Y planes (sum of X with a sum of Y), providing a trigger signal for the data acquisition system. The trigger pulse was to adhere to the NIM standard.
- Multichannel data acquisition system similar to the one used for the ECAL0, i.e., MSADC cards [119], which use 12-bit, 80 MSPS analog-to-digital converters.
- Minimize the mass within the beam to suppress unwanted particle interactions with the detector material. One should note that for physics related to the planned ECAL0 measurements, the hodoscope was a ‘necessary evil’. In essence, it was to produce the trigger signal and to check the beam position, yet it should not affect the beam noticeably. That, of course, is impossible – beam electrons need to interact with the detector, as otherwise there will be no signals at all. The goal was to make these interactions as small as possible so that they would not affect data analysis.

- A relatively relaxed requirement for timing performance of the hodoscope, since a low-intensity beam was expected ($\approx 2 \cdot 10^3$ particles/s).
- Ability to determine the center of the active area through a survey, utilizing a theodolite. It was, therefore, necessary to provide a point for fixing a theodolite target². That point was to have a well-defined position relative to the center of the active area.
- ELSA tests were not the only ones planned for ECAL0, so the hodoscope was to have a compact construction that would allow easy transportation and quick assembly and disassembly at various test sites.
- Finally, a somehow down-to-earth requirement was that everything had to be ready in little under four months, which was the time between agreeing on the above specification and the planned time of the beam test.

The first attempts to formulate the concept of a new detector revealed that it was the last requirement that turned out to be the most crucial one. As such, given tight timing constraints, the whole process of designing and building the detector had to be performed in a way that minimized the risk of failure. The preliminary risk assessment showed that significant risks to the construction process were:

- a) Wrong design decisions, including bad choice of technology used to produce detector elements. In the most severe case, the consequence could have been an unusable system.
- b) Mistakes made during designing or manufacturing a particular component, especially painful in case of mechanical parts. In the worst case, it may have been necessary to redesign or remake particular parts, which usually would be both expensive and time-consuming.
- c) Logistic issues related to the availability of components and tools needed for detector construction. This time the result would have been an inability to complete the project on time.

Minimizing the first risk was achieved by relying on already established and verified technologies, tried in previous projects [24] – not very scientific³, but the only viable option given the circumstances. Reduction of the second risk was possible thanks to

² $\varnothing=10$ mm cylinder, H7 tolerance of outer dimension.

³Nevertheless, the author did participate in the development of some of these technologies, though not for this particular project.

the extensive usage of various CAD tools⁴. A tremendous advantage of this approach was the ability to pinpoint any problems early in the design phase. An equally important convenience was the subsequent streamlined handover of the designs to the manufacturing companies. Finally, using components and tooling that were either already in possession of our team or available on supplier stocks mitigated the third of the risks.

With the above in mind, the design decisions were as follows:

- The detector was to have a round frame with the inner diameter at least 1.5 times greater than the diameter of the beam pipe. After consulting with the ELSA accelerator team, the inner diameter has been fixed at 200 mm. The inside of the frame was to be filled with light material that would act as fiber support. Extruded polystyrene (XPS) has been chosen as support material, since it is cheap, readily available in large quantities⁵, has good-enough mechanical rigidity and satisfactory tolerance to temperature and humidity variations.
- Mounting of the detector to a support structure was to be done using four M8 countersunk screws.
- The relative tolerance of the theodolite target's position to the center of the active area was to be better than ≈ 0.2 mm.
- The active part of the detector was to use fiber mats made of round $\varnothing=1$ mm Kuraray SCSF-78MJ scintillating fibers [32] since both the fibers and the tooling necessary to produce the fiber mats were already available (leftovers from the previous project). The detector was to have two perpendicular planes, 32 channels each, with a pitch of 0.7 mm (hence no dead area between the fibers). The total area of the active part would be 22.7×22.7 mm², in agreement with the requirements.
- In order to apply the principle of 'minimum mass within the beam', the active part of the detector was to have only a single fiber per channel, with the far fiber ends⁶ equipped with mirrors in order to maximize light signal. Furthermore, an opening was foreseen in the fiber support, so that the beam traverses only the fiber mats.
- Each detector plane was to be read out by two 16-channel photomultiplier tubes (Hamamatsu H8711-10), placed at the opposite sides of the fiber mat. Even though it was tempting to try a more innovative approach and use SiPMs, the H8711-10 PMTs were already available, and hence were selected due to time and cost

⁴Computer Aided Design. The two most used tools were Mentor Graphics PADS (electronics design) and Autodesk Inventor (3D mechanical design).

⁵XPS is a standard construction material for civil engineering used for thermal isolation of basements and floors in case they need to support larger weights (for example in garages).

⁶End of the fiber located on the opposite side from the photosensor.

constraints. Nonetheless, these PMTs do exhibit good timing performance – well above the requirements of this project.

- Light signals from the fiber mats, comprising the active area of the detector, were to be transported to the photosensors using the same scintillating fibers used for constructing the mats (i.e., it was decided not to use clear fibers at all). An advantage of this solution was avoiding fiber joints. Measurements done during previous projects⁷ showed that joints do introduce non-negligible attenuation. As such, if the length of the scintillating fibers is short, then getting rid of the joints would still provide lower overall attenuation of the whole optical system, despite inferior transmission properties of the scintillating fibers. On the other hand, the disadvantage of this solution was a potentially higher rate of pulses per channel because the ‘transportation’ part of the fiber was also sensitive to radiation. However, the trigger rate would not be affected, since producing a trigger requires an X-Y coincidence. As such, the only drawback was the higher average anode current of the photomultipliers, but given low expected beam intensity, it did not pose a problem.
- Photomultiplier housings were to be round on the outside, fixed to the frame using rubber O-rings, which would be compressed by the frame (press-fit mounting), thereby ensuring light tightness. As a consequence, it was necessary to provide relatively tight mechanical tolerance of the outer diameter of the housings and the inner diameter of the openings in the frame at the level of approx. 0.1 mm. Furthermore, to facilitate assembly of the PMT housings, the frame has been divided into top and bottom parts.
- No magnetic shielding was foreseen for the PMTs, as the detector would not operate in strong magnetic fields, and H8711-10 photomultipliers do not require shielding from Earth’s magnetic field.
- Initially, it was considered to use 3D-printing technology for manufacturing the frame and the photomultiplier housings. Unfortunately, after enquiring several commercial companies, it turned out that it is impossible to obtain the required 0.1 mm precision – the best offer could guarantee the precision of approx. 0.4 mm. As such, the decision was to produce mechanical parts using machining. The frame was made of Aluminum (PA6), and the outer diameter was set to 280 mm. Type-C black polyacetal (POM-C)⁸ has been selected as the material for the photomultiplier housings. POM-C was appropriate for this application because it is rigid, is well suited for machining, and has excellent properties related to the stability of dimensions due to

⁷Large scintillating fiber tracker that was built for the COMPASS experiment [24].

⁸Other common names of the compound are polyoxymethylene, acetal, polyformaldehyde.

temperature and humidity changes. Furthermore, thanks to its widespread use in the industry, it is affordable and easily available in large quantities, with minimal lead times. Moreover, it is a dielectric, so it prevents too high electric field between the housing and the photocathode of the PMT.

- The PMTs were to be coupled with the fiber mountings using an optical grease, to increase the number of photons reaching the photocathode. The additional photons would mostly travel along helical paths, and without the grease would reflect into the fiber. As such, they would arrive too late to contribute to the formation of the leading edge of the PMT response [23], which for the H8711-10 PMTs is only 835 ps [159]. However, since the pulses would need to be severely bandwidth-limited to be digitized using the 80 MSPS MSADC system, the leading edge would be significantly stretched by the anti-aliasing filter preceding the ADC converter. Consequently, the previously ‘late photons’ would become ‘early photons’ and hence contribute to the amplitude of the shaped pulses, thus increasing the signal to noise ratio.
- All the front-end and trigger electronics were to be mounted on the detector frame, to produce as self-contained system as possible. Each channel was to have signal shaping suitable for MSADC-based readout used by ECAL0, with 2-3 samples at the leading edge. A 4-pole RC low-pass filter was selected to achieve a semi-Gaussian pulse shape. Since the trigger was to use an analog fixed threshold discriminator acting on the sum signal from particular PMTs, a parallel signal path would be provided, without any shaping, to preserve sharp edges of PMT response. The voltages at the trigger output were to adhere to the NIM standard. The signals from the detector were to be transmitted using twisted pair flat cables, while the trigger signal was to use a standard 50-ohm coaxial cable.
- It has been decided not to provide on-board high voltage supplies, as there is an abundance of them in nearly every experimental hall. Instead, independent SHV connectors would be provided for every photomultiplier tube.

Fig. 3.6 presents the resulting detector concept (picture does not show the placement of the electronics modules).

3.3 Concept Validation and Expected Performance

With the primary guidelines concerning the construction of the detector defined, it was advisable to check whether it can provide the required performance. Note that, given the short time to complete the project, only rough estimates were necessary at this stage of

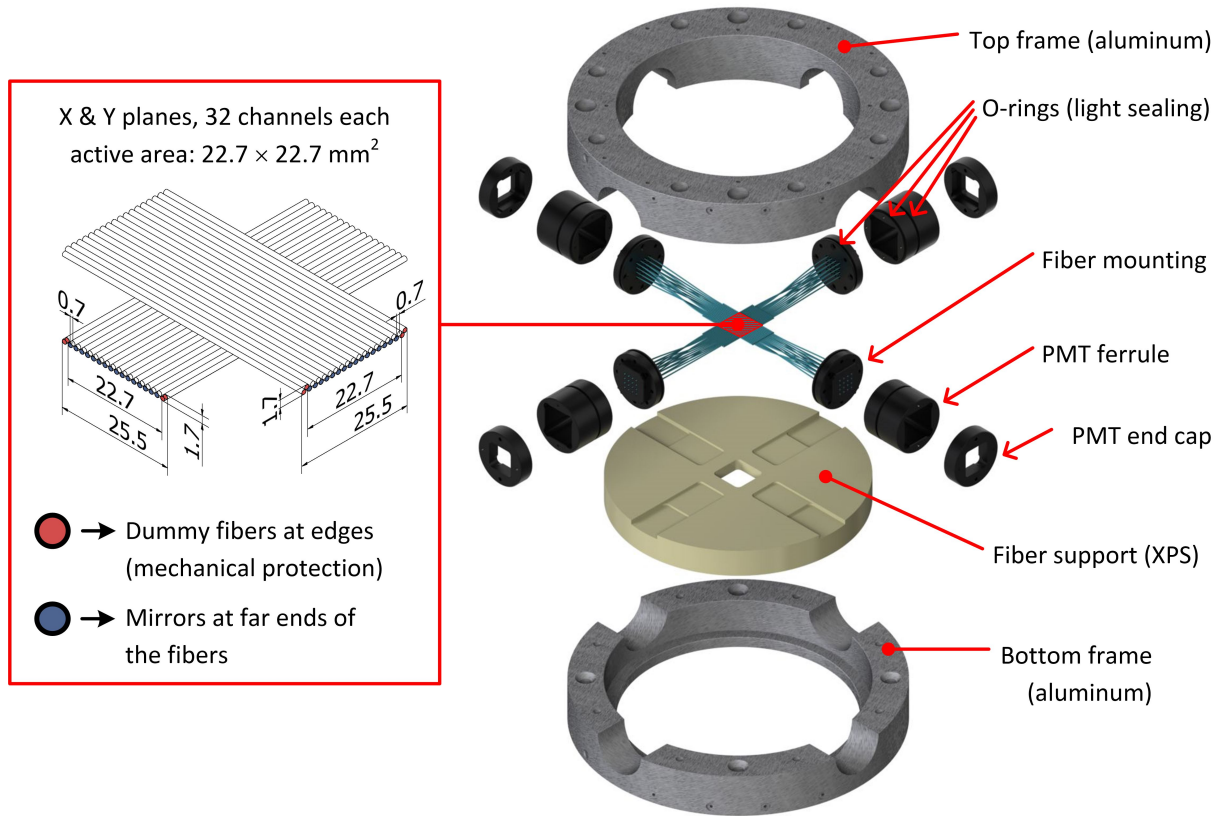


Figure 3.6: Exploded view of a detector concept. The active part consists of two perpendicular detector planes (X&Y), each with 32 channels. Fiber mats are made of $\text{Ø}=1.0 \text{ mm}$ scintillating fibers arranged in a sandwich-type structure (single layer per channel), with 0.7 mm pitch. The readout is done using multichannel photomultiplier tubes, placed in light-tight housings. Everything is housed in a round aluminum frame ($\text{Ø}_{\text{inner}}=200 \text{ mm}$, $\text{Ø}_{\text{outer}}=280 \text{ mm}$).

the design process. So, rather than trying to develop and validate a full detector model, it was decided to adhere to the theory to get the needed numbers. The two main questions were:

- a) Will the signal to noise ratio be sufficiently high to allow for a reasonable value of the threshold. Reasonable meant that, on the one hand, it would be high enough to effectively suppress false hits from noise, on the other that it would be low enough to avoid missing hits from particles.
- b) The timing resolution should allow for accurate triggering. Given expected low intensities, the main requirement was to ensure that the pulses occur at more-or-less similar samples within the event buffers of the MSADC cards. The buffer length for a single event was 32 samples. As such, an arbitrary requirement of 3σ accuracy roughly equal to half a sample. This way, analysis of the data would be simpler, as one could define fixed integration windows on a per-channel basis. With the sampling clock of 12.5 ns ($F_S = 80 \text{ MSPS}$), this meant that σ_{time} should not

exceed ≈ 2 ns. With such a precision and beam intensities at the level of $2 \cdot 10^3$ particles per second, associating hits with events would not pose any problem.

The first step in an attempt to get an engineering estimate of the detector's performance was to determine the number of photons exiting the fiber. The prerequisite to doing that was to calculate the average Landau-Vavilov-Bichsel most probable energy loss $\overline{\Delta p}$ of the traversing particle, using Eq. 2.21. In the case of the planned test at ELSA, the particles of interest were 800 MeV, 1.6 GeV, and 3.2 GeV electrons. Given the presence of logarithmic terms in Eq. 2.21, the easiest way to do this was a numerical evaluation, using simple geometrical relationships to calculate the track length of the particle within the fiber. Fig. 3.7 shows the result of these calculations, along with the calculated average $\overline{\Delta p}$, under the assumption of uniform distributions of particle tracks along the direction perpendicular to the fiber axis. Note that the value of the diameter used for the calculation was $\varnothing = 0.88$ mm rather than $\varnothing = 1.0$ mm, as both claddings do not contain scintillating dopants. Not surprisingly (see flat lines for $\Delta p/(\rho x)$ in Fig. 2.5), the differences in the value of the $\overline{\Delta p}$ are negligible among the particles planned for the test, so that one could use a single average of 101 keV:

$$\overline{\Delta p} = 101 \text{ keV} \quad (3.1)$$

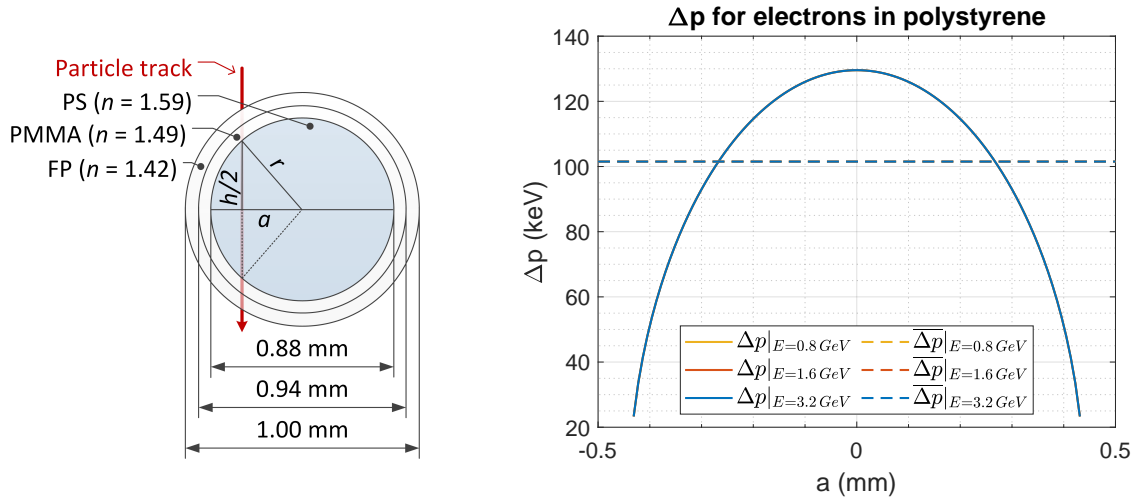


Figure 3.7: *Left:* Geometrical relationships and fiber dimensions used for the numerical calculation of the Landau-Vavilov-Bichsel most probable energy loss (Δp). *Right:* Solid lines show numerical calculations of Δp as a function of the distance from the fiber center a , for a fiber with a diameter of $\varnothing = 1.0$ mm and different particle energies. The dashed lines represent average Δp assuming uniform distributions of particle tracks. The plot shows only one visible color since due to overlapping curves for different energies – consequently, a single mean $\overline{\Delta p}$ of approx. 101 keV can be used for the whole energy range of interest.

The number of photons corresponding to the calculated average $\overline{\Delta p}$ is provided by Eq. 2.22. Assuming that, in polystyrene, one photon requires approx. 120 eV of deposited

energy, we get:

$$N_0 = \Delta p \frac{dn_\gamma}{dE} = \frac{101 \times 10^3}{120} \cong 846 \quad (3.2)$$

The trapping efficiency is given by Eq. 2.25. Since the refractive indices depend on the wavelength of light, one can use the manufacturer's datasheet [32] to determine the peak wavelength for the type and length of the fibers used in the detector. In our case, the length is approx. 15 cm, the peak in the emission spectrum is around 440 nm. Consequently, from tabulated data of refractive indices, one gets $n_{co} = 1.615$ for the polystyrene and $n_{cl} = 1.42$ for the fluorinated polymer (the outer cladding), so the trapping efficiency is:

$$\varepsilon_{br} = \frac{1}{2} \left(1 - \frac{n_{cl}}{n_{co}} \right) = \frac{1}{2} \left(1 - \frac{1.42}{1.615} \right) \cong 6.0\% \quad (3.3)$$

The corresponding critical angle for the total internal reflection is (Eq. 2.26):

$$\theta_{crit} = \arccos(n_{cl}/n_{co}) = \arccos \left(\frac{1.42}{1.615} \right) \cong 28.5^\circ \quad (3.4)$$

Since the fiber is too short, it is forbidden to use the meridional approximation of the attenuation length. So, one way to go would be to assume worse than real conditions and see if things work out – i.e., if the signal will be high enough with longer fibers, then it certainly will not be worse in case of shorter fibers. Note that even in case of a non-negligible fraction of skewed rays arriving at significantly delayed times compared to the ‘early’ photons, there would be no harm, as it is the leading edge of the pulse that is crucial for timing applications. Long pulse tails will also not cause problems due to the low expected average particle rate.

The minimum fiber length allowing the use of meridional approximation requires fulfilling the criterion of $L_F/\Lambda_m \leq 0.2$ (L_F is fiber length, Λ_m is the meridional approximation of the attenuation length). Assuming similar values of the bulk absorption length and the reflection coefficient as in section 2.3 (i.e., $\Lambda_{bulk} = 3$ m and $q = 0.99999$) and neglecting different attenuation of the outer cladding, Eq. 2.35 gives the following meridional estimate of the attenuation length:

$$\Lambda_m = \frac{\cos \theta_{crit}}{1/\Lambda_{bulk} + (1-q)(\sin \theta_{crit})/2r} = \frac{0.8793}{\frac{1}{3} + \frac{0.4763 \times 10^{-5}}{0.94 \times 10^{-3}}} \cong 2.6 \quad (\text{m}) \quad (3.5)$$

Assuming the minimum fiber length of $0.2 \times 2.6 = 0.52$ m, $\Lambda_{eff} = 0.86 \times 3 = 2.58$ m and reflectance of the mirror equal to 0.9, Eq. 2.36 yields the following expected light output of the fiber:

$$N_{ph} = (1 + 0.9)N_0 \varepsilon_{br} e^{-L_F/\Lambda_{eff}} = 1.9 \times 846 \times 0.06 \times e^{-0.52/2.58} \cong 79 \quad (3.6)$$

If we violate the requirement of $L_F/\Lambda_m \leq 0.2$ and nonetheless use Eq. 2.36 with the actual fiber length, and also use the effective attenuation length provided by the manufacturer

of the SCSF-78MJ fibers ($\Lambda_{eff} = 4 \text{ m}$ – see datasheet [32]), then we get:

$$N_{ph} = (1 + 0.9)N_0 \varepsilon_{br} e^{-L_F/\Lambda_{eff}} = 1.9 \times 846 \times 0.06 \times e^{-0.15/4} \cong 93 \quad (3.7)$$

The real value is somewhere in between.

The next step was to estimate the effects of the coupling. Since we already had the Loctite 8104 silicone grease at stock in our lab, it was natural to use it. Loctite 8104 is a translucent lubricant suitable for plastic components, based on silicone oil and silica gel. Its datasheet does not provide the exact value of its refractive index. However, based on its composition [160], it could be estimated [72, 161] to be around 1.4 to 1.5 – which was suitable for this application, given findings presented in section 2.4. The translucency of the grease should not pose a problem since a relatively thin layer would be present between the fiber mounting and the window of the PMT, so its attenuation should have been negligible. Consequently, again assuming a worst-case scenario, with light output of the fiber defined by Eq. 3.6 and the refractive index of the grease n_e equal to 1.4, which is a bit far from the optimum predicted by Eq. 2.57 for polystyrene ($n_{co} = 1.615$) and borosilicate glass ($n_{glass} = 1.517$), the amount of photons reaching the photocathode is:

$$\begin{aligned} N_{ph,pmt} &= N_{ph} T_{12} = N_{ph} \frac{16 n_{co} n_{glass} n_e^2}{(n_{co} + n_e)^2 \cdot (n_{glass} + n_e)^2} = \\ &= 79 \times \frac{16 \times 1.615 \times 1.517 \times 1.4^2}{(1.615 + 1.4)^2 \times (1.517 + 1.4)^2} = 79 \times 0.9944 \cong 78.6 \quad (3.8) \end{aligned}$$

with T_{12} defined by Eq. 2.54. The above equations does not account for the fact that some rays travel through the inner cladding, but given the calculated transmission coefficient it is hardly meaningful. One might argue that Eq. 2.54 is valid for normal incidence only, which is not the case for almost all rays propagated through the fiber. Nonetheless, a quick look at Fig. 2.18 reveals that for angles of incidence characteristic to ‘bound rays’ only⁹ (i.e., those below θ_{crit}) the transmission is nearly constant. Out of curiosity, it was worth to check the scenario with no grease (i.e., $n_e = n_{air} = 1.0$), in which case $N_{ph,pmt}$ would be:

$$\begin{aligned} N_{ph,pmt} &= N_{ph} T_{12} = N_{ph} \frac{16 n_{co} n_{glass} n_{air}^2}{(n_{co} + n_{air})^2 \cdot (n_{glass} + n_{air})^2} = \\ &= 79 \times \frac{16 \times 1.615 \times 1.517 \times 1^2}{(1.615 + 1)^2 \times (1.517 + 1)^2} = 79 \times 0.9081 \cong 71.7 \quad (3.9) \end{aligned}$$

Knowing the number of photons impinging upon the photocathode, one could calculate the parameters of the PMT response. The following information was available from the datasheet of H8711-10 PMT [159]:

⁹The reason for not accounting for significantly skewed rays traveling with angles of incidence above θ_{crit} was justified in section 2.3

- The quantum efficiency at 440 nm is approx. 22%. For the sake of our calculations, let us assume that this value is a combination of the quantum efficiency and the collection efficiency (i.e., $\eta\alpha = 0.22$ – see Eq. 2.67).
- The electron gain at a nominal supply voltage is $G = 0.9 \times 10^6$.
- The rise time of the response is 835 ps, and the fall time is 2047 ps, with FWHM equal to 1658 ps.

Therefore, the average number of photoelectrons is:

$$\bar{N}_{phe} = \alpha \eta \bar{N}_{ph} = 0.22 \times 78.6 \cong 17.3 \quad (3.10)$$

The above corresponds to the following average charge of the anode pulse:

$$\bar{q} = G e N_{phe} = 0.9 \times 10^6 \times 1.6 \times 10^{-19} \times 17.3 \cong 2.49 \times 10^{-12} \quad (C) \quad (3.11)$$

Assuming that the photoemission from the fiber is a Poisson process and that the average secondary emission coefficient of each dynode is approximately six (i.e., $\delta \approx 6$), the resulting signal to noise ratio at the anode output is (Eq. 2.67):

$$SNR_{anode} = \sqrt{\frac{\bar{N}_{phe}}{\frac{\delta}{\delta-1}}} = \sqrt{\frac{17.3}{6/5}} \cong 3.80 \quad (3.12)$$

Consequently, the expected standard deviation of charge at the anode output is:

$$\bar{\sigma}_q = \frac{\bar{q}}{SNR_{anode}} = \frac{2.49 \times 10^{-12}}{3.80} \cong 0.65 \times 10^{-12} \quad (C) \quad (3.13)$$

Given asymmetric edges of the PMT response, it was modeled with the exponentially modified Gaussian function (Eq. 2.90). Fig. 3.8 shows the waveform from the datasheet compared the one predicted by the model, whereas Table 3.1 lists the parameters of the model.

Parameter	Value	Unit
C	7.9465×10^{-5}	A
λ	1.1021	ns ⁻¹
μ_1	0	ns
σ_1	0.4268	ns
A_1	7.7883×10^{-5}	A

Table 3.1: Values of parameters of the function used to model single photoelectron response of H8711-10 PMT. The modeled waveform had the following properties: $t_{rise} = 0.83$ ns, $t_{fall} = 2.05$ ns amplitude of ≈ 78 μ A.

Knowing the parameterization of the PMT response as well as the average number of photoelectrons, it was possible to estimate the waveform corresponding to the response

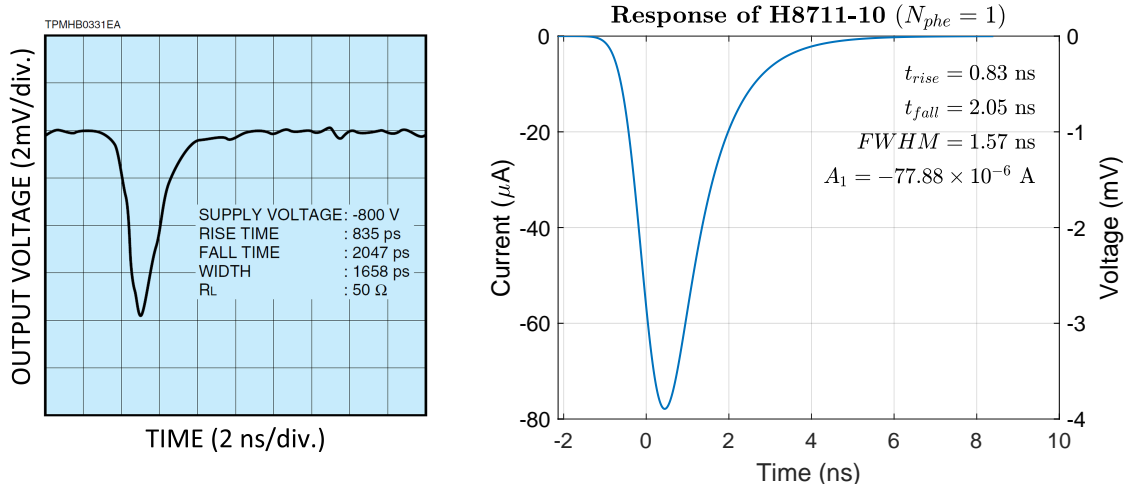


Figure 3.8: *Left*: Example PMT response provided in the datasheet of H8711-10 [159]. *Right*: Model of a single photoelectron response parameterized with an exponentially modified Gaussian function (Eq. 2.90), $t_{rise} = 0.83$ ns and $t_{fall} = 2.05$ ns. The values are provided for PMT gain equal to $G = 0.9 \times 10^6$ and load resistance $R_L = 50\Omega$.

of the whole detector by convolving normalized time responses related to each of the elements. Doing that required accounting for the decay constant of the scintillator, the transit time spread (TTS) of the PMT, and the time spread of photons due to varying lengths through the fiber.

The decay constant was available in manufacturer's datasheet [32] and for SCSF-78MJ it is $\tau_{decay} = 2.8$ ns. Consequently, time spread due to scintillator decay time constant was:

$$x_{decay}(t) = e^{-\frac{t}{\tau_{decay}}} \quad (3.14)$$

Next, a Gaussian function models the TTS of the PMT with relatively good accuracy. Finally, the following reasoning can be applied to deduce the time distribution due to differences in photon paths.

The relationship between the photon path and the propagation angle is defined in Eq. 2.33 – we will repeat it here for the sake of clarity, slightly changing notation:

$$L(\theta) = \frac{L_F}{\cos \theta} \quad (3.15)$$

where L_F denoting the fiber length. Since the source of light is isotropic, the probability of occurrence of particular angle of propagation is proportional to the circumference of a circle with a radius given by $\tan \theta$:

$$p(\theta) = \frac{1}{\int_0^{\theta_{crit}} \tan \theta_1 d\theta_1} \tan \theta \quad (3.16)$$

Consequently, one can easily achieve the desired time response by plotting $p(\theta)$ while

neglecting normalization and substituting θ with $L^{-1}(l)$:

$$L^{-1}(l) = \arccos\left(\frac{L_F}{l}\right) \quad (3.17)$$

$$x(t) = \tan \left[\arccos \left(\frac{L_F}{t c / n_{co}} \right) \right] \quad (3.18)$$

where c is speed of light in vacuum and n_{co} is the refractive index of the core. Fig. 3.9 presents this method applied to the case of the planned detector.

In order to get a rough estimate of the amplitude walk error at the trigger output, one can apply a technique with modeling the leading edge of the pulse with a Gaussian, matched in terms of rise time with the exponentially modified Gaussian that represents response of the system – as described in section 2.6. Fig. 3.10 presents the achieved model of the the response to the average number of photoelectrons, based on the final waveform $x_4(t)$ presented in Fig. 3.9. The parameters of the model are presented in Table 3.2

Parameter	Value	Unit
C	4.1348×10^{-4}	A
λ	0.3314	ns ⁻¹
μ_1	0	ns
σ_1	0.6201	ns
A_1	5.6010×10^{-4}	A
μ_2	0.8996	ns
σ_2	0.7901	ns
α_q	0.4447	

Table 3.2: Values of parameters of the function used to model the response of the detector. The properties of the resulting waveform are: $t_{rise} = 1.31$ ns, $t_{fall} = 6.53$ ns and amplitude of ≈ 560 μ A. The table also provides parameterization of the Gaussian used to estimate the effects of the walk error (A_1 , μ_2 and σ_2).

With known parameters of the model, it was finally possible to estimate the amplitude walk error. Setting the threshold to ≈ 2.5 photoelectrons seemed a reasonable choice – it was still relatively low compared to the average amplitude of the signal, while it already provided significant suppression of the random hits from the dark rate of the PMT. Assuming the load resistance of $R_L = 50$ Ω and the PMT gain of $G = 0.9 \times 10^6$, the resulting threshold voltage is $v_{thr} \cong 4$ mV. Substituting appropriate values into Eq. 2.94, i.e.: \bar{q} and $\bar{\sigma}_q$ from Eq. 3.11 and Eq. 3.13, respectively, α_q and c from Table 3.2,

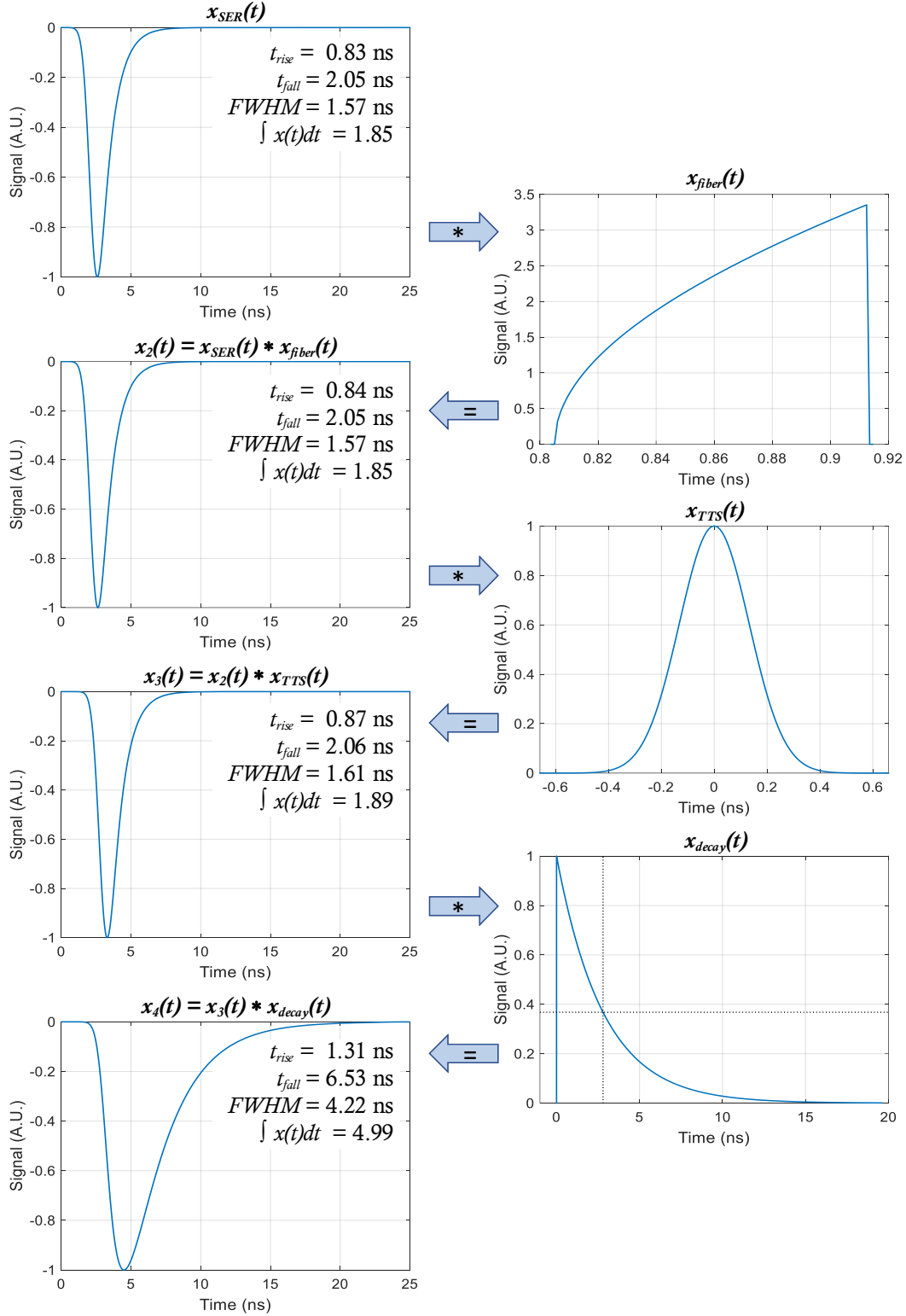


Figure 3.9: Calculation of response of the system using multiple convolutions of normalized time responses of particular elements of the system. x_{SER} is the single photoelectron response of the PMT. x_{fiber} is the result of time dispersion due to differences in lengths of photon paths, for a 15 cm fiber. x_{TTS} models transit time spread of the PMT. x_{decay} models the time dispersion due to the decay time constant of the scintillator used in the fiber's core. $x_4(t)$ is the shape of the final response of the system.

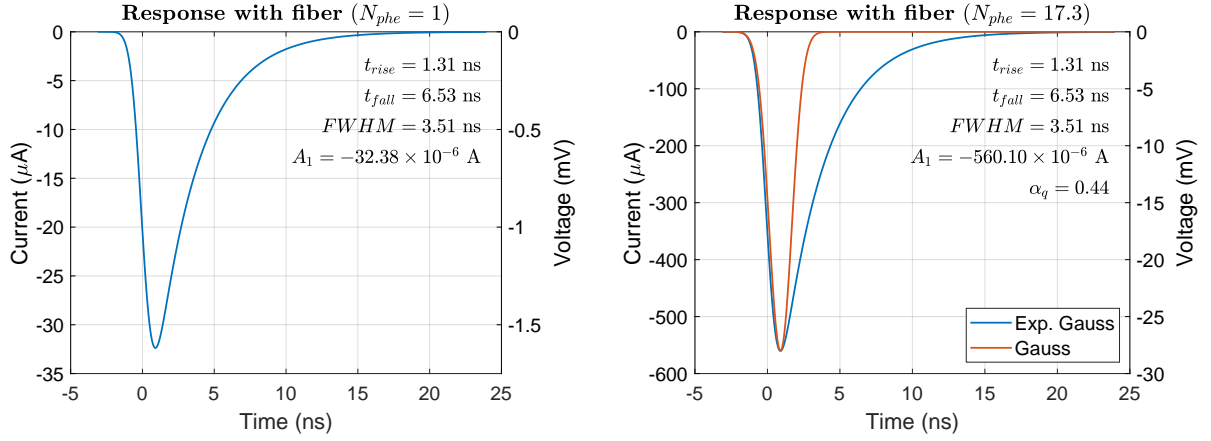


Figure 3.10: Model of response from the whole detector. *Left*: Pulse shape projected to a single photoelectron response, useful for calculating the threshold corresponding to certain number of photoelectrons. *Right*: Blue curve shows parameterization of response for the expected average number of photoelectrons. An exponentially modified Gaussian function was used (Eq. 2.90), matched to have $t_{rise} = 1.31$ ns and $t_{fall} = 6.53$ ns. The values are provided for PMT gain equal to $G = 0.9 \times 10^6$ load resistance $R_L = 50\Omega$ and an average of 17.3 photoelectrons. The orange curve show the Gaussian used for estimating the time walk.

with $c = \sigma_2$, one gets:

$$\begin{aligned}
 \bar{\sigma}_{walk} &= \frac{\sigma_2}{\bar{q} \sqrt{2 \ln \left(\frac{R_L \alpha_q \bar{q}}{\sqrt{2\pi} v_{thr} \sigma_2} \right)}} \bar{\sigma}_q = \\
 &= \frac{0.7901 \times 10^{-9}}{2.49 \times 10^{-12} \times \sqrt{2 \ln \left(\frac{50 \times 0.4447 \times 2.49 \times 10^{-12}}{\sqrt{2\pi} \times 4 \times 10^{-3} \times 0.7901 \times 10^{-9}} \right)}} \times 0.65 \times 10^{-12} \cong 105 \times 10^{-12} \quad (\text{s})
 \end{aligned} \tag{3.19}$$

Noting that the t_{rise} represents the 10% to 90% rise time and taking into account the predicted current pulse amplitude for an average number of photoelectrons equal to $A_1 \cong 0.56$ mA, one can translate the above error into RMS current noise:

$$\bar{\sigma}_{walk,i} = \frac{0.8 A_1}{t_{rise}} \bar{\sigma}_{walk} = \frac{0.8 \times 0.56 \times 10^{-3}}{1.31 \times 10^{-9}} \times 105 \times 10^{-12} \cong 36 \times 10^{-6} \quad (\text{A}) \tag{3.20}$$

The corresponding RMS voltage noise on a 50Ω load is then:

$$\bar{\sigma}_{walk,v} = R_L \bar{\sigma}_{walk,i} \cong 1.8 \quad (\text{mV}) \tag{3.21}$$

Consequently, it was determined that the remaining parts of the signal path of the trigger chain should have at most comparable noise levels, so that the ‘walk effect’ remains the dominant source of errors. Note that one could relax this restriction, as given the chosen limit for the overall time resolution of $\sigma_{time} \leq 2$ ns, there is plenty of headroom to move the threshold higher. However, considerable charge fluctuation at the expected

signal levels meant that moving the threshold too high would result in loss of efficiency, as the pulses on the low-charge tail of the distribution would not produce sufficiently high signals. Since the design of the front-end electronics circuits was not ready at this stage, it was not possible to verify whether the noise requirements are met. Nonetheless, the 1.8 mV RMS noise was well within limits of standard design using commercial components, so it was concluded that there is no danger from this side.

A final step in the concept verification stage was related to estimation of timing accuracy achievable from the sampled signals – as those would be used in the analysis of the calorimeter data to correlate hits from the hodoscope with the hits in the calorimeter. The desired rise time defined in the requirements (section 3.2) was approx. 2.5 samples:

$$t_{r,out} = 2.5 T_S = 2.5 \times 12.5 = 31.25 \quad (\text{ns}) \quad (3.22)$$

According to [119], the MSADC system used for ECAL2 (ECAL0 uses the same cards) has a 12-bit ADC working at 80 MSPS, which is implemented by two ADS5270 converters working in interleaved mode [162]. The datasheet of ADS5270 [163] gives the typical value of SINAD as 70 dBFS, with full scale voltage defined as 2.03 V. According to Eq. 2.101, the equivalent RMS voltage noise is:

$$\sigma_{n,adc} = \frac{V_{PP}}{2\sqrt{2} \times 10^{\frac{SINAD}{20}}} = \frac{2.03}{2\sqrt{2} \times 10^{\frac{70}{20}}} \cong 0.23 \times 10^{-3} \quad (\text{V}) \quad (3.23)$$

Now, assuming that the ADC noise is uncorrelated¹⁰ and one intends to use the digital constant fraction algorithm defined in [164] with an inverted waveform gain of two, the fluctuation of each sample of the bipolar waveform used to detect the zero-crossing point is (Eq. 2.114):

$$\overline{\sigma_{n,b}} = \sqrt{\frac{2(1+a^2)}{3}} \sigma_{n,adc} = \sqrt{\frac{2(1+4)}{3}} \times 0.23 \times 10^{-3} \cong 0.42 \times 10^{-3} \quad (\text{V}) \quad (3.24)$$

The second quantity needed for estimation of the timing resolution provided by the digital constant fraction algorithm (Eq. 2.115) is the slope of the analog signal. Knowing that the intention was to use a 4-th order RC low-pass shaping with equal stages, the transmittance of a the shaper is:

$$H(s) = \frac{k_u}{(1+s\tau)^n} = \frac{k_u}{(1+s\tau)^4} \quad (3.25)$$

with k_u representing the gain. Consequently, the impulse response will be:

$$h(t) = \mathcal{L}^{-1}(H(s)) = k_u \frac{\tau^n}{(n-1)!} t^{n-1} e^{-t/\tau} = k_u \frac{\tau^4}{6} t^3 e^{-t/\tau} \quad (3.26)$$

¹⁰Note that at this stage the front-end circuits were not designed, so it was impossible to include their noise contribution – hence only ADC noise was used in the calculations.

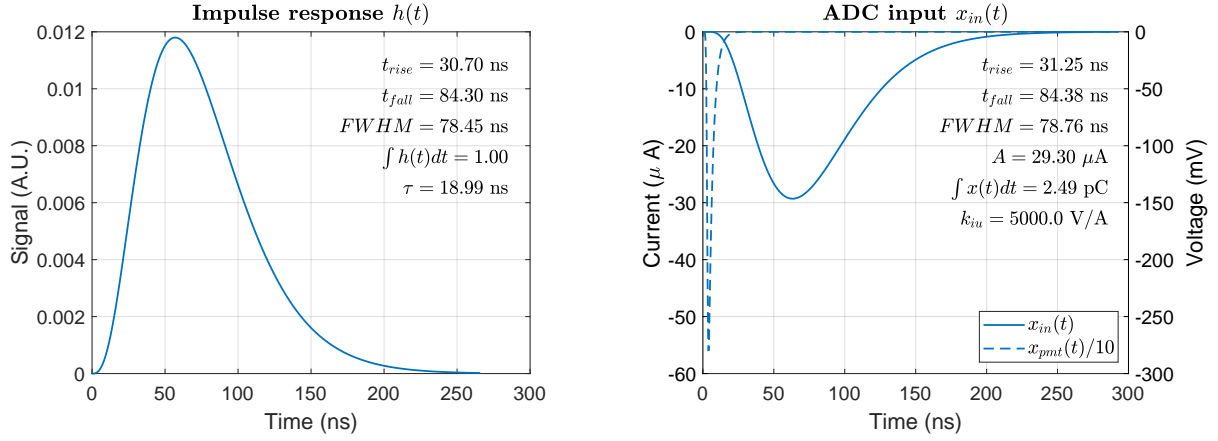


Figure 3.11: *Left*: Impulse response of the shaper, tuned so that the rise time at the output equals approx. 2.5 samples (i.e. 31.25 ns). *Right*: Expected average signal at the input of the ADC, assuming average number of photoelectrons $N_{phe} = 17.3$. Transimpedance gain of the shaper was arbitrarily assumed as $k_{iu} = 5000V/A$.

Therefore, average an waveform reaching the ADCs is:

$$x_{in}(t) = x_{pmt}(t) * h(t) \quad (3.27)$$

with $x_{pmt}(t)$ representing the signal from the PMT (bottom left plot in Fig. 3.10) and $h(t)$ the output of the shaper. The easiest way to get the shape of $x_{in}(t)$ with the desired 10%-90% rise time is to again use numerical calculation. Left plot of Fig. 3.11 presents results of this calculation. Once $x_{in}(t)$ is known, the only remaining step is to match the integral with the charge corresponding to the PMT gain and the average number of photoelectrons, thus arriving at the waveform of the signal reaching the ADC. Note that since PMT is a current source, the actual voltage will depend on the transimpedance gain of the shaper. Taking all the above into account, one can finally calculate the slope of the signal :

$$\left. \frac{dx_{in}}{dt} \right|_{t_{zero}} = \frac{0.8 k_{iu} A}{t_{r,out}} = k_{iu} \frac{0.8 \times 29.30 \times 10^{-6}}{31.25 \times 10^{-9}} \cong k_{iu} \times 750 \quad (V/s) \quad (3.28)$$

with k_{iu} representing the passband transimpedance gain of the shaping circuit. Thus, assuming that the delay of the digital constant fraction discriminator algorithm is such that the slope of bipolar waveform is similar to the slope of the original signal, the final timing resolution becomes (Eq. 2.115):

$$\overline{\sigma_{time,n}} = \frac{\overline{\sigma_{n,b}}}{(dx_{in}/dt|_{t_{zero}})} = \frac{0.42 \times 10^{-3}}{k_{iu} \times 750} \cong \frac{1}{k_{iu}} \times 0.56 \times 10^{-6} \quad (s) \quad (3.29)$$

Since the gain of the shaping circuits was not known, as they were not yet designed, then rather than providing the value of the timing resolution one could define the minimum

passband transimpedance gain of the shaper that would allow meeting the requirement of the overall $\sigma_{time} \leq 2$ ns:

$$k_{iu} \geq \frac{0.56 \times 10^{-6}}{2 \times 10^{-9}} \Rightarrow k_{iu} \geq 280 \quad (3.30)$$

Again, one can see that the requirement was reasonable, but should also notice that the noise estimate did not account for the front-end circuit nor any extra clock jitter that might have been present in the MSADC cards.

One last element that deserved consideration was the contribution of the TTS of the PMT. Using value of 300 ps from the datasheet of H8711-10 photomultiplier tube and taking the average signal level of 17.3 photoelectrons, it was:

$$\sigma_{tts} = \frac{300 \times 10^{-12}}{2.35 \times \sqrt{17.3}} \cong 30.7 \times 10^{-12} \quad (\text{s}) \quad (3.31)$$

Since the above number is small, the contribution of the TTS to the overall timing resolution of the system was deemed insignificant compared to the uncertainties related to the amplitude walk or the ADC noise.

Given the fact that the presented analysis did not reveal any design faults that could render the detector unsuitable for the planned application, it was decided to commence with the construction process.

3.4 Planning and Schedule

Usually, building a scintillating fiber detector is preceded by relatively long research, which aims at optimizing the technology to be used during the actual construction of the detector. The design and manufacturing phases start once this research produces a satisfactory outcome. Furthermore, given the prototype-like nature of such projects, it is not uncommon to face unforeseen difficulties during either of the above stages of the project, leading to a necessity for additional investigations. Fortunately, the author's group already built a similar type of detector for the COMPASS experiment at CERN¹¹. Hence, most of the technologies were already there and required only minor adjustments related to the small size of the new detector. More importantly, there was an in-house experience in using them. Since the theoretical analysis presented in section 3.3 did not reveal any show-stoppers, then, given demanding time constraints of the project, it was possible to jump straight to the detector design phase.

¹¹The project aimed to develop technologies for and subsequently manufacture a large scintillating fiber tracker consisting of two fiber planes. Each plane had 196 channels, with four fiber layers per channel – a total of eight layers in a sandwich-type configuration. The project was very successful – the detector has been working flawlessly for over ten years and is still used by the experiment. More details can be found in [24].

A two-people team conducted most of the work¹², with all the activities grouped into the following general categories:

- a) Design and the subsequent manufacturing of the mechanical structure of the detector, including additional tools that were required to produce the detector.
- b) Design, manufacturing, and testing of the electronics.
- c) Refurbishment of the tools used for the production of the mats.
- d) Production of fiber mats, including all the preparatory work needed for fibers.
- e) Integration of the whole detector, i.e., mounting of fibers into photosensor housings, final assembly of all the mechanical parts and electronics.
- f) Commissioning of the new system, including tests with a radioactive source to see whether everything works as expected.

Fig. 3.12 shows the actual schedule of the project. Wherever possible, the work was done simultaneously, with some of the above steps significantly intertwined – mainly a) and b), as the mechanics needed to accommodate the electronics, and it was necessary to reflect mounting of the circuit boards in the design of the frame.

3.5 Building the Detector

3.5.1 Preparation of Scintillating Fibers

The very first step in constructing a brand new scintillating fiber detector was to prepare far ends of scintillating fibers. After cutting to the desired length, the fibers were polished using Struers LaboPol-5 grinding machine (Fig. 3.13b) and water-resistant sandpapers of various grit sizes (see Table 3.3). A specially prepared tool (Fig. 3.13a) ensured the perpendicularity of the polished fiber ends to their axis. It consisted of two machined pieces made of type-C polyacetal. The choice of material was relevant since it needed to be more resistant to abrasive materials than the fibers. This way, the polishing of multiple batches of fibers introduced negligible skew to the polished surface, thereby significantly reducing the number of times that re-machining of the tool was necessary to de-skew it. The bottom part of the polishing tool had machined grooves that allowed placing several fibers and maintained perpendicularity of their axes to the polished surface, while the

¹²Two people participated in this project, with occasional minor help from other team members. The author's role was the coordination of the whole project, design of detector's mechanics and various assembly tools, manufacturing of fiber mats, and finally, all the subsequent data analysis. All the work related to providing electronics circuits was done by the co-worker, while the integration of the detector was a shared effort.

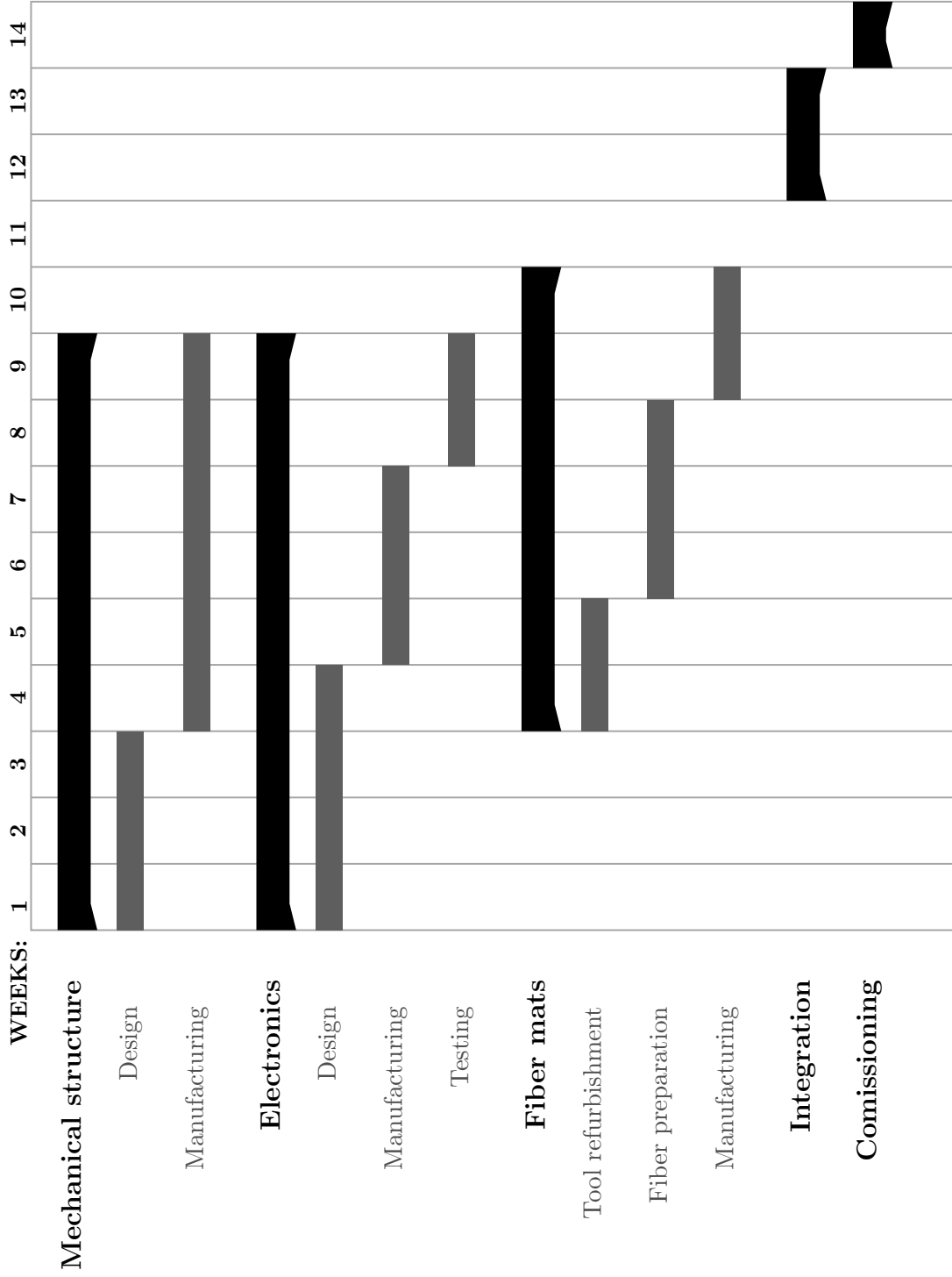


Figure 3.12: Actual schedule of the project. The break in week 11 was for Christmas.

Abrasive	Grit Size	Grinder speed [rpm]	Operation
Sandpaper	P500	100	Flattening
Sandpaper	P1200	180	Coarse polishing
Sandpaper	P2400	350	Fine polishing
Sandpaper	P4000	500	Fine polishing
Diamond paste	1 μm	—	Final polishing

Table 3.3: Polishing steps applied during the preparation of far ends of scintillating fibers. Sandpaper grit sizes are specified according to ISO 6344 standard [165].

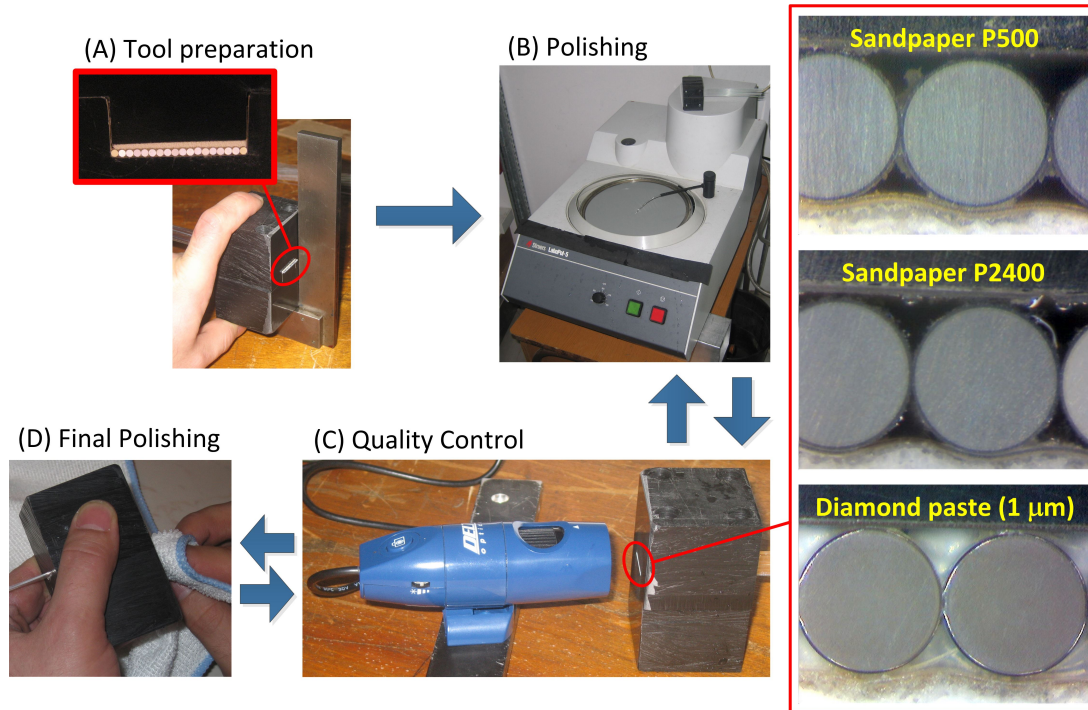


Figure 3.13: Polishing of far ends of scintillating fibers, with arrows showing the flow of operations. (A) Tool used to hold fibers during polishing. A set of four screws squeezed the top and bottom parts (made of polyacetal), while fibers were pressed onto the bottom part by an elastic foam. The alignment was controlled using a try square. (B) Polishing machine – see table 3.3 for specification of polishing steps. (C) Quality control using a digital microscope. (D) Final polishing using a micro-fiber cleaning cloth and a diamond paste.

role of the top part was to keep the fibers in place. A set of four screws squeezed both parts together. A layer of foam attached to the top part of the tool prevented potential damage to the fibers due to squeezing. The alignment of top and bottom parts, as well as perpendicularity of the polished surface, was checked using a precise try square. Quality of the polishing was checked using a digital microscope – a Delta Optical unit with a 1.3-megapixel camera (Fig. 3.13c). Final polishing was done using a micro-fiber cloth and a diamond paste with a grit size of 1 μm (Fig. 3.13d).

Once polished, the fibers were cleaned of any residues using an ultrasonic cleaner – first

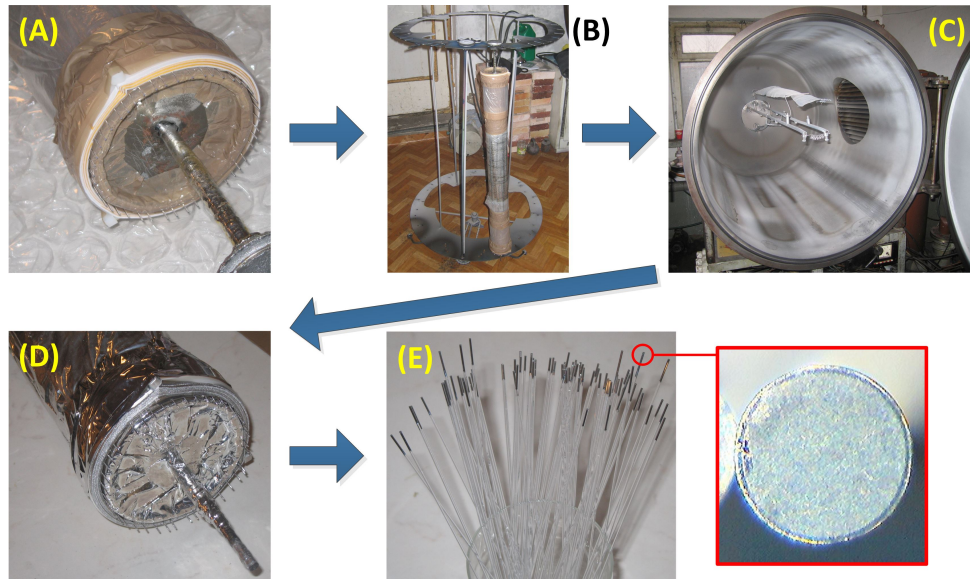


Figure 3.14: Application of mirrors at far ends of scintillating fibers. (A) Fibers protected by several layers of foam mounted on a rod used by the vacuum chamber. (B) Rod with fibers prepared for insertion into the vacuum chamber. (C) Vacuum chamber used during aluminum evaporation. (D) Rod with fibers, after application of aluminum via the vacuum evaporation process. (E) Fibers with mirrors at the ends.

with distilled water to remove any debris from the diamond paste (it was water-soluble), then with isopropyl alcohol to remove any fat or fingerprints. Later, mirrors were applied to the far ends of the fibers, via vacuum evaporation of aluminum (Fig. 3.14). Since the whole process was done at an external workshop, a non-trivial issue arose related to the preparation of fibers to facilitate their placement into the available vacuum chamber (Fig. 3.14c). Successful application of mirrors required fulfillment of two conditions:

- a) The constant movement of the fibers during the vacuum evaporation process so that thickness of aluminum deposition was as uniform as possible.
- b) Preventing potential damage to the fibers due to transportation or their handling by the personnel of the external workshop.

As such, it was decided to lend a rod dedicated to the vacuum chamber and attach fibers to it (Figs. 3.14a, 3.14b). Since the shape of the rod was not very ‘fiber friendly’, as it had a non-uniform surface, multiple layers of foam were used to protect the fibers. Furthermore, since mirrors were to be applied only at fiber ends, a layer of foil was used to cover most of their surface. Figs. 3.14d, 3.14e show the final results of application of the aluminium layer.

3.5.2 Fiber Mats

The next step after completion of mirrors was the manufacturing of fiber mats, which would later be used to create the active area of the detector. Each mat was to consist of thirty-two round 1 mm Kuraray SCSF-78MJ multi-cladding scintillating fibers. Fiber pitch was to be 0.7 mm, and a single fiber per channel was foreseen. As such, a sandwich-type structure has been manufactured, made of two fiber layers, with each layer having its fibers placed at a pitch of 1.4 mm (Fig. 3.15). An advantage of such an arrangement of fibers was good rigidity of the mat. Furthermore, in order to prevent damage to scintillating fibers that could occur during mat production or its subsequent handling, dummy fibers were added to the outer edges of each fiber layer. This way, each mat provided an active area that was 22.7 mm wide, and the total mat width was 25.5 mm.

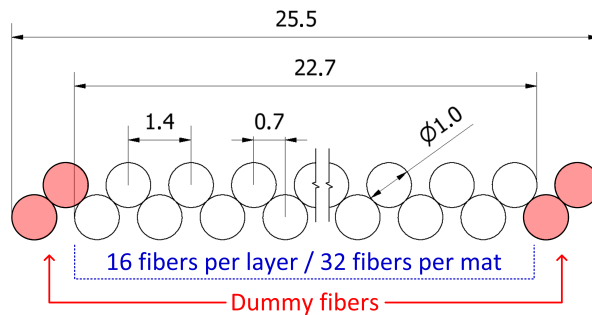


Figure 3.15: Cross-section of a fiber mat of each detector plane. Each mat is composed of two fiber layers in a sandwich-type configuration. Each layer has sixteen scintillating fiber and a single dummy fiber at each edge, added for mechanical protection.

When it came to the production of fiber mats, it has been decided to use the same technology that was used by our team during the construction of a large scintillating fiber tracker for the COMPASS experiment at CERN. The main reasons for this choice were as follows:

- The technology had already proven itself, as high-quality fiber mats were already produced, and their long-term performance was confirmed.
- The significant experience was already available in using this technology, so all the potential pitfalls were known.
- All the tooling was already available.

A conceptual drawing illustrating the adopted technology of fiber mat production is shown in Fig 3.16. The mats were produced based on a layer-by-layer principle. Epoxy glue was chosen to bond the fibers together, as it did not change its dimensions during curing – thus preventing mat deformations. Fiber alignment was ensured by a tool consisting of two identical jigs, which had precisely machined trapezoidal grooves every 1.4 mm, which

corresponded to fiber pitch foreseen for each layer. The first fiber layer would use the bottom jig as a fiber guide, while every consecutive layer would be guided by the inter-fiber grooves of the previous layer. Achieving the above required equipping the top jig with a layer of $\varnothing=1.0$ mm steel rods, which ‘simulated’ the next layer during curing of the glue. Each production step involved aligning the fibers using either the bottom jig or the previous mat layer, followed by the application of the glue, and finally, the top jig was pressed onto everything, thus ensuring the proper position of the fibers and at the same time removing excessive glue. Two side panels assured jig alignment, and thin polyethylene foil prevented any jig contamination.

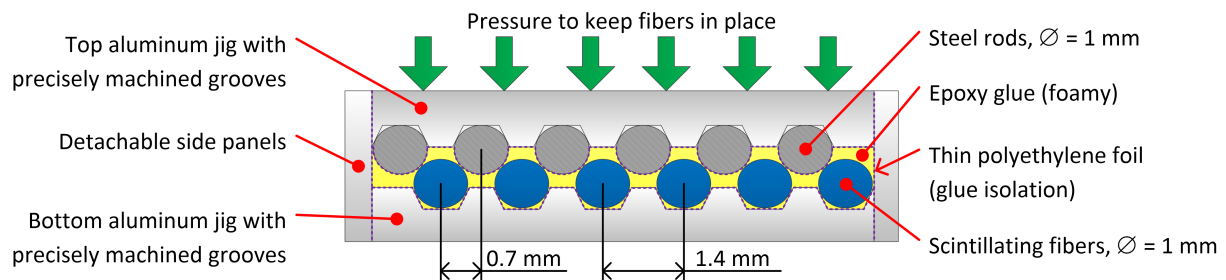


Figure 3.16: Conceptual drawing of a tool used to glue fiber mats. Two identical jigs with precisely machined grooves were used. The top jig was equipped with $\varnothing=1.0$ mm steel rods. The fibers were aligned using the bottom jig and pressed using the top jig. Steel rods from the top jig form grooves serving as a guide for the next fiber layer. The jigs were aligned using side panels. Thin polyethylene foil prevented jig contamination with the glue.

Fig. 3.17 presents the actual implementation of the above method. At first, all the metal elements (i.e., jigs, side panels, and a front panel) were covered with standard, commercially available $50\ \mu\text{m}$ polyethylene foil, nominally used for paint-masking. The foil was self-adhesive, which turned out to be extremely useful, as it ensured firm attachment of the foil to the covered surfaces and prevented any unwanted folds. Next, side panels were attached to the bottom jig, followed by squeezing both jigs together using screws, with steel rods in place of fibers. Such a configuration was necessary to push the foil into the grooves and to attach the front panel properly – its grooves would later need to match the alignment of the second layer. Then, fibers were laid out in the grooves of the bottom jig and were kept in place using positioning bars with machined grooves matching the grooves of the jig (Fig. 3.17a). Bottom parts of the positioning bars were made from PTFE¹³, which allowed for easy cleaning thanks to poor adhesion of epoxy glues to the PTFE. Since the jigs were originally designed for a much wider mat, it was possible to produce all fiber layers at once – the jig had 98 grooves whereas only 72 were needed (4×18 fibers). However, given the fragility of a single fiber layer, additional steel rods

¹³Polytetrafluoroethylene. A commonly used trade name is ‘Teflon’.

were added at the sides of each layer to facilitate handling during subsequent operations. After securing the fibers in their nominal grooves, the top jig was placed onto them, and the positioning bars were shifted forward. At this point, epoxy glue was applied, and the top jig was gently slid forward, with the positioning bars removed one by one (Fig. 3.17b). Previously attached front panel prevented fiber movement, which would be inevitable due to small friction between fibers and the foil covering the top jig. Once the glued section of the fibers was fully covered, everything was left until the glue has hardened (Fig 3.17c). Later on, produced fiber layers were inspected visually for proper fiber alignment and any fiber damage. The damage check was done by using a strong light source to illuminate fibers from their mirror-free end. This way, should there be any cracks or scratches, they would be visible, as they would emit light. At the same time, it was relatively easy to verify the proper application of mirrors, as no light should come out of the far ends of the scintillating fibers. Fig. 3.17d shows that one can easily distinguish dummy fibers at the edges of each layer, while fibers with applied aluminum layer remain dark. Afterward, fiber mats were made by gluing the fibers layers together (Fig. 3.17e). This time, proper positioning of the fibers was ensured using positioning bars, which were aligned using screws. Finally, after the glue had cured, steel rods were removed from the mats using a sharp knife (as well as any glue remaining at the edges). There was no risk of damage to the scintillating fibers, as there were dummy fibers at the borders of each mat, added specifically for that purpose. Fig. 3.17f presents a ready detector mat, before removal of the steel rods.

3.5.3 Photomultiplier Housings

The primary role of light-tight housing for the photomultipliers was to provide good optical coupling between the fibers and the photo-sensors. Additionally, since multi-channel photomultipliers were chosen for this application, it was necessary to ensure the alignment of the fibers with correct regions of the photocathode (as the region of the photocathode determined the PMT channel that would register the signal).

The housing consists of three elements made from machined type-C polyacetal: a fiber mounting, a ferrule and an end cap (Fig. 3.18, right). The fibers were to be attached to the mounting using epoxy glue, and subsequently, the surface facing the PMT was to be flattened and polished. Then, the mounting and the ferrule would be screwed together, while the end cap was to move along the guides freely. This way, the photomultiplier could be gently pushed towards the fibers, using springs placed at the end of the guides (with nuts used to lock the springs). Black PVC tape would provide light sealing of the space between the ferrule and the end cap.

At this point, a remark should be made concerning the design of the mounting

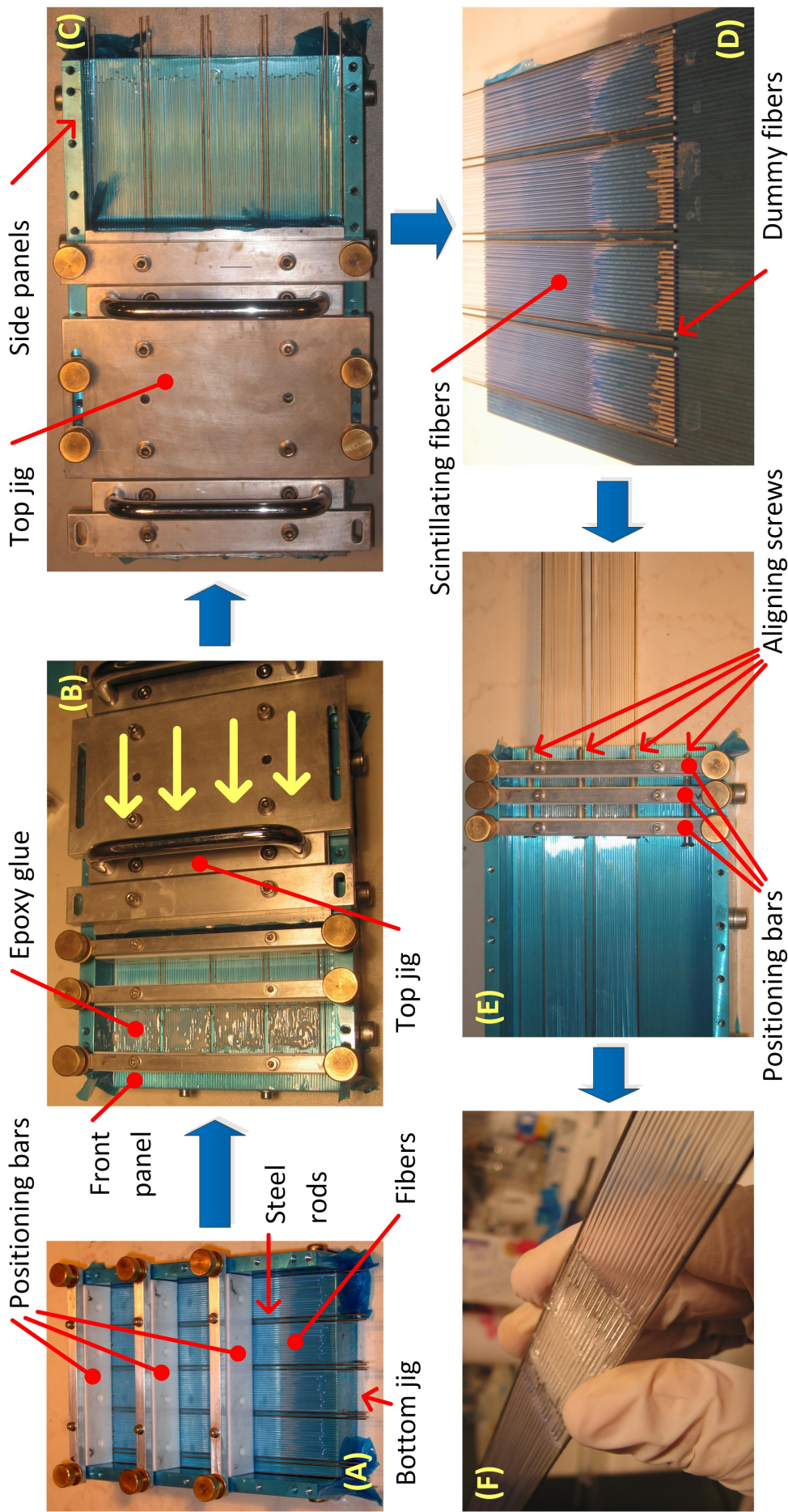


Figure 3.17: Manufacturing of fiber mats. (A) The fibers are aligned using the bottom jig and are kept in place using positioning bars. Steel rods at the sides facilitate subsequent mat handling. (B) Application of epoxy glue. The top jig placed on top of fibers and is gently slid onto the glued section, while the positioning bars are removed one by one. The front panel prevents fiber movement. (C) Top jig in 'glue hardening' position. (D) Glued fiber mats illuminated from the back. Dummy fibers are easily identifiable, as they have no mirrors. (E) Gluing of two fiber layers into a mat. The layers are pressed onto each other by positioning bars aligned with screws. (F) Ready fiber mat. Steel rods will be subsequently removed with a knife.

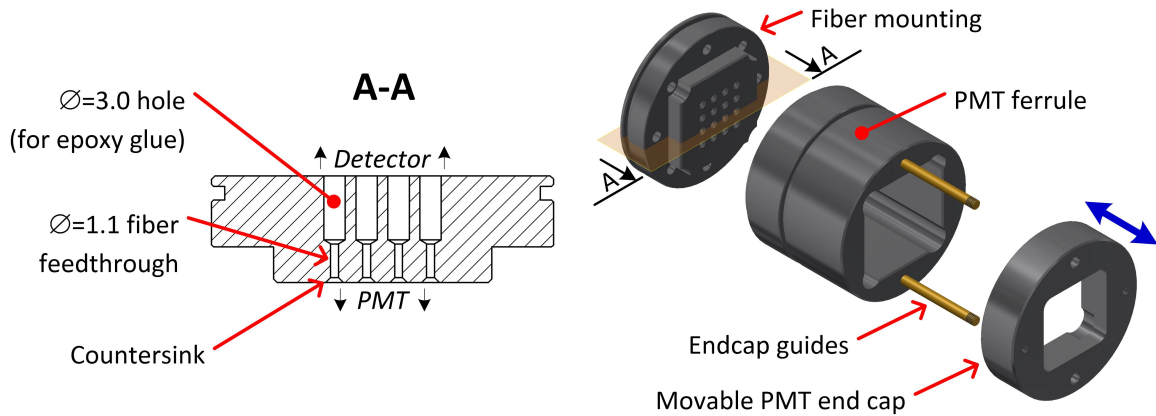


Figure 3.18: Left: Cross-section of fiber mounting. All dimensions are in mm. Right: Conceptual drawing of photomultiplier housing. Fiber mounting and PMT ferrule are screwed together, whereas PMT end cap can freely move alongside the guides.

(Fig. 3.18, left). The tolerance of fiber dimensions provided in the datasheets was 2% for round fibers [32], so the theoretical maximum fiber diameter (3σ level) was expected to be at most 1.06 mm. Therefore, it was decided to make $\text{Ø}=1.1$ mm fiber feed-throughs – wide enough to accommodate almost any fiber and at the same time sufficiently small to prevent too much fiber tilt. In order to facilitate glue application, the detector-side part of the feed-through was made with a larger diameter of $\text{Ø}=3.0$ mm, hence allowing for easy glue penetration into the hole. Since polyacetal is generally considered as a difficult-to-bond material, then producing bonds with sufficient strength requires enlarging their area. One way of achieving this is to use various abrasives or apply various primers, which create a kind of microporous structure by chemical etching. The other is to increase physical dimensions of the bonded parts – and this approach was adopted by this project, as there was plenty of space available. Tensile strength tests of a fiber-to-POM bond (with an area similar to the one foreseen for the actual fiber mounting) showed that the adhesion to both POM and an outer cladding of the fiber is satisfactory. Nonetheless, additional countersinks were machined at the PMT-side of the mounting, and it was decided to apply glue at both sides of the mounting. Therefore, should the glue detach from the mounting, the fiber would still be held in place – purely due to the shape of the cured glue at both sides of the feed-through. One might ask, what is the chance that the glue will not detach from the fibers rather than the mounting? The answer is that good adhesion of the epoxy glue to the outer cladding of the fibers was confirmed during the author’s past projects [24, 25], as well as various other projects described in the literature, for example, [3, 7, 12].

One of the requirements for the detector (see section 3.2) was decent accuracy of positioning of the active area relative to the geometrical center of the frame, on the order of ≈ 0.5 mm. That, in turn, meant that gluing of the fibers with the mountings needed

to be done in the final configuration of the involved parts. In the best-case scenario, this method would almost guarantee that the fiber mats would stay in the proper position even without any support, purely because no stress would be applied to the fibers. Therefore, it was decided that the glue will be applied after the pre-assembling of the detector so that the fiber mountings and the PMT ferrules would be in their nominal positions. An additional tool was developed to keep fiber mats in the center of the detector at the height that matched the height of the fiber support. The tool consisted of a precisely machined cross with four square vertical bars that ensured alignment of fiber mats. A metal plate with a layer of foam was pressed from the top, thus immobilizing the mats. The concept of the method is shown in Fig. 3.19.

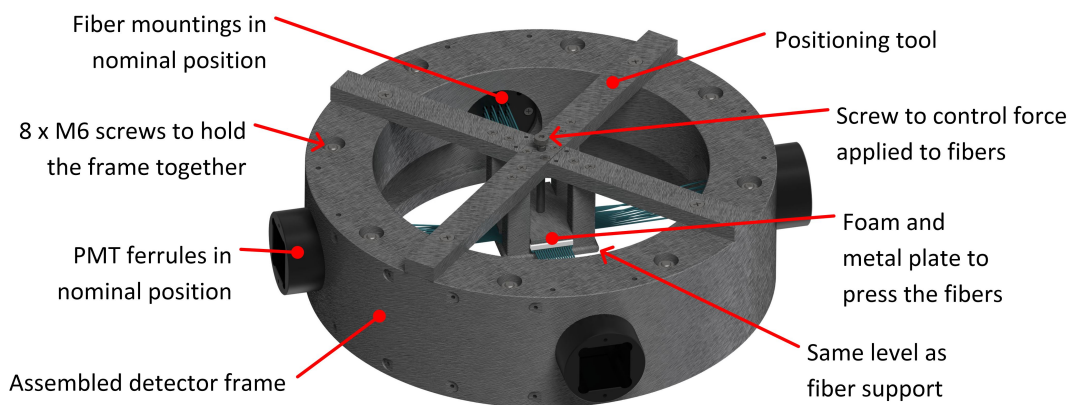


Figure 3.19: Conceptual drawing of detector configuration foreseen for gluing fiber mountings. Special positioning tool was used to keep fiber mats in their nominal position (i.e., same as if they were put on support). Fiber mountings and photomultiplier ferrules were also in their nominal positions. The detector frame is in the final configuration, with top and bottom parts kept together using eight M6 screws.

One thing should be noted here – the detector was to be portable, which meant that it had to withstand frequent transportation. Consequently, it would face frequent ambient temperature changes. Moreover, the temperatures at various experimental halls also vary a lot. All in all, the allowable temperature range of $-10\text{ }^{\circ}\text{C}$ to $50\text{ }^{\circ}\text{C}$ seemed like a reasonable assumption. Various mechanical handbooks report that the linear thermal expansion coefficient of aluminum is $22.2 \times 10^{-6}\text{ m/m}\cdot\text{K}$, whereas that of general-purpose polystyrene is $70.0 \times 10^{-6}\text{ m/m}\cdot\text{K}$. Given a round frame with $\text{\O}_{\text{inner}}=200\text{ mm}$ and $\Delta T=60\text{ }^{\circ}\text{C}$, a rough calculation yields an approx. 0.6 mm difference between elongation or contraction of the fibers compared to that of the frame. Unfortunately, it was difficult to estimate similar difference due to humidity changes, as material datasheets specify water absorption coefficient according to the ISO 62 standard [166], and therefore report this value in terms of weight rather than dimension changes (various manufacturers specify this value between 0.2% to 0.4% for 24-hour immersion). As such, there was a risk that fibers may experience significant stress due to environmental conditions, which could potentially

lead to the formation of crack. The consequences could be catastrophic, as the light transmission of the fibers might be ruined, rendering the detector useless. To prevent this, the spatial configuration of the fibers provided a slight bend on the way from the mat to the mounting. Thus, slight changes of mat-to-mounting distance would result in changing fiber radius, and the forces exerted on the fibers would be much smaller than in the case of using straight sections (Fig. 3.20).

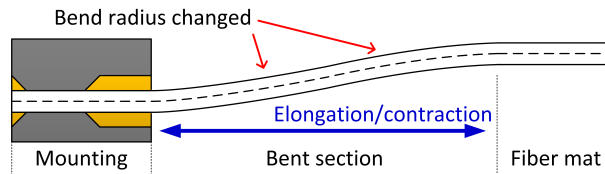


Figure 3.20: Idea behind fiber arrangement that prevents too much stress due to thermally induced contraction or elongation of the fibers.

The actual preparation of photomultiplier housings is shown in Fig. 3.21. First, the fiber mats were put in the positioning tool. Next, the frame, the fiber mounting, and PMT ferrules were assembled. Then, the positioning tool with the fibers was accurately aligned with the frame and subsequently fixed to it. Afterward, the fibers were placed in the feed-throughs in the mountings. After that, the glue was applied to each mounting, using a syringe with a needle-type applicator. Before application, the vacuum oven was used to slightly heat and degas the glue, which decreased its viscosity, shortened curing time, and prevented air bubbles. The mountings were glued one at a time, with the detector put in vertical position – so that the gravity could do its job and nicely keep the glue inside the holes (Fig. 3.21a). Later, once the glue cured, the fiber mountings were removed from the frame, and the glue was applied to their other side (the one facing the PMT). Next, each assembly (i.e., a fiber mat with glued mountings) was prepared for polishing. Steel threaded brace rods were used to reinforce them (Fig. 3.21c), as the mountings were too heavy to be supported by the fibers only. Since the polished surface was relatively small, an additional metal piece was used to increase the overall surface (Fig. 3.21b), which had the following benefits:

- It tightened the threaded brace rods to the polished part firmly.
- It facilitated the polishing process – the boundaries of the polished surface were matched to the edges of the mounting.
- The skew of the polished surface was significantly reduced since metal's resistance to abrasion was higher than that of polyacetal.

The polishing process (Fig. 3.21d) was similar to the one used for preparing fibers (see table 3.3), with the quality control once again done using a digital microscope. Finally,

after confirming satisfactory polish quality, the mountings were assembled with the ferrules using screws, and rubber o-rings were placed in their designated grooves (Fig. 3.21e). This step concluded all the preparatory work related to mechanical and optical parts of the detector.

3.5.4 Electronics

The primary tasks of the front-end electronics include:

- Providing high voltage (HV) for the photomultipliers.
- Stretching the PMTs signals so that they can be recorded using 80 MSPS analog-to-digital converters (MSADC cards developed for the ECAL0 calorimeter).
- Converting single-ended PMT signals into differential form, suitable for transmission via unshielded twisted pair flat cables (120Ω characteristic impedance).
- Producing a trigger signal (NIM standard, output to 50Ω coaxial cable).

Given the widespread availability of HV supplies in nearly any high energy physics laboratory, it was decided to only provide a panel with SHV connectors, rather than generating the HV locally. The added benefit of this approach was the ability to move the power supplies further away from the beam, thus minimizing any risk related to insufficient radiation hardness of the used units. Furthermore, since Hamamatsu Photonics H8711-10 are, in fact, photomultiplier tube assemblies – i.e., they consist of both the R7600-M16 tube and the associated voltage divider – it was sufficient to limit HV-related functionality to distribution only.

Adjusting the signals for 80 MSPS sampling was achieved by equipping each channel with a four-pole RC shaper (Fig. 3.22, top). The peaking time of the output pulse was ≈ 40 ns, providing around 2.5 samples at the leading edge – matching requirements set out in section 3.2. The 1-st stage of the shaper is a transimpedance amplifier attached directly to the anode pin of the photomultiplier. The remaining stages were: a passive RC circuit, an active single pole low pass filter, which also provided single-ended to differential conversion and finally a passive differential RC circuit. The time constants of particular stages were tuned experimentally to achieve the desired rise time at the output of the shaper. Note that they are slightly different from ≈ 19 ns calculated during the concept validation stage (left plot in Fig. 3.11).

The trigger chain consists of summing amplifiers, leading-edge discriminators, a logic AND gate, a re-triggerable monostable multivibrator, and a CMOS-to-NIM level shifter (Fig. 3.22, bottom). The operation of the circuitry is as follows:

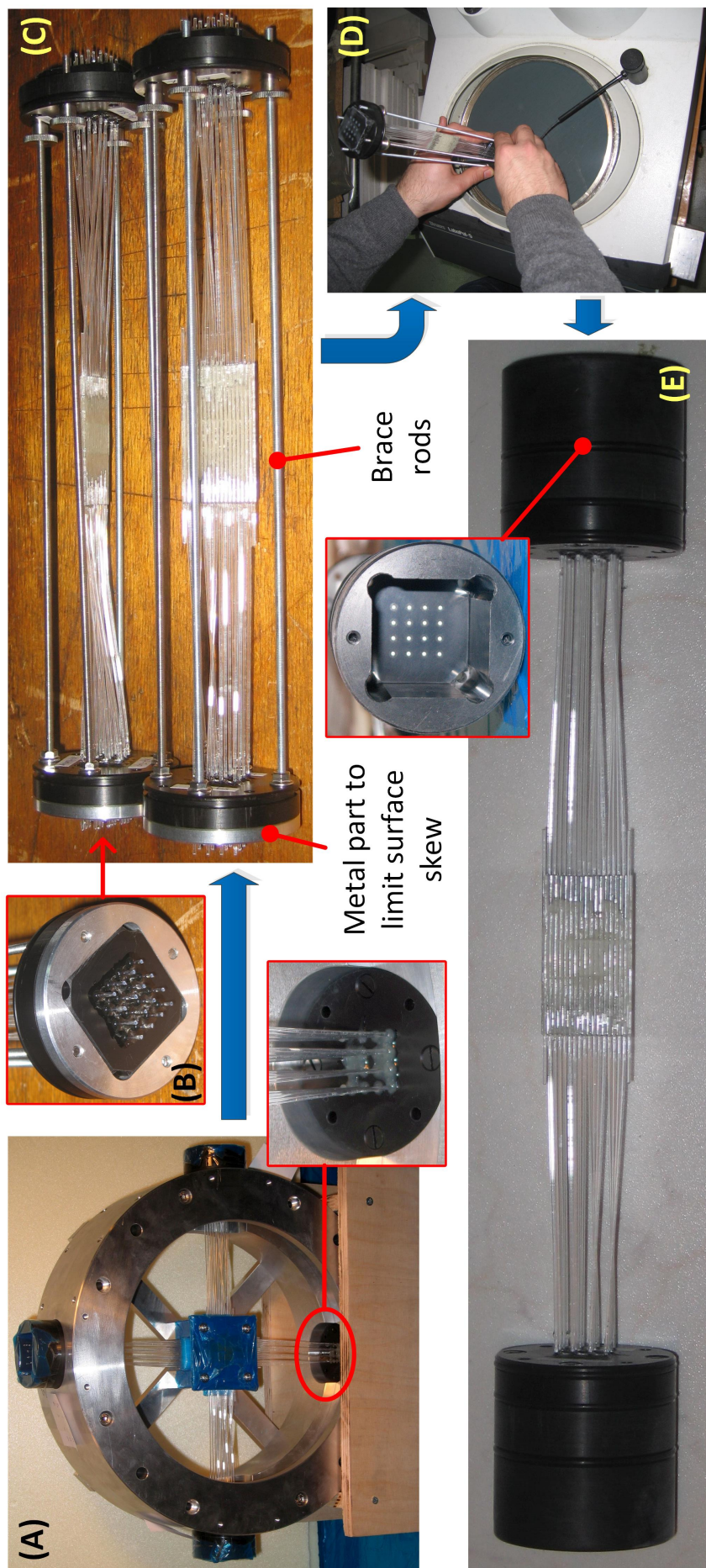


Figure 3.21: Preparation of fiber mountings. (A) Gluing of fiber mounting. Epoxy glue was slightly heated, degassed, and injected into holes in the mounting using a syringe with a needle-type applicator. (B) Fiber mounting before polishing. An additional aluminum element was used to prevent the skew of the polished surface. (C) Fiber mounting prepared for polishing. Threaded steel brace rods were used to minimize the risk of breaking the fibers. (D) Polishing of fiber mountings (see table 3.3 for details). (E) Fiber mats along with assembled photomultiplier housings.

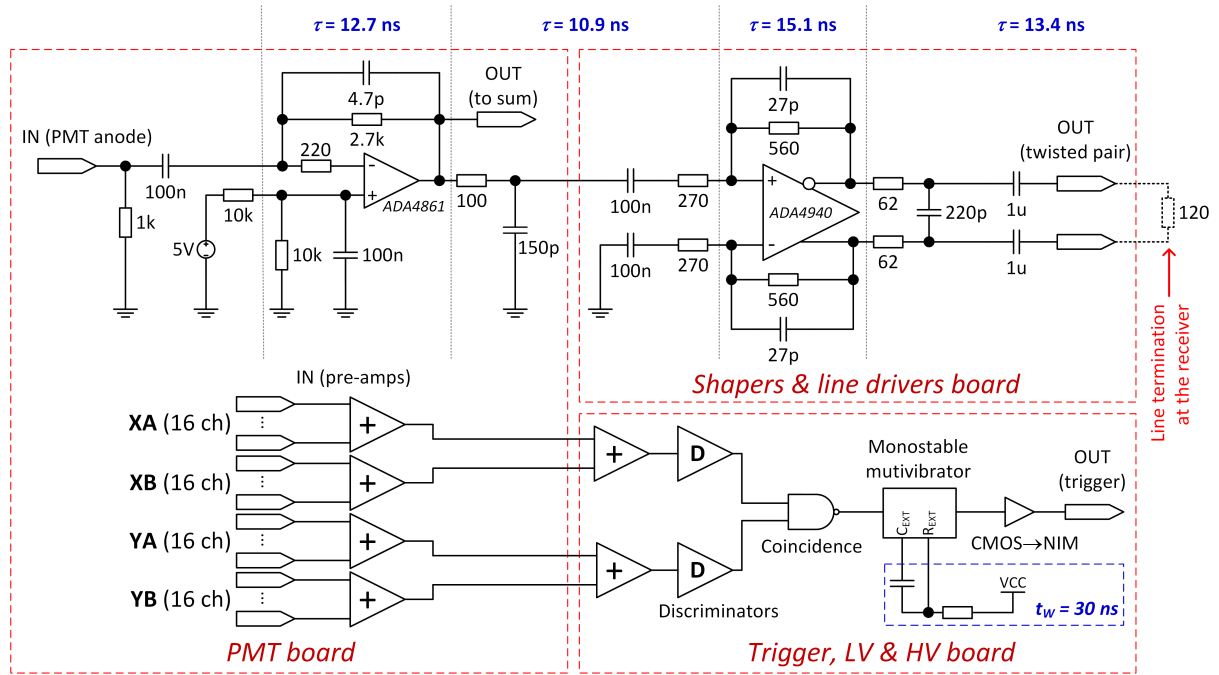


Figure 3.22: Top – analog electronics chain of each channel. Fourth-order RC shaping was used, with the first stage configured as a transimpedance amplifier, a passive second stage, an active third stage with a conversion to a differential signal, and a passive fourth stage. Note that a line terminating resistor at the receiver side is part of the filter. Bottom – configuration of the trigger system. After passing through the first RC stage, signals from each detector plane are analog-summed and compared to a fixed threshold. Next, if there is an X-Y coincidence, then an output pulse is produced using a monostable multivibrator. The trigger pulse conforms to the NIM standard.

1. An analog sum of all channels comprising a particular detector plane is produced. The summing is a two-stage operation – the 1-st stage sums all the signals from outputs of the transimpedance preamplifiers connected to a single photomultiplier, then the 2-nd stage sums the ‘sum-of-PMT’ signals.
2. Leading-edge fixed-threshold discriminators are used to detect signals above a given threshold. The threshold voltage is set using a multi-turn potentiometer and is common for both detector planes.
3. A logic NAND gate is used to detect coincidence of X and Y discriminator outputs, which then triggers a monostable multivibrator. The result is approx. 30 ns wide output pulse.
4. The pulse is level-shifted to meet the requirements of the NIM standard.

Once the final schematics of the realized circuits were known, it was possible to calculate noise contribution from the front-end circuits. Fig. 3.23 shows Bode plots for the first stage amplifier and the full shaping circuit. The plots are useful in determining the -3dB

cutoff frequency, which in turn can be used to calculate the noise equivalent bandwidth (from hereon denoted as ENBW). Table 3.4 presents a summary of these calculations, along with the computation of the overall transimpedance gain, needed for revised estimations of the time resolution of the detector.

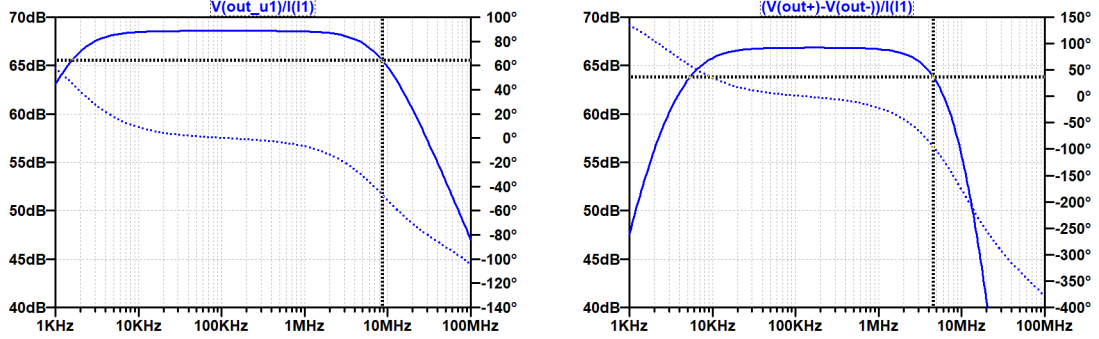


Figure 3.23: Bode plots of frequency response of the pre-amplifier circuit, created using the LTSpice program. Cursor marks the -3 dB cutoff frequency. Vertical axes represent the transimpedance gain (in dB) and the phase shift (degree). *Left*: Characteristics of the 1-st stage transimpedance amplifier. *Right*: Frequency response of the full chain prior to an ADC converter.

Circuit	Passband Gain (V/A)	Number of RC Stages	f_{3dB} (MHz)	$ENBW$ vs. f_{3dB}	$ENBW$ (MHz)
1-st stage	2686	1	8.54	1.57	13.41
Full shaper	2200	4	4.55	1.13	5.14

Table 3.4: Summary of the parameters obtained from the LTSpice program, subsequently used for revised performance estimation of the detector. f_{3dB} denotes frequency at which gain drops by -3dB, $ENBW$ stands for the effective noise bandwidth.

The method of analyzing the noise level present at the input of the ADC was as follows. The first step in estimating noise levels was creating a noise model of the system, shown in Fig. 3.24. Then, a non-inverting gain of each feedback loop was calculated:

$$k_{u1} = 1 + \frac{2.7 \times 10^3}{1 \times 10^3} = 3.7 \quad (3.32)$$

$$k_{u2} = 1 + \frac{560}{370} \cong 2.5 \quad (3.33)$$

$$k_{u3} = 1 + \frac{560}{270} \cong 3.1 \quad (3.34)$$

Next, each feedback loop was cut (marked as bold ‘**X**’ in Fig. 3.24), allowing calculation of equivalent resistances seen from inputs of the amplifiers:

$$R_{S1} = 1k\Omega \parallel 2.7k\Omega + 220\Omega \cong 950\Omega \quad (3.35)$$

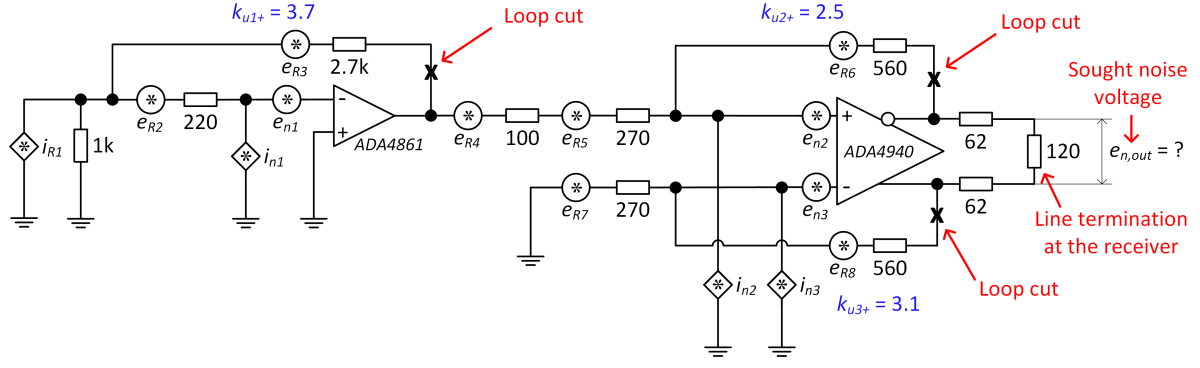


Figure 3.24: Noise model of a single channel. Voltage and current sources are marked for all the elements that were included in the noise analysis. Note that current noise of the non-inverting input of ADA4861 (1-st stage) is omitted, as it is blocked by a 100 nF capacitor.

$$R_{S2} = (100\Omega + 270\Omega) \parallel 560\Omega \cong 223\Omega \quad (3.36)$$

$$R_{S3} = 270\Omega \parallel 560\Omega \cong 182\Omega \quad (3.37)$$

With the above steps completed, it was possible to create a simplified noise model (Fig. 3.25), with the equivalent noise sources defined as:

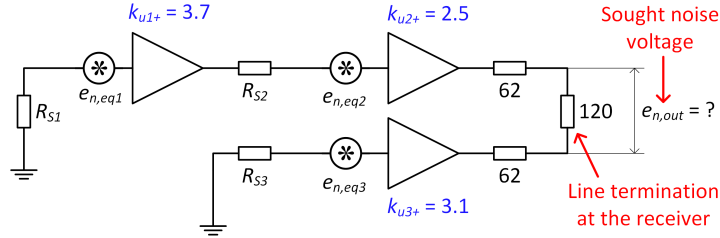


Figure 3.25: Simplified noise model of a single channel.

$$\begin{aligned} e_{n,eq1}^2 &= 4kTR_{S1} + (i_{n1}R_{S1})^2 + e_{n1}^2 = \\ &= 4 \times 1.38 \times 10^{-23} \times 300 \times 950 + (5.5 \times 10^{-12} \times 950)^2 + (3.8 \times 10^{-9})^2 = \\ &\cong 1.57 \times 10^{-17} + 2.73 \times 10^{-17} + 1.44 \times 10^{-17} = 5.74 \times 10^{-17} \quad (\text{V}^2/\text{Hz}) \quad (3.38) \end{aligned}$$

$$\begin{aligned} e_{n,eq2}^2 &= 4kTR_{S2} + (i_{n2}R_{S2})^2 + e_{n2}^2 = \\ &= 4 \times 1.38 \times 10^{-23} \times 300 \times 223 + (0.81 \times 10^{-12} \times 223)^2 + (3.9 \times 10^{-9})^2 = \\ &\cong 3.69 \times 10^{-18} + 3.26 \times 10^{-20} + 1.52 \times 10^{-17} = 1.89 \times 10^{-17} \quad (\text{V}^2/\text{Hz}) \quad (3.39) \end{aligned}$$

$$\begin{aligned} e_{n,eq3}^2 &= 4kTR_{S3} + (i_{n3}R_{S3})^2 + e_{n3}^2 = \\ &= 4 \times 1.38 \times 10^{-23} \times 300 \times 182 + (0.81 \times 10^{-12} \times 182)^2 + (3.9 \times 10^{-9})^2 = \\ &\cong 3.01 \times 10^{-18} + 2.17 \times 10^{-20} + 1.52 \times 10^{-17} = 1.82 \times 10^{-17} \quad (\text{V}^2/\text{Hz}) \quad (3.40) \end{aligned}$$

Afterward, all the noise sources are summed, taking into account gains of particular stages:

$$\begin{aligned}
e_{n,out}^2 &= [(k_{u1} k_{u2} e_{n,eq1})^2 + (k_{u2} e_{n,eq2})^2 + (k_{u3} e_{n,eq3})^2] \times (120/244)^2 = \\
&= [(3.7 \times 2.5)^2 \times 5.74 \times 10^{-17} + 2.5^2 \times 1.89 \times 10^{-17} + 3.1^2 \times 1.82 \times 10^{-17}] \times 0.24 = \\
&\cong (4.91 \times 10^{-15} + 1.18 \times 10^{-16} + 1.75 \times 10^{-16}) \times 0.24 \cong 1.25 \times 10^{-15} \quad (\text{V}^2/\text{Hz}) \quad (3.41)
\end{aligned}$$

Finally, after accounting for the effective noise bandwidth, the RMS of the voltage noise present at the ADC input is:

$$\sigma_{input} = \sqrt{e_{n,out}^2 \times ENBW_{shaper}} = \sqrt{1.25 \times 10^{-15} \times 5.14 \times 10^6} \cong 80 \times 10^{-6} \quad (\text{V}) \quad (3.42)$$

Thus, using Eq. 2.103 and substituting $\sigma_{n,adc}$ with values from Eq. 3.23, the revised estimate of the total noise in the digitized signal is:

$$\sigma_{noise,adc} = \sqrt{\sigma_{n,adc}^2 + \sigma_{input}^2} = \sqrt{(0.23)^2 + (0.08)^2} \times 10^{-3} \cong 244 \times 10^{-6} \quad (\text{V}) \quad (3.43)$$

It is therefore straightforward to conclude that the contribution of the noise originating in the analog circuitry is marginal compared to the noise inherent to ADC converters. Consequently, the revised estimate of the timing resolution of the digital constant fraction discriminator algorithm¹⁴ would be (Eq. 2.115):

$$\overline{\sigma_{time}} = \sqrt{\frac{2(1+a^2)}{3}} \times \frac{\sigma_{noise}}{dx/dt|_{t_{zero}}} = \sqrt{\frac{10}{3}} \times \frac{0.244 \times 10^{-3}}{2200 \times 750} \cong 270 \times 10^{-12} \quad (\text{s}) \quad (3.44)$$

When it comes to the performance of the trigger chain, the noise estimate is affected mainly by the 1-st stage. Since the signal reaching the discriminator is a result of two-stage analog summing, the noise contributions from the summing amplifier and the discriminator are negligible compared to the noise of the sum of 32 channels. Assuming that noise in each channel is independent of the others, the RMS analog noise at the input of the discriminator is:

$$\begin{aligned}
\sigma_{noise,trig} &= \sqrt{32 \times e_{n,eq1}^2 \times ENBW_{preamp}} = \\
&= \sqrt{32 \times 5.74 \times 10^{-17} \times 13.41 \times 10^6} \cong 160 \times 10^{-6} \quad (\text{V}) \quad (3.45)
\end{aligned}$$

Since the above RMS voltage is small compared to the 1.8 mV equivalent RMS voltage noise originating from the amplitude walk effect (see Eq. 3.21), its effect on the timing resolution of the trigger system is negligible.

Implementation wise, the whole electronics subsystem is divided into three printed circuit boards: the ‘photomultiplier board’, the ‘shapers and line drivers board’, and the ‘trigger, HV and LV board’. The ‘photomultiplier board’ includes PMT connectors,

¹⁴Assuming a digital constant fraction algorithm with an inverted waveform gain is two and the delay of two samples.

transimpedance preamplifiers, part of an RC circuit forming the 2-nd pole, and finally, the 1-st stage summing amplifiers. It is attached directly to the PMT end cap. The ‘shapers and line drivers board’ accommodates shaping circuitry responsible for 3-rd and 4-th poles, while the ‘trigger, HV and LV board’ provides power distribution functions and also encompasses the remainder of the trigger circuitry.

Since one of the essential requirements was the portability, a single +5V line provides power for all the electronics, with the idle power consumption of approx. 3 W. As such, a standard, low-cost power supply can be used to power all the front-end modules on the detector.

3.5.5 Final Assembly

Drawing with a 3D CAD model of a nearly final configuration of the detector (i.e., all elements except covers) is presented in Fig 3.26. The actual assembly was a relatively straightforward process. First, the fiber mat assemblies were bonded together at a right angle. For that purpose, they were placed in the same positioning tool that was previously used during gluing of fiber mountings – the only difference was that this time the glue was applied in between the mats. Then, the tool has been assembled with the upper half of the frame, turned upside down, and left until the glue had cured (Fig 3.27a). Afterward, the bottom plate of the positioning tool was removed, and glue was once again applied onto the mats. Next, the fiber support and the bottom half of the frame were assembled, and the two halves of the frame were secured using eight M6 screws with self-locking nuts (Fig. 3.27b). The fiber support had a machined opening just under the active area of the detector so that unnecessary material had been removed from the path of the beam (see Fig. 3.26, top-right corner). Based on assumed clearances used in the design, it is estimated that the achieved accuracy of fiber mat placement was ± 0.4 mm for the position of the center and ± 0.4 degrees for the angle.

The next step after putting the frame together was the addition of electronic modules, followed by the installation of photomultipliers (Fig. 3.27c). The latter step began by assembling ‘PMT boards’ with PMT end caps and the PMTs themselves. After that, the PMT assemblies were inserted into the housings, and subsequently, black PVC tape was used to seal gaps between ferrules and end caps. Firm contact between the surfaces of the PMT window and that of the fiber mounting was assured by using springs positioned along the end cap guides, which gently pushed the PMTs in the direction of the fibers. As mentioned in section 3.3, Loctite-8104 [160] silicon grease was used to couple the PMTs to the fibers, since it was suitable for the application and readily available in the lab. The careful application technique prevented the formation of air bubbles between the surface of the mounting and the PMT.

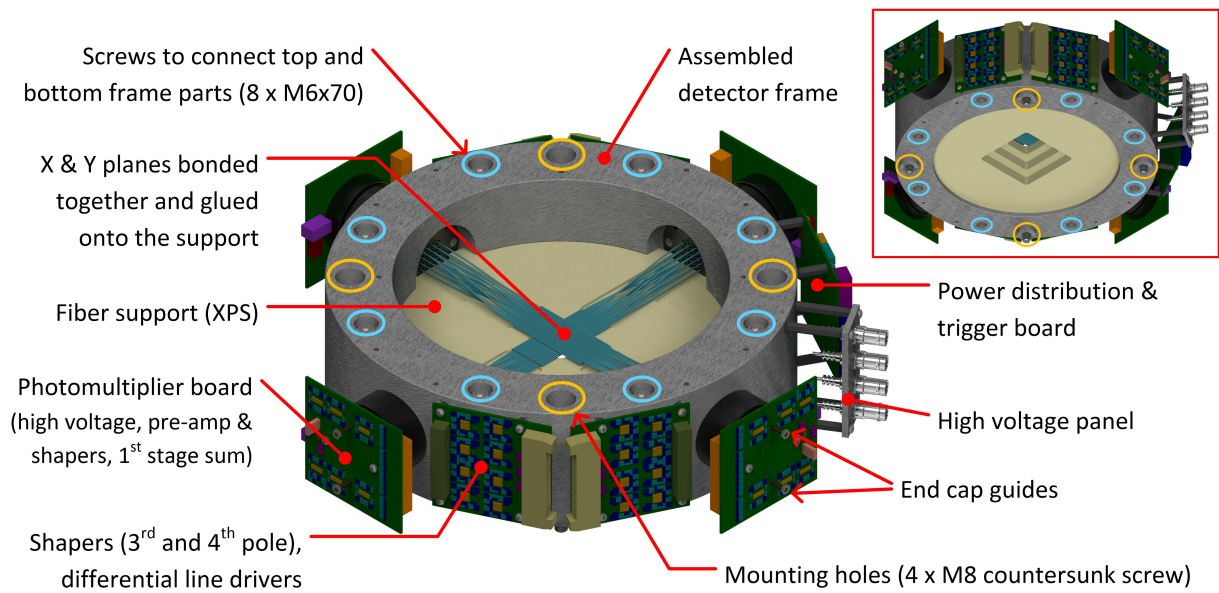


Figure 3.26: 3D CAD model of the detector in final configuration (top view), with assembled electronics modules. Upper right corner shows bottom view of the detector, with clearly visible opening in fiber support that removed unnecessary material from the beam.

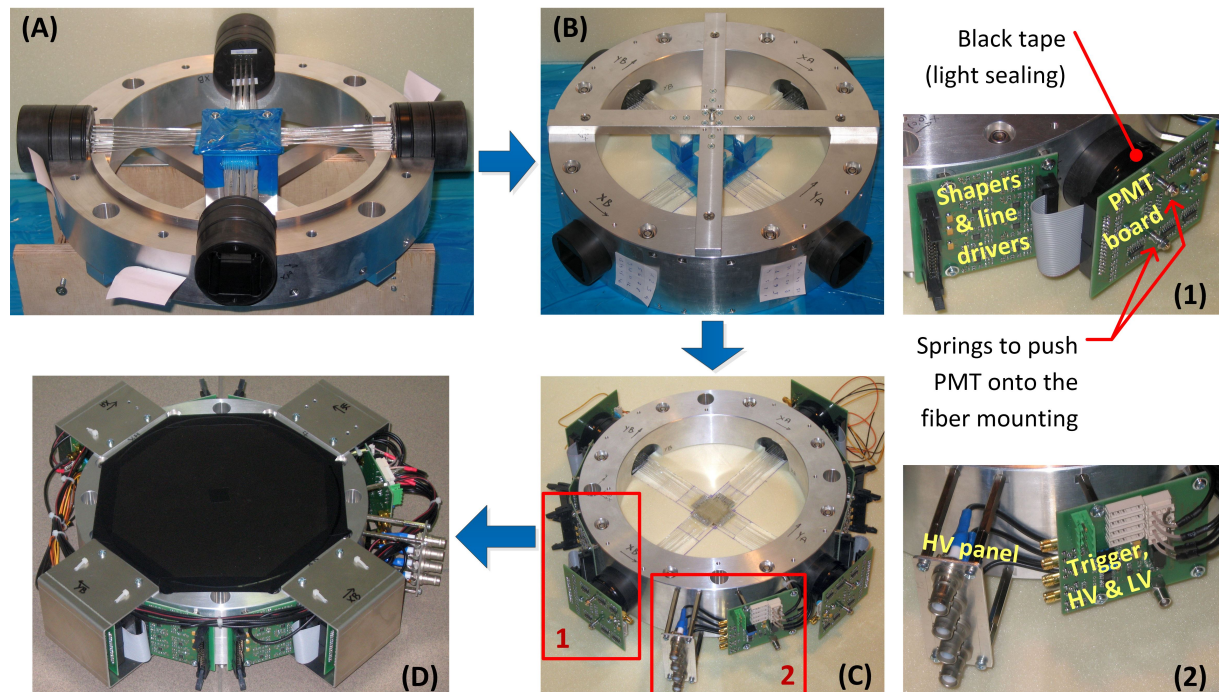


Figure 3.27: Final assembly. (A) Gluing of fiber mats at a right angle. (B) Gluing of fiber mats to XPS support. (C) Detector with installed photomultipliers and assembled electronics. Details (1) and (2) show zoom-ins of particular modules. (D) Detector in final configuration, with installed photomultiplier covers and light-sealing foils.

With the photomultipliers and electronics in place, the only remaining task was to finish cabling the detector and then to mount covers for mechanical protection of the PMTs as well as for ensuring light-tightness of the detector (Fig. 3.27d). The latter ones were made from an 0.5 mm thick black polypropylene (PP) foil. The central part had a cutout which was covered with a thin Kapton foil – again, to minimize the mass within the beam.

One of the requirements for the detector (section 3.2) was the ability to determine the center of its active area using a survey by a theodolite and achieving this goal required a dedicated configuration of the detector, which is shown in Fig. 3.28 (left). The front light cover was removed, and the positioning tool was attached to the frame (it was the same tool that was used during the gluing of the fiber mats to the XPS support). However, this time it was stripped down from vertical bars and instead a holder for the theodolite target ($\varnothing=10$ mm cylinder, H7 tolerance of diameter) was attached to the top of the cross. Since the countersunk screws, used to mount the positioning tool to the frame, did not provide satisfactory alignment of the positioning tool with the frame, proper adjustment of the two was achieved by ensuring the smooth surface of the transition between the outer surface of the frame and the four ends of the cross. Fig. 3.28 (right) show the actual survey in the experimental hall at the ELSA test site.

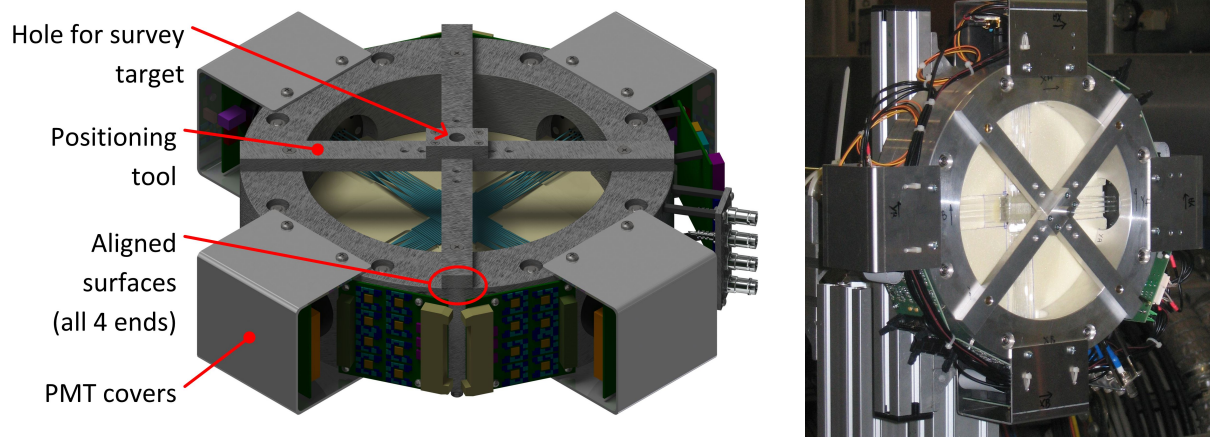


Figure 3.28: Detector in configuration for a survey using a theodolite. Survey target (see right picture) is put into an H7 tolerated hole in an adapter attached to the top part of the positioning tool – the same that was previously used during assembly of the detector, to ensure proper position of fiber mats.

Chapter 4

Performance Evaluation

4.1 Initial Commissioning

The purpose of the in-lab commissioning of the detector was to verify signal presence in every channel and also to confirm that there is no high-voltage related sparking on the boards connected to the PMTs. Furthermore, it was interesting to verify whether waveform shapes obtained from the detector are on par with the expectations and, if not, then by how much they differ. All the waveforms from the detector were recorded using a Tektronix DPO4104 oscilloscope. A Tektronix TDP1500 differential probe was used to acquire differential signals, and a $120\ \Omega$ termination has been used to closely match the conditions that would be present when an MSADC card would be plugged in. The bandwidth limit for the differential signal was set at 20 MHz, which seemed sufficient given the small-signal (AC) analysis of the shaper, presented in section 3.5.4. The signals after the 1-st stage transimpedance amplifier were acquired using a Tektronix TAP1500 active probe, with channel bandwidth set to the full 1 GHz offered by the oscilloscope and the probe.

The first check after turning on the detector was to verify the presence of dark pulses. Fig. 4.1 presents an example oscillogram of the dark pulses in one of the channels, taken in the waveform persist mode, while Fig. 4.2 shows an averaged dark pulse, along with two variants of applied fits. The average dark pulse amplitude was approx. 2.3 mV, the leading and trailing edges were 32.0 ns and 79.2 ns, respectively, with the pulse width of 73.1 ns – roughly in line with the expectation (Fig. 3.10). In terms of fit performance, it seems that using a combination of exponentially modified Gaussian (representing the 1-st stage) followed by a model of three-stages of RC low-pass filter yields optimal results.

The measured pulse charge at the output of the PMT was 84.7 fC. Assuming passband transimpedance gain of 2200 (see section 3.5.4) and noting that the majority of the pulses are from single photoelectron events, the equivalent PMT gain is at the level of 0.53×10^6

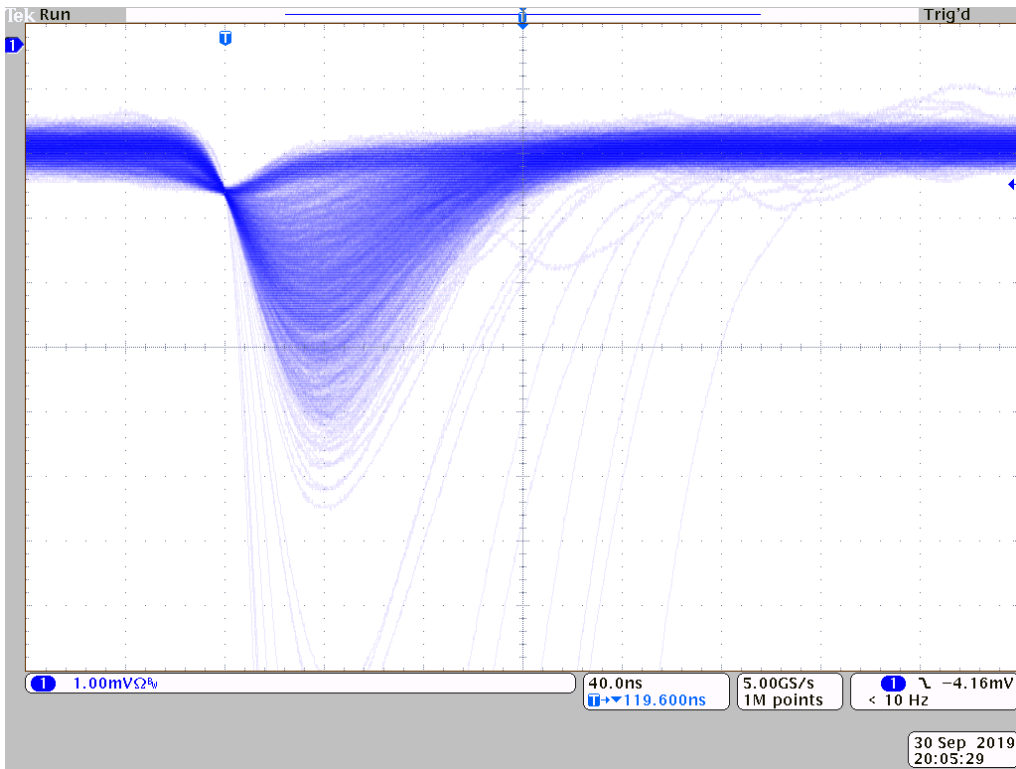


Figure 4.1: Persistence plot of dark pulses at the output of the shaper. The waveforms were recorded using a Tektronix DPO4104 oscilloscope equipped with a TDP1500 differential probe (bandwidth limit: 20 MHz, probe range: 850 mV).

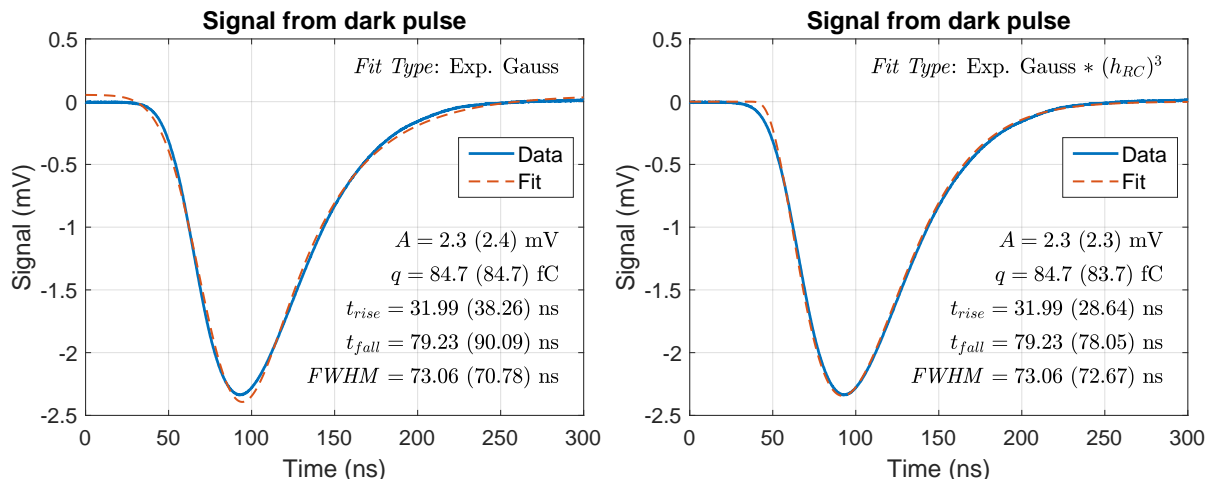


Figure 4.2: Average of 512 dark pulses at the output of the shaper, along with results of the fitting using exponentially modified Gaussian (*left*) and a combination of exponentially modified Gaussian and an impulse response of a 3-stage RC low-pass filter (*right*). The values in brackets correspond to metrics of the pulse obtained from the fit. The waveforms were recorded using a Tektronix DPO4104 oscilloscope equipped with a TDP1500 differential probe (bandwidth limit: 20 MHz, probe range: 850 mV).

– roughly in line with the datasheet value of 0.9×10^6 . One should note that per-channel deviations from the nominal gain value are not uncommon in PMTs, and can occur due to the dynode chain and the anode non-uniformities. The other reason for potential deviation from the nominal PMT gain can be related to very little time that was left for the commissioning (see section 3.4), which prevented detailed PMT characterization. Unfortunately, at the time of this project, we did not have access to a multi-channel readout system that would allow parallel acquisition of all the signals from the detector. As such, all four PMTs were supplied using the same negative voltage of 800V. Given the exponential relationship between the supply voltage and the PMT gain, variations among average gain of different PMTs were expected, in addition to per-channel variations – as each individual PMT is slightly different from the others, even if the type is the same..

With all PMTs and front-end channels alive, the next step in the commissioning process involved testing using a ^{90}Sr (strontium-90) radioactive source (Fig. 4.3). The ^{90}Sr is an almost pure beta-emitter, first undergoing a β^- decay into ^{90}Y (yttrium-90) with endpoint energy of 546 keV (average: 196 keV) and then from ^{90}Y to ^{90}Zr (zirconium-90, stable) with endpoint energy of 2.28 MeV (average: 935 keV) [167]. Since the energies of emitted electrons are low, especially from the $^{90}\text{Sr} \rightarrow ^{90}\text{Y}$ decay, a significant fraction of them would be almost completely absorbed the first layer of the fibers (Table 4.1). As such, it was expected that event rates in different layers of the detector will vary. Besides, the signal level could also vary among particular layers of the detector, due to differences in average energies of electrons hitting particular layers. Fig 2.5 in section 2.2 clearly shows that at such low energies, electronic losses strongly depend on particle energy.

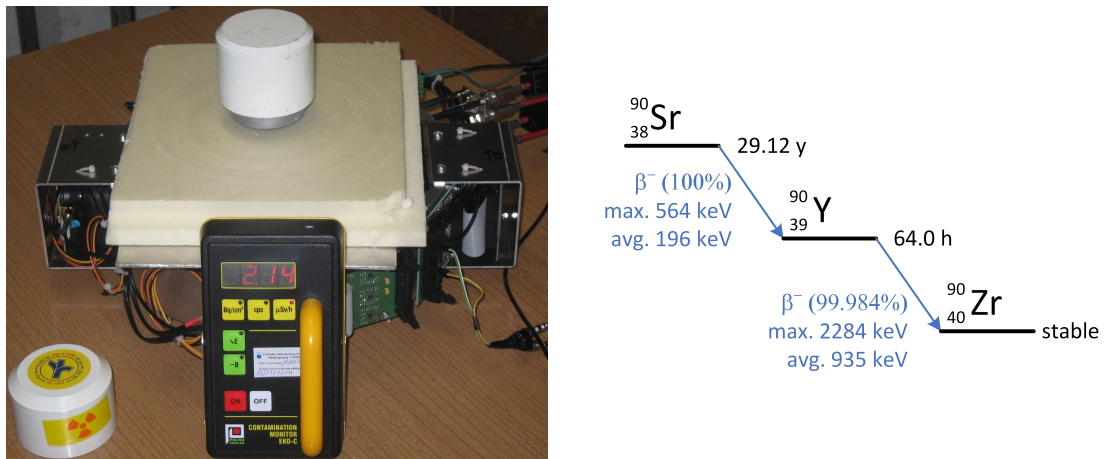


Figure 4.3: Tests of the detector with the ^{90}Sr source (Strontium-90). *Left*: Radioactive source was placed on top of the active part of the detector. *Right*: Simplified decay scheme of ^{90}Sr [167].

With the above in mind, the primary goal of these tests was to verify detector operation as a whole – i.e., that it detects passing particles. The first thing to check was the

Decay	E_{\max} (keV)	E_{avg} (keV)	R_{\max} (mm)	R_{50} (mm)
$^{90}\text{Sr} \rightarrow ^{90}\text{Y}$	564	196	1.5	0.19
$^{90}\text{Y} \rightarrow ^{90}\text{Zr}$	2284	935	9.7	1.85

Table 4.1: Energies and ranges in polystyrene for electrons emitted in β^- decays of ^{90}Sr . E_{\max} and E_{avg} denote endpoint and average energies, respectively. R_{\max} and R_{50} stand for maximum range and the distance at which the number of particles is halved, respectively [167, 168].

presence of the signal in every fiber, in order to find the ones with either no signal or severely deteriorated signal, compared to other fibers connected to the same PMT. Potential causes of damage could include cracks, cladding damage, poor condition of the mirrors at the far end of the fibers, lousy quality of the coupling of the fiber to the PMT. Another interesting thing was a comparison of pulses shapes of the signals from the fibers to the ones caused by the dark emission of the photocathode.

Fig 4.4 shows example average waveforms at the output of the 1-st stage transimpedance amplifier and at the output of the shaper, respectively, while Table 4.2 presents a summary of pulse shape metrics at different locations within the front-end circuit and under various conditions. The pulse shape at the output of the shaper roughly matched the expectation. It was similar to the shape of the previously examined single photoelectron pulses from the dark emission of the PMTs. As such, it proved that the scintillator is fast enough so that the change in the shape of the output signal is negligible. In other words, the combined signal from the scintillator and the PMT is almost a delta-type input to the shaper. Consequently, one can assume that the signal shape from passing particles is constant, with the impulse response of the shaper determining its shape.

Location	Condition	t_{leading} (ns)	t_{trailing} (ns)	$FWHM$ (ns)
PMT output	calculated	1.3	6.5	3.5
1-st stage amplifier	^{90}Sr , measured	3.7	32.7	18.1
Shaper output	^{90}Sr , measured	28.2	79.3	74.5
Shaper output	dark, measured	32.0	79.2	73.1
Shaper output	MIP, measured	31.2	86.6	73.0

Table 4.2: Summary of pulse shapes at various locations within the front-end circuit, recorded in various conditions.

A thing to note is that the signal shape after the 1-st stage amplifier is very different from the calculated shape of the current pulse from the PMT (Fig. 3.10). The above

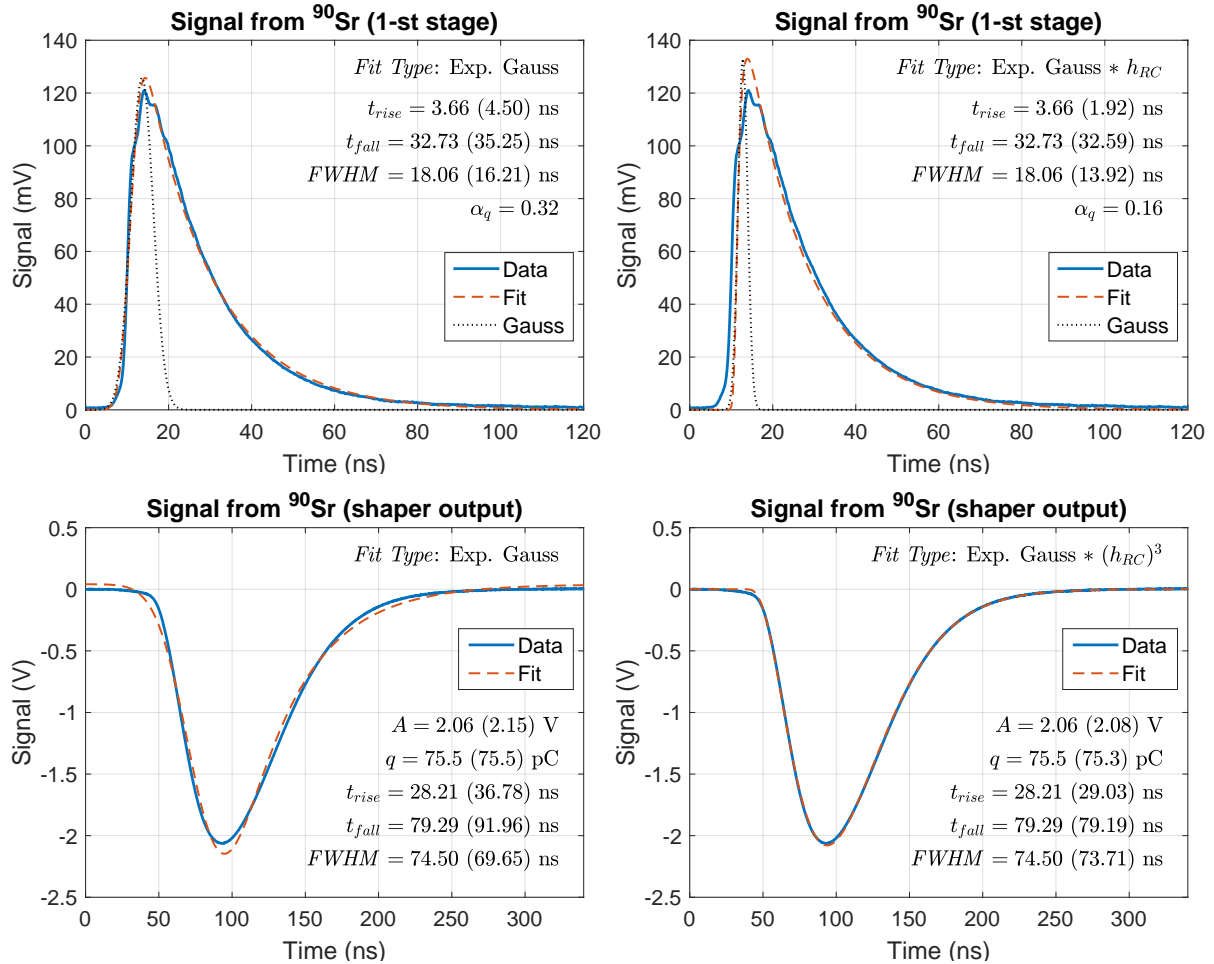


Figure 4.4: Example averaged signals during tests with a ^{90}Sr source (random channels). Top row shows waveform at the output of the 1-st stage transimpedance amplifier, bottom row shows outputs of the shaper. The waveforms were recorded using a Tektronix DPO4104 oscilloscope equipped with active probes: TAP1500 active probe, channel bandwidth 1 GHz (top) and TDP1500 differential probe, range 850 mV, channel bandwidth 20 MHz (bottom). Average waveforms were computed using 512 events. Left column shows results of fitting with an exponentially modified Gaussian, while the right column shows fits done using a convolution of an exponentially modified Gaussian with an impulse response of an RC low-pass filter. The values in brackets corresponds to metrics calculated from the curves produced by the fits. The fits for the 1-st stage also show the Gaussian curve used in estimation of the time resolution of the trigger chain.

stems from the fact that the pre-amplifier, apart from being a low-impedance driver for subsequent stages, is also the 1-st stage of the RC low-pass filter circuit. Such topology of the front-end circuit was a trade-off necessary to achieve a quasi-Gaussian shape at the output of the shaper, which required as many RC stages as possible while minimizing the number of amplifiers. The origin of the somehow oscillatory peak of the waveform was not clear. However, the timescales of the ringing are too big to attribute them to optical effects, especially after taking into account the dimensions of the detector. Therefore, it is believed to be an electrical effect – either present in the actual circuit or a measurement artifact introduced by the probe.

When it comes to fit accuracy, it is somehow puzzling in the case of the first stage amplifier, most probably due to ‘ringing’ visible in the peak of the signal. The exponentially modified Gaussian gives a reasonable fit quality but overestimates edge duration. On the other hand, a convolution of the exponentially modified Gaussian and the impulse response of a first-order RC low-pass filter gives a good match of both rise and fall times but underestimates the pulse width. The latter also reconstructs higher pulse amplitude, which may or may not be valid. All in all, the variant using only exponentially modified Gaussian seems a better match to data. In the case of signal from the shaper, similarly to the dark pulse case, the best match was achieved using a convolution of the exponentially modified Gaussian modeling the first stage and an impulse response of a third-order RC low-pass filter. Table 4.3 lists the parameters of the best fits.

Parameter	First stage	Shaper	Unit
Fit type	<i>Exp. Gauss</i>	<i>Exp. Gauss * (h_{RC})³</i>	
C	0.0819	1	V
λ	0.0611	0.0611	ns ⁻¹
μ_1	10.91	0	ns
σ_1	2.047	2.047	ns
A_2	0.1258		V
μ_2	14.40		ns
σ_2	2.707		ns
α_q	0.3188		
τ		18.3	ns
μ_3		93.8	ns
A_3		2.079	V

Table 4.3: Parameters of the fits applied to registered average waveforms obtained during testing with the ⁹⁰Sr source.

Having the actual waveforms from the detector, one could revise the previous estimation of the timing resolution of the trigger chain (Eq. 3.19) to account for lower PMT gain and the bandwidth cut introduced in the first stage. In order to achieve an even

better estimate, it was also desirable to measure the actual noise level of the system – however, this was not possible, as the noise level of the probe surpassed that of the pre-amplifier¹. Using the technique with the Gaussian matched in terms of pulse rise time (see section 2.6.1), the revised estimate of the walk error of the analog trigger system becomes:

$$\bar{\sigma}_q = \frac{\bar{q}}{SNR_{anode}} = \frac{17.3 \times 5.3 \times 10^5 \times 1.6 \times 10^{-19}}{3.80} = 0.386 \times 10^{-12} \quad (\text{C}) \quad (4.1)$$

$$\begin{aligned} \bar{\sigma}_{walk} &= \frac{\sigma_2}{\bar{q} \sqrt{2 \ln \left(\frac{k_{iu} \alpha_q \bar{q}}{\sqrt{2\pi} v_{thr} \sigma_2} \right)}} \bar{\sigma}_q = \\ &= \frac{2.707 \times 10^{-9}}{17.3 \times 84.7 \times 10^{-15} \times \sqrt{2 \ln \left(\frac{2686 \times 0.3188 \times 17.3 \times 84.7 \times 10^{-15}}{\sqrt{2\pi} \times 4 \times 10^{-3} \times 2.707 \times 10^{-9}} \right)}} \times 0.386 \times 10^{-12} = \\ &\cong 257 \times 10^{-12} \quad (\text{s}) \quad (4.2) \end{aligned}$$

In order to calculate the corresponding timing error due to electronics noise, it is first necessary to calculate the amplitude of the signal at the output of the first stage, for the average number of photoelectrons expected from the minimum ionizing particles. A convenient technique to accomplish this task is to use fit parameters for the first stage waveform, take into account the transimpedance gain of the amplifier and then match the integrals. The simple numerical calculation yields an amplitude of approx. 185 mV. Then, the sought timing error becomes (see Eq. 2.82 and Eq. 3.45):

$$\sigma_{thr} = \frac{\sigma_{noise, trig}}{dx/dt|_{thr}} = \frac{160 \times 10^{-6}}{0.8 \times 185 \times 10^{-3} / (4.5 \times 10^{-9})} \cong 4.9 \times 10^{-12} \quad (\text{s}) \quad (4.3)$$

As such, it is still negligible compared to the amplitude walk error. Since one is usually interested in the worst-case estimate, the estimation presented in Eq. 4.2 and Eq. 4.3 relies on the leading edge time provided by the fit of the averaged output of the first stage amplifier, done using the exponentially modified Gaussian.

The next test verified the mapping of detector channels – i.e., the association between the channel number and the position. The test involved measuring the number of counts for every channel, with an uncollimated ⁹⁰Sr source first placed at the center of the detector and then in one of the corners. The measurements were done using a fixed threshold discriminator and a scaler set to a constant time interval. Then, count histograms were

¹Unfortunately, the manufacturer's datasheet does not provide the value of noise level – however, it was clear that the RMS voltage of the noise is significantly above the calculated value of 160 μ V (Eq. 3.45).

created (Fig. 4.5) – from here on denoted as ‘A’ for the center position and ‘B’ for the corner position of the source. Since channel-to-channel and PMT-to-PMT efficiency variations were expected, due to anode nonuniformities, unequal PMT gain, and uneven range of beta particles in particular fiber layers, new histograms were created by dividing ‘B’ histograms by ‘A’ histograms. Such operation canceled differences in channel efficiencies. Now, if the mapping was correct, then the new ‘B/A’ histograms should show a smooth, monotonic curve, with individual points affected by statistical fluctuations. The test was successful, proving correct channel mapping and also proper placement of the fibers in the PMT mountings.

The final test was a check of signal level from the minimum ionizing particles – in lab condition those were cosmic muons. Randomly selected detector channel was connected to the oscilloscope via a differential probe (Textronix TDP1500), and another channel was hooked up to the trigger output of the detector (i.e., the coincidence of both planes). The trigger condition for the oscilloscope was a logic AND of both signals. Such a configuration was then left running over two days in order to accumulate sufficient statistics. Fig. 4.6 shows the result of this measurement. The average signal level in this particular channel was 58.5 mV, with the pulse shape similar to the one observed for dark pulses and the signal from ^{90}Sr . Note that one should not conclude as to the number of photoelectrons by comparing Fig. 4.6 to Fig. 4.1, as these particular measurements were done using different, randomly selected channels.

The overall results of the in-lab commissioning were satisfactory so that the detector was deemed ready for transportation to the test site.

4.2 Beam Tests

4.2.1 Test Setup at the ELSA Accelerator in Bonn

Test setup at the ELSA accelerator is presented in Fig. 4.7. The hodoscope was placed on a dedicated frame prepared by the accelerator team, according to the previously agreed design details. After installation, the detector was surveyed using a theodolite, so that its position was well known in the beam coordinates. Finally, a test was made using a small ^{90}Sr source to check whether a positive change in the beam axis corresponds to a positive change in the detector axis and vice versa.

4.2.2 Beam Profiles

Fig. 4.8 presents example beam profiles registered during actual tests of ECAL0, while Table 4.4 shows measured beam metrics. The location and width of the beam were

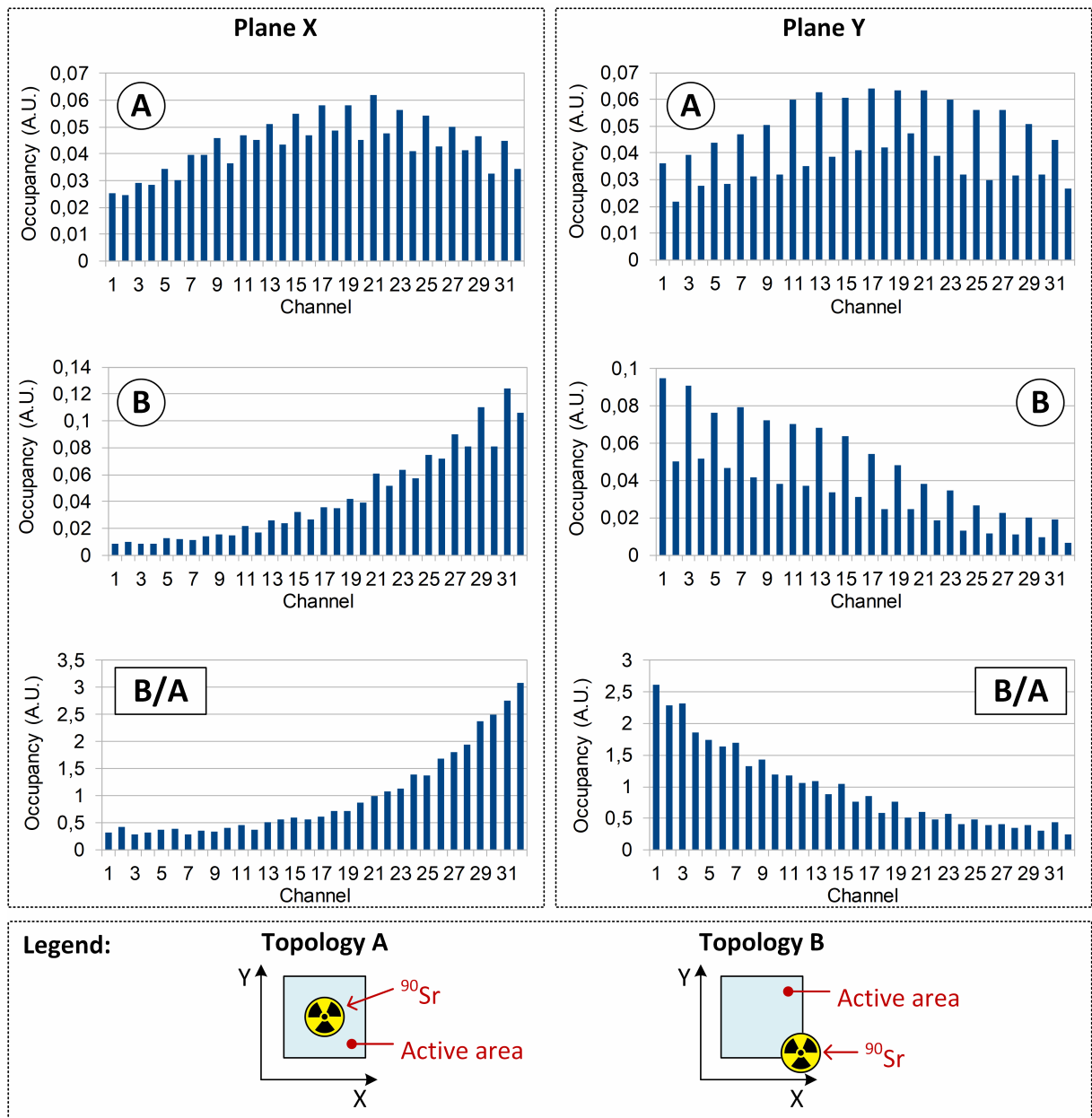


Figure 4.5: Mapping check using a ^{90}Sr source. The source was placed at two different positions: center (A) and corner (B). Then, histograms were created by measuring the number of counts during a fixed time interval. Next, the 'B' histograms were divided by the 'A' histograms. The smooth shape of the final histograms proves correct mapping. Significant differences between the adjacent channels result from the fact that they are read out by two different PMTs with different gains. In the case of plane 'Y', an additional difference is due to a small range of β particles originating from $^{90}\text{Sr} \rightarrow ^{90}\text{Y}$ decay, with most of them absorbed in the top-most layer of fibers, closest to the source.

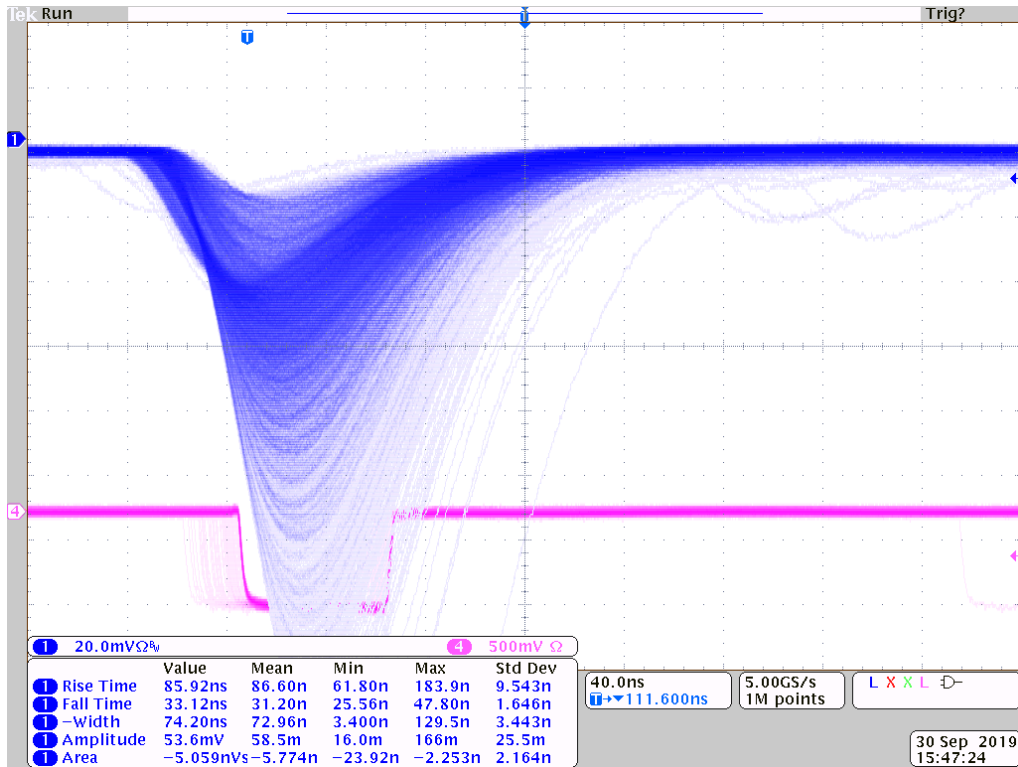


Figure 4.6: Persistence plot of signals from cosmic muons (minimum ionizing particles – MIP). Blue waveforms are MIP signals recorded from a randomly selected detector channel. The purple waveform shows the coincidence output from the detector (NIM standard). The MIP waveforms were recorded using a Tektronix DPO4104 oscilloscope equipped with a TDP1500 differential probe (probe range: 850 mV, channel bandwidth: 20 MHz). The trigger signal was directly coupled to the oscilloscope, terminated with 50Ω.

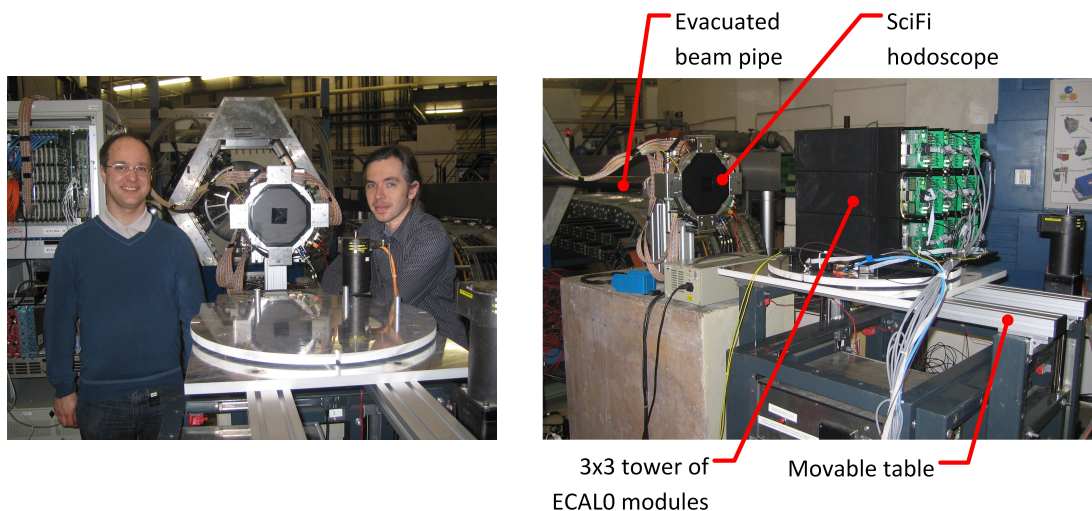


Figure 4.7: *Left*: Fully installed detector at the test stand for ECAL0, along with two-people team involved in building the detector (author on the left). In the back the frame of the Crystal Barrel experiment. *Right*: Test setup at ELSA. Beam was delivered via an evacuated beam pipe that terminated just before the hodoscope. The hodoscope was placed on dedicated frame. ECAL0 modules were placed on a movable, 3-axis table.

calculated by fitting registered beam profiles with the Gaussian fits. The beam had an elliptical cross-section. It was very narrow – below 5 mm FWHM in the horizontal axis and below 2 mm FWHM in the vertical axis for 0.8 GeV and 1.6 GeV, slightly wider for 3.2 GeV (below 4 mm FWHM). The position of the beam spot was well controlled. A peculiar behavior was observed at 3.2 GeV, where the horizontal profile had a strange shape extended to the left. Subsequent analysis showed that it was not the shape that changed, but the position that was shifted for different spills. This behavior was not foreseen by the accelerator team and was attributed to small issues with the beam extraction. They were not perceived as problematic, since the beam position was recorded by the hodoscope, for every spill – so we always knew where it hit the calorimeter.

E (GeV)	Units: channel				Units: mm			
	x	y	σ_x	σ_y	x	y	σ_x	σ_y
0.8	14.06	15.35	1.804	0.731	9.8	10.7	1.3	0.5
1.6	15.84	17.51	1.957	0.689	11.1	12.3	1.4	0.5
3.2	15.46	16.96	2.350	1.645	10.8	11.9	1.6	1.1

Table 4.4: Measured metrics of the beam during tests of ECAL0. Position and width values were obtained from Gaussian fits to the registered beam profiles. Fit parameters are in columns with units of ‘channel’. The channel width is 0.7 mm.

Thanks to the courtesy of the ELSA accelerator team, some beam time was dedicated to the hodoscope study. During these runs², few of the focusing magnets were turned off. This way, the size of the beam spot was enlarged, thereby increasing statistics in channels far from the center of the detector. Fig. 4.9 shows beam profiles taken in such conditions.

4.2.3 Signal Level from Minimum Ionizing Particles

The very first step in estimating the signal level from the scintillator was to estimate the level of each channel’s single photoelectron signals (i.e., the gain of the PMT). One possible way to perform such a measurement is to run the acquisition in a random trigger mode, which, in case of a sampling system, is equivalent to periodically acquiring fixed-length buffers. The next step is to calculate a histogram of integrals in pre-defined windows within the acquired segments. Once the histogram is ready, the difference in location between the pedestal and the single photoelectron peak is the sought level of the single photoelectron signal. Calculating the signal level expressed in photoelectrons is then straightforward – one needs to find the signal peak and divide its distance to the pedestal peak by the previously calculated level of the single photoelectron response.

²A ‘run’ is a fixed period of time during which data is recorded.

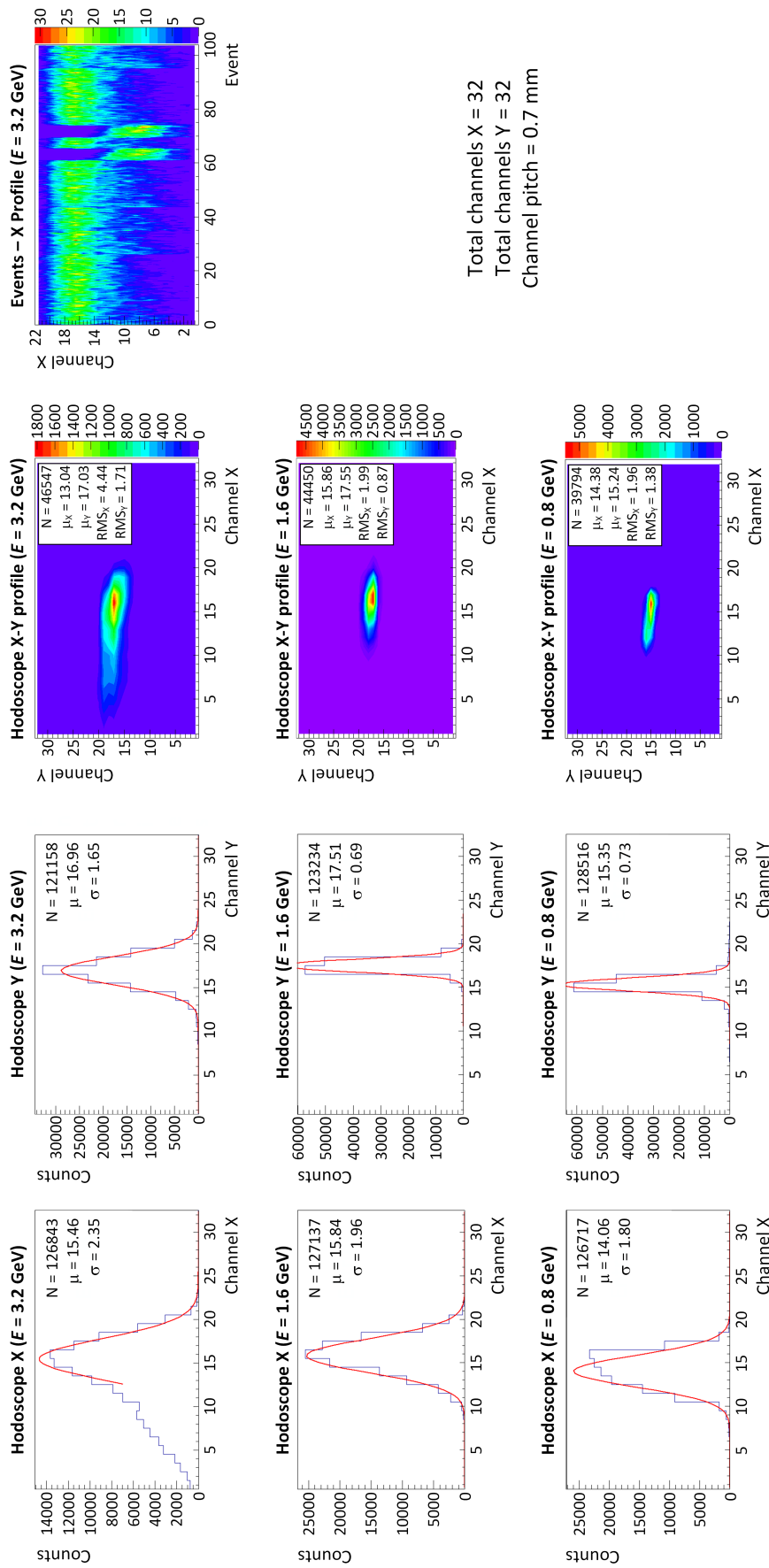


Figure 4.8: Example beam profiles registered during beam tests at ELSA accelerator. The channel pitch is 0.7 mm. Peculiar beam shape at 3.2 GeV was a result of an extraction problem – during few spill the beam was in wrong position.

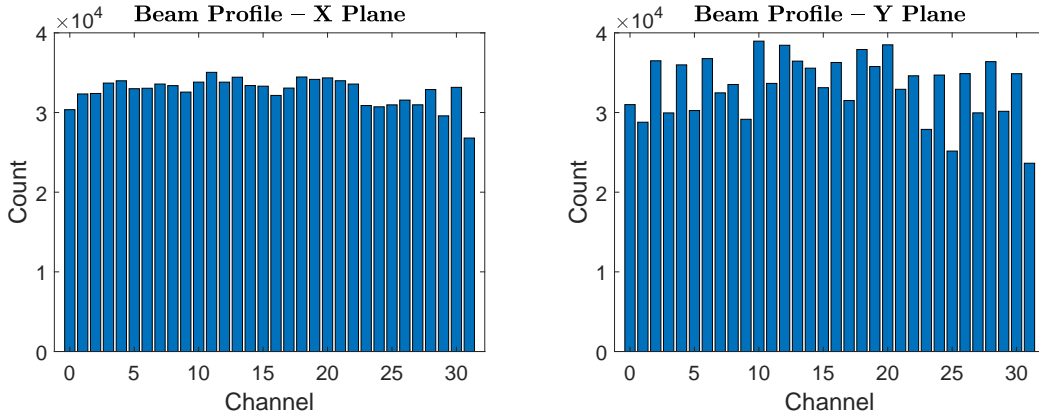


Figure 4.9: Beam profiles during runs dedicated to the hodoscope study. Selected focusing magnets of the beamline were turned off, thereby increasing beam spot size and allowing bigger statistics in detector channels that were far from the center. The channel pitch is 0.7 mm.

Unfortunately, a dedicated dark rate run taken during the beam test was not available due to a mistake made while recording the data. One way to correct this error was to collect dark rate data in the lab, but doing so would not guarantee conditions similar to the time of the test. We also did not have access to the required amount of MSADC cards. Fortunately, we could take advantage of the operation mode of the data acquisition system used during the test, as the zero-suppression feature of the MSADC cards was turned off for the runs dedicated to the hodoscope study. Therefore, instead of dumping all buffers without signals exceeding a pre-defined threshold, the acquisition system recorded data from all channels, for every hit – even though the majority of the hits affected not more than two fibers per plane. The above meant that a signal from a particle, occurring in one fiber, could, in principle, be regarded as a random trigger signal for the channels that were not hit. Fig. 4.10 presents an example histogram of integrals calculated for one of the channels – pedestal, single photoelectron, and signal peaks are easily distinguishable. For the sake of further processing, the histograms were divided into two sections – one containing pedestal and dark emission events and the other related to events with signals from the scintillation.

The actual calculation of the peak positions was a two-step process. The first step was to apply an adaptive Gaussian filter in order to get initial estimates of peak positions. The width of its impulse response was adjusted iteratively based on the estimated distance between the peaks. The fraction of inter-peak distance that was used to determine the standard deviation of the impulse response was different for estimation of single photoelectron peaks and signal peaks, as the latter were much broader. This approach was more efficient than trying pre-fits using a combination of two Gaussians and was also more stable. Moreover, it allowed identifying a valley between the sections of the histogram

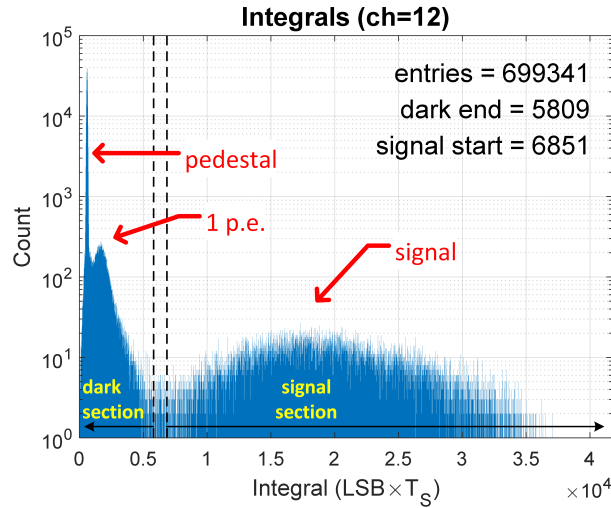


Figure 4.10: Example histogram of pulse integrals for a single detector channel. Pedestal, single photoelectron, and signal peaks are easily identifiable. The sections of the histogram corresponding to dark pulses and events correlated with signals from the scintillators were processed separately.

corresponding to the pedestal / dark emission events and the events with signals from the scintillation. The estimates of peak position obtained this way (Fig. 4.11, left) defined the starting point for the actual fit used to determine the correct position of the single photoelectron peak.

The final step in estimating the signal level from the single photoelectron involved fitting the integral spectrum with a formula presented in [169]. The formula provides for accurate modeling of the charge response of the PMT – it accounts for the Poissonian character of the photoemission and secondary emission from the dynodes, as well as two types of background events:

- low-charge events that result in non-zero pedestal width (type I)³;
- discrete events that may result in additional pulses accompanying the primary event, for example, thermal emission, afterpulsing, the radioactivity of the glass (type II).

A combination of Gaussians models the response of the ideal PMT. The means of the Gaussians are integer multiples of the charges corresponding to the single photoelectron response. At the same time, the areas are governed by the Poisson distribution with the rate parameter corresponding to the average number of photoelectrons emitted from the photocathode. The standard deviation of each of the Gaussians increases with the square root of the number of photoelectrons. The ‘type I’ background events are modeled

³The ‘type I’ and ‘type II’ classification of background events comes from the paper introducing the fit formula [169].

with a separate Gaussian distribution, while the ‘type II’ events with the exponential distribution. The exact mathematical formulas of the model are:

$$S_{\text{real}}(x) = A \times \left\{ \sum_{n=0}^{\infty} \frac{\mu^n e^{-\mu}}{n!} \times [(1-w)G_n(x-Q_0) + wI_{G_n \otimes E}(x-Q_0)] \right\} \quad (4.4)$$

$$G_n(x) = \frac{1}{\sigma_1 \sqrt{2\pi n}} \exp\left(-\frac{(x-nQ_1)^2}{2n\sigma_1^2}\right) \quad (4.5)$$

$$I_{G_n \otimes E}(x-Q_0) = \frac{\alpha}{2} \exp[-\alpha(x-Q_n-\alpha\sigma_n^2)] \times \left[\operatorname{erf}\left(\frac{|Q_0-Q_n-\sigma_n^2\alpha|}{\sigma_n\sqrt{2}}\right) + \operatorname{sign}(x-Q_n-\sigma_n^2\alpha) \times \operatorname{erf}\left(\frac{|x-Q_n-\sigma_n^2\alpha|}{\sigma_n\sqrt{2}}\right) \right] \quad (4.6)$$

$$Q_n = Q_0 + nQ_1 \quad (4.7)$$

$$\sigma_n = \sqrt{\sigma_0^2 + n\sigma_1^2} \quad (4.8)$$

Table 4.5 provides the meaning of the symbols used in Eq. 4.4 to Ex. 4.8, while the right plot in Fig. 4.11 shows example results of the fit to the experimental data. The fit performance was satisfactory, though one should note a simplification that was applied. The formula by Bellamy et al. accurately describes the case of a PMT illuminated with a Poisson source resulting in an average of μ photoelectrons generated in the photoemission process. The dark emission, in this case, is considered a ‘type II’ background. In our case, since we had no LED, it was the dark emission that was the primary emission process. As such, a simplification was made by assuming that the dark emission is a Poisson process. The above necessitated restricting the fitting algorithm to a combination of Gaussians only. Consequently, the free parameters of the fit were: μ , Q_0 , σ_0 , Q_1 and σ_1 , with w and α fixed at 0 and 1, respectively.

Fig. 4.12 shows histograms of per-channel single photoelectron levels, obtained from the ‘Bellamy’ fits, for the four PMTs used in the detector. As mentioned in the preceding section, the PMT gain was not equalized, which is easy to observe in the Figure. The Figure also reveals substantial gain non-uniformities among the channels of a single PMT, confirming that trying to equalize average PMT gain without a multi-channel acquisition would require a significant amount of work. One would need to measure every single channel of each of the PMTs and subsequently average the results. Achieving proper equalization of the PMT gain would, quite possibly, require at least two iterations of the process.

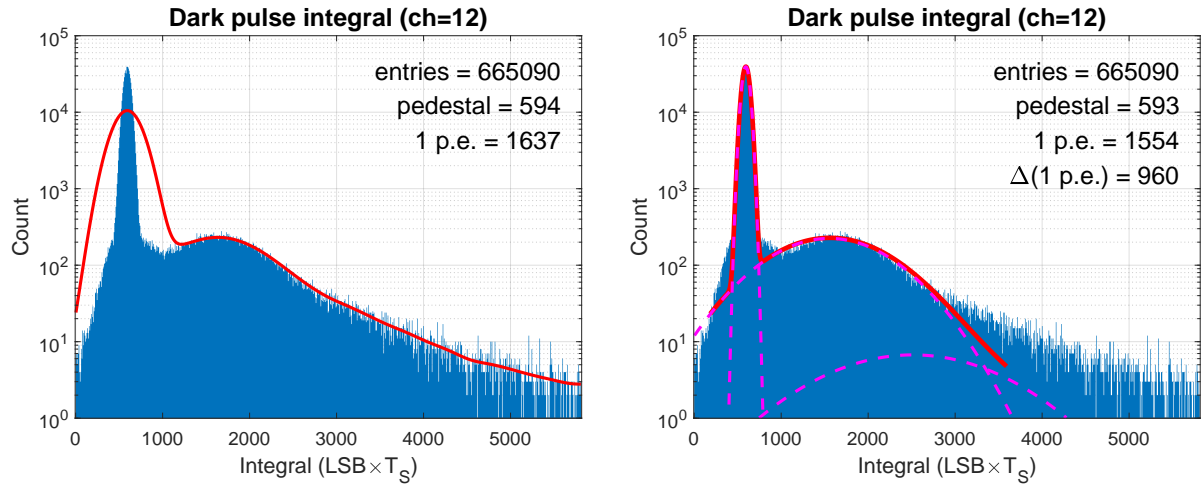


Figure 4.11: ‘Dark’ section of the example histogram of integrals for a single channel. *Left:* Red curve shows results of filtering with an adaptive Gaussian filter. The filtered curve is used to determine initial locations of pedestal and single photoelectron peaks. *Right:* Final fit done using a model of the PMT response proposed by Bellamy et al. [169]. Dashed purple lines show Gaussians comprising the fit, while the red curve shows the overall result over the fitted range of the histogram. The areas under the Gaussians follow the Poisson distribution. $\Delta(1\text{p.e.})$ denotes value of integral of the single photoelectron response.

Parameter	Description
A	Scaling factor
μ	Mean number of photoelectrons collected by the first dynode
n	Number of the Gaussian peak in an ideal PMT response (i.e. number of photoelectrons in a particular event)
$G_n(x)$	Ideal response to n photoelectrons – a convolution of n ideal single photoelectron responses
w	Probability that events are accompanied by a ‘type II’ background events (modeled by exponential distribution)
α	Coefficient of exponential decrease of ‘type II’ background
Q_0	Mean pedestal charge
σ_0	Standard deviation of the pedestal
Q_1	Mean anode charge corresponding to the single photoelectron response
σ_1	Standard deviation of the single photoelectron response
Q_n	Mean of an ideal response to n photoelectrons $G_n(x)$
σ_n	Standard deviation of an ideal response to n photoelectrons $G_n(x)$
$\text{erf}(x)$	Error function
$\text{sign}(x)$	Sign function

Table 4.5: Description of the symbols used in the formulas proposed by Bellamy et al. [169]

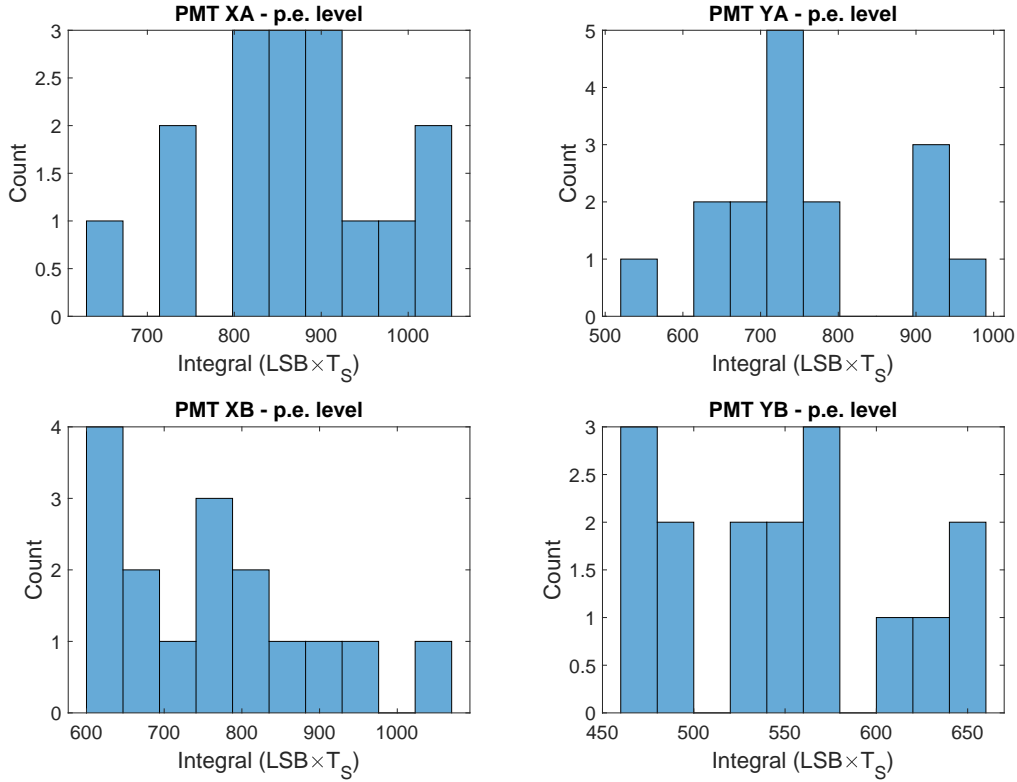


Figure 4.12: Histograms of per-channel integrals of single photoelectron response, for each of the PMTs.

The estimation of the average photoelectron level in particular channels involved yet another fitting using the Bellamy formula. Since both the pedestal level and the single photoelectron gain were already known from the previous analysis of the ‘dark’ section of the integral histograms, it was possible to restrict the free parameters of the fit to just the scaling factor and the average number of photoelectrons. Fig. 4.13 presents an example result of this fitting, which had good agreement with the data. The performance of the fit for other channels of the detector was similar to that shown in Fig.4.13.

Fig. 4.14 shows the final estimation of the mean of the average number of photoelectrons observed in all the channels of the detector. For convenience, the left plot once again shows the full histogram for one of the channels, this time with overlaid fit waveforms. The right plot presents a histogram of average signal levels calculated for every channel of the detector. The mean average signal level was $17.1 (\pm 1.1)$ photoelectrons per single minimum ionizing particle – remarkably close to the expectation calculated in section 3.3, which was 17.3 photoelectrons (Eq. 3.10).

4.2.4 Timing Resolution

The timing resolution was estimated from recorded waveforms, by making a histogram of differences between calculated hit times for the ‘X’ and the ‘Y’ fibers, for every X-Y

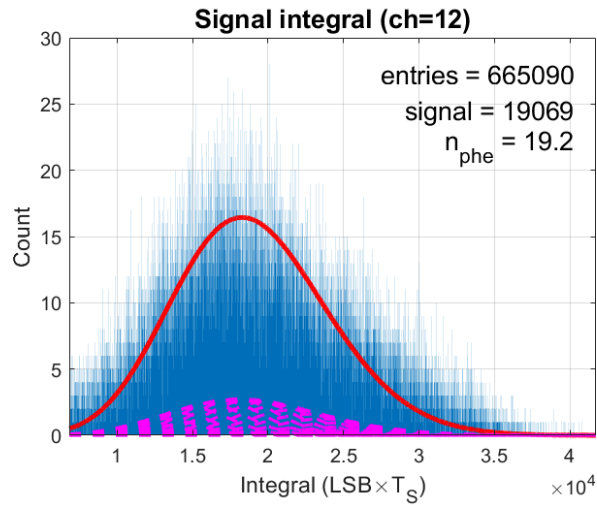


Figure 4.13: ‘Signal’ section of an example histogram of integrals from pulses registered for a single channel. The red curve shows the fit made with the Bellamy formula [169], while the dashed magenta lines show individual Gaussians corresponding to a discrete number of photoelectrons. The only two free parameters of the fit were the scale factor and the mean number of photoelectrons. Parameterization of the pedestal and the single photoelectron response was done previously during an analysis of the ‘dark’ section of the integrals histogram.

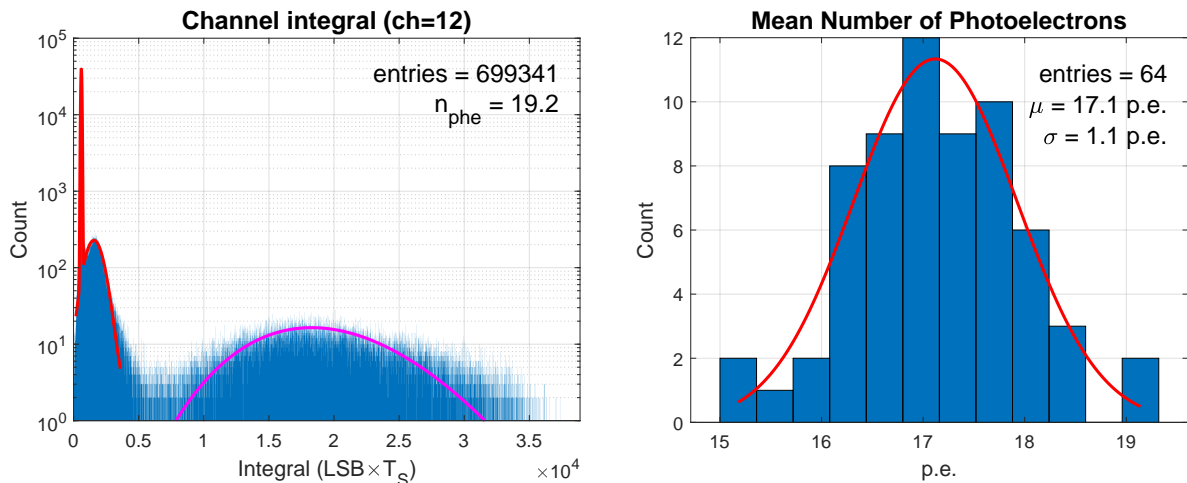


Figure 4.14: *Left*: Example charge spectrum from a single channel, with combined fits of the ‘dark’ (red) and ‘signal’ (magenta) parts of the histogram. *Right*: Histogram of a mean number of average signal levels observed in the detector channels.

coincidence. The hit time of each channel was estimated using the digital constant fraction discriminator (CFD) algorithm. Given the fact that every channel had a slightly different constant delay, a delay map was created by calculating mean $t_x - t_y$ times for every point of the detector, thus removing this systematic error (Fig. 4.15).

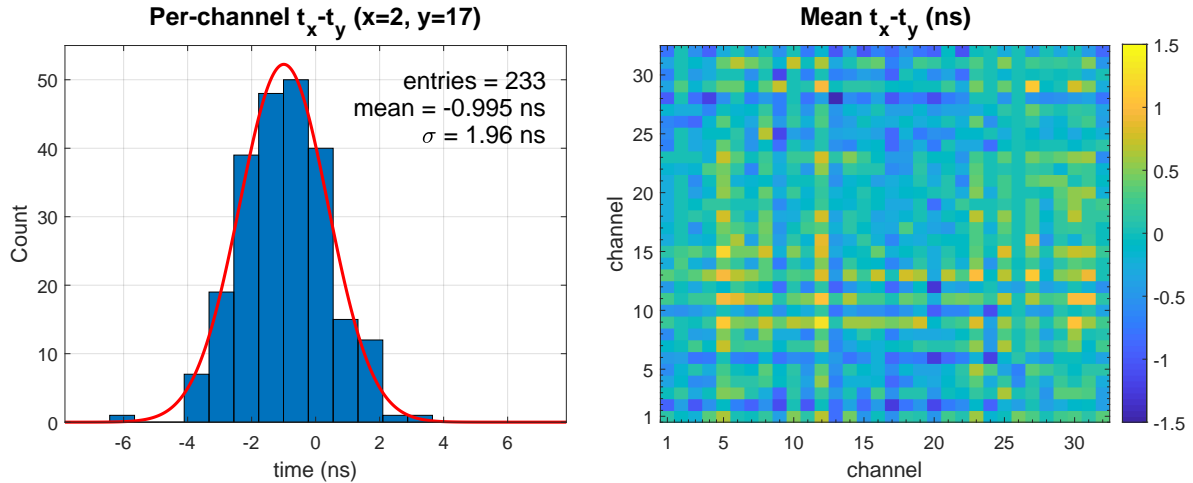


Figure 4.15: *Left:* Example histogram of $t_x - t_y$ delays for a single channel. *Right:* Map of mean $t_x - t_y$ delays for every point of the detector.

Afterward, a histogram of delay-adjusted $t_x - t_y$ differences was created (Fig. 4.16). Performing a Gaussian fit to the histogram gave a value of $\sigma = 1.88$ ns. Given the fact that noise in each of the channels is uncorrelated, the average timing resolution of a single channel was $\sigma_{ch} = 1.88/\sqrt{2} \cong 1.32$ ns. Even though the above result was sufficient for our tests at the low-intensity electron beam (a few tens of kHz), it was far worse than the expected 270 ps (Eq. 3.44). Furthermore, the results described in the literature, measured under similar conditions – i.e., the same scintillating fiber and photomultiplier types, histograms of time differences between two channels fired by the same particle, and signal level between 10 to 22 photoelectrons, report time resolutions between $\sigma_{ch} = 330$ ps and $\sigma_{ch} = 360$ ps [2, 3] – not that far from the expectation. Therefore, the above issue was something that certainly deserved a closer look.

The three factors that impact the timing accuracy of the digital constant fraction algorithm are the slope of the signal edge, the noise at the input, and the timebase jitter (Eq. 2.114 to Eq. 2.116). Since the edges of the signal matched the expectations (Fig. 4.4 and Fig. 4.6), the obvious candidate for the leading cause of the observed inferior timing resolution was the noise – or, more precisely, insufficient signal to noise ratio.

Fig. 4.17 presents persistence plots of noise waveforms. It is not difficult to notice a relatively broad distribution of the recorded segments – well above a single LSB (least significant bit), as well as the presence of some deterministic components. Of the two plots shown in the figure, the right one is more important, as it shows the same segments after the subtraction of the pedestal estimate, as those are the waveforms processed with the

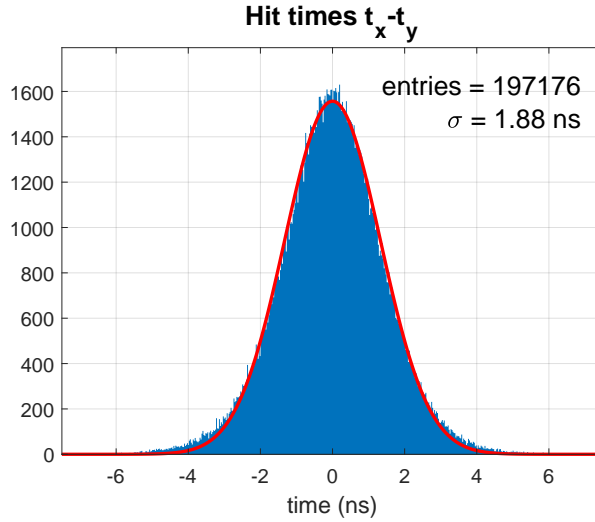


Figure 4.16: Timing resolution of the detector measured based on $t_x - t_y$ differences, after correcting for mean per-point $t_x - t_y$ differences.

digital CFD algorithm. The pedestal estimate was calculated as a mean of a rectangular window that spanned eight samples (indexes 2 to 9) before the second rectangular window used to calculate signal integral (samples 12 to 23). The blurring of waveforms outside the pedestal estimation window indicates that there are low-frequency components (either interference or noise), uncorrelated to the trigger of the system from the passing particles.

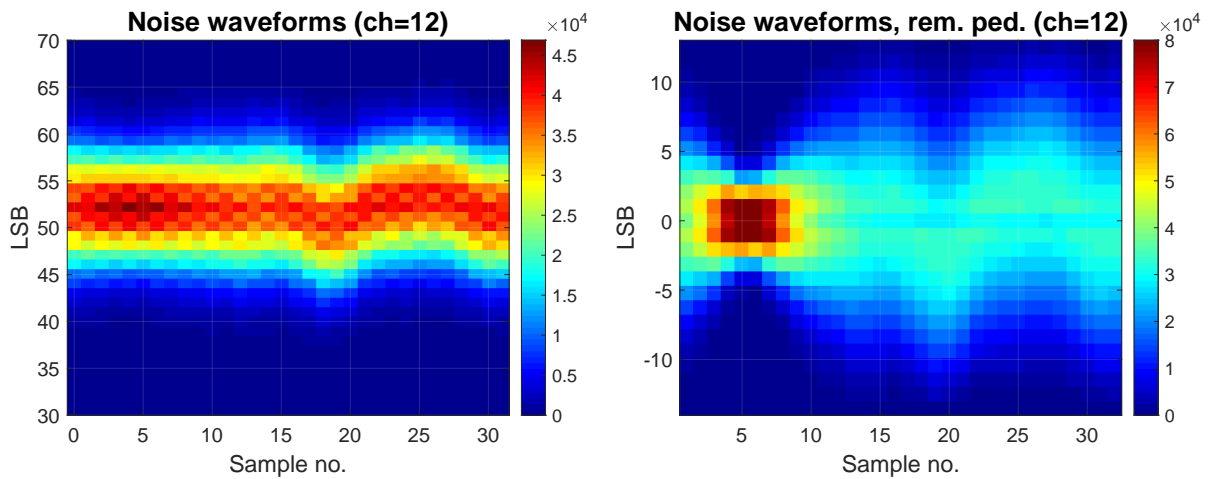


Figure 4.17: *Left:* Persistence plot of buffers containing only noise samples. *Right:* Persistence plot of the same segments after removing the pedestal. The pedestal estimate was calculated as the average of the samples in a rectangular window that spanned samples with indexes from 2 to 9.

Fig. 4.18 presents a histogram of pedestal estimates calculated for one of the channels of the detector, as well as a histogram of standard deviations calculated for pedestal-subtracted buffers containing only noise waveforms. Fortunately, it seems that subtracting the pedestal cancels a significant fraction of the effects caused by low-frequency noise

or interference components, as the standard deviation of the pedestal-subtracted noise segments is well below that of pedestal estimates – 0.9 LSB vs. 4.3 LSB. Nonetheless, one should mention that pedestal estimation does introduce degradation of the performance of the digital CFD algorithm, as the ‘zero’ level is not a real zero – just a mean of only eight samples, so subject to non-negligible uncertainty, which manifests itself as additional noise in the vertical axis.

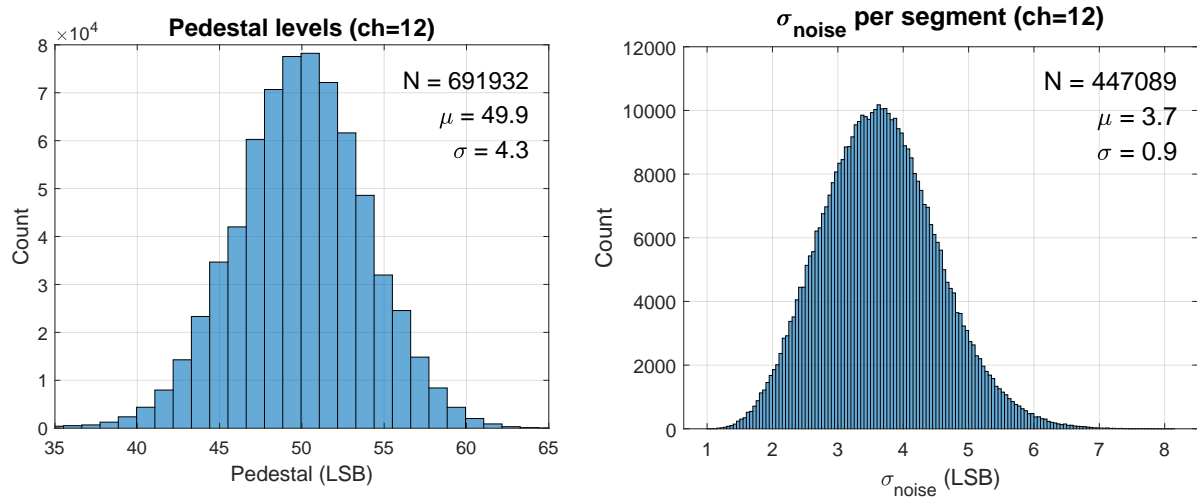


Figure 4.18: *Left*: Histogram of pedestal estimates calculated for an example channel of the detector. *Right*: Histogram of per-event estimates of the standard deviation, calculated for pedestal-subtracted buffers containing noise samples.

A standard practice applied when analyzing the nature of noise present in the system is to calculate its periodogram. Unfortunately, it was not very useful in this case, as 400 ns buffers (32 samples of 12.5 ns each) used by the acquisition system were too short and did not provide sufficient frequency resolution. Nonetheless, computing auto-correlation function and noise covariance matrix (Fig. 4.19) did provide some idea on the nature of the noise present in the system. The most important thing to note are differences in the diagonal of the covariance matrix, which indicates non-ergodicity of the noise process. Since the coordinates of the smallest diagonal elements correspond to the indexes of the samples used to calculate pedestal estimates, it was worth to compare the covariance matrix after the pedestal subtraction with the one calculated for non-processed buffers (Fig. 4.20). One can still observe non-uniformities in the values of the diagonal elements, though not as huge as was the case of pedestal-subtracted segments.

After analyzing the per-channel noise, the next step was to check the signal-to-noise ratio. Fig. 4.21 shows a histogram of signal amplitudes for events recorded for a single channel, along with the calculated SNR. The signal level was significantly higher than the noise, resulting in an excellent SNR – the mean SNR was 57.2 dB, while the minimum still visible in the histogram is around 43 dB. One thing to note, though, is that there

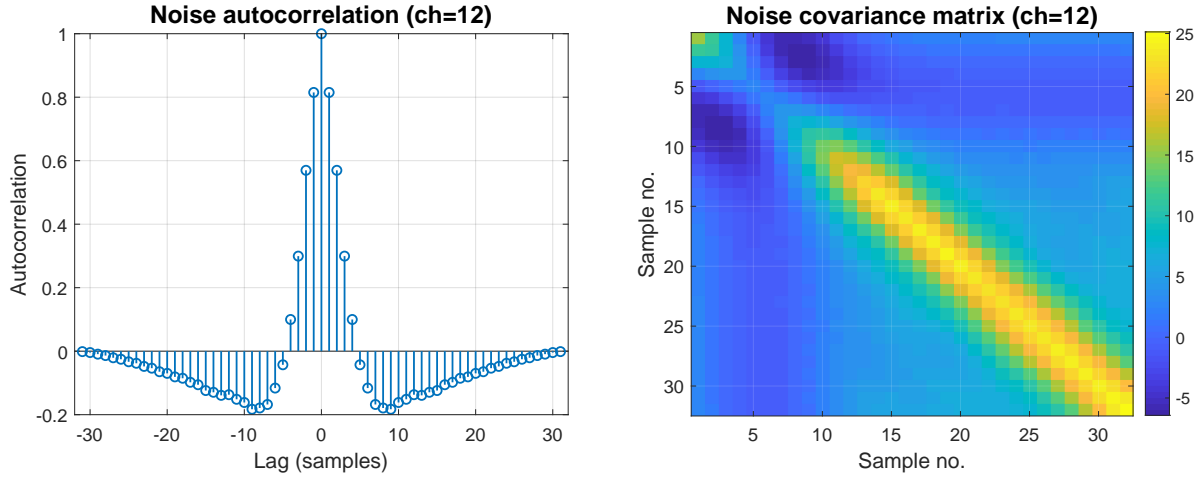


Figure 4.19: *Left*: Autocorrelation function of pedestal-subtracted noise waveforms, calculated for one of the detector’s channels. *Right*: Corresponding noise covariance matrix. Unequal values along the diagonal indicate non-ergodicity of the noise process.

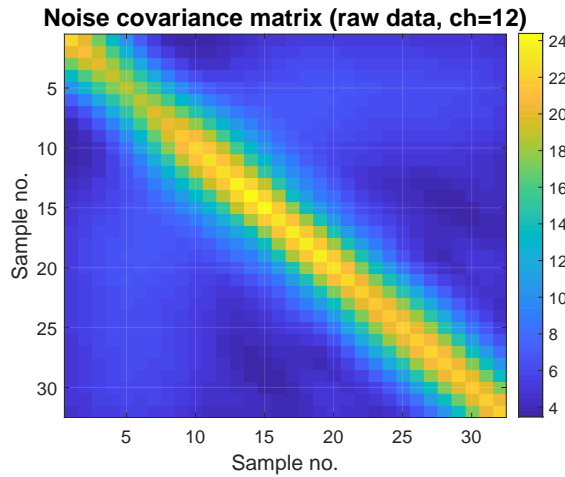


Figure 4.20: Noise covariance matrix calculated on raw data, prior to pedestal subtraction. One can still observe variations of the values of diagonal elements, meaning that even before applying pedestal subtraction the noise process is not ergodic.

is a peak at the high amplitudes, suggesting that a fraction of the pulses saturated the readout circuit. The saturation effect is also clearly observable in the top part of Fig. 4.22.

One of the consequences of saturation-induced cut in the maximum value of the signal pulse is shortening its rise time (Fig. 4.23). That, in turn, may lead to a situation when the leading edge becomes shorter than the delay of the digital CFD algorithm, leading to a slope of the bipolar waveform that is no longer a function of the actual shape of the ‘real’ input signal. Since the time of arrival is estimated from the position of the ‘zero-crossing’ point of the bipolar waveform (see section 2.6.3), the saturation effect can contribute to the errors of the algorithm. Though, judging from the fraction of saturated pulsed compared to the total number of registered signals, it was not considered as a significant error contributor. Nonetheless, it was worth to verify this hypothesis and

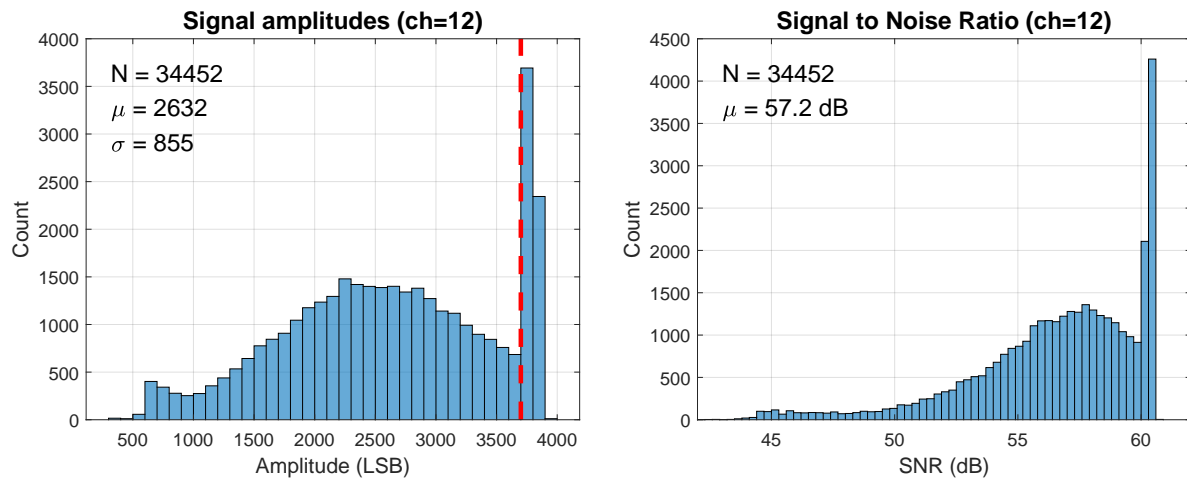


Figure 4.21: *Left:* Histogram of pulse amplitudes for a single channel. The significantly increased occupancy of the bins at the right end is due to the saturation of the readout circuit. The red line marks a cut on signal amplitudes, which was applied to check whether the deterioration of timing resolution results from amplifier saturation. *Right:* Histogram of the corresponding signal-to-noise ratios, calculated on a per-event basis.

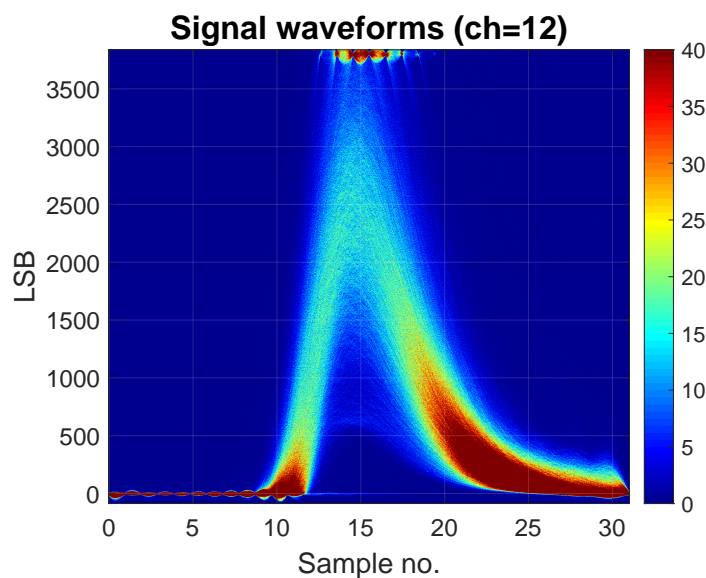


Figure 4.22: Persistence plot of actual signals from the detector recorded for one of the channels. Points in between the samples were reconstructed using the FFT interpolation.

Fig. 4.24 presents the results of the timing resolution study for a case discarding all the events with saturated pulses. There was a small improvement – $\sigma = 1.83$ ns compared to $\sigma = 1.88$ ns for the case with all the events included (Fig. 4.16). Nevertheless, the pulse saturation could not be blamed for the observed degradation of the timing resolution of the detector.

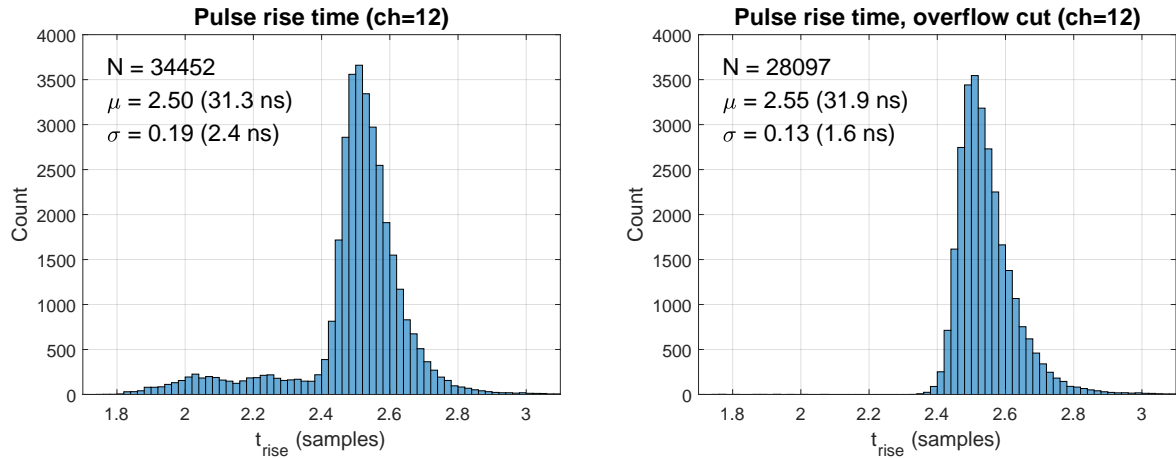


Figure 4.23: *Left*: Histogram of calculated pulse rise times (leading edge) for a single channel. The tail towards shorter times is due to saturation of the readout circuit. Part of the pulse is ‘eaten’ due to exceeding maximum voltage levels tolerated by the circuit, resulting in shorter edges. *Right*: The same histogram calculated for a case with removed saturated pulses.

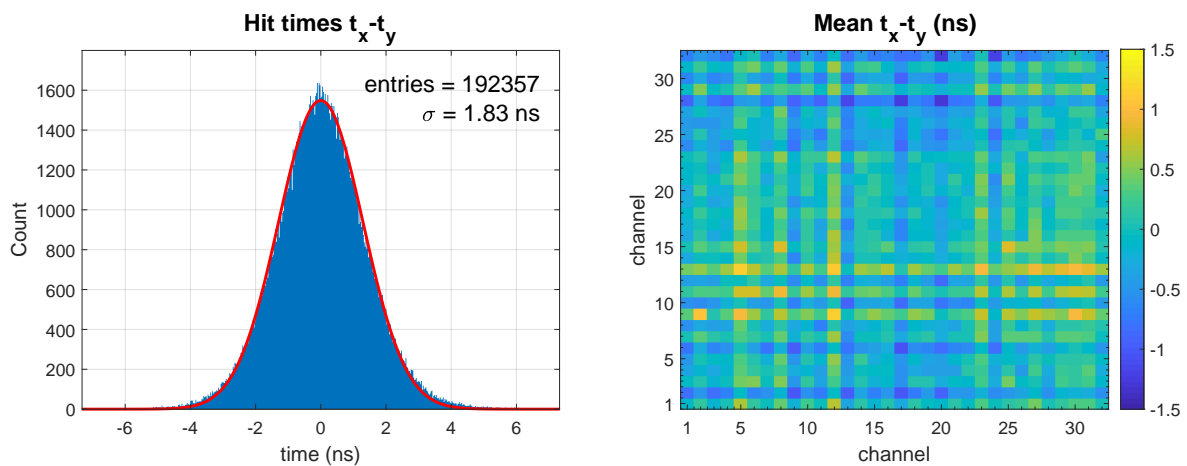


Figure 4.24: Timing resolution of the detector after excluding saturated pulses from the analysis. *Left*: Re-calculated timing resolution of the detector measured based on $t_x - t_y$ differences *Right*: Revised map of mean $t_x - t_y$ delays for every point of the detector.

Another factor that deserved investigation was whether all the channels of the detector exhibit similar performance. Since the method of estimating the timing resolution involved calculating differences in time of pulse arrivals between the ‘X’ and the ‘Y’ planes, differences in per-channel SNR levels or pulse rise times could have lead to deteriorations in the timing resolution, with the worst channels determining the overall accuracy of the

system. Fig. 4.25 presents aggregated results of noise, SNR, and rise time analyses. As can be seen, there were no significant differences in the metrics of the individual channels, thus ruling out yet another potential cause of the lower-than-expected timing performance.

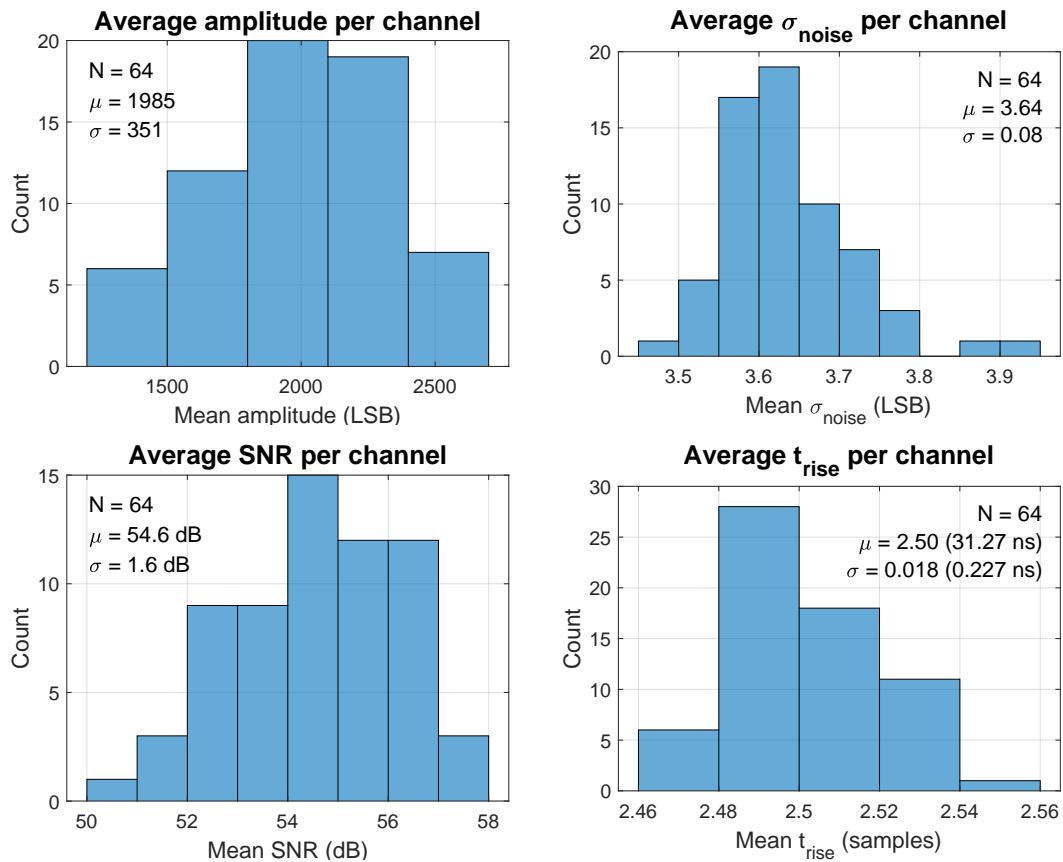


Figure 4.25: Aggregated results for the whole detector. *Top-Left*: Histogram of per-channel mean pulse amplitudes. *Top-Right*: Histogram of per-channel average standard deviation of noise samples. *Bottom-Left*: Histogram of per-channel average SNR. *Bottom-Right*: Histogram of per-channel average pulse rise times.

Since all the channels exhibited decent SNR values and similar pulse rise times, there was a possibility that the leading cause of the timing errors may, in fact, not originate from the noise in the vertical axis. One way to test this hypothesis was to calculate the expected timing resolution according to the theory presented in section 2.6.3. Such a calculation will be presented below for one of the channels.

The first step in this calculation is to select the samples of interest. The applied implementation of the digital CFD algorithm uses a delay of two samples, which means that a total of four samples are used to determine the coordinate of the zero-crossing point. Fig. 4.22 reveals that samples with indexes 11 to 14 might be the right choice for the case of the considered channel. Next, it is necessary to estimate the variance of a single sample. Now, the formulas defined in Eq. 2.114 and Eq. 2.115 were derived assuming noise ergodicity, which is not the case given the form of the noise covariance matrix shown in Fig. 4.19. Nonetheless, if we consider only a four-sample subset, then

the variance does not change a lot, so there would only be a small error associated with using an approximation of noise ergodicity. With the above in mind, the estimate of the sample variance becomes:

$$\overline{\sigma_n^2} = \frac{1}{4} \sum_{k=11}^{14} C(k, k) = \frac{17.3 + 19.5 + 22.0 + 23.6}{4} \cong 20.6 \quad (\text{LSB}^2) \quad (4.9)$$

with k being the sample index and C the calculated noise covariance matrix. Then, denoting the inverted waveform gain as a , the estimated variance of the zero-crossing point of the bipolar waveform that is composed of the sum of the original and the inverted waveform is:

$$\begin{aligned} \overline{\text{Var}(\Delta Y)} = & \\ & \frac{2(1+a^2)}{3} \overline{\sigma_n^2} - \frac{4a}{3} C(13, 11) + \frac{1+a^2}{3} C(12, 11) - \frac{a}{3} C(13, 12) - \frac{a}{3} C(14, 11) \cong \\ & \frac{10}{3} \times 20.6 - \frac{8}{3} \times 15.1 + \frac{5}{3} \times 16.8 - \frac{2}{3} \times 18.8 - \frac{2}{3} \times 12.4 \cong 35.6 \quad (\text{LSB}^2) \quad (4.10) \end{aligned}$$

Translating the above into the variance along the time axis requires the calculation of the slope of the signal. At the CFD delay equal to two samples and the gain of the inverted waveform equal to two, the slope at the zero-crossing point will more-or-less match the slope of the original signal. Therefore, taking into account the results shown in Fig. 4.21 and Fig. 4.23, the estimate of the slope becomes:

$$\left. \frac{dx}{dt} \right|_{t_{zero}} = \frac{0.8 \times 2632}{2.50} \cong 842.2 \quad (\text{LSB}/T_S) \quad (4.11)$$

with T_S denoting the sampling period. Consequently, the resulting variance of the jitter in the horizontal axis is:

$$\overline{\sigma_{time,n}^2} = \frac{\overline{\text{Var}(\Delta Y)}}{(dx/dt|_{t_{zero}})^2} = \frac{35.6}{842.2^2} = \frac{35.6}{709301} \cong 50.2 \times 10^{-6} \quad (T_S^2) \quad (4.12)$$

Translating the above into the time domain yields:

$$\overline{\sigma_{time,n}} = \sqrt{\overline{\sigma_{time,n}^2}} \times T_S = 0.0071 \times 12.5 \times 10^{-9} \cong 88.6 \times 10^{-12} \quad (\text{s}) \quad (4.13)$$

The above result of $\overline{\sigma_{time,n}}$ below 90 ps is more than an order of magnitude better than the observed experimental result. Since, as mentioned before, the SNR and rise time metrics were consistent among the channels, the only viable conclusion was that it was not the vertical axis noise (i.e., voltage and quantization noise) that was responsible for the timing resolution at the nanosecond level. This statement is further supported by the author's studies of the digital CFD algorithm [170], which suggests that at the SNR levels of approx. 55 dB, the timing accuracy should be at the level of approx. 1.5×10^{-3} of the pulse rise time (Fig. 4.26). With the average rise time of 31.27 ns (Fig. 4.25),

the corresponding error contribution should be $\sigma_{time,n} \approx 47$ ps, so even better than the calculation presented in the preceding paragraphs. Even if considering only the lower part of the amplitude spectrum equivalent to SNR around 40 dB, one should still achieve $\sigma_{time,n} \approx 220$ ps.

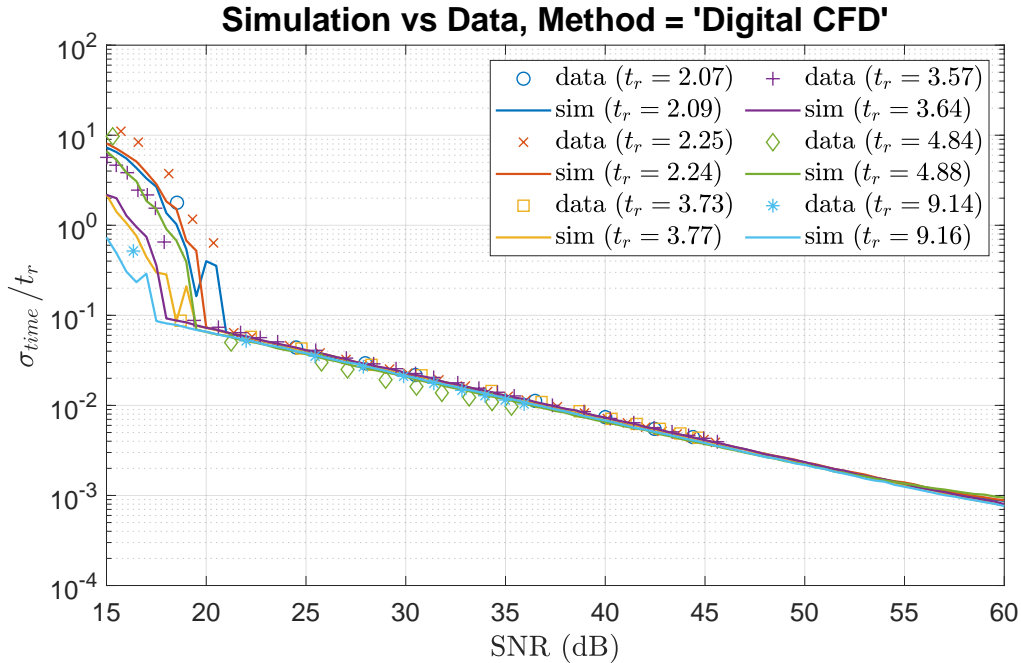


Figure 4.26: Results of author’s study of the timing resolution of the digital constant fraction algorithm, for scenarios with varying pulse rise time and SNR. The t_r denotes the rise time of the pulse and is expressed in samples (i.e. multiples of T_S). Markers correspond to measurement data, solid lines present results of a simulation [170].

The easiest way to try to investigate the problem is to look at the actual waveforms corresponding to the registered events (Fig. 4.27). One can immediately notice shifts among the leading edges of the pulses. Given the fact that the trigger signal from the detector is uncorrelated with the sampling clock, one would expect jumps at the level of only one sample. Plots in Fig. 4.27 reveal that these jumps span more samples, which could indicate an issue with the trigger processing unit, but does not explain roughly single nanosecond jitter. Since all the ADCs use the same clock, synchronized shifts among the buffers should not introduce errors in the time differences between the X and Y planes. Moreover, if the sampling clock of the ADC had such a high jitter level, then the SNR must have been deteriorated. The spread in pulse rise times would also increase, compared to the results from the commissioning phase (Fig. 4.23 and Fig. 4.6). Such effects were not observed, which further complicates the overall picture. So, where is the catch?

The architecture of the MSADC-based acquisition system can provide some hints as to the nature of the problem – or at least point in a direction where one should search for

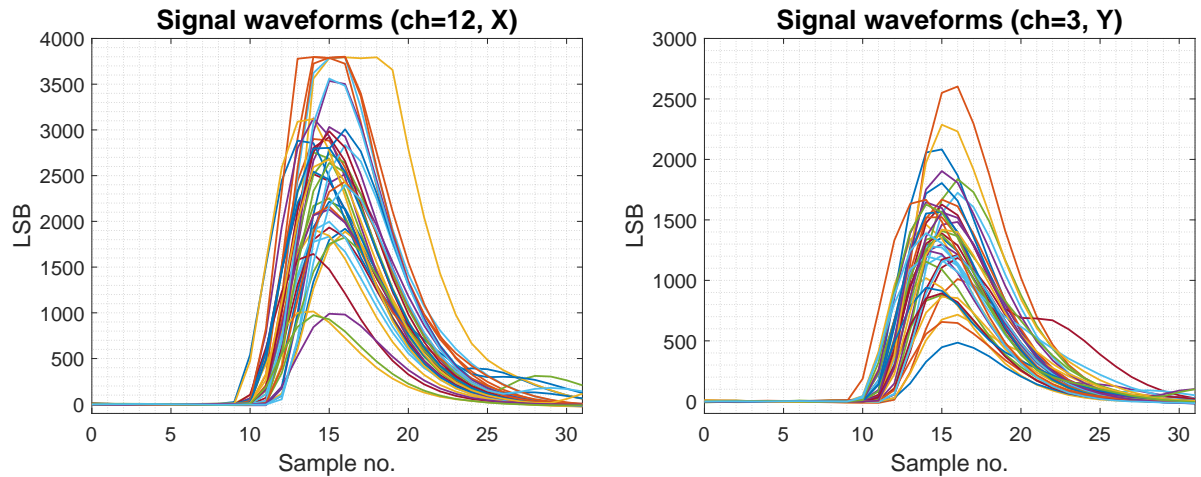


Figure 4.27: Actual signals from the detector for randomly selected channel from (*left*) X and (*right*) Y planes, overlaid on a single plot, 40 waveforms each. One can clearly observe that leading edges and peak locations span over at least four samples.

the cause. The MSADC card is composed of four mezzanine modules, housed on a single carrier card. The carrier card provides power, clock, and control signals to the mezzanines [119]. Now, if the clock distributing circuitry on the carrier card would introduce unequal phase shifts to the clock signals supplied to individual mezzanines while maintaining stable frequency, then one could experience deteriorated timing resolution if calculating it as the time difference between two channels, each digitized with a different mezzanine. Precisely such a method was used in this work. That being said, the author would like to mention that the above statement is a hypothesis only, and dedicated measurements are needed to verify it. Since the MSADC card is a design of another team involved in the COMPASS experiment, making these measurements is beyond the scope of this work. Still, the intention is to investigate the issue and to rectify the problem.

Chapter 5

Summary

The origin of the work presented in this thesis resulted from the author's participation in a different project, related to the design and construction of a new Shashlyk-type electromagnetic calorimeter for the COMPASS experiment. One stage of this process involved a test of the response of a small subset of calorimeter modules to a low-intensity electron beam with well-defined energies, impinging at various positions and with different angles of incidence. This test was performed using the beam provided by the ELSA accelerator in Bonn and required significant changes to the test site, which resulted in a loss of beam tracking capability and inability to generate trigger signals. Consequently, an urgent need arose to build a scintillating fiber hodoscope to provide these functionalities.

The unique aspect of this project was related to timing constraints related to the whole assignment, which had to be completed in a little over three months. Consequently, there was no time to develop a full model of the detector. Instead, the author had to rely on his own experience from previous projects [5, 19, 20, 23–25, 38, 99, 105] and various engineering approximations provided by the theory related to principles governing operation of each element of the detector. Though challenging, these conditions created a compelling scientific case – first to see if the project is at all doable, and then to verify how well one can design a detector relying only on theory and the ‘engineering approximations’ mentioned earlier, without the full numerical model of the detector. Finally, there was a unique opportunity to deepen the understanding of the mechanisms behind its operation.

The presented work covered the full design and manufacturing process of a scintillating fiber detector, followed by a review of its performance. Chapter 2 gave an in-depth study of the theory behind the operation of a scintillating fiber detector, which involved discussion of particle interactions, scintillation and light collection process, the transmission of light through the fiber, photosensors and readout systems. It also described selected methods of data analysis. Chapter 3 showed how to formulate and verify requirements for the detector based on the needs of the physics phenomenon that was to be measured, fol-

lowed by a detailed description of an actual construction process of the detector. Finally, chapter 4 provided an overview of the commissioning process and the real performance of the detector using an electron beam from the ELSA accelerator. The measured performance of the detector was in line with the expectation, except for the timing resolution. An investigation of this discrepancy led to pinpointing a potential issue with the clock system of the MSADC modules. The one thing missing from the performance evaluation is the study of the detector efficiency. However, it was not possible because the detector was the only source of the trigger – and for this type of test, one needs an additional source of a reference trigger, which unfortunately was not available due to modifications of the test site mentioned above.

The project was successful – the detector was built on time and provided adequate performance, allowing the recording of valuable data from the test. The results were presented during conferences¹ [26, 154]. Consequently, in the author’s view, it was beneficial to document the whole experience in an attempt to create a useful reference for anyone that may be involved in a similar project related to the design or construction of a scintillating fiber detector. It was also shown that a deep understanding of the theory is beneficial not only for the construction process but also during the analysis stage, which can help in identifying potential causes of sub-optimal performance. Moreover, certain aspects of this work, especially those related to a review of readout systems and signal processing methods are of general nature and can be applied in other experiments.

¹Some papers do not have the author as the first author – but the beam test was a team project and ordering of authors is alphabetical. The hodoscope project was also a team project involving two people, with the author playing the leading role (coordination, review of the theory, detector design, detector construction – except for front-end circuits, data analysis).

Bibliography

- [1] L. Reiffel and N. S. Kapany. “Some Considerations on Luminescent Fiber Chambers and Intensifier Screens”. In: *Review of Scientific Instruments* 31.10 (Oct. 1960), pp. 1136–1142. ISSN: 0034-6748, 1089-7623. DOI: 10.1063/1.1716826.
- [2] J Bisplinghoff et al. “A scintillating fibre hodoscope for high rate applications”. In: *Nuclear Instruments and Methods in Physics Research Section A: Accelerators, Spectrometers, Detectors and Associated Equipment* 490.1–2 (Sept. 2002), pp. 101–111. ISSN: 0168-9002. DOI: 10.1016/S0168-9002(02)01064-1.
- [3] S Horikawa et al. “Development of a scintillating-fibre detector with position-sensitive photomultipliers for high-rate experiments”. In: *Nuclear Instruments and Methods in Physics Research Section A: Accelerators, Spectrometers, Detectors and Associated Equipment* 516.1 (Jan. 2004), pp. 34–49. ISSN: 0168-9002. DOI: 10.1016/j.nima.2003.07.038.
- [4] S. Horikawa et al. “A scintillating fiber tracker with high time resolution for high-rate experiments”. In: *IEEE Transactions on Nuclear Science* 49.3 (June 2002), pp. 950–956. ISSN: 0018-9499. DOI: 10.1109/TNS.2002.1039596.
- [5] P. Abbon et al. “The COMPASS experiment at CERN”. In: *Nuclear Instruments and Methods in Physics Research Section A: Accelerators, Spectrometers, Detectors and Associated Equipment* 577.3 (July 2007), pp. 455–518. ISSN: 0168-9002. DOI: 10.1016/j.nima.2007.03.026.
- [6] V. M. Abazov et al. “The upgraded DØ detector”. In: *Nuclear Instruments and Methods in Physics Research Section A: Accelerators, Spectrometers, Detectors and Associated Equipment* 565.2 (Sept. 2006), pp. 463–537. ISSN: 0168-9002. DOI: 10.1016/j.nima.2006.05.248.
- [7] G. Suft, G. Anton, R. Bogendörfer, A. Ehmanns, A. Fösel, J. Höfl, H. Kalinowsky, C. Küppersbusch, and D. Walther. “A scintillating fibre detector for the Crystal Barrel experiment at ELSA”. In: *Nuclear Instruments and Methods in Physics Research Section A: Accelerators, Spectrometers, Detectors and Associated Equipment*

- 538.1–3 (Feb. 2005), pp. 416–424. ISSN: 0168-9002. DOI: 10.1016/j.nima.2004.09.029.
- [8] E. Aker et al. “The crystal barrel spectrometer at LEAR”. In: *Nuclear Instruments and Methods in Physics Research Section A: Accelerators, Spectrometers, Detectors and Associated Equipment* 321.1 (Sept. 1992), pp. 69–108. ISSN: 0168-9002. DOI: 10.1016/0168-9002(92)90379-I.
- [9] W. Hillert. “The Bonn Electron Stretcher Accelerator ELSA: Past and future”. In: *The European Physical Journal A - Hadrons and Nuclei* 28.1 (May 2006), pp. 139–148. ISSN: 1434-6001, 1434-601X. DOI: 10.1140/epja/i2006-09-015-4.
- [10] P. Annis. “The CHORUS scintillating fiber tracker and its monitoring systems”. In: *Nuclear Instruments and Methods in Physics Research Section A: Accelerators, Spectrometers, Detectors and Associated Equipment* 409.1–3 (May 1998), pp. 629–633. ISSN: 0168-9002. DOI: 10.1016/S0168-9002(97)01338-7.
- [11] E. Eskut et al. “The CHORUS experiment to search for $\nu(\mu) \rightarrow \nu(\tau)$ oscillation”. In: *Nuclear Instruments and Methods in Physics Research Section A: Accelerators, Spectrometers, Detectors and Associated Equipment* 401.1 (Dec. 1997), pp. 7–44. ISSN: 0168-9002. DOI: 10.1016/S0168-9002(97)00931-5.
- [12] A. Suzuki et al. “Design, construction, and operation of SciFi tracking detector for K2K experiment”. In: *Nuclear Instruments and Methods in Physics Research Section A: Accelerators, Spectrometers, Detectors and Associated Equipment*. Proc. 7th Int. Conf on Instrumentation for colliding Beam Physics 453.1–2 (Oct. 2000), pp. 165–176. ISSN: 0168-9002. DOI: 10.1016/S0168-9002(00)00624-0.
- [13] K. Nishikawa. “Status of K2K (KEK to Kamioka long baseline neutrino oscillation experiment)”. In: *Nuclear Physics B - Proceedings Supplements* 77.1 (May 1999), pp. 198–203. ISSN: 0920-5632. DOI: 10.1016/S0920-5632(99)00418-1.
- [14] The LHCb Collaboration. *LHCb Tracker Upgrade Technical Design Report*. CERN-LHCC-2014-001 ; LHCb-TDR-015. Feb. 21, 2014. URL: <http://cds.cern.ch/record/1647400>.
- [15] The LHCb Collaboration et al. “The LHCb Detector at the LHC”. In: *Journal of Instrumentation* 3.8 (Aug. 1, 2008), S08005. ISSN: 1748-0221. DOI: 10.1088/1748-0221/3/08/S08005.
- [16] B. Beischer, H. Gast, R. Greim, W. Karpinski, T. Kirn, T. Nakada, G. Roper Yearwood, S. Schael, and M. Wlochal. “A high-resolution scintillating fiber tracker with silicon photomultiplier array readout”. In: *Nuclear Instruments and Methods in Physics Research Section A: Accelerators, Spectrometers, Detectors and Asso-*

- ciated Equipment* 622.3 (Oct. 2010), pp. 542–554. ISSN: 0168-9002. DOI: 10.1016/j.nima.2010.07.059.
- [17] M Altmeier et al. “A helical scintillating fiber hodoscope”. In: *Nuclear Instruments and Methods in Physics Research Section A: Accelerators, Spectrometers, Detectors and Associated Equipment* 431.3 (July 1999), pp. 428–436. ISSN: 0168-9002. DOI: 10.1016/S0168-9002(99)00382-4.
- [18] EDDA Collaboration et al. “Proton-Proton Elastic Scattering Excitation Functions at Intermediate Energies”. In: *Physical Review Letters* 78.9 (Mar. 1997), pp. 1652–1655. DOI: 10.1103/PhysRevLett.78.1652.
- [19] K. Abe et al. “The T2K experiment”. In: *Nuclear Instruments and Methods in Physics Research Section A: Accelerators, Spectrometers, Detectors and Associated Equipment* 659.1 (Dec. 11, 2011), pp. 106–135. ISSN: 0168-9002. DOI: 10.1016/j.nima.2011.06.067.
- [20] S. Aoki et al. “The T2K Side Muon Range Detector (SMRD)”. In: *Nuclear Instruments and Methods in Physics Research Section A: Accelerators, Spectrometers, Detectors and Associated Equipment* 698 (Jan. 11, 2013), pp. 135–146. ISSN: 0168-9002. DOI: 10.1016/j.nima.2012.10.001.
- [21] P. -A. Amaudruz et al. “The T2K fine-grained detectors”. In: *Nuclear Instruments and Methods in Physics Research Section A: Accelerators, Spectrometers, Detectors and Associated Equipment* 696 (Dec. 22, 2012), pp. 1–31. ISSN: 0168-9002. DOI: 10.1016/j.nima.2012.08.020.
- [22] I. Chirikov-Zorin, Z. Krumshtein, A. Olchevski, V. Utkin, and P. Zhmurin. “The design of a module of a new electromagnetic calorimeter for COMPASS II”. en. In: *Physics of Particles and Nuclei Letters* 11.3 (May 2014), pp. 252–258. ISSN: 1547-4771, 1531-8567. DOI: 10.1134/S1547477114030066.
- [23] M. Ziembicki, J. Marzec, and M. Dziewiecki. “Monte Carlo study of the time resolution of scintillating fibre detectors”. In: *Measurement Science and Technology* 18.8 (Aug. 1, 2007), p. 2477. ISSN: 0957-0233. DOI: 10.1088/0957-0233/18/8/024.
- [24] M. Ziembicki, A. Nawrot, K. Klimaszewski, P. Zabowski-Zychowicz, M. Dziewiecki, and R. Kurjata. “Construction and performance of a scintillating fiber detector”. In: *IEEE Nuclear Science Symposium Conference Record, 2008. NSS '08*. Oct. 2008, pp. 1191–1194. DOI: 10.1109/NSSMIC.2008.4774615.
- [25] M. Ziembicki et al. “The SMRD Subdetector at the T2K Near Detector Station”. In: *Acta Physica Polonica B* 41.7 (July 2010). WOS:000281068200015, pp. 1579–1584. ISSN: 0587-4254.

- [26] M. Ziembicki et al. “Construction, performance and modeling of a compact SciFihodoscope for use in detector testing at various test beams”. In: *2015 IEEE Nuclear Science Symposium and Medical Imaging Conference (NSS/MIC)*. Oct. 2015, pp. 1–4. DOI: 10.1109/NSSMIC.2015.7581876.
- [27] Joseba Zubia and Jon Arrue. “Plastic Optical Fibers: An Introduction to Their Technological Processes and Applications”. In: *Optical Fiber Technology* 7.2 (Apr. 2001), pp. 101–140. ISSN: 1068-5200. DOI: 10.1006/ofte.2000.0355.
- [28] Shinji Ando. “Optical Properties of Fluorinated Polyimides and Their Applications to Optical Components and Waveguide Circuits”. In: *Journal of Photopolymer Science and Technology* 17.2 (2004), pp. 219–232. DOI: 10.2494/photopolymer.17.219.
- [29] Bo-Tau Liu, Wei-De Yeh, and Wei-Hong Wang. “Preparation of low refractive index fluorinated materials for antireflection coatings”. In: *Journal of Applied Polymer Science* 118.3 (Nov. 5, 2010), pp. 1615–1619. ISSN: 1097-4628. DOI: 10.1002/app.32539.
- [30] Wenqiang Yao, Yongjun Li, and Xiaoyu Huang. “Fluorinated poly(meth)acrylate: Synthesis and properties”. In: *Polymer* 55.24 (Nov. 18, 2014), pp. 6197–6211. ISSN: 0032-3861. DOI: 10.1016/j.polymer.2014.09.036.
- [31] Scientific Polymer Products, Inc. *Refractive Index of Polymers by Index*. URL: <http://scientificpolymer.com/technical-library/refractive-index-of-polymers-by-index/>.
- [32] Kuraray Co. Ltd. *Plastic Scintillating Fibers*. URL: <http://kuraraypsf.jp/psf/>.
- [33] C. Patrignani and Particle Data Group. “Review of Particle Physics”. In: *Chinese Physics C* 40.10 (2016), p. 100001. ISSN: 1674-1137. DOI: 10.1088/1674-1137/40/10/100001.
- [34] Christopher C. Augerson and John M. Messinger. “Controlling the Refractive Index of Epoxy Adhesives with Acceptable Yellowing after Aging”. In: *Journal of the American Institute for Conservation* 32.3 (1993), pp. 311–314. ISSN: 0197-1360. DOI: 10.2307/3179552.
- [35] Martin A. Afromowitz and Kai-Yuen Lam. “Optical Properties Of Curing Epoxies And Applications To The Fiber Optic Composite Cure Sensor”. In: vol. 1170. 1990, pp. 138–142. DOI: 10.1117/12.963091.
- [36] Peter R. Cooper. “Refractive-index measurements of paraffin, a silicone elastomer, and an epoxy resin over the 500–1500-nm spectral range”. In: *Applied Optics* 21.19 (Oct. 1, 1982), pp. 3413–3415. ISSN: 1539-4522. DOI: 10.1364/AO.21.003413.

- [37] S. Aota et al. “Development of fiber-to-fiber connectors for scintillating tile/fiber calorimeters”. In: *Nuclear Instruments and Methods in Physics Research Section A: Accelerators, Spectrometers, Detectors and Associated Equipment* 357.1 (Apr. 1, 1995), pp. 71–77. ISSN: 0168-9002. DOI: 10.1016/0168-9002(94)01523-6.
- [38] Marcin Ziembicki, Piotr Żabowski-Żychowicz, Janusz Marzec, Krzysztof Zaremba, Adam Nawrot, and Andrzej Krypa. “Sposób i urządzenie do łączenia włókien światłowodowych”. Pat. 216879. Henkel Polska Sp. z o.o.; Instytut Radioelektroniki Politechniki Warszawskiej; Instytut Problemów Jądrowych. May 30, 2014.
- [39] K. Hara, K. Horiuchi, S. Kim, I. Nakano, T. Takebayashi, K. Takikawa, K. Yasuoka, M. Koyano, S. Matsui, and H. Takeuchi. “Heat splicing of plastic fibers using a PEEK tube”. In: *Nuclear Instruments and Methods in Physics Research Section A: Accelerators, Spectrometers, Detectors and Associated Equipment* 348.1 (Aug. 21, 1994), pp. 139–146. ISSN: 0168-9002. DOI: 10.1016/0168-9002(94)90852-4.
- [40] Glenn F. Knoll. *Radiation Detection and Measurement*. John Wiley & Sons, Aug. 16, 2010. 857 pp. ISBN: 978-0-470-13148-0.
- [41] Edwin A. Uehling. “Penetration of Heavy Charged Particles in Matter”. In: *Annual Review of Nuclear Science* 4.1 (1954), pp. 315–350. DOI: 10.1146/annurev.ns.04.120154.001531.
- [42] R. M. Sternheimer. “The Density Effect for the Ionization Loss in Various Materials”. In: *Physical Review* 88.4 (Nov. 15, 1952), pp. 851–859. DOI: 10.1103/PhysRev.88.851.
- [43] R. M. Sternheimer and R. F. Peierls. “General Expression for the Density Effect for the Ionization Loss of Charged Particles”. In: *Physical Review B* 3.11 (June 1, 1971), pp. 3681–3692. DOI: 10.1103/PhysRevB.3.3681.
- [44] R. M. Sternheimer, M. J. Berger, and S. M. Seltzer. “Density effect for the ionization loss of charged particles in various substances”. In: *Atomic Data and Nuclear Data Tables* 30.2 (Mar. 1, 1984), pp. 261–271. ISSN: 0092-640X. DOI: 10.1016/0092-640X(84)90002-0.
- [45] Geant4 Collaboration. *Geant4 Physics Reference Manual*. Dec. 9, 2016.
- [46] D. I. Thwaites. “Bragg’s Rule of Stopping Power Additivity: A Compilation and Summary of Results”. In: *Radiation Research* 95.3 (1983), pp. 495–518. ISSN: 0033-7587. DOI: 10.2307/3576096.
- [47] Claude Leroy and Pier-Giorgio Rancoita. *Principles of Radiation Interaction in Matter and Detection*. 2nd ed. DOI: 10.1142/6872. WORLD SCIENTIFIC, Feb. 2009. ISBN: 978-981-281-827-0 978-981-281-829-4.

- [48] Stephen M. Seltzer and Martin J. Berger. “Evaluation of the collision stopping power of elements and compounds for electrons and positrons”. In: *The International Journal of Applied Radiation and Isotopes* 33.11 (Nov. 1, 1982), pp. 1189–1218. ISSN: 0020-708X. DOI: 10.1016/0020-708X(82)90244-7.
- [49] *ESTAR, PSTAR, and ASTAR: Computer Programs for Calculating Stopping-Power and Range Tables for Electrons, Protons, and Helium Ions (version 1.2.3)*. In collab. with M.J. Berger, J.S. Coursey, M.A. Zucker, and J. Chang. Gaithersburg, MD, 2005.
- [50] Donald E. Groom, Nikolai V. Mokhov, and Sergei I. Striganov. “MUON STOPPING POWER AND RANGE TABLES 10 MeV–100 TeV”. In: *Atomic Data and Nuclear Data Tables* 78.2 (July 1, 2001), pp. 183–356. ISSN: 0092-640X. DOI: 10.1006/adnd.2001.0861.
- [51] P. B. Pal, V. P. Varshney, and D. K. Gupta. “Total stopping power formulae for high energy electrons and positrons”. In: *Nuclear Instruments and Methods in Physics Research Section B: Beam Interactions with Materials and Atoms* 16.1 (May 1, 1986), pp. 1–4. ISSN: 0168-583X. DOI: 10.1016/0168-583X(86)90220-X.
- [52] L.D. Landau. “56 - ON THE ENERGY LOSS OF FAST PARTICLES BY IONISATION”. In: *Collected Papers of L.D. Landau*. Ed. by D. TER HAAR. DOI: 10.1016/B978-0-08-010586-4.50061-4. Pergamon, 1965, pp. 417–424. ISBN: 978-0-08-010586-4.
- [53] P. V. Vavilov. “Ionization losses of high-energy heavy particles”. In: *Sov. Phys. JETP* 5 (1957). [*Zh. Eksp. Teor. Fiz.* 32, 920 (1957)], pp. 749–751.
- [54] N. N. Mikheev. “Most probable and average energy losses of the beam of monoenergetic charge particles with average and low energies at multiple scattering”. In: *Journal of Surface Investigation. X-ray, Synchrotron and Neutron Techniques* 4.2 (Apr. 1, 2010), pp. 289–294. ISSN: 1027-4510, 1819-7094. DOI: 10.1134/S1027451010020217.
- [55] Hans Bichsel. “Straggling in thin silicon detectors”. In: *Reviews of Modern Physics* 60.3 (July 1, 1988), pp. 663–699. DOI: 10.1103/RevModPhys.60.663.
- [56] A. B. Migdal. “Bremsstrahlung and Pair Production in Condensed Media at High Energies”. In: *Physical Review* 103.6 (Sept. 15, 1956), pp. 1811–1820. DOI: 10.1103/PhysRev.103.1811.
- [57] Spencer Klein. “Suppression of bremsstrahlung and pair production due to environmental factors”. In: *Reviews of Modern Physics* 71.5 (Oct. 1, 1999), pp. 1501–1538. DOI: 10.1103/RevModPhys.71.1501.

- [58] M. J. Berger and S. M. Seltzer. *Tables of energy losses and ranges of electrons and positrons*. NASA SP-3012. National Aeronautics and Space Administration, Jan. 1, 1964.
- [59] T. O. White. “Scintillating fibres”. In: *Nuclear Instruments and Methods in Physics Research Section A: Accelerators, Spectrometers, Detectors and Associated Equipment* 273.2 (Dec. 15, 1988), pp. 820–825. ISSN: 0168-9002. DOI: 10.1016/0168-9002(88)90102-7.
- [60] R. C. Ruchti. “The Use of Scintillating Fibers for Charged-Particle Tracking”. In: *Annual Review of Nuclear and Particle Science* 46.1 (1996), pp. 281–319. DOI: 10.1146/annurev.nucl.46.1.281.
- [61] Ph Rebourgeard et al. “Fabrication and measurements of plastic scintillating fibers”. In: *Nuclear Instruments and Methods in Physics Research Section A: Accelerators, Spectrometers, Detectors and Associated Equipment* 427.3 (May 1999), pp. 543–567. ISSN: 0168-9002. DOI: 10.1016/S0168-9002(99)00053-4.
- [62] A. Alfieri, A. B. Cavalcante, C. Joram, and M. W. Kenzie. *An experimental set-up to measure Light Yield of Scintillating Fibres*. LHCb-PUB-2015-012. CERN, Feb. 7, 2015.
- [63] J. B. Birks. “Scintillations from Organic Crystals: Specific Fluorescence and Relative Response to Different Radiations”. In: *Proceedings of the Physical Society. Section A* 64.10 (1951), p. 874. ISSN: 0370-1298. DOI: 10.1088/0370-1298/64/10/303.
- [64] D. Albers et al. “Studies on scintillating fiber response”. In: *Nuclear Instruments and Methods in Physics Research Section A: Accelerators, Spectrometers, Detectors and Associated Equipment* 371.3 (Mar. 11, 1996), pp. 388–396. ISSN: 0168-9002. DOI: 10.1016/0168-9002(95)01005-X.
- [65] A. E. Baulin et al. “Attenuation length and spectral response of Kuraray SCSF-78MJ scintillating fibres”. In: *Nuclear Instruments and Methods in Physics Research Section A: Accelerators, Spectrometers, Detectors and Associated Equipment* 715 (July 1, 2013), pp. 48–55. ISSN: 0168-9002. DOI: 10.1016/j.nima.2013.03.027.
- [66] Z. Papandreou et al. *BCAL Scintillating Fibre Performance: Half Way Milestone*. Technical Report GlueX-doc-1647. University of Regina, Dec. 2010.
- [67] T. D. Beattie et al. “Light yield of Kuraray SCSF-78MJ scintillating fibers for the Gluex barrel calorimeter”. In: *Nuclear Instruments and Methods in Physics Research Section A: Accelerators, Spectrometers, Detectors and Associated Equipment* 767 (Dec. 11, 2014), pp. 245–251. ISSN: 0168-9002. DOI: 10.1016/j.nima.2014.08.038.

- [68] C. P. Achenbach and J. H. Cobb. “Computational studies of light acceptance and propagation in straight and curved multimodal active fibres”. In: *Journal of Optics A: Pure and Applied Optics* 5.3 (2003), p. 239. ISSN: 1464-4258. DOI: 10.1088/1464-4258/5/3/316.
- [69] Jonathan D. Weiss. “Trapping efficiency of fluorescent optical fibers”. In: *Optical Engineering* 54.2 (2015), pp. 027101–027101. ISSN: 0091-3286. DOI: 10.1117/1.OE.54.2.027101.
- [70] C. P. Achenbach. “Active optical fibres in modern particle physics experiments”. In: *arXiv:nucl-ex/0404008* (Apr. 5, 2004). arXiv: nucl-ex/0404008.
- [71] C. D’Ambrosio, H. Leutz, M. Taufer, T. Shimizu, O. Shinji, and J. Sun. “Reflection losses in polystyrene fibres”. In: *Nuclear Instruments and Methods in Physics Research Section A: Accelerators, Spectrometers, Detectors and Associated Equipment* 306.3 (Sept. 1, 1991), pp. 549–556. ISSN: 0168-9002. DOI: 10.1016/0168-9002(91)90051-Q.
- [72] Mikhail N. Polyanskiy. *Refractive index database*. URL: <https://refractiveindex.info/>.
- [73] Simon Nieswand. “Measurement of the exit characteristics of light from optical multimode plastic fibres”. M.Sc. Thesis. Aachen: Fakultät für Mathematik, Informatik und Naturwissenschaften der Rheinisch-Westfälischen Technischen Hochschule, Dec. 2014. 94 pp.
- [74] S. Agostinelli et al. “Geant4—a simulation toolkit”. In: *Nuclear Instruments and Methods in Physics Research Section A: Accelerators, Spectrometers, Detectors and Associated Equipment* 506.3 (July 1, 2003), pp. 250–303. ISSN: 0168-9002. DOI: 10.1016/S0168-9002(03)01368-8.
- [75] J. Allison et al. “Geant4 developments and applications”. In: *IEEE Transactions on Nuclear Science* 53.1 (Feb. 2006), pp. 270–278. ISSN: 0018-9499. DOI: 10.1109/TNS.2006.869826.
- [76] J. Allison et al. “Recent developments in Geant4”. In: *Nuclear Instruments and Methods in Physics Research Section A: Accelerators, Spectrometers, Detectors and Associated Equipment* 835 (Nov. 1, 2016), pp. 186–225. ISSN: 0168-9002. DOI: 10.1016/j.nima.2016.06.125.
- [77] G. E. Giakoumakis. “Matching factors for various light-source—Photodetector combinations”. In: *Applied Physics A* 52.1 (Jan. 1, 1991), pp. 7–9. ISSN: 0947-8396, 1432-0630. DOI: 10.1007/BF00323677.

- [78] S. Baccaro et al. “Radiation Damage Tests on Diamond and Scintillation Detector Components for the ITER Radial Neutron Camera”. In: *IEEE Transactions on Nuclear Science* 65.8 (Aug. 2018), pp. 2046–2053. ISSN: 0018-9499. DOI: 10.1109/TNS.2018.2807841.
- [79] E. Garutti and Yu. Musienko. “Radiation damage of SiPMs”. In: *Nuclear Instruments and Methods in Physics Research Section A: Accelerators, Spectrometers, Detectors and Associated Equipment*. Silicon Photomultipliers: Technology, Characterisation and Applications 926 (May 11, 2019), pp. 69–84. ISSN: 0168-9002. DOI: 10.1016/j.nima.2018.10.191.
- [80] Yu. Musienko, A. Heering, R. Ruchti, M. Wayne, A. Karneyeu, and V. Postoev. “Radiation damage studies of silicon photomultipliers for the CMS HCAL phase I upgrade”. In: *Nuclear Instruments and Methods in Physics Research Section A: Accelerators, Spectrometers, Detectors and Associated Equipment*. New Developments in Photodetection NDIP14 787 (July 1, 2015), pp. 319–322. ISSN: 0168-9002. DOI: 10.1016/j.nima.2015.01.012.
- [81] M. Moll, E. Fretwurst, and G. Lindström. “Leakage current of hadron irradiated silicon detectors – material dependence”. In: *Nuclear Instruments and Methods in Physics Research Section A: Accelerators, Spectrometers, Detectors and Associated Equipment* 426.1 (Apr. 21, 1999), pp. 87–93. ISSN: 0168-9002. DOI: 10.1016/S0168-9002(98)01475-2.
- [82] A. G. Wright. *The Photomultiplier Handbook*. Oxford, New York: Oxford University Press, June 22, 2017. 640 pp. ISBN: 978-0-19-956509-2.
- [83] Hamamatsu Photonics K.K. *Photomultiplier Tubes - Basics and Applications*. v3aE. Aug. 27, 2014.
- [84] Burle Technologies. *Photomultiplier Handbook*. 1980.
- [85] S.O. Flyckt and Carole Marmonier. *Photomultiplier Tubes Principles and Applications*. Brive, France: Photonis, 2002.
- [86] Hamamatsu Photonics K.K. *Opto-Semiconductor Handbook*. URL: http://www.hamamatsu.com/jp/en/hamamatsu/overview/bsd/solid_state_division/related_documents.html.
- [87] Andreas Teufel. “Entwicklung und Bau von Hodoskopen aus szintillierenden Fasern für das COMPASS-Experiment”. PhD thesis. Erlangen-Nürnberg: Naturwissenschaftlichen Fakultäten der Universität Erlangen-Nürnberg, 2003.

- [88] W. E. Spicer and F. Wooten. “Photoemission and photomultipliers”. In: *Proceedings of the IEEE* 51.8 (Aug. 1963), pp. 1119–1126. ISSN: 0018-9219. DOI: 10.1109/PROC.1963.2447.
- [89] W. E. Spicer and R. L. Bell. “The III-V Photocathode: A Major Detector Development”. In: *Publications of the Astronomical Society of the Pacific* 84.497 (Feb. 1972), p. 110. ISSN: 1538-3873. DOI: 10.1086/129256.
- [90] Kimitsugu Nakamura, Yasumasa Hamana, Yoshihiro Ishigami, and Toshikazu Matsui. “Latest alkali photocathode with ultra high sensitivity”. In: *Nuclear Instruments and Methods in Physics Research Section A: Accelerators, Spectrometers, Detectors and Associated Equipment*. 1st International Conference on Technology and Instrumentation in Particle Physics 623.1 (Nov. 1, 2010), pp. 276–278. ISSN: 0168-9002. DOI: 10.1016/j.nima.2010.02.220.
- [91] Hamamatsu Photonics K.K. *Photocathode technology*. URL: <http://www.hamamatsu.com/eu/en/technology/innovation/photocathode/index.html>.
- [92] P. Timmer, E. Heine, and H. Peek. “Very low power, high voltage base for a Photo Multiplier Tube for the KM3NeT deep sea neutrino telescope”. In: *Journal of Instrumentation* 5.12 (Dec. 2010), pp. C12049–C12049. ISSN: 1748-0221. DOI: 10.1088/1748-0221/5/12/C12049.
- [93] V. A. Dorofeev, A. V. Ivashin, V. V. Kalendarev, I. A. Katchaev, V. F. Konstantinov, V. D. Matveev, B. F. Polyakov, V. P. Sugonyaev, M. S. Kholodenko, and Y. A. Khokhlov. “A new electromagnetic calorimeter for the updated VES setup”. In: *Instruments and Experimental Techniques* 59.5 (Sept. 1, 2016), pp. 658–665. ISSN: 1608-3180. DOI: 10.1134/S0020441216040175.
- [94] Mikio Yamashita. “Hysteresis Effect in Photomultiplier Gain Variations with Count Rate”. In: *Japanese Journal of Applied Physics* 15.12 (Dec. 1976), p. 2493. ISSN: 1347-4065. DOI: 10.1143/JJAP.15.2493.
- [95] Mikio Yamashita. “Observation of a hysteresis effect in rate-dependent photomultiplier gain variations”. In: *Nuclear Instruments and Methods* 142.3 (May 1, 1977), pp. 435–437. ISSN: 0029-554X. DOI: 10.1016/0029-554X(77)90677-2.
- [96] Mikio Yamashita. “Anomalous gain changes in photomultiplier tubes for use in scintillation counting”. In: *Review of Scientific Instruments* 49.4 (Apr. 1, 1978), pp. 499–502. ISSN: 0034-6748. DOI: 10.1063/1.1135442.
- [97] Mikio Yamashita. “Mechanism of the hysteresis effect in rate-dependent photomultiplier gain variations”. In: *Review of Scientific Instruments* 49.9 (Sept. 1, 1978), pp. 1336–1342. ISSN: 0034-6748. DOI: 10.1063/1.1135580.

- [98] Mikio Yamashita. “Time dependence of rate-dependent photomultiplier gain and its implications”. In: *Review of Scientific Instruments* 51.6 (June 1, 1980), pp. 768–775. ISSN: 0034-6748. DOI: 10.1063/1.1136309.
- [99] Marcin Ziembicki and Michał Dziewiecki. *Nowoczesne techniki kalorymetrii elektromagnetycznej w eksperymentach fizyki wysokich energii*. Raport końcowy IP2010 049570. Warszawa: Politechnika Warszawska, Aug. 16, 2012.
- [100] P. B. Coates. “Thermionic emission from photocathodes”. In: *Journal of Physics D: Applied Physics* 5.8 (Aug. 1972), pp. 1489–1498. ISSN: 0022-3727. DOI: 10.1088/0022-3727/5/8/319.
- [101] M. Calvi, A. Giachero, C. Gotti, M. Maino, C. Matteuzzi, and G. Pessina. “Characterization of a Hamamatsu R7600 multi-anode photomultiplier tube with single photon signals”. In: *Journal of Instrumentation* 8.2 (Feb. 2013), P02012–P02012. ISSN: 1748-0221. DOI: 10.1088/1748-0221/8/02/P02012.
- [102] Ardavan Ghassemi, Kenichi Sato, and Kota Kobayashi. *A technical guide to silicon photomultipliers (MPPC)*. Mar. 2017.
- [103] Claudio Piemonte and Alberto Gola. “Overview on the main parameters and technology of modern Silicon Photomultipliers”. In: *Nuclear Instruments and Methods in Physics Research Section A: Accelerators, Spectrometers, Detectors and Associated Equipment*. Silicon Photomultipliers: Technology, Characterisation and Applications 926 (May 11, 2019), pp. 2–15. ISSN: 0168-9002. DOI: 10.1016/j.nima.2018.11.119.
- [104] Frank Simon. “Silicon photomultipliers in particle and nuclear physics”. In: *Nuclear Instruments and Methods in Physics Research Section A: Accelerators, Spectrometers, Detectors and Associated Equipment*. Silicon Photomultipliers: Technology, Characterisation and Applications 926 (May 11, 2019), pp. 85–100. ISSN: 0168-9002. DOI: 10.1016/j.nima.2018.11.042.
- [105] A. Vacheret et al. “Characterization and simulation of the response of Multi-Pixel Photon Counters to low light levels”. In: *Nuclear Instruments and Methods in Physics Research Section A: Accelerators, Spectrometers, Detectors and Associated Equipment* 656.1 (Nov. 11, 2011), pp. 69–83. ISSN: 0168-9002. DOI: 10.1016/j.nima.2011.07.022.
- [106] D. Marano et al. “Silicon Photomultipliers Electrical Model Extensive Analytical Analysis”. In: *IEEE Transactions on Nuclear Science* 61.1 (Feb. 2014), pp. 23–34. ISSN: 0018-9499. DOI: 10.1109/TNS.2013.2283231.

- [107] S. Cova, M. Ghioni, A. Lacaita, C. Samori, and F. Zappa. “Avalanche photodiodes and quenching circuits for single-photon detection”. In: *Applied Optics* 35.12 (Apr. 20, 1996), pp. 1956–1976. ISSN: 2155-3165. DOI: 10.1364/AO.35.001956.
- [108] S. Seifert, H. T. van Dam, J. Huizenga, R. Vinke, P. Dendooven, H. Lohner, and D. R. Schaart. “Simulation of Silicon Photomultiplier Signals”. In: *IEEE Transactions on Nuclear Science* 56.6 (Dec. 2009), pp. 3726–3733. ISSN: 0018-9499. DOI: 10.1109/TNS.2009.2030728.
- [109] F. Corsi, A. Dragone, C. Marzocca, A. Del Guerra, P. Delizia, N. Dinu, C. Piemonte, M. Boscardin, and G. F. Dalla Betta. “Modelling a silicon photomultiplier (SiPM) as a signal source for optimum front-end design”. In: *Nuclear Instruments and Methods in Physics Research Section A: Accelerators, Spectrometers, Detectors and Associated Equipment*. Frontier Detectors for Frontier Physics 572.1 (Mar. 1, 2007), pp. 416–418. ISSN: 0168-9002. DOI: 10.1016/j.nima.2006.10.219.
- [110] Martin A. Green. “Self-consistent optical parameters of intrinsic silicon at 300K including temperature coefficients”. In: *Solar Energy Materials and Solar Cells* 92.11 (Nov. 1, 2008), pp. 1305–1310. ISSN: 0927-0248. DOI: 10.1016/j.solmat.2008.06.009.
- [111] F. Acerbi, A. Ferri, A. Gola, M. Cazzanelli, L. Pavesi, N. Zorzi, and C. Piemonte. “Characterization of Single-Photon Time Resolution: From Single SPAD to Silicon Photomultiplier”. In: *IEEE Transactions on Nuclear Science* 61.5 (Oct. 2014), pp. 2678–2686. ISSN: 0018-9499. DOI: 10.1109/TNS.2014.2347131.
- [112] Isamu Nakamura. “Radiation damage of pixelated photon detector by neutron irradiation”. In: *Nuclear Instruments and Methods in Physics Research Section A: Accelerators, Spectrometers, Detectors and Associated Equipment*. New Developments In Photodetection NDIP08 610.1 (Oct. 21, 2009), pp. 110–113. ISSN: 0168-9002. DOI: 10.1016/j.nima.2009.05.086.
- [113] T. Tsang, T. Rao, S. Stoll, and C. Woody. “Neutron radiation damage and recovery studies of SiPMs”. In: *Journal of Instrumentation* 11.12 (Dec. 2016), P12002–P12002. ISSN: 1748-0221. DOI: 10.1088/1748-0221/11/12/P12002.
- [114] Pietro P. Calò, Fabio Ciciriello, Savino Petrigiani, and Cristoforo Marzocca. “SiPM readout electronics”. In: *Nuclear Instruments and Methods in Physics Research Section A: Accelerators, Spectrometers, Detectors and Associated Equipment* 926 (May 11, 2019). ISSN: 0168-9002. DOI: 10.1016/j.nima.2018.09.030.
- [115] F. S. Goulding. “Pulse-shaping in low-noise nuclear amplifiers: A physical approach to noise analysis”. In: *Nuclear Instruments and Methods* 100.3 (May 1, 1972), pp. 493–504. ISSN: 0029-554X. DOI: 10.1016/0029-554X(72)90828-2.

- [116] V Radeka. “Low-Noise Techniques in Detectors”. In: *Annual Review of Nuclear and Particle Science* 38.1 (1988), pp. 217–277. DOI: 10.1146/annurev.ns.38.120188.001245.
- [117] A Gorin, A Kuznetsov, I Manuilov, A Riazantsev, A Sidorov, M Kobayashi, K Kuroda, K Okada, and F Takeutchi. “Peak-sensing discriminator for multichannel detectors with cross-talk”. In: *Nuclear Instruments and Methods in Physics Research Section A: Accelerators, Spectrometers, Detectors and Associated Equipment* 452.1 (Sept. 21, 2000), pp. 280–288. ISSN: 0168-9002. DOI: 10.1016/S0168-9002(00)00336-3.
- [118] Ruitong Zheng and Guanhao Wu. “The Constant Fraction Discriminator in Pulsed Time-of-Flight Laser Rangefinding”. In: *Frontiers of Optoelectronics* 5 (Nov. 19, 2011). DOI: 10.1007/s12200-012-0229-2.
- [119] A. B. Mann et al. “The universal sampling ADC readout system of the COMPASS experiment”. In: *2009 IEEE Nuclear Science Symposium Conference Record (NSS/MIC)*. 2009 IEEE Nuclear Science Symposium Conference Record (NSS/MIC). Oct. 2009, pp. 2225–2228. DOI: 10.1109/NSSMIC.2009.5402077.
- [120] J. Fleury, S. Callier, C. de La Taille, N. Seguin, D. Thienpont, F. Dulucq, S. Ahmad, and G. Martin. “Petiroc and Citiroc: front-end ASICs for SiPM read-out andToF applications”. In: *Journal of Instrumentation* 9.1 (Jan. 2014), pp. C01049–C01049. ISSN: 1748-0221. DOI: 10.1088/1748-0221/9/01/C01049.
- [121] D. Impiombato et al. “Characterization and performance of the ASIC (CITIROC) front-end of the ASTRI camera”. In: *Nuclear Instruments and Methods in Physics Research Section A: Accelerators, Spectrometers, Detectors and Associated Equipment* 794 (Sept. 11, 2015), pp. 185–192. ISSN: 0168-9002. DOI: 10.1016/j.nima.2015.05.028.
- [122] S. Blin, S. Callier, S. Conforti Di Lorenzo, F. Dulucq, C. De La Taille, G. Martin-Chassard, and N. Seguin-Moreau. “Performance of CATIROC: ASIC for smart readout of large photomultiplier arrays”. In: *Journal of Instrumentation* 12.3 (Mar. 10, 2017), p. C03041. ISSN: 1748-0221. DOI: 10.1088/1748-0221/12/03/C03041.
- [123] F. Anghinolfi, P. Jarron, F. Krummenacher, E. Usenko, and M. C. S. Williams. “NINO: an ultrafast low-power front-end amplifier discriminator for the time-of-flight detector in the ALICE experiment”. In: *IEEE Transactions on Nuclear Science* 51.5 (Oct. 2004), pp. 1974–1978. ISSN: 0018-9499. DOI: 10.1109/TNS.2004.836048.

- [124] Christian Grewing. “A new ADC chip Vulcan for PMT readout”. In: Next Generation Nucleon Decay and Neutrino Detectors (NNN '16). Beijing, Nov. 2, 2016, p. 21.
- [125] André Zambanini et al. “Test strategy for low failure rates and status of a highly integrated readout chip for PMTs in JUNO”. In: *Proceedings of Topical Workshop on Electronics for Particle Physics — PoS(TWEPP2018)*. Topical Workshop on Electronics for Particle Physics. Antwerp, Belgium: Sissa Medialab, June 6, 2019, p. 145. DOI: 10.22323/1.343.0145.
- [126] Henry W. Ott. *Electromagnetic compatibility engineering*. OCLC: ocn301885689. Hoboken, N.J: John Wiley & Sons, 2009. 843 pp. ISBN: 978-0-470-18930-6.
- [127] Dariusz Makowski. “The Impact of Radiation on Electronic Devices with the Special Consideration of Neutron and Gamma Radiation Monitoring”. PhD thesis. Łódź: Technical University of Łódź, 2006.
- [128] ORTEC-AMETEK. *Fast-Timing Discriminator Introduction*. Aug. 27, 2009.
- [129] J. Wu, Y. Shi, and D. Zhu. “A low-power Wave Union TDC implemented in FPGA”. In: *Journal of Instrumentation* 7.1 (2012), p. C01021. ISSN: 1748-0221. DOI: 10.1088/1748-0221/7/01/C01021.
- [130] M. L. Simpson, G. R. Young, R. G. Jackson, and M. Xu. “A monolithic, constant-fraction discriminator using distributed R-C delay line shaping”. In: *1995 IEEE Nuclear Science Symposium and Medical Imaging Conference Record*. 1995 IEEE Nuclear Science Symposium and Medical Imaging Conference Record. Vol. 1. Oct. 1995, 292–296 vol.1. DOI: 10.1109/NSSMIC.1995.504229.
- [131] S. Y. Kim, G. B. Ko, S. I. Kwon, and J. S. Lee. “Development of a non-delay line constant fraction discriminator based on the Padé approximant for time-of-flight positron emission tomography scanners”. In: *Journal of Instrumentation* 10.1 (2015), P01005. ISSN: 1748-0221. DOI: 10.1088/1748-0221/10/01/P01005.
- [132] M. L. Simpson and M. J. Paulus. “Discriminator design considerations for time-interval measurement circuits in collider detector systems”. In: *IEEE Transactions on Nuclear Science* 45.1 (Feb. 1998), pp. 98–104. ISSN: 0018-9499. DOI: 10.1109/23.659559.
- [133] E. Delagnes, Y. Degerli, P. Goret, P. Nayman, F. Toussenel, and P. Vincent. “SAM: A new GHz sampling ASIC for the H.E.S.S.-II front-end electronics”. In: *Nuclear Instruments and Methods in Physics Research Section A: Accelerators, Spectrometers, Detectors and Associated Equipment*. Proceedings of the 4th International Conference on New Developments in Photodetection BEAUNE 2005 Fourth Inter-

- national Conference on New Developments in Photodetection 567.1 (Nov. 1, 2006), pp. 21–26. ISSN: 0168-9002. DOI: 10.1016/j.nima.2006.05.052.
- [134] S. Ritt. “Design and performance of the 6 GHz waveform digitizing chip DRS4”. In: *2008 IEEE Nuclear Science Symposium Conference Record*. 2008 IEEE Nuclear Science Symposium Conference Record. Oct. 2008, pp. 1512–1515. DOI: 10.1109/NSSMIC.2008.4774700.
- [135] Stuart A. Kleinfelder, Edwin Chiem, and Tarun Prakash. “The SST Multi-G-Sample/s Switched Capacitor Array Waveform Recorder with Flexible Trigger and Picosecond-Level Timing Accuracy”. In: *arXiv:1508.02460 [astro-ph, physics:physics]* (Aug. 10, 2015). arXiv: 1508.02460.
- [136] Jarred M. Roberts, Gary S. Varner, Patrick Allison, Brendan Fox, Eric Oberla, Ben Rotter, and Stefan Spack. “LAB4D: A low power, multi-GSa/s, transient digitizer with sampling timebase trimming capabilities”. In: *Nuclear Instruments and Methods in Physics Research Section A: Accelerators, Spectrometers, Detectors and Associated Equipment* 925 (May 1, 2019), pp. 92–100. ISSN: 0168-9002. DOI: 10.1016/j.nima.2019.01.091.
- [137] Alessandro Bravar. “Digitizers Based on Capacitor Arrays”. Hyper-Kamiokande Proto-Collaboration Meeting. Kashiwa, Japan, July 11, 2016.
- [138] Walt Kester, ed. *Data Conversion Handbook*. Analog Devices. Google-Books-ID: 0aeBS6SgtR4C. Newnes, 2005. 977 pp. ISBN: 978-0-7506-7841-4.
- [139] Eric Delagnes. “What is the theoretical time precision achievable using a dCFD algorithm ?” In: *arXiv:1606.05541 [hep-ex, physics:nucl-ex, physics:physics]* (June 16, 2016). arXiv: 1606.05541.
- [140] R. Abbiati, L. Bertossi, A. Geraci, Emilio Gatti, and Giancarlo Ripamonti. “High-resolution digital online linear procedure for timing of detected events”. In: *IEEE Transactions on Nuclear Science* 53.3 (June 2006), pp. 1270–1274. ISSN: 0018-9499. DOI: 10.1109/TNS.2006.874797.
- [141] V. Radeka and N. Karlovac. “Least-square-error amplitude measurement of pulse signals in presence of noise”. In: *Nuclear Instruments and Methods* 52.1 (June 1, 1967), pp. 86–92. ISSN: 0029-554X. DOI: 10.1016/0029-554X(67)90561-7.
- [142] M. Bertolaccini, C. Bussolati, S. Cova, I. De Lotto, and E. Gatti. “Optimum processing for amplitude distribution evaluation of a sequence of randomly spaced pulses”. In: *Nuclear Instruments and Methods* 61.1 (Apr. 15, 1968), pp. 84–88. ISSN: 0029-554X. DOI: 10.1016/0029-554X(68)90453-9.

- [143] E. Gatti, P. F. Manfredi, M. Sampietro, and V. Speziali. “Suboptimal filtering of 1/f-noise in detector charge measurements”. In: *Nuclear Instruments and Methods in Physics Research Section A: Accelerators, Spectrometers, Detectors and Associated Equipment* 297.3 (Dec. 10, 1990), pp. 467–478. ISSN: 0168-9002. DOI: 10.1016/0168-9002(90)91331-5.
- [144] E. Gatti, A. Geraci, and G. Ripamonti. “Automatic synthesis of optimum filters with arbitrary constraints and noises: a new method”. In: *Nuclear Instruments and Methods in Physics Research Section A: Accelerators, Spectrometers, Detectors and Associated Equipment* 381.1 (Oct. 21, 1996), pp. 117–127. ISSN: 0168-9002. DOI: 10.1016/0168-9002(96)00653-5.
- [145] S. Riboldi, A. Geraci, R. Abbiati, Emilio Gatti, and Giancarlo Ripamonti. “A new method for LMS synthesis of optimum finite impulse response (FIR) filters with arbitrary time and frequency constraints and noises”. In: *2002 IEEE Nuclear Science Symposium Conference Record*. 2002 IEEE Nuclear Science Symposium Conference Record. Vol. 1. Nov. 2002, 198–202 vol.1. DOI: 10.1109/NSSMIC.2002.1239298.
- [146] E. Gatti, A. Geraci, S. Riboldi, and G. Ripamonti. “Digital Penalized LMS method for filter synthesis with arbitrary constraints and noise”. In: *Nuclear Instruments and Methods in Physics Research Section A: Accelerators, Spectrometers, Detectors and Associated Equipment* 523.1 (May 1, 2004), pp. 167–185. ISSN: 0168-9002. DOI: 10.1016/j.nima.2003.12.032.
- [147] V. Olshevsky and L. Sakhnovich. “Matched Filtering for Generalized Stationary Processes”. In: *IEEE Transactions on Information Theory* 51.9 (Sept. 2005), pp. 3308–3313. ISSN: 0018-9448. DOI: 10.1109/TIT.2005.853319.
- [148] S. Riboldi, R. Abbiati, A. Geraci, and Emilio Gatti. “Experimental Comparison of State-of-the-Art Methods for Digital Optimum Filter Synthesis With Arbitrary Constraints and Noise”. In: *IEEE Transactions on Nuclear Science* 52.4 (Aug. 2005), pp. 954–958. ISSN: 0018-9499. DOI: 10.1109/TNS.2005.852649.
- [149] Wen Xiangyang and Wei Yixiang. “Constrained digital matched filter method for optimum filter synthesis”. In: *Nuclear Instruments and Methods in Physics Research Section A: Accelerators, Spectrometers, Detectors and Associated Equipment* 560.2 (May 10, 2006), pp. 346–351. ISSN: 0168-9002. DOI: 10.1016/j.nima.2005.12.199.
- [150] R. Abbiati, A. Geraci, Emilio Gatti, and Giancarlo Ripamonti. “Application of a Digital Technique for Timing of Events From Scintillation Detectors”. In: *IEEE*

- Transactions on Nuclear Science* 53.6 (Dec. 2006), pp. 3850–3854. ISSN: 0018-9499. DOI: 10.1109/TNS.2006.885222.
- [151] F. Gautheron et al. *COMPASS-II Proposal*. CERN-SPSC-2010-014 ; SPSC-P-340. May 17, 2010. URL: <https://cds.cern.ch/record/1265628>.
- [152] Andrzej Sandacz. “The GPD program at COMPASS”. In: *arXiv:1509.07732 [hep-ex]* (Sept. 25, 2015). arXiv: 1509.07732.
- [153] N. Anfimov et al. “Shashlyk EM calorimeter prototype readout by MAPD with superhigh pixel density for COMPASS II”. In: *Nuclear Instruments and Methods in Physics Research Section A: Accelerators, Spectrometers, Detectors and Associated Equipment*. Proceedings of the 12th Pisa Meeting on Advanced Detectors La Biodola, Isola d’Elba, Italy, May 20 – 26, 2012 718 (Aug. 1, 2013), pp. 75–77. ISSN: 0168-9002. DOI: 10.1016/j.nima.2012.11.104.
- [154] M. Dziewiecki et al. “Study of a 3x3 module array of the ECAL0 calorimeter with an electron beam at the ELSA”. In: *Journal of Physics: Conference Series* 587.1 (2015), p. 012040. ISSN: 1742-6596. DOI: 10.1088/1742-6596/587/1/012040.
- [155] *Electron Stretcher and Accelerator ELSA*. URL: http://www-elsa.physik.uni-bonn.de/index_en.html.
- [156] H. Schmieden. “Physics at ELSA”. In: *NSTAR 2007*. DOI: 10.1007/978-3-540-85144-8_3. Springer Berlin Heidelberg, 2008, pp. 14–19.
- [157] B. Bantes et al. “The bgo-od experiment at elsa”. In: *International Journal of Modern Physics: Conference Series* 26 (Jan. 1, 2014), p. 1460093. DOI: 10.1142/S2010194514600933.
- [158] The CBELSA/TAPS Collaboration. *Crystal Barrel: Homepage*. URL: <https://www1.cb.uni-bonn.de/index.php?id=4&L=1>.
- [159] Hamamatsu Photonics K.K. *Multianode Photomultiplier Tube Assemblies H8711 Series*. Nov. 2010.
- [160] Henkel Corporation. *LOCTITE LB 8104 - Technical Data Sheet*. URL: http://www.henkel-adhesives.co.uk/2838_UKE_HTML.htm?nodeid=8797715529729.
- [161] Dong-Hoon Lee, Sang-Hoon Rah, and Ie-Na Yoon. “Refractive Change Caused Silicone Oil Adhesion to the Intraocular Lens Following Nd:YAG Posterior Capsulotomy”. In: *Korean Journal of Ophthalmology : KJO* 23.4 (Dec. 2009), pp. 309–311. ISSN: 1011-8942. DOI: 10.3341/kjo.2009.23.4.309.

- [162] A. Mann, I. Konorov, and S. Paul. “A Versatile Sampling ADC System for On-Detector Applications and the AdvancedTCA Crate Standard”. In: *2007 15th IEEE-NPSS Real-Time Conference*. 2007 15th IEEE-NPSS Real-Time Conference. Apr. 2007, pp. 1–5. DOI: 10.1109/RTC.2007.4382728.
- [163] Texas Instruments. *ADS5270 8-Channel, 12-Bit, 40 MSPS Analog-to-Digital Converter with Serial LVDS Interface*. Jan. 2009. URL: <http://www.ti.com/lit/ds/symlink/ads5270.pdf>.
- [164] S. Huber, J. Friedrich, B. Ketzer, I. Konorov, M. Kramer, A. Mann, T. Nagel, and S. Paul. “A Digital Trigger for the Electromagnetic Calorimeter at the COMPASS Experiment”. In: *IEEE Transactions on Nuclear Science* 58.4 (Aug. 2011), pp. 1719–1722. ISSN: 0018-9499. DOI: 10.1109/TNS.2011.2152854.
- [165] International Organization for Standardization. *ISO 6344-1:1998 - Coated abrasives – Grain size analysis – Part 1: Grain size distribution test*. ISO. URL: http://www.iso.org/iso/catalogue_detail.htm?csnumber=12643.
- [166] International Organization for Standardization. *ISO 62:2008 - Plastics – Determination of water absorption*. ISO. URL: http://www.iso.org/iso/catalogue_detail.htm?csnumber=41672.
- [167] United Nations Environmental Programme. *Selected radionuclides. Tritium, carbon-14, krypton-85, strontium-90, iodine, caesium 137, radon, plutonium*. World Health Organization (WHO): WHO, 1983. ISBN: 92-4-154085-0.
- [168] E. Amato and D. Lizio. “Plastic materials as a radiation shield for β - sources: a comparative study through Monte Carlo calculation”. In: *Journal of Radiological Protection* 29.2 (May 19, 2009), p. 239. ISSN: 0952-4746. DOI: 10.1088/0952-4746/29/2/010.
- [169] E. H. Bellamy, G. Bellettini, J. Budagov, F. Cervelli, I. Chirikov-Zorin, M. Incagli, D. Lucchesi, C. Pagliarone, S. Tokar, and F. Zetti. “Absolute calibration and monitoring of a spectrometric channel using a photomultiplier”. In: *Nuclear Instruments and Methods in Physics Research Section A: Accelerators, Spectrometers, Detectors and Associated Equipment* 339.3 (Feb. 1, 1994), pp. 468–476. ISSN: 0168-9002. DOI: 10.1016/0168-9002(94)90183-X.
- [170] Marcin Ziembicki. “Photosensors and front-end electronics for the Hyper-Kamiokande experiment”. In: *Nuclear Instruments and Methods in Physics Research Section A: Accelerators, Spectrometers, Detectors and Associated Equipment* (Jan. 22, 2019). ISSN: 0168-9002. DOI: 10.1016/j.nima.2019.01.055.

List of Acronyms

3HF	3-hydroxyflavone
AC	Alternating Current
ADC	Analog to Digital Converter
APD	Avalanche Photodiode
ASIC	Application-Specific Integrated Circuit
ASTAR	A program for calculating stopping power and range tables for helium ions in various materials
CAD	Computer Aided Design
CAMERA	New 4 m long recoil proton detector in the COMPASS experiment
CCD	Charge-Coupled Device
CE	Collection Efficiency
CERN	European Laboratory for Particle Physics
CFD	Constant Fraction Discriminator
CMOS	Complementary Metal-Oxide-Semiconductor
COMPASS	COmmon Muon Proton Apparatus for Structure and Spectroscopy
DAQ	Data Acquisition System
DC	Direct Current
DNL	Differential Non-Linearity
DPLMS	Digital Penalized Least Means Square
ECAL0	Electromagnetic Calorimeter for the COMPASS experiment, closest to the target

ELSA	ELektronen-Stretcher-Anlage
EMI	Electromagnetic Interference
ENBW	Effective Noise Bandwidth
ENOB	Effective Number of Bits
ESTAR	A program calculates stopping power, density effect parameters, range, and radiation yield tables for electrons in various materials
FF	Fill Factor
FFT	Fast Fourier Transform
FIR	Finite Impulse Response
FMECA	Failure Mode, Effects, and Criticality Analysis
FMEDA	Failure Modes, Effects, and Diagnostic Analysis
FP	Fluorinated Polymer
FPGA	Field-Programmable Gate Array
FWHM	Full Width at Half-Maximum
GPD	Generalized Parton Distributions
HV	High Voltage
K2K	KEK to Kamioka
LED	Light-Emitting Diode
LINAC	Linear accelerator
LSB	Least Significant Bit
LV	Low Voltage
MPPC	Multi-Pixel Photon Counter
MSADC	Mezzanine Sampling Analog-to-Digital Converter
MSPS	Mega-Sample per Second
NA	Numerical Aperture
NIM	Nuclear Instrumentation Module

P-MOS	P-channel Metal Oxide Semiconductor transistor
PA6	Aluminum alloy type PA-6
PBBO	2-(4'-biphenyl)-6-phenylbenzoxazole
PBD	2-(4-biphenyl)-5-(4-tert-butylphenyl)-1,3,4-oxadiazole
PDE	Photon Detection Efficiency
PE	Photoelectron
PMMA	Poly(Methyl MethAcrylate
PMP	1-phenyl-3-mesityl-2-pyrazoline
PMT	Photomultiplier Tube
POM-C	Type-C Polyacetal
POPOP	1,4-bis(5-phenyloxazol-2-yl) benzene
PP	Polypropylene
PS	Polystyrene
PSTAR	A program for calculating stopping power and range tables for protons in various materials
PTFE	Polytetrafluoroethylene
PTP	paraterphenyl
PVC	Polyvinyl chloride
PVT	PolyVinylToluene
RC	Resistor-Capacitor
RMS	Root-Mean-Square
RSS	Root-Sum-Square
SBA	Super Bialakali
SCA	Switched Capacitor Array
SciFi	Scintillating Fiber
SHV	Safe High Voltage connector

SINAD	Signal-to-Noise-And-Distortion
SiPM	Silicon Photomultiplier
SNR	Signal-to-Noise Ratio
SPS	Super Proton Synchrotron
SPTR	Single Photon Timing Resolution
T2K	Tokai to Kamioka
TAPS	An experiment at ELSA accelerator in Bonn
TDC	Time to Digital Converter
TT	Transit Time
TTS	Transit Time Spread
UBA	Ultra Bialkali
XPS	Extruded Polystyrene